ON THE BIOMECHANICS OF CELL NUCLEI:
INSIGHTS FROM COMBINED FORCE AND LIGHT MICROSCOPY

Chad Michael Hobson

A dissertation submitted to the faculty at the University of North Carolina at Chapel Hill in partial fulfillment of the requirements for the degree of Doctor of Philosophy in the Department of Physics and Astronomy

Chapel Hill
2021

Approved by:

Richard Superfine

Michael R. Falvo

Kerry Bloom

Wesley Legant

Nicholas M. Law

ABSTRACT

Chad Michael Hobson: On the Biomechanics of Cell Nuclei: Insights from Combined Force and Light Microscopy
(Under the direction of Richard Superfine)

Cell nuclei are multifunctional. Not only do they house and protect the genome, but they additionally provide mechanical stability to the surrounding cell and convert extracellular mechanical cues into biochemical responses. For example, forces exerted upon integrins at the cell surface propagate through the cytoskeleton and into the nucleus, resulting in local stretching of chromatin and transcription upregulation. The mechanical integrity of the nucleus, however, is often compromised in an array of diseases ranging from cancers to laminopathies. These diseases have targeted effects on specific nuclear constituents, and in turn lead to altered cellular migration properties, increases in DNA damage and genomic instability, and compromised nuclear mechanotransduction. Consequently, the mechanobiology of the cell nucleus has garnered increasing attention over the past several decades. Studies in nuclear biomechanics primarily make use of force probes and/or light microscopy to quantify mechanical properties of nuclei and their responses to physical perturbations. In the first half of this thesis, I describe two novel methodologies for studying nuclear mechanobiology. The first is a side-view, light-sheet fluorescence microscope combined with an atomic force microscope (AFM-LS) that enables time-correlated, multi-color, 3D light-sheet imaging coupled with AFM. The second method is a unique combination of light-sheet microscopy and fluorescence recovery after photobleaching (FRAP) known as SPIM-FRAP, which I used to simultaneously quantify diffusion across an entire 2D image. In the latter half of this thesis, I describe how I have used both AFM-LS and SPIM-FRAP to study nuclear mechanobiology. SPIM-FRAP is used to show how intranuclear diffusion of NLS-GFP is slowed in nucleoli, but overall uncorrelated with chromatin structure on the length scale of single fluorophores. Additionally, I use SPIM-FRAP to show that sites of DNA damage are more stable than the surrounding diffuse repair proteins. AFM-LS is used to separate of the roles of chromatin and lamin A/C in nuclear

compression, regarding both the mechanical response of the nucleus as well as local nuclear curvature. I also use multi-channel, 3D AFM-LS to show how compression alone via AFM, independent of nuclear rupture, is sufficient to induce DNA damage in nuclei. This indicates a novel mechanism by which nuclei incur double-stand DNA breaks. Finally, I provide the first review of mechanical models of nuclei, along with the development of a continuum mechanical model for AFM indentation. Together, these developments in methodologies along with the coupled insights into intranuclear dynamics, nuclear mechanics, and DNA damage improve both our means of studying and our current understanding of nuclear mechanobiology.

To my wife, Ashlie, without whom this would not be possible.

ACKNOWLEDGEMENTS

Before discussing any matter of science, I must first thank my family. My mother, Diana, and my father, Greg, are responsible for the person and the scientist I am today. They provided me the foundation upon which I was able to thrive, and I am forever grateful for all they have done for me. My sister, Sandi, has shown me what it means to be committed and driven. Her forceful hammer into the glass ceiling in medicine is inspiring, and provides a constant reminder about the importance of diversity and inclusion. My brother, Jake, has taught me the importance of effective communication and social skills. Though not a scientist, Jake is a fantastic salesman and manager of the family business. I have a great appreciation for how he interacts with clients and maintains relationships with such a broad range of people; I seek to emulate this in how I communicate science and build connections across disciplines. To Meghan and Gijs, thank you for always being supportive of me through this process. It is without doubt that this work is, in part, a result of my family's impact on me.

Equally important to my career is my wife, Ashlie. Having been together since January of 2013, we became engaged in March of 2017 right as I committed to pursuing my graduate education. Ashlie, her family (Josie, Bob, Justin, and Carlie), and our pets – Petey and Rosie – have been alongside me throughout this journey. Ashlie has taught me more than I can put into words, from what it means to have passion for your work to the importance of taking a break. She has been my backbone for years. She has listened to my endless rants about experimental problems and has taken the time to watch my movies, even when they are just in black and white. She cared for the home and the animals when I had late nights in the lab without complaint, and did everything she could to help me be successful during my PhD. I hope I have been able to do the same for her during her first years of teaching, but I doubt I come even close to matching her level of generosity and selflessness. I love you Ash, thank you.

Though this dissertation features only one author, it would be an egregious error to take sole credit for the work presented below. Science, at its core, is incremental. This work stands upon the work

done before me, both in our lab and in others. The instrumentation I describe is a further iteration of the systems developed first by Kellie Beicker, and next by Evan Nelson (optics and AFM) and Joe Hsiao (hardware and software control). My work would not exist without theirs. I also had the pleasure to work alongside two outstanding graduate students – Megan Kern and Jake Brooks. Megan developed two of the cells lines featured in this work and provided helpful insight throughout my experiments. Jake, though working in the field of microfluidics and microfabrication, was always quick to provide a fresh perspective and excitement for collaboration across our projects. He and Evan Nelson were generous in their time helping me adjust and become acquainted with the lab. Additionally, Jeremy Cribb has been instrumental in helping me navigate graduate school, both through practical measures of giving me computer access to broader guidance on finishing my PhD. Tim O'Brien, the unsung hero of the lab, deserves an immense amount of credit for the work I have completed. His expert handling of cells and sample preparation allowed me to focus on the microscopy and mechanics, and together we were able to move at a pace that would have been laughable without his assistance. Finally, I must give thanks to the undergraduates and high school students I've had the pleasure of working with over the last few years. Melissa Kissling and Loren Fox both wrote fantastic python scripts to quantify image texture and analyze AFM force maps respectively. Will McLain developed Mathematica software for tracking photobleached sections in deforming nuclei. Rasheeq Azad wrote a SPIM-FRAP analysis package in python that makes use of GPU-accelerated computing to massively parallelize curve fitting. Each of these students have been extremely helpful with the work they have produced, and also have helped me to grow as a researcher and mentor. Without each and every one of these lab members, this work would not exist and my aspirations of finishing graduate school would be just that: aspirations.

I have also had the pleasure of working with and learning from a variety of collaborators that I would like to acknowledge. Bei Liu, Fred Pimenta, and Klaus Hahn (UNC) were an integral part of our microscopy developments. Additionally, Brett Condon and Michael Boyce (Duke) provided us with useful samples for testing the limits of our single-objective light-sheet microscope. Andrew Stephens (UMass Amherst) provided useful consultation and experimental guidance during my work on nuclear mechanics, and additionally aided me in writing a review of mechanical modeling of cell nuclei. Pragya Shah and Jan Lammerding (Cornell) collaborated with us in studying DNA damage due to external force, providing us

with cell lines, useful guidance, and the initial invitation to collaborate. The Harvard Medical School Nikon Imaging Center team and others (Jennifer Waters, Talley Lambert, Anna Jost, Florian Jug, and Hunter Elliot) that taught me the basics of microscopy and image analysis were key in propelling my research and launching my career in advanced microscopy. Finally, to the team at the Advanced Imaging Center at Janelia Research Campus (Leong Chew, Jesse Aaron, John Henddleston, Ulrike Boehm, Michael Reiche, Blair Rossetti, Eric Wait, Satya Khuon, and Michelle Quiambao), thank you for giving me a chance to pursue my career in microscopy.

In conclusion, I must acknowledge my committee – Rich Superfine, Mike Falvo, Kerry Bloom, Wes Legant, and Nick Law. Thank you all for guiding me through this process and shaping my dissertation into what it is today. Rich – thank you for teaching me what it means to be passionate about science. Your never-ending excitement for any topic that crosses your desk is contagious and inspiring. Mike – thank you for always being there. Whether it was for questions about science, guidance in moving through this process, or getting a beer during the world cup, you were always there when I needed you. Kerry – thank you for being an example of what it means to be engaged with science outside of your training. Your appreciation for studying the physics of biological systems has taught me how to appreciate more of the biology I encounter. Wes – thank you for being an example of someone who truly knows his craft. Your seemingly bottomless knowledge and every detail of the systems you build is inspiring, and I strive to develop that level of expertise in my work. Nick – thank you for giving me an appreciation of how astronomy has guided the field of microscopy. Your work is always a fresh reminder of how physics and methods can cross multiple disciplines and length scales, and that I should not restrict my knowledge base only to the realm of biophysics. Thank you all for the countless meetings, conversations, revisions, and suggestions. This dissertation would be a shell of itself without your guidance.

TABLE OF CONTENTS

LIST OF TABLES

LIST OF FIGURES

LIST OF ABBREVIATIONS

AFM	Atomic Force Microscopy
AFM-LS	Atomic Force Microscopy – Light Sheet
AOTF	Acoutso-Optic Tunable Filter
BFP	Back Focal Plane
CM	Continuum Mechanics
CM-A	Analytically-Solved Continuum Mechanics
CM-C	Computationally-Solved Continuum Mechanics
DZNep	3-Deazaneplanocin-A
ETL	Electrically Tunable Lens
FCS	Fluorescence Correlation Spectroscopy
FEA	Finite Element Analysis
FM	Fluorescence Microscopy
FRAP	Fluorescence Recovery After Photobleaching
FRET	Förster Resonance Energy Transfer
GFP	Green Fluorescent Protein
GRIN	Gradient Index of Refraction
H2B	Histone 2B
H3K9ac	Histone 3 Lysine 9 Acetylation
H3K9me3	Histone 3 Lysine 9 Trimethylation
HAT	Histone Acetyltransferase
HDAC3	Histone Deacetylase 3
HGPS	Hutchinson-Gilford Progeria Syndrome
HLS	Horizontal Light Sheet
IF	Intermediate Filament
INM	Inner Nuclear Membrane
JF	Janelia Fluor

KASH	Klarsicht ANC-1 Syne Homology
LA/C KD	Lamin A/C Knock Down
LAD	Lamin-Associated Domain
LBS	Line Bessel Sheet
LINC	Linker of the Nucleoskeleton and Cytoskeleton
LSFM	Light Sheet Fluorescence Microscopy
MA	Micropipette Aspiration
MD	Molecular Dynamics
MK	Megakaryoblastic Leukemia
MRTF	Myocardin Related Transcription Factor
NE	Nuclear Envelope
NF-κB	Nuclear Factor Kappa-light-chain-enhancer of activated B cells
NLS	Nuclear Localization Sequence
NPC	Nuclear Pore Complex
ONM	Outer Nuclear Membrane
OPIM	Oblique Plane Illumination Microscopy
OPP	Orthogonal Plane Photobleaching
PALM	Photo Activated Localization Microscopy
PSF	Point Spread Function
PTC	Photon Transfer Curve
QPD	Quadrant Photodiode
sCMOS	Scientific Complementary Metal-Oxide Semiconductor
SEM	Scanning Electron Microscopy
SLD	Super-Luminescent Diode
SM	Steering Mirror
soLSFM	Single-Objective Light Sheet Microscopy
SPIM	Selective Plane Illumination Microscopy
STORM	Stochastic Optical Reconstruction Microscopy

SUN	Sad1 and UNC-84
TAZ	Tafazzin
TIRF	Total Internal Reflection Fluorescence
TSA	Trichostatin A
VIEW-MOD	Versatile Illumination Engine With a Modular Optical Design
VLS	Vertical Light Sheet
WT	Wild Type
YAP	Yes-Associated Protein

CHAPTER 1: INTRODUCTION

1.1 A Brief Overview

Until the past several decades, cells were viewed primary as chemical input-output systems. Specific drugs or chemical signals trigger biochemical responses within a cell that then governs both fate and function. However, there is a growing appreciation for the *physical* nature of biology, leading to the relatively new field of mechanobiology. Studies in mechanobiology have revealed how cells use mechanical forces to pull and tug on their environment to migrate [1], how cells are mechanosensors and can regulate differentiation based upon the stiffness of the surrounding environment [2], and how cancerous cells can be characterized and discerned from healthy cells by their mechanical properties [3], amongst many other groundbreaking results. Under the broad umbrella of mechanobiology lie numerous nascent sub-fields. This dissertation resides within one of the most promising sub-fields known as nuclear mechanics.

The cell nucleus is the largest and stiffest subcellular structure, and akin to the growing appreciation of mechanics in biology is the new understanding that mechanics is equally important to the cell nucleus. Parallels to each of the aforementioned mechanobiology results exist in the subfield of nuclear mechanobiology. For example, the nucleus acts as a propagator of force during cell migration [4] and serves as the rate limiting step in constricted environments [5]. Additionally, the nucleus is a mechanosensor that regulates chromatin compaction to mitigate DNA damage [6]. Nuclear shape and mechanics are also known to be compromised in various cancers and diseases [7, 8]. In studying nuclear mechanobiology, it is first prudent to understand the connections from nuclear mechanics to pathologies and cell functions. It is next important to establish the mechanical properties of the nucleus itself, so that we can predict how the nucleus translates mechanical forces to biochemical signals (Figure 1.1). Nuclear mechanics is far from a simple problem. The nucleus itself is comprised of intricate substructures that are precisely organized and interlinked. Each substructure and its connections have mechanical roles, and our understanding of these roles are informed by combinations of microscopy and force probes. In

parallel, nuclear mechanics can be investigated through computational modeling wherein each nuclear substructure is treated as a specific material and simulations of physiological processes inform the roles of each structure. Modeling and live-cell studies iteratively inform each other, with simulations providing predictions to be tested through experimentation and experimental observations being validated by simulations.

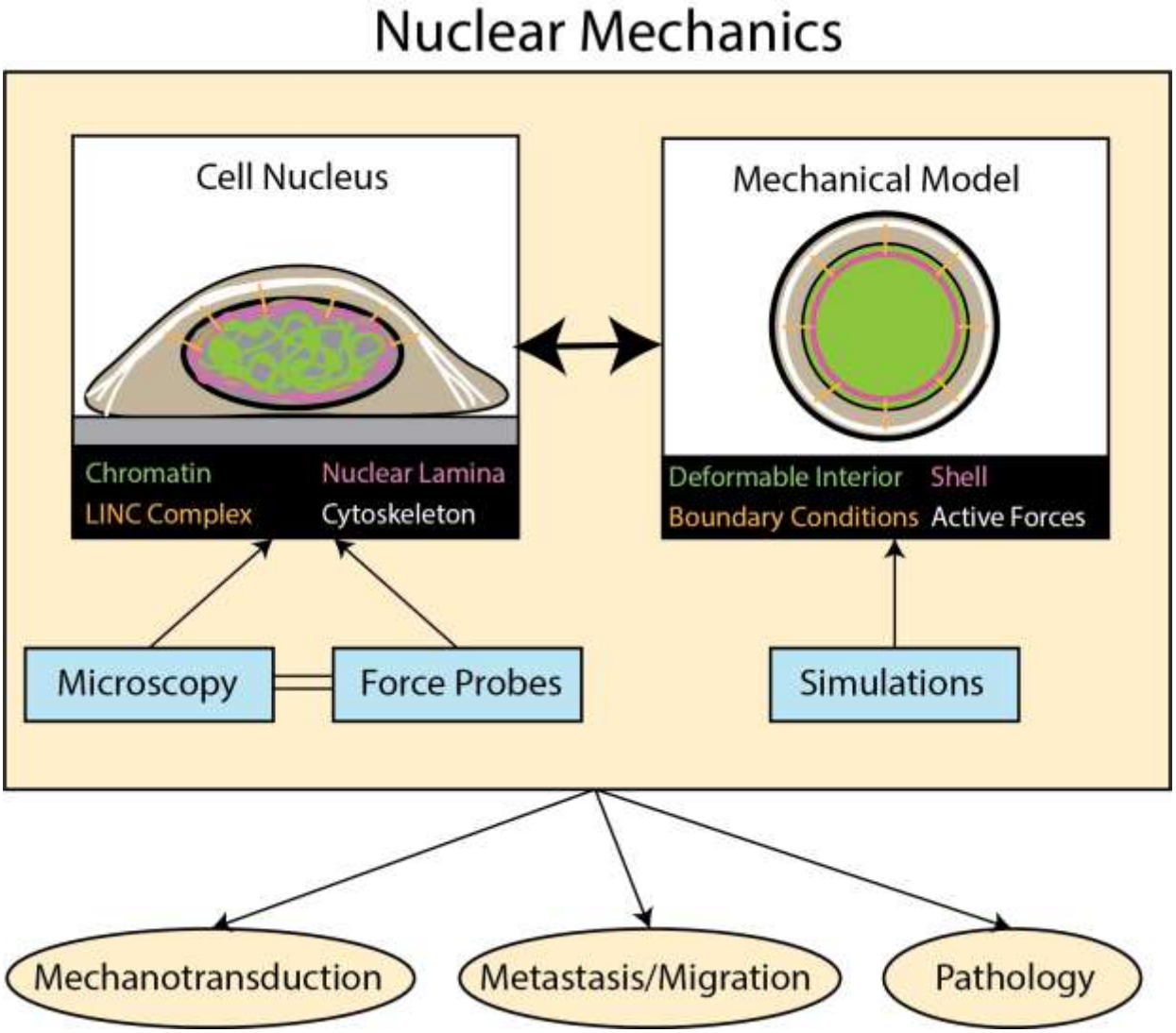

Figure 1.1: A schematic representation of studying nuclear mechanobiology.

This thesis describes advances in methodologies for studying nuclear mechanobiology (Chapters 2 – 4), discoveries in nuclear mechanics and computational modeling (Chapters 5, 6), and preliminary observations for promising future directions (Chapter 7). The conclusions and details of these chapters assume first a working knowledge of the structures within the cell nucleus. The following section 1.2

serves to provide this base. Next, I describe in brief some of the existing technologies for studying nuclear mechanobiology as to lay the foundation for why my methodological advances are of interest. Finally, to appreciate the conclusions of my work in nuclear mechanobiology, it is crucial to understand the broader scope in which this work exists. Section 1.4 aims to provide the reader an understanding of *why* nuclear mechanobiology is an important topic to study.

1.2 Nuclear Substructures

The cell nucleus itself is made up of a myriad of subnuclear components (Figure 1.2). Here, I step through each substructure and note how it has been modeled in simulation. A more thorough treatment of mechanical modeling of cell nuclei is presented in Chapter 6, constituting the first published review on the topic [9]. Beginning with the nuclear interior, approximately three meters of DNA is condensed to fit within the nuclear volume (~100s of cubic microns for mammalian cell nuclei). This DNA is surrounded by fluid known as the nucleoplasm, which is roughly eight times more viscous than water [10]. DNA is compacted by wrapping itself around a group of proteins collectively called a nucleosome, to form the fundamental unit of compacted DNA known as chromatin. In turn, the nucleosomes are comprised of histones, of which there are five (H1, H2A, H2B, H3, H4) [11]. The latter four histones make up the core histones and two copies of each of the core histone form a nucleosome. The H1 histone is a linker histone which mediates interactions between nucleosomes [11]. Chromatin is further organized into closed and open regions, known as heterochromatin and euchromatin respectively. Heterochromatin is generally located towards the nuclear periphery and is transcriptionally inactive while euchromatin is more central and transcriptionally active. Each individual chromosome is positioned within the nucleus in a non-random way in regions known as chromosome territories. Chromatin provides mechanical resistance to nuclei [12], specifically at small length-scale deformations [13, 14]. In simulations, chromatin has been treated as an elastic, viscoelastic, or poroelastic solid in continuum models or as crosslinked polymers in discrete models [9].

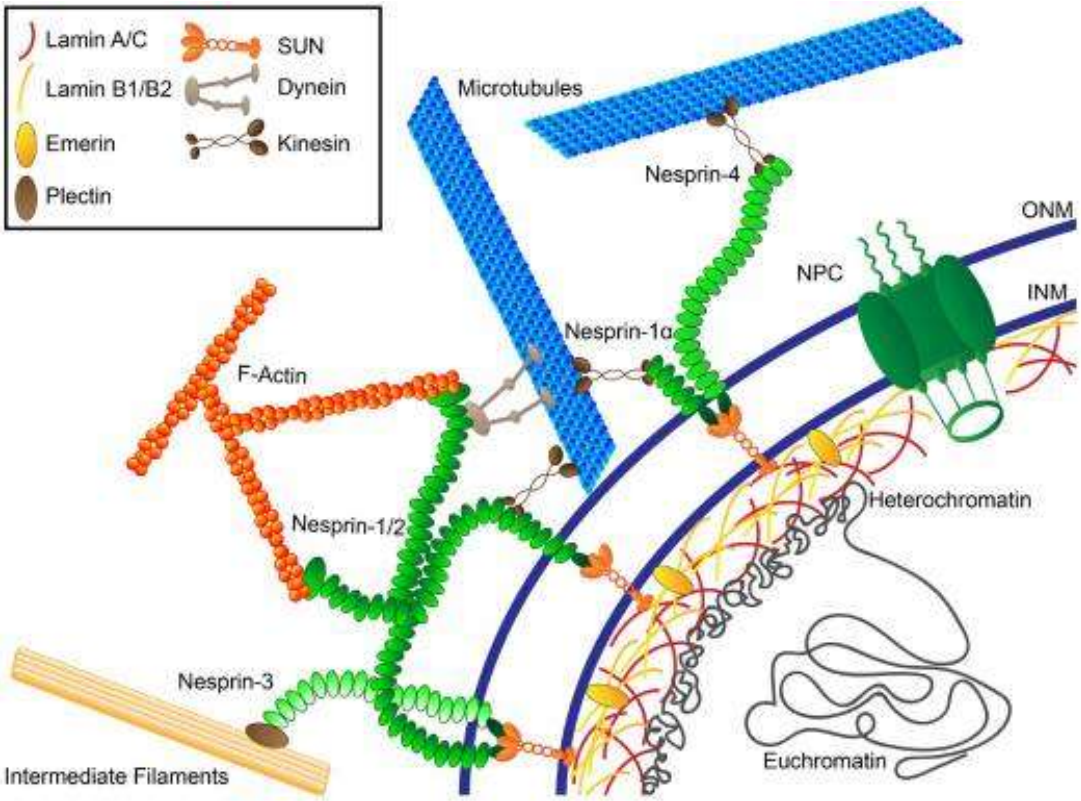

Figure 1.2: Schematic view of the cell nucleus and its connections to the cytoskeleton. Reproduced with permission from Maurer et al [15]

Also within the nuclear interior, but localized to the periphery is the nuclear lamina, which interacts with chromatin at lamin-associated domains (LADs). The nuclear lamina is comprised of A- and B-type lamins, which are type V intermediate filament proteins [16]. A-type lamins consist of lamin A and lamin C and are encoded by the gene *LMNA*. B-type lamins consist of lamin B1 and B2 and are encoded by the genes *LMB1* and *LMB2* respectively [16]. The primary difference between A- and B-type lamins is that A-type lamins are not farnesylated when incorporated into the nuclear lamins while B-type lamins retain the farnesyl group [16]. Additionally, lamin B1/B2 reside slightly (~1 – 2 nm) closer to the nuclear envelop (NE) than lamin A/C [17]. Historically, the nuclear lamina was thought to be the primary mechanical constituent of the cell nucleus prior to studies on the role of chromatin [18]. Given that it forms a shell surrounding the chromatin, the nuclear lamina is often treated as a thin, elastic or viscoelastic shell or a dense polymer meshwork [9].

The NE is a comprised to two lipid bilayers: the outer nuclear membrane (ONM) and the inner nuclear membrane (INM). The ONM and the INM are separated by the perinuclear space, which is

approximately 50 nm wide [19]. The NE also is contiguous with the endoplasmic reticulum, which serves as a reservoir to expand the surface area of the NE. The INM and the ONM are connected adjacent to nuclear pore complexes (NPCs). NPCs are selectively permeable channels which mediate nucleocytoplasmic transport [19]. Furthermore, there exist a set of proteins that span the NE, connecting the cytoskeleton outside of the nucleus to the nuclear lamina inside the nucleus. This complex of proteins is known as the linker of nucleoskeleton and cytoskeleton (LINC) complex [20]. The LINC Complex is made up primarily of two sets of protein: SUN domain proteins and KASH domain proteins. SUN domain proteins span the INM, binding to the nuclear lamina [20]. KASH domain proteins, primarily nesprins, span the ONM and bind to the cytoskeleton [20]. SUN and KASH domain proteins interact within the perinuclear space, completing the mechanical link from the inside to outside of the nucleus. These connections to the cytoskeleton often present themselves as boundary conditions in models that consider both the nucleus and the surrounding cytoskeleton [9].

While not a direct constituent of the nucleus, the cytoskeleton – composed of actin, microtubules, and intermediate filaments – serves as a filamentous network that protects the nucleus from external stresses [21-25], transfers force signals from the cell surface to the chromatin [26-29], and assists in nuclear translation during migration [30]. One of the most studied cytoskeletal proteins relevant to nuclear mechanics is actin. In spread cells, actin forms a series of filaments that run atop the nucleus parallel to its long axis [31]. This specific structure has been named the “actin cap”, which exerts a compressive stress on the nucleus from above [31-33]. The integrity of the actin cap is dependent on cellular morphology. This was confirmed by plating cells on fibronectin micropatterned substrates with varied geometries; cells plated on long, rectangular patterns formed distinct actin caps that shrunk nuclear height, while cells plated on circular patterns exhibited taller, rounded nuclei [31, 34, 35]. Furthermore, temporal fluctuations in nuclear shape were shown to be dependent on these same micropatterns. Disruption of actin was also shown to increase these temporal fluctuations, showing that actin helps determine both overall nuclear morphology as well as small, temporal fluctuations. This implies that cells’ sensitivity to the local environment indirectly regulates nuclear morphology. Similarly, microtubules have also been shown to help regulate shape fluctuations [34]. The actin cap prestresses the nucleus, which is critical for transducing forces from integrins to the cell surface [28]. The degree of prestress is dependent

on the stiffness of the substrate upon which cells are plated, with stiffer substrates showing an increase in actin prestress and a decrease in nuclear height [36, 37]. In fact, cells plated on polyacrylamide gels show a similar reduction in the percentage of the actin cap that is present to cells plated on glass and treated with Latrunculin B to depolymerize actin. In some instances, this prestress is sufficient to cause rupture on the nuclear membrane [33]. Basal actin is also important for nuclear positioning, as it provides a link between focal adhesions on the substrate to the nucleus that can pull the nucleus during cell spreading and migration [23, 30, 38]. In the context of mechanical modeling, the cytoskeleton is often either ignored or treated as a means of applying external forces upon the nucleus.

This complex nuclear architecture maintains proper nuclear function and mechanical integrity. However, individual components of this architecture can be modified to compensate for or respond to the extracellular environment. For example, it is well documented the heterochromatin resides primarily towards the periphery of nuclei while euchromatin is more centrally located [39]. Strikingly, this positioning is reversed in the rod photoreceptor cells of nocturnal animals [40]. In this case, positioning has an optical effect. Positioning the dense heterochromatin towards the center and the less dense euchromatin towards the nuclear periphery provides a lensing effect akin to a gradient index of refraction (GRIN) lens. The allows for increased light collection for these nocturnal animals. A second example is a landmark result in the field of mechanobiology. Stem cells direct their differentiation based upon the stiffness of the extracellular matrix [2]. Later studies showed tissues adjust their elasticity based on the collagen content of the surrounding matrix, which then subsequently adjusts levels of lamin A in positive correlation with elasticity [41]. These studies illustrate how individual constituents of the nucleus are intricately related to global mechanical properties, which furthermore have implications for fundamental processes such as differentiation and proliferation.

1.3 Methods in Studying Nuclear Mechanobiology

With a working understanding of nuclear architecture, it is next prudent to discuss the currently available techniques for studying nuclear mechanics and dynamics. Here, I review some of the most prevalent methodologies for physically perturbing nuclei, extracting nuclear mechanical properties, and

studying intranuclear diffusive processes. This serves to set the stage for my innovations in microscopy and force measurements, as are discussed in Chapters 2 – 4.

1.3.1 Mechanics

Methods for studying nuclear mechanics can broadly be broken down into two categories: force measurements and cellular deformation measurements (Figure 1.3). Though both of these classes serve to physically perturb the cell nucleus, force measurements provide a direct readout of the force being applied while cellular deformation measurements primarily leverage microscopy to monitor the deformation of particular structures due to external stresses. Each are useful in their own right, however uniquely powerful techniques make use of both force and deformation measurements, which when measured together lead to direct characterizations of mechanical properties with minimal assumptions. In Chapters 2 and 3, I will describe the microscopy advances and coupling of force and deformation measurements that we use to overcome some of these hurdles.

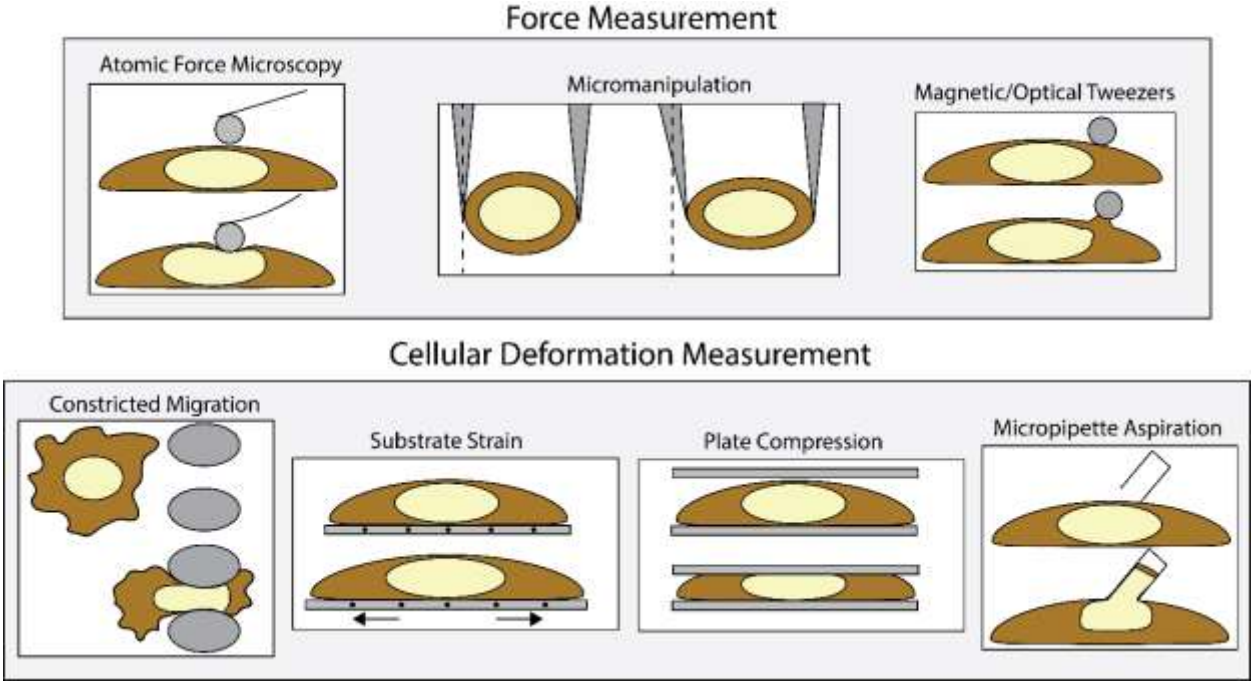

Figure 1.3: Techniques for physically probing the cell nucleus.

Atomic Force Microscopy (AFM, Figure 1.3) is a prevalent technique for measuring forces on cell nuclei, both isolated [25, 42-45] an intact [22, 24, 25, 43, 46-52]. AFM is our preferred choice for measuring forces on nuclei, and I will describe AFM in greater detail in Chapter 3. In a conventional AFM

experiment, a flexible cantilever is lowered upon a cell or nucleus of interest as a means of measuring and applying an external force. The deflection of the cantilever is measured by reflecting a super-luminescent diode off of the back of the cantilever and monitoring its displacement on a quadrant photodiode [53]. The spring constant of the cantilever is most commonly determined either through the thermal tune method [54] or the Sader method [55]. The cantilever is treated as a simple spring system and thus the force applied to the cell or nucleus is given by Hooke's Law. Often various contact mechanics models, most notably the Hertz model, are applied to the resulting force versus displacement curves (FD curves) which allow users to extract effective elastic moduli: a parameter often used as a metric for nuclear stiffness [56]. AFM has been integrated with both confocal microscopy [22, 24, 25, 43, 47, 48] as well as light sheet microscopy [49] in order to monitor nuclear structure and integrity during an AFM experiment. This has allowed users to determine separate elastic moduli for the nucleus and the whole cell that contribute at different levels of indentation [25, 43, 49], monitor nuclear anisotropy during indentation [22], measure changes in nuclear height at various levels of force [24], and monitor nuclear rupture events during compression [47].

Micromanipulation is a second technique that provides an explicit readout of forces being applied to cell nuclei [13]. In the configuration shown in Figure 1.3, two pipettes are attached to adjacent ends of a cell. One pipette is translated to stretch the cell while the other is fixed in place at the rear end of the pipette, allowing the free end to deflect. The effective spring constant of the fixed pipette is calibrated prior to the experiment, and the deflection is measured as the cell is stretched. Given the spring constant of the pipette and the amount it is deflected, one can back out an applied force. This has been used to separate the contributions of chromatin and lamin A/C in extension-based measurements [13], as well as to establish the role of HP1α in the mechanical integrity of chromatin [57].

Magnetic or optically-trapped beads (Figure 1.3) can also be used to apply and measure forces on cells or nuclei through either twisting or pulling [27-29, 58-60]. Similar to the two aforementioned techniques, magnetic and optically-trapped beads require careful calibration in order to extract a measure of applied force [61]. For optically-trapped beads, a focused, high-intensity laser traps the particle and based upon the mean-squared displacement of the trapped particle one can extract an effective stiffness of the trap itself. For magnetic beads, the applied force can be extracted from the magnetic properties of

the bead itself and the applied field. Typically, these techniques are used for confidently measuring forces on the single-molecules level, that is in the range of 10s - 100s of pN. AFM, on the other hand, has a noise floor around 10s of pN but can measure forces up to 100s of nN. While trapped beads have been used to directly probe nuclear mechanics in detecting higher bead displacements in LMNA -/- MEF cells [60] and strain stiffening in isolated nuclei [58], it has primarily been a tool for studying force transmission from the cell surface into the nucleus. By coating magnetic beads in fibronectin, beads can bind to integrins along the cell surface. Twisting and pulling of integrin-bound magnetic beads has shown that there exists a mechanical link from the cell surface to the chromatin capable of transmitting force, providing a pathway for mechanotransduction to the nucleus [27]. Interventions to LINC complex proteins, actin, and lamin A/C have been shown to break this mechanical path [28, 29], and furthermore this technique has shown that gene transcription can be upregulated through stretching of chromatin resulting from mechanical perturbations at the cell surface [29].

The second suite of techniques are targeted at visualizing deformations within the nucleus as opposed to measuring the force being applied. These techniques are more common in nuclear mechanobiology as they require only a physical perturbation without a specific force calibration. They generally use optical microscopy to quantify the deformation of the nucleus as it is subjected to external stresses. Figure 1.3 highlights four main methods: constricted migration, substrate stretching, plate compression, and micropipette aspiration (MA). Constricted migration assays are simply transwell membranes [62] or microfluidic chambers [5, 63] with micron-scale constrictions through which cells can migrate. Chemoattractant gradients are used to spur this directed migration. When coupled with fluorescence microscopy, such studies (as reviewed in Xia *et al* [64]) have quantified both migration speed [5, 65] and nuclear strain [63, 66] as well as monitored nuclear plastic damage [63, 66, 67], nuclear envelope rupture [33, 62, 68-71], and subsequent DNA damage and repair [68, 69, 71, 72]. Substrate stretching is a technique that can be used to apply either constant or cyclic strain to cell monolayers. This is traditionally done with flexible gel substrates coated with adhesion proteins that are subjected to motorized strain. Substrate stretching has been used extensively for studying chromatin mechanotransduction, which will be discussed in detail in Section 1.4.1. Plate compression similarly applies uniform stress to cell monolayers, just in the orthogonal direction. For example, an investigator

has developed multi-cellular compressive strain assays by which a weighted coverslip is placed atop cells plated on fibronectin-patterned substrates, thus providing a uniform compressive stress across hundreds of cells simultaneously [35]. This allowed for the discovery that compressive forces cause reversible condensation of chromatin through transport of HDAC3 into the nucleus, rendering it into a less transcriptionally active state.

Finally, and potentially the most utilized technique in nuclear mechanobiology, we have micropipette aspiration. Used to study both isolated and intact nuclei, MA is a technique by which a small pipette tip with an opening of a few microns is brought adjacent to a cell, a pressure gradient is applied, and the cell is pulled into the pipette. Dynamically monitoring the geometry of the nucleus during this time allows for the extraction of relevant mechanical properties such as effective stiffness or tension [41, 45, 67, 73-79] and viscosity [41, 45, 76]. One of the more powerful aspects of MA comes from coupling the aspiration with high temporal-resolution fluorescence microscopy. This has allowed investigators to study the dynamics of specific cellular structures under deformation by MA. Specifically, investigators have observed nuclear plasticity [76], stretching of the nuclear lamina [75] and chromatin [80], chromatin flow [76], segregation of chromatin and mobile nuclear proteins (53BP1) [62], and nuclear rupture [62]. Volumetric imaging during MA experiments has also shown decreases in both volume and surface area [73], suggesting that water is actively being forced out of the nucleus during severe compressions.

Together, these techniques have provided tremendous insight into nuclear mechanobiology. Yet, there is always room for development and improvement. Many of the aforementioned deformation measurement techniques use confocal or widefield fluorescence microscopy, which are limited in that they lead to significant photobleaching and phototoxicity. This subsequently compromises fast, live-cell volumetric imaging. There is a need for microscopes that can perform gentle, fast, 3D, multi-color imaging that can be integrated with force probes. In Chapter 2, I describe our open-top, single-objective light-sheet microscope that remedies many of these issues. Furthermore, many of the probes that measure forces directly are generally not coupled with microscopy at all. This can happen for a variety of reasons, but a dominant one is that coupling of physical motion of microscope parts with the force probe can compromise the force measurements themselves. In Chapter 3, I will describe how we have coupled AFM with our microscope detailed in Chapter 2. Our system provides synchronized force measurements with

fluorescence microscopy in the plane of applied force with effectively no compromise in the sensitivity of our force measurements.

1.3.2 Dynamics

Dynamics within the nucleus are equally important as mechanical properties when studying nuclear mechanobiology. The nucleus relies on effect transport of proteins and small molecules both throughout the nuclear volume as well as across the nuclear envelope. Such dynamics inherently rely on the viscous properties of the nucleoplasm along with supplementary effects of binding and crowding. In studying intranuclear dynamics, investigators have turned to three primary tools: particle tracking, fluorescence correlation spectroscopy (FCS), and fluorescence recovery after photobleaching (FRAP). Single particle tracking is a relatively straightforward technique in that it simply requires imaging a single fluorescent tracer particle as it diffuses through a sample. Based upon the trajectory over time, one can then extract the mean-squared displacement which can be used to infer both the type of diffusion (free, confined, etc.) as well as the rheological properties of the surrounding fluid [81]. In the context of nuclear dynamics, this technique has been used to show how nanospheres diffusing in the nucleus can become confined within chromosome territories [82]. Furthermore, by varying the size of the tracer fluorescent proteins, investors have been able to study the specific material behavior of chromatin across length scales [83]. FCS, on the other hand, makes use of intensity fluctuations in a fluorescence image sequence to infer how single particles are diffusing in and out of a region of interest [84]. One of the primary benefits of FCS is that it can be used on diffuse samples such as GFP tagged with a nuclear localization sequence (NLS). This is in contrast to having to inject fluorescent nanospheres into a biological specimen. FCS has been extensively used in nuclear dynamics to quantify the diffusion coefficient of small fluorescent proteins within the nucleus [85-88]. FRAP is the final technique most notably used for single-cell diffusion studies. The principle of FRAP is to use a high-intensity focused laser spot to selectively photobleach a region of interest within a sample. Diffusion or binding kinetics then leads to a recovery of fluorescent signal within the previously bleached region. One can then quantify both the rate of recovery and the recovery percentage as metrics of diffusion and the strength of binding

[89]. Similar to FCS, FRAP has been used to study diffusion of small molecules within the cell nucleus [86].

While each of these techniques have clearly proven useful in quantifying intranuclear dynamics, each method has inherent drawbacks. With single particle tracking, one must insert foreign particles within a biological sample, which could have unknown consequences. Furthermore, you are limited in the number of probes that may be tracked simultaneously, and often tracking in 3D requires quite sophisticated instrumentation in order to gently image at a high rate for an extended period of time while maintaining cell viability. With FCS, there is sufficient sampling requirements and intensity conditions that must be met in order to extract useful information. FRAP measurements are restricted to single regions of interests, and cannot address any heterogeneity within a sample. In Chapter 4, I will describe my approach to mitigate some of these issues by combining light-sheet microscopy with FRAP to provide simultaneous FRAP measurements across all pixels in a given image. Furthermore, in Chapter 7 I describe how I have incorporated this method with AFM to study how compressive force can locally alter intranuclear diffusion.

1.4 The Relevance of Nuclear Mechanobiology

1.4.1 Chromatin and Nuclear Mechanotransduction

Increasing evidence has shown that the nucleus behaves as a mechanosensor [15, 90-96], meaning that it converts mechanical forces and changes in the extracellular environment into biochemical signals that subsequently alter cellular and nuclear functions. These responses vary in nature, from modulation of chromatin compaction [97] to decoupling of the nucleus from the cytoskeleton [98]. Several mechanisms exist for mediating nuclear mechanotransduction – that is, the conversions of mechanical stimuli into biochemical signals and responses. One such mechanism is the altered transport of biochemical effectors across the nuclear envelope. A remarkable example of this is the localization of YAP/TAZ to the nucleus. YAP/TAZ is a transcription coactivator that alters its localization within the cell in response to mechanical force and subsequently modulates transcriptional activity within the nucleus [99-103]. In Chapter 7, I provide insight into how precisely force may lead to local influxes of YAP into the nucleus due to heterogeneous strain in the nuclear envelope. As a second example, calcium signaling is

known to be necessary for many nuclear mechanotransduction pathways [104, 105]. Calcium oscillations increase in magnitude and frequency in response to mechanical force [106, 107], and blocking mechanosensitive ion channels can mitigate the ability of the nucleus to respond to mechanical stimuli [97, 98, 102, 108]. Beyond these examples, nucleocytoplasmic shuttling of other transcription cofactors such as MKL [109], NF-κB [110], and MRTF [111] as well as enzymes regulating histone acetylation [112, 113], and their subsequent activation, also serves to control nuclear mechanotransduction. This nucleocytoplasmic shuttling is presumably mediated by stretch-activation of NPCs [96]. Many of the above examples of nucleocytoplasmic shuttling subsequently lead to altered chromatin compaction for the purposes of either nuclear protector or altered gene transcription.

Within the nucleus, chromatin serves two primary functions: (i) packing of DNA in a non-random organization to facilitate proper gene expression and cell function, and (ii) providing mechanical integrity and protection to the nucleus. Mechanosensation through the nucleus subsequently serves to regulate both of these functions through altering chromatin compaction, chromosome dynamics and gene expression. Chromatin compaction is modulated through either histone (de)acetylation or methylation [114, 115]. Adding or removing an acetyl group to the histone tail either removes or adds a positive charge respectively. This then alters the electrostatic interaction with the negatively charged DNA. Histone acetylation then decompacts chromatin, while histone deacetylation compacts chromatin [114]. Acetylation or deacetylation is generally mediated by enzymatic reactions with histone acetyltransferase (HAT) or histone deacetylase (HDAC) [114]. Histone methylation is the process by which methyl group(s) are added to specific lysine residues [115]. These are mediated by epigenetic factors such as H3K9me3, which is a trimethylation of the 9^{th} lysine of histone 3. Methylation can either compact or decompact chromatin based upon the location at which the methyl groups are added [115]. Several drug treatments exist to modulate chromatin compaction, either through modifying histone (de)acetylation (ex. Trichostatin A (TSA), histone deacetylation inhibitor [116], later used in Chapters 4 and 5) or histone methylation (ex. 3-Deazaneplanocin-A (DZNep), histone methyltransferase inhibitor [117]). More interestingly, however, is that cells respond dynamically to external mechanical stimuli and regulate the compaction of chromatin through these epigenetic factors and enzymatic reactions.

One of the primary means of studying such nuclear mechanotransduction is through the application of tensile strain to a monolayer of cells. These assays serve as a model for the strain the cells undergo during tissue morphogenesis; understanding how mechanical forces regulate the formation of tissue is paramount as dysregulation can lead to a variety of disease states [118]. This strain can be constant or cyclic with varied amplitudes, frequencies, and durations. Surprisingly, the chromatin-based response of nuclei to tensile strain varies widely with the stress application parameters. That is, chromatin has been shown to either compact [98, 102, 119, 120] or decompact [97, 113] itself due to tensile strain. Intriguingly, these mechanoresponses seemingly have little to do with transcriptional activity. Strain-induced chromatin compaction has been shown to either have minimal impact on transcriptional activity [98] or lead to an overall suppression of transcription [120]. This is not to be confused with changes in transcriptional activity that have been shown to occur at sites of local chromatin strain [29, 121], but rather these results show that actual alterations in the compaction state as a result of global nuclear strain tend to occur as transcriptionally inactive sites. For example, strain-induced chromatin decompaction occurs primarily at the edges of chromosomes and at non-coding regions, leading to little correlation between increased epigenetic markers for euchromatin and transcriptional activity [97]. This agrees well with other assays such as plate compression and constricted migration, which show either transcriptional repression [112] or chromatin remodeling at transcriptionally inactive sites [122] respectively. It then appears as though modulation of chromatin compaction in response to external strain is not for regulation of transcriptional activity, however recent work may suggest otherwise [123]. The alternate hypothesis is that this mechanoresponse is for regulation of nuclear mechanics.

The full parameter space of tensile strain frequency, duration, and magnitude has yet to be explored. Nonetheless, some trends still emerge from current literature. First, low strain magnitude (~3% - 10%) generally leads to chromatin compaction [98, 102, 119, 120]. Intriguingly, this low-strain regime has been previously shown to be dominated by chromatin mechanics [13, 124]. Increasing nuclear stiffness in the low-strain regime via chromatin compaction mitigates the amount of strain that is propagated to the nucleus. Therefore, it seems as though cells respond to low magnitude tensile strain by compacting chromatin in order to minimize nuclear deformation. Furthermore, high tensile strain (~40%) has been shown to decompact chromatin on short timescales (~30 minutes) in order to reduce DNA damage [97];

this high strain regime is dominated by lamin mechanics [13, 124]. A second trend present in the current literature is that low frequency deformations (< 0.1 Hz) lead to chromatin decompaction [97, 113]. At present, there is little explanation as to why lower frequency strain application induces this response, however it is presumably related the relative timescales of the deformation and nuclear viscosity.

It should finally be noted that modulations of chromatin compaction are not the only mechanoresponse to cyclic tensile strain. Nuclei protect themselves from such strain in a manner of ways. First, strain can lead to nuclei decoupling from the cytoskeleton via turnover of SUN2 proteins [98], which minimizes force propagation to the nucleus. Additionally, cell monolayers will align perpendicular to the direction of strain [97] and form actin fibers with correlated lines of LINC complex proteins and NPCs [103]. This alignment and structural organization helps to mitigate deformation of the nucleus. Finally, cyclic strain can cause altered localization of nuclear proteins, such as emerin localizing to the outer nuclear membrane [120] or lamin A/C localized to the nuclear periphery [102]..

Cyclic strain, however, is not the only means of demonstrating chromatin-related nuclear mechanotransduction. Osmotic stress can reversibly alter the compaction levels of chromatin [125]. Furthermore, increasing extracellular divalent cations can lead to a calcium influx through mechanosensitive ion channels and subsequent chromatin compaction. This serves to mechanically stabilize the nucleus and mitigate nuclear blebbing [108]. Global compression via a weighted coverslip also depolymerizes apical actin and increases chromatin compaction through shuttling of HDAC3 into the nucleus in order to render the nuclear into a transcriptionally inactive state [112]. These results can be mimicked by depolymerization of actin fibers alone without compressive force. The induction of cellular migration also leads to an upregulation of heterochromatin [126], which has recently come to light as a necessary part of wound healing and constricted migration [127]. The sites of chromatin that are remodeled during constricted migration are generally transcriptionally inactive [122], pointing towards this response as being purely for mechanical benefit.

As previously mentioned, chromatin not only functions as a mechanical and rheological element providing stability to the nucleus, but also serves to compact the DNA into a non-random organization which subsequently regulate transcription and gene expression. This function of chromatin is also regulated by mechanical signals and cues. The mechanical pathway linking integrins at the cell surface to

chromatin serves as a means of transmitting mechanical signals [26, 27]. It has been shown that by mechanically perturbing the cell surface, chromatin is stretched and transcription is upregulated in the exact region that is being stretched [29]. Furthermore, this phenomenon is dependent upon the alignment of the force with actin stress fibers and the integrity of the stress fibers themselves [128]. It has also been shown that changes in cell shape can lead to chromatin alterations, which subsequently regulate gene expression that adapts the cell to a given surface. To study this, NIH 3T3 fibroblasts were plated on micropatterned substrates of varying size and shape [111]. They observed that elongated shapes (rectangular versus circular) led to an increase in expression of genes related to actomyosin contractility and motility as well as a downregulation of genes related to apoptosis and cell division [111]. Furthermore, increases in euchromatin markers (H3K9ac) were shown to correlate with increases in nuclear volume and that decreased actomyosin contractility led to increased heterochromatin via shuttling of HDAC3 into the nucleus. Together, these studies show how the nucleus acts a mechanosensor that alters which genes are expressed in order to adapt the cell to different substrate shapes [111]. Recently, a mechanical model was proposed to better understand this feedback loop between the cytoskeleton, the nucleus, and cell adhesions [129]. Cell morphology has also been shown to alter chromosome volume, location, and intermingling, which again alters gene expression [130]. This is also shown to be true for cyclic strain application [120].

1.4.2 The Nucleus and Pathology

One of the primary motivations for studying the cell nucleus is its implication in a myriad of pathological conditions. Here, we briefly review two of these instances in which nuclear integrity and mechanics are altered in disease. Arguably the largest subset of these disease states arises from mutations in the nuclear lamina, also known as laminopathies [16]. Laminopathies primarily occur from alterations in lamin A/C, which are the lamin isoforms which govern, in part, nuclear mechanical properties [18]. Laminopathies can be further broken down into four categories based on which systems they effect, namely striated muscles, adipose tissue, peripheral nerves, and multiple systems. The first laminopathy to be discovered was autosomal-dominant Emery–Dreifuss muscular dystrophy [131], which affects striated muscles and cause joint contractures and muscle weakening [16]. Interestingly, mutations

in the gene encoding for emerin – a protein spanning the INM – can also lead to autosomal-dominant Emery-Dreifuss muscular dystrophy [132]. Laminopathies also effect adipose tissue, such as in Dunnigan-type familial partial lipodystrophy [133]. Intriguingly, alterations in the mechanical properties of the cell nucleus are only observed for laminopathies affecting muscle phenotypes and not adipose phenotypes, despite both being caused by mutations in *LMNA* [134]. Laminopathies can further affect the peripheral nerves, leading to, for example, Charcot-Marie-Tooth type 2 peripheral neuropathy [135]. Finally, laminopathies have been shown to alter multiple systems simultaneously, most notably leading to Hutchinson-Gilford Progeria Syndrome (HGPS) [136]. HGPS occurs because abnormally processed prelamin A known as progerin, results in lamin A maintaining its farnesyl group as opposed to having it cleaved as in the case of healthy processing of prelamin A [16]. These association of lamin A/C with these rare and often fatal disease has spurred on research into the mechanical properties of the nuclear lamina, revealing that nuclear stiffness is decreased in striated muscle laminopathies, unchanged in adipose tissue laminopathies, and increased in HGPS [74, 134].

The cell nucleus, specifically chromatin organization, is also subjected to mutations and alterations in various cancers. These alterations occur at different levels, including the nucleosome level, the chromatin loop level, the chromatin domain level, and the whole nucleus level [137]. At the level of the nucleosome, chromatin can either be aberrantly compacted (ex. colon cancer) [138] or decompacted (ex. Leukemia) [139]. Furthermore, chromatin loops and domains can experience conformational changes as a result of cancer [137]. At the whole nucleus level, nuclear morphology is known to be altered not only in cancer [140, 141] but also in many of the aforementioned laminopathies [16]. It is clear then that to understand these complex diseases, we need to first understand the connections between mutations and altered nuclear mechanics and morphology. In Chapter 5, I address this topic by studying how chromatin compaction and lamin A/C knockdowns (as a surrogate for disease sates) alter the nuclear responses to external forces in terms of shape, stiffness, and curvature.

1.4.3 The Nucleus and Migration

Cell migration is one of the most intuitively physical processes in biology. It can be both beneficial, as in wound healing, or detrimental, as in cancer metastasis. Within dense tissue, cells must

navigate complex interstitial spaces in order to relocate. The nucleus is known to be the stiffest and largest subcellular structure, and subsequently is the rate-limiting factor as cells migrate through tight pores [5]. It is then likely that altered nuclear mechanical properties can contribute to the ability of a cancerous cell to metastasize, as it has been shown that lower lamin levels alter constricted migration speeds [67]. Not only does constricted migration deform nuclei significantly, but it can also lead to nuclear rupture [69]. This rupture then leads to cytoplasmic nucleases entering the nucleus and subsequently cleaving DNA. This DNA damage is thought to lead to further alterations in the genome and may be at the heart of several rare diseases. Recent studies, however, have shown that this DNA damage can occur by deformation alone during migration [142], highlighting multiple cell-line dependent mechanisms at play. In Chapter 5, I provide the first quantification of nuclei incurring DNA damage due to targeted compression with AFM, independent of nuclear rupture.

The nucleus is highly relevant for healthy migration as well. A topic of recent interest is the role of chromatin compaction in migration [143]. At the onset of migration, such as in a scratch wound assay, investigators have observed increased in epigenetic marks for heterochromatin [126]. Additionally, through traction force microscopy studies it has been shown that the nucleus acts to transmit forces throughout the cell to facilitate migration [4]. Connecting these two results, it may be inferred that the stiffening due to chromatin compaction leads to more effective force propagation, which then increases the ability of a cell to migrate efficiently. It is then clear that at the heart of both metastasis and healthy migration lies the nucleus, and its inherent mechanical properties serve to regulate the process of cell migration.

1.5 Significance and Goals

The goals of the work fall into two categories: instrumentation and cell nuclear mechanics. Regarding the former, I have sought to improve upon the work of previous graduate students (Kellie Beicker and Evan Nelsen) who laid the groundwork for our combined atomic force microscopy and light-sheet microscopy system (AFM-LS) [144, 145]. These specific improvements include transitioning from a Gaussian light sheet (GLS) to a line Bessel light sheet (LBS) as well as transitioning from 2D, single-channel imaging with AFM to 3D, multi-channel imaging with AFM. The transition from using a GLS to an

LBS significantly improves our depth of field for a given light sheet thickness, meaning that we can image taller samples with similar contrast and signal-to-noise as the previous generation instrument. The further improvement of multi-channel, 3D imaging is significant in that we now can study multiple structures of interest throughout the entirety of the cell with coupled force measurements, providing a more complete view of the cell and nucleus as mechanical elements. My second goal regarding instrumentation is the development of a novel methodology for studying intracellular dynamics, namely selective plane illumination fluorescence recovery after photobleaching (SPIM-FRAP). SPIM-FRAP improves on traditional FRAP by including additional spatial information while also improving on FCS through an order of magnitude improvement in data acquisition rate. Together, these instrumentation developments constitute significant contributions to microscopy community and open up new suites of questions to be answer in the field of mechanobiology.

The second category of goals surround studies of cell nucleus mechanics. As is mentioned above, the cell nucleus is implicated in many disease states, and also serves as a mechanosensor to regulate cell function in response to external mechanical stimuli. My goals are to utilize our AFM-LS system to better understand the roles of chromatin and lamin A/C in nuclear compression both through experimentation and mechanical modeling. Specifically, I sought to correlate nuclear morphology – a common alteration in cancer and laminopathies – with external force. This allows us to understand which nuclear mechanical constituents are deformed at different magnitudes of strain, which improves our understanding of how and why alterations in chromatin compaction and the nuclear lamina lead to misfunction. Furthermore, I sought to understand how compressive forces can lead to double-stranded DNA breaks. Such DNA breaks are thought to alter cell function, so my work then illuminates how cells in mechanically stressful environments may be more susceptible to genomic alterations due to external strain. Together, these goals have led to an improved understanding of nuclear mechanics which lays the base for further studies of mechanotransduction and disease.

This dissertation is organized into seven chapters:

1. Chapter 1 provides an introduction to the constituents of the cell nucleus and means of studying their mechanical properties. Additionally, I discuss the relevance of nuclear mechanobiology in the context of mechanotransduction, migration, and pathology.
2. In Chapter 2, I discuss our multi-modal microscope known as the versatile illumination engine with modular optical design (VIEW-MOD). Specifically, this includes my design for LBS illumination, how we implement multi-color 3D imaging in a single-objective LSFM, and characterizations of the system's dynamic optical elements. This original system features multiple modalities and is able to perform the light-sheet imaging of orthogonal planes in a single-objective system.
3. Chapter 3 discusses how we combine single-objective LSFM with AFM, constituting the first system capable of multi-color, volumetric LSFM imaging with time-correlated, 10 pN sensitive force measurements. To do so, I give an introduction to AFM and other combinations with fluorescence microscopy, followed by 2D (membrane tether mechanics) and 3D (nucleoli translocation) AFM-LS examples.
4. Chapter 4 details my invention of SPIM-FRAP, which provides simultaneous, FRAP-based 2D maps of diffusion. I discuss the specifics of the methodology as well as its applications to intranuclear diffusion of NLS-GFP and turnover of 53BP1-mCherry.
5. In Chapter 5, I show how we have used AFM-LS to study the mechanical properties of cell nuclei. In doing so, I discover the separate roles of chromatin and lamin A/C in nuclear compression – both regarding nuclear stiffness as well as nuclear curvature. Furthermore, I show the first observed instances of AFM compression leading to DNA damage independent of nuclear rupture, and perform a mechanical characterization of two cell lines that show different mechanisms of DNA damage formation.
6. Chapter 6 is the first review of mechanical models of cell nuclei [9]. I both discuss my model for AFM-LS compression of cell nuclei to validate the conclusions from Chapter 5 as well as review the current literature on modeling cell nuclei.
7. In Chapter 7, I discuss further directions for this work. Specifically, this includes measuring intranuclear strain, combining AFM-LS and SPIM-FRAP, and studying mechanotransduction at

the nuclear surface. Though this chapter is exclusively unpublished results, it constitutes many one-of-a-kind measurements using correlative force and microscopy methods for study nuclear mechanobiology.

CHAPTER 2: VERSATILE ILLUMINATION ENGINE WITH MODULAR OPTICAL DESIGN[1]

In studying nuclear mechanobiology, having the right tools is half the battle. As I described in Chapter 1, microscopy is a fundamental tool in monitoring deformation and strain of nuclei as they are subjected to external force. However, there is a current need for microscopes that can image with high spatiotemporal resolution in 3D and multiple-channels, while also being able to accommodate force probes and maintain sample viability. In this Chapter, I present our custom microscope termed VIEW-MOD (Versatile Illumination Engine with Modular Optical Design). This single-objective light-sheet microscope is unique in that it can image directly either x-z or x-y cross sections with simple software adjustments. Additionally, the VIEW-MOD system can be modified slightly to perform a suite of applications ranging from variable angle total internal reflection fluorescence (TIRF) microscopy to localized photoactivation. Chapter 2 will describe in detail my design of a Line Bessel Sheet (LBS) illumination scheme, highlight imaging of orthogonal planes of cell nuclei, and demonstrate fast, multi-color volumetric imaging on an open-top, single-objective light sheet system.

2.1 Introduction

Fluorescence microscopy (FM) is one of most powerful techniques in biological and biomedical research. A handful of FM techniques have been developed to accelerate acquisition speed, improve resolution, reduce background and/or reduce phototoxicity. The excitation strategies of FM can be divided into three major categories: widefield, point-scanning, and light-sheet illumination. In a widefield configuration collimated light exits the objective illuminating the entire sample. We are specifically interested in TIRF microscopy which effectively channels the illumination light to within a few hundred

[1] Portions of this chapter are previously published in Nelsen, E., et al. (2020). "Combined Atomic Force Microscope and Volumetric Light Sheet System for Correlative Force and Fluorescence Mechanobiology Studies." Sci Rep **10**(1): 8133. and Liu*, B. and Hobson* C., et al. (2019). "VIEW-MOD: a versatile illumination engine with a modular optical design for fluorescence microscopy." Opt Express **27**(14): 19950-19972.

nanometers of the substrate. With point-scanning, the objective focuses a collimated light source onto a diffraction limited point, which is raster scanned across the sample to render an image. In light-sheet illumination a thin sheet of excitation light is created either by focusing one axis of the illumination source or rapidly scanning a focused beam along a single direction. Scanning the light sheet across the sample can then create a 3D volume. In the following, we briefly introduce these three modes to highlight the advantages of a combined system.

Total internal reflection fluorescence microscopy (TIRF) is a widefield illumination technique that suppresses out-of-focus fluorescence by adopting evanescent waves for excitation. TIRF has been broadly used for single molecule detection and for studying dynamic events near the membrane. Data acquisition, however, suffers from the interference fringes due to the coherent nature of lasers. Several groups have reduced the coherence of the laser light prior to illumination either through a multi-mode fiber [146] or spinning/vibrating a diffusor [147, 148]. Other groups have performed fast scanning of the azimuth angle during a single exposure through a rotating wedge [149], a steering mirror [150-152], an Acoustic Optical Deflector [153], or a Digital Micromirror Device [154]. The former may lead to loss of light polarization that is critical in many applications. Uniform TIRF illumination can alternatively be achieved by forming a ring of laser illumination at the back-focal-plane (BFP) of the objective. The 360-degree in-plane (from all sides), polarized illumination will generate a radially symmetric evanescent field exhibiting a flattop intensity profile across the field-of-view [155]. This technique is commonly referred to as variable angle or spinning TIRF (vaTIRF or spinTIRF). Commercially available vaTIRF systems such as iLas2 from Roper Scientific and TILL/ FEI's iMIC with the Polytrope illuminator are expensive and lack the flexibility to combine other imaging modalities.

Point illumination is also a powerful technique as it allows researchers to selectively illuminate a portion of the sample without perturbing other areas. This technique is particularly useful in the field of optogenetics to precisely activate or inhibit particular proteins with precise spatiotemporal resolution. However most of the experiments were carried out with either a separate photoactivation module [156] or a commercialized confocal microscope [157]. Implementing both point and widefield in the same light path is non-trivial, yet would allow for further techniques to be employed in separate paths of an optical system.

Light sheet fluorescence microscopy (LSFM) is an increasingly popular technique for imaging biological specimens at high spatiotemporal resolution with reduced background and phototoxicity; therefore LSFM is well suited for long-term 3D imaging of both single cells and tissue [158]. Numerous variations of light sheets (Gaussian, Bessel beam, line Bessel sheet, Airy beam, etc.) have been demonstrated in the past, each providing a unique means of illuminating a thin slice of a given sample [158]. The most notable of these techniques is lattice light sheet, where a two-dimensional optical lattice is used to create thin, structured illumination sheets that are dithered during a single exposure [159]. Traditionally LSFM requires two objective lenses, one for illumination and one for detection, placed at a 90-degree angle relative to each other such that the light sheet from the illumination source coincides with the imaging plane of the detection objective [159-166]. Such systems can be less user-friendly than conventional microscopes. High numerical aperture (N.A.) immersion objectives are almost precluded from LSFM applications due to the geometry configurations and the physical dimensions of the objectives. Both our research group and others have implemented LSFM in a single-objective system [144, 167-179]; here we present how we can combine single-objective LSFM into a microscope design that allows for other FM techniques.

Each of the above imaging modalities has distinct advantages; a system capable of each technique is then ideal for studying various biological processes. In the past few decades, tremendous efforts have been done to integrate different imaging modalities, such as combining force measurements with fluorescence imaging [180-182], combing Raman spectroscopy with fluorescence imaging [183, 184], and combining electron microscopy with light microscopy [180, 185, 186]. Other groups have also explored multi-modality fluorescence microscopes that combine wide-field illumination with optical tweezers [187], two separate super resolution methods [188], multiple light sheets [189], or epifluorescence and TIRF [190-192]. Groups have also integrated multiple excitation approaches with different detection schemes, such as combining dark-field, TIRF and confocal illumination with wide-field, confocal and spectroscopy detection [193]. These systems are however not adaptable to all the illumination techniques we have outlined. Here, we present a novel microscope design capable of widefield (particularly vaTIRF), point scanning, and LSFM. Our design is compact, modular for customization, cost effective, and built upon a conventional inverted microscope, allowing it to be

implemented in most laboratories. The different illumination modes can run independently or be switched in a single experiment, allowing one to combine or change the imaging modality to fit the experiment at hand. The microscope is operated with an open-source software package to calibrate and control the system, which is independent of the microscope automation software

2.2 System Design

Here we present a versatile optics design that provides precise control of the translation, tilt, and shape of illumination light at the back focal plane (BFP) of the objective and/or the sample plane, as well as axial control of the imaging plane through a series of electrically tunable lenses (ETL) and scanning mirrors (SM) (Figure 2.1). Our design is conceptually divided into a series of modules (Figure 2.1, dashed box 1-5), each with a specific purpose for shaping and controlling the light through the system. Modules 1-4 govern the illumination pathway while module 5 lies in the detection pathway. Through using some or all of the modules available, our system can implement a variety of imaging modalities. Here, we outline the theory and purpose of each module, with the reader directed to Figure 2.1 for the optical layout.

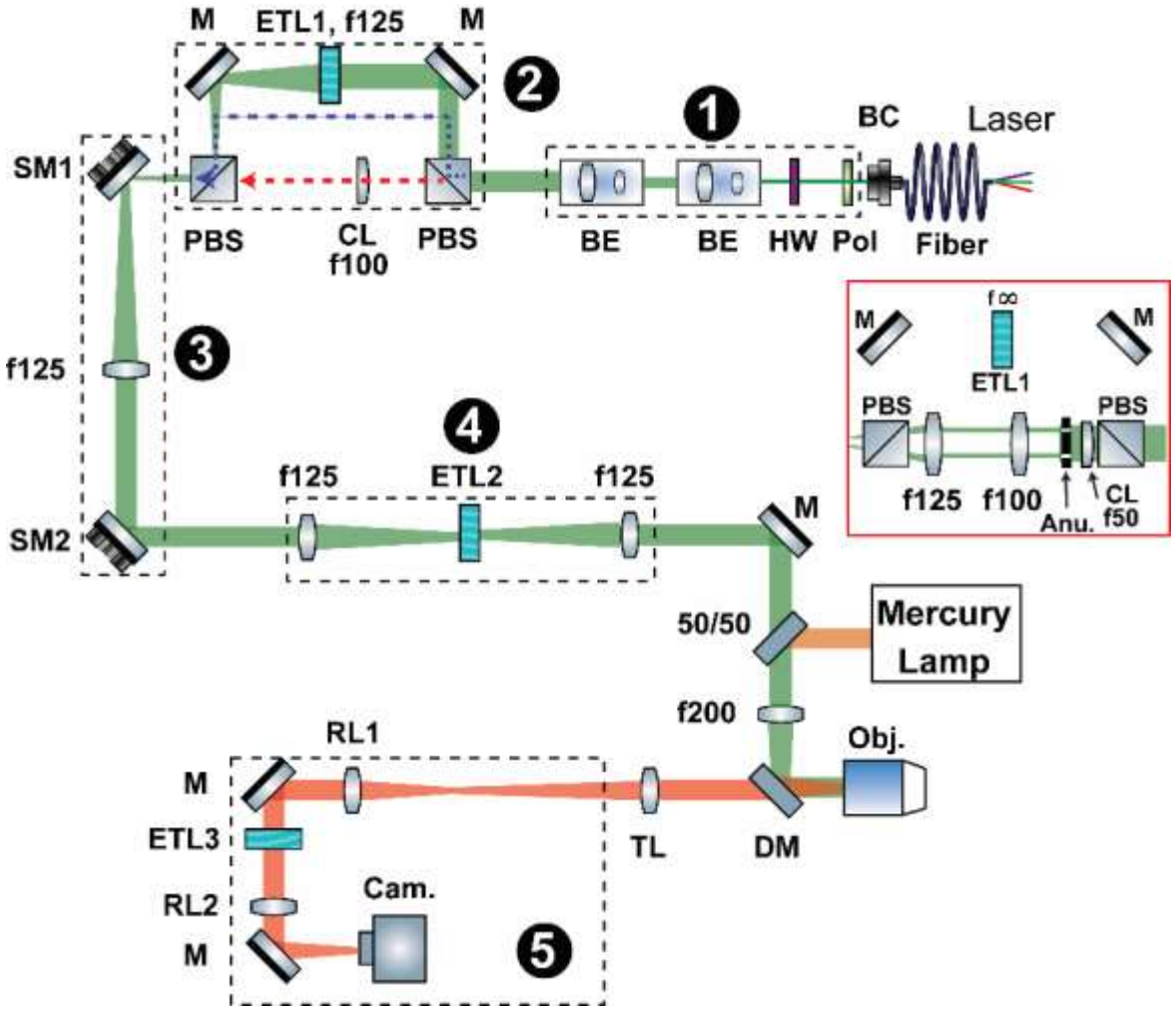

Figure 2.1: Schematic of the VIEW-MOD system. Linearly polarized lasers are expanded, collimated and exit Module 1. The light propagates to Module 2 through either pathway 1 (blue dashed-line) for TIRF and point-scanning or pathway 2 (red dashed-line) for LSFM, depending on the orientation of its polarization axis. For TIRF, ETL1 is adjusted to 125 mm effective focal length to focus the beam onto SM1, resulting in a collimated light beam coming out the objective. For point-scanning ETL1 is set to ~ 0 volts, equivalent to f=∞ (flat plate). For LSFM, we either put a 125 mm cylindrical lens to create a Gaussian light sheet or use a combination of a cylindrical lens and an annulus to create a Line Bessel Sheet (LBS) (red insert box). Steering Mirrors 1 and 2 (SM1 and SM2) are optically conjugated with the specimen plane and the Back Focal Plane (BFP) of the objective, respectively. ETL2 provides axial scanning of the illumination light. In the detection module (Module 5), the image is projected to the camera through a relay lens group (RL1 and RL2) with ETL3 placed in the center (mimicking Module 4) to achieve an adjustable image plane. Schematic was generated with GW Optics component library (http://www.gwoptics.org/ComponentLibrary/).

2.2.1 Module 1: beam expansion and polarization modulation

Module 1 controls the size and polarization of the illumination light. Multiple linearly polarized lasers are coupled into a single-mode, polarization-maintaining fiber (PM-S405-XP, Thorlabs). The light from the fiber is collimated by an achromatic beam collimator (BC) (PAF-X-18-PC-A, Thorlabs) and is

then expanded/collimated through two commercially available expanders/collimators (BE052-A and GBE03-A, Thorlabs). The first is a 0.5-2x beam expander/reducer; the second has a fixed 3x zooming capability. Both beam expanders can adjust the output light collimation and feature an achromatic design. With two expanders, we can modulate beam size from 4.5 mm to 18 mm and fine-tune the collimation. This properly sizes the incident beam for a given application, such as filling the back aperture of the objective lens for point illumination to obtain the tightest focus. The beam size from the expanders will not change during the following experiments. The polarization axis of the light exiting the optical fiber is then adjusted by either rotating a half-wave plate (AHWP05M-600, Thorlabs) or through a liquid crystal retarder (LCC1111T-A, Thorlabs). A polarized beam splitter (PBS) redirects the light to different light paths of module 2 to switch between a circular beam cross section or a cylindrical (light sheet) cross section. The PBS determines the orientation of the polarization of the beam, and the tunable waveplate governs the amplitude of the light going into each arm of the following module. We note that the system is designed such that when using light sheet illumination, the polarization vector of the illumination light is aligned with the plane of the light sheet. In some cases, it may be useful to switch the polarization state of the illumination beam at the specimen. That can be accomplished by adding a second waveplate after module 2. The use of a tunable filter allows computer control of these operations.

2.2.2 Module 2: beam shaping

The beam-shaping module accommodates two light paths for different applications. The switching between light path 1 (LP1) or LP2 is achieved by altering the polarization direction of the incident laser using module 1. This can be computer controlled by employing the liquid crystal retarder. LP1 retains the incident circular cross section, while allowing for quick transitions from widefield illumination to point illumination with ETL1 (EL-16-40-TC, Optotune). When the ETL is set such that the focal length approaches infinity, light is not deflected resulting in a collimated beam at the BFP of the objective; the objective focuses the light to a diffraction-limited point at the sample. This will be useful, for example, for photoactivation employed below. The focal length of the ETL can be adjusted such that the beam is focused at the BFP of the objective, resulting in a wide, collimated illumination at the sample. This will be employed for our TIRF imaging. The response and settling times of the ETL are 5 ms and 25 ms

respectively, allowing for dynamic switching of imaging modalities on the order of exposure times for biological imaging. LP2 is used to shape the illumination light to be cylindrical in cross section, which is frequently used in light sheet imaging. LP2 contains an optic, typically a cylindrical lens, to converge one of the transverse axes of the light while keeping the second axis collimated, creating a cylindrical pattern. Alternatively, we can use a combination of a cylindrical lens and an annulus to achieve Line Bessel Sheet (LBS) (Figure 2.1, red solid-line box). These two paths are then rejoined through a second polarized beam splitter. Having two illumination geometries in a single system allows one to employ drastically different illumination techniques (e.g. LSFM and point scanning) on a single sample.

2.2.3 Module 3: beam steering

Module 3 controls the steering of the illumination light both at the BFP of the objective and at the sample plane using two fast steering mirrors (SM1,2) (OIM 101 1", Optics In Motion LLC). SM1 is optically conjugate to the BFP of the objective while SM2 is optically conjugate to the sample plane. The former controls the position of the beam at the sample plane and the latter adjusts the tilt at the sample plane. SM1 and SM2 are driven by voice coils and are each able to control two axes of tilt in a single mirror. This allows a more compact design for optical conjugation with a single mirror compared with using galvo-scanners, which typically needs two mirrors in a 4f configuration. While galvo-scanners are notably faster, SM1 and SM2 can execute a 1 mrad step in under 5 ms, providing enough speed for sub-second volumetric imaging.

2.2.4 Module 4: axial beam scanning

Module 4 provides control of the axial position of the illumination light without physical displacement of the objective lens. Keeping the objective motionless is ideal as it reduced small motions of the sample that are coupled to objective movement. We use a 4f system to relay the beam and position a second ETL (ETL2) (EL-16-40-TC, Optotune) midway between the second and third relay lens (conjugate to the BFP of the objective). Adjusting the focal length of ETL2 subsequently scans the focus of the illumination light axially [194]. This can be especially useful for both LSFM and point scanning to ensure that the tightest focus of the illumination light is at the desired axial location in the sample.

2.2.5 Module 5: axial image plane scanning

Module 5 is an identical 4f system to that of module 4, lying in the detection path. Similarly, we place an ETL (ETL3) (EL-16-40-TC, Optotune) midway between two relay lenses. Adjusting the focal length of ETL3 then shifts the axial position of the imaging plane [168, 195, 196]. One can dynamically manipulate the focus of an image during an experiment without moving the objective lens or the illumination light. It should be noted that large scale changes of the optical power of ETL3 will (de)magnify the image [163, 197]. Other groups have used an ETL for axial control of the imaging plane by placing the ETL directly behind the detection objective [163, 197-200], however using ETL3 in a 4f system makes it easier to access and adjust as well as minimizes the (de)magnification effects [195, 196]. We ensure that ETL3 lies flat (its optical axis is normal to the table) to avoid gravitational effects which would distort the Optotune lens.

2.3 Single-Objective Light-Sheet Fluorescence Microscopy Implementation

2.3.1 Line Bessel Sheet Illumination Design

To implement LSFM, we employ modules 1-5. Module 1 properly sizes the beam and rotates the polarization state such that the light passes through LP2, the cylindrical cross section path of module 2, and the polarization vector is in the plane of the light sheet. One could easily create a Gaussian light sheet by placing a cylindrical lens, CL f100 (LJ1567RM-A, Thorlabs), before SM1 in place of the current LBS pathway (Figure 2.1, module 2, LP2). To gain an extended depth of field for a given waist size, we use a Line Bessel Sheet (LBS). To create an LBS we use a cylindrical lens (LJ1567RM-A, Thorlabs) to focus one axis of a collimated light source at the location of the annulus (R1DF200, Thorlabs), resulting in two coherent bands of light that propagate through the remaining optical path (Figure 2.1, red insert box). The annulus is optically conjugate to the BFP of the objective. When the two coherent bands pass through the objective lens (UplanSAPO 60x/1.2 W, Olympus), they interfere with each other resulting in a Line Bessel Sheet [166]. Our light sheet is not a theoretical Bessel light sheet as the central lobe is not propagation invariant. It is then a Bessel-Gauss light sheet as the bands at the BFP of the objective are of finite thickness [201].

When designing the LBS illumination scheme, we sought to model the theoretical light sheet profile at the sample plane. To do so, we first use the matrix method to propagate the illumination light through our optical path to the back focal plane (BFP) of the objective [202]. In this matrix-based approach to Gaussian optics, each lens in the system is represented by a refraction matrix, given by

$$R(f) = \begin{pmatrix} 1 & 0 \\ -\frac{1}{f} & 1 \end{pmatrix} \tag{2.1}$$

where f is the focal length of the lens. Likewise, a propagation through free space is represented by a transfer matrix, given by

$$T(d) = \begin{pmatrix} 1 & d \\ 0 & 1 \end{pmatrix} \tag{2.2}$$

where d is the distance between lenses. The optical path is represented by a product of these matrices beginning with the first lens and ending with a propagation to the BFP. That is, the system matrix is given by

$$M(f_n, \dots, f_2, f_1, d_n, \dots, d_2, d_1) = \begin{pmatrix} A & B \\ C & D \end{pmatrix} = T(d_n) \cdot R(f_n) \cdot \dots \cdot T(d_2) \cdot R(f_2) \cdot T(d_1) \cdot R(f_1) \tag{2.3}$$

Knowing that the laser light coming out of the optical fiber and into our system is collimated with an initial beam waist, $\omega_{0\,i}$, and an initial Raleigh length, $z_{0\,i}$, which is calculated through the relationship

$$\omega_0(\lambda, z_0) = \sqrt{\frac{\lambda\, z_0}{\pi}} \tag{2.4}$$

where λ is the wavelength of light. We can use the system matrix, M, to understand the beam profile at the BFP. Specifically, we can calculate the Raleigh length at the BFP, $z_{0\,bfp}$, through the relationship

$$z_{0\,bfp}(z_{0\,i}) = \frac{z_{0\,i}}{D^2} \tag{2.5}$$

where D is given in Eq. 2.3. We then can convert the $z_{0\,bfp}$ to the beam waist at the BFP, $\omega_{0\,bfp}$, through Eq. 2.4 to understand the beam profile propagating into the objective. However, because we have a cylindrical lens in our optical path, the system matrix is different for the two axes orthogonal to the propagation direction. That is, we can calculate a separate M_x and M_y to propagate the two axes separately and subsequently calculate the beam waist at the BFP in each direction, $\omega_{0x\,bfp}$ and $\omega_{0y\,bfp}$. Knowing the beam profile at the BFP is crucial for properly modeling the LBS at the sample plane. As

Gaussian optics does not hold for objective lenses, we make use of the full 3D electromagnetic wave propagation theory [203-205]. The magnitude of the electric field at the BFP is given by

$$E_0(\theta_{bfp}, \phi_{bfp}) = A\, e^{-\left(\frac{f\ \sin\theta_{bfp}\ \cos\phi_{bfp}}{\omega_{0x\,bfp}}\right)^2} e^{-\left(\frac{f\ \sin\theta_{bfp}\ \sin\phi_{bfp}}{\omega_{0y\,bfp}}\right)^2} \tag{2.6}$$

where A is a constant representing peak magnitude of the electric field, f is the characteristic focal length of the objective lens, and θ_{bfp} and ϕ_{bfp} are the polar and azimuthal angle coordinates at the BFP. The three components of the electric field at the sample plane, represented by the polar coordinates r_s θ_s, and ϕ_s, are given by the following equations.

$$E_x(r_s, \theta_s, \phi_s) = \frac{-i}{\pi} \int_{\alpha_1}^{\alpha_2} \int_{0}^{2\pi} E_0(\theta_{bfp}, \phi_{bfp}) \cos^{\frac{1}{2}}\theta_{bfp}\ \sin\theta_{bfp}\ \left(\cos\theta_{bfp} + \left(1 - \cos\theta_{bfp}\sin^2\phi_{bfp}\right)\right) \times e^{i\,k\,r_s\,(\cos\theta_s\cos\theta_{bfp} + \sin\theta_s\sin\theta_{bfp}\cos\phi_{bfp} - \phi_s)}\, d\phi_{bfp}\, d\theta_{bfp} \tag{2.7}$$

$$E_y(r_s, \theta_s, \phi_s) = \frac{i}{\pi} \int_{\alpha_1}^{\alpha_2} \int_{0}^{2\pi} E_0(\theta_{bfp}, \phi_{bfp}) \cos^{\frac{1}{2}}\theta_{bfp}\ \sin\theta_{bfp}\ (1 - \cos\theta_{bfp}) \cos\phi_{bfp} \sin\phi_{bfp} \times e^{i\,k\,r_s\,(\cos\theta_s\cos\theta_{bfp} + \sin\theta_s\sin\theta_{bfp}\cos\phi_{bfp} - \phi_s)}\, d\phi_{bfp}\, d\theta_{bfp} \tag{2.8}$$

$$E_z(r_s, \theta_s, \phi_s) = \frac{i}{\pi} \int_{\alpha_1}^{\alpha_2} \int_{0}^{2\pi} E_0(\theta_{bfp}, \phi_{bfp}) \cos^{\frac{1}{2}}\theta_{bfp}\ \sin^2\theta_{bfp} \cos\phi_{bfp} \times e^{i\,k\,r_s\,(\cos\theta_s\cos\theta_{bfp} + \sin\theta_s\sin\theta_{bfp}\cos\phi_{bfp} - \phi_s)}\, d\phi_{bfp}\, d\theta_{bfp} \tag{2.9}$$

Here, $k = 2\pi/\lambda$ is the wave vector, and α_1 and α_2 are the polar angles that correspond to the minimum and maximum $NA = n\sin\alpha$ of the annular aperture used to create the LBS magnified to the BFP. If α_1 is set to zero and α_2 is set to match the NA of the objective lens, Eqs. 2.7 – 2.9 can be used to model a typical Gaussian light sheet. For our system, however, NA_1 = 0.08 and NA_2 = 0.38.

After modeling the LBS at the sample, we subsequently characterized the actual lateral and axial beam profiles. The measured lateral and axial FWHM of the LBS is 771 nm (Figure 2.2(a)) and 14.8 μm (Figure 2.2(b)) respectively, both of which match well with the theoretical value as determined via the theory given above. A Gaussian light sheet of the same lateral FWHM would have an axial FWHM of 4.81 μm [202]. Our LBS then has a three-fold larger characteristic propagation length. The lateral FWHM is designed to approximately match the axial FWHM of the point-spread function (PSF) of the objective lens such that the side-lobes of the LBS are minimized in the overall system PSF [166].

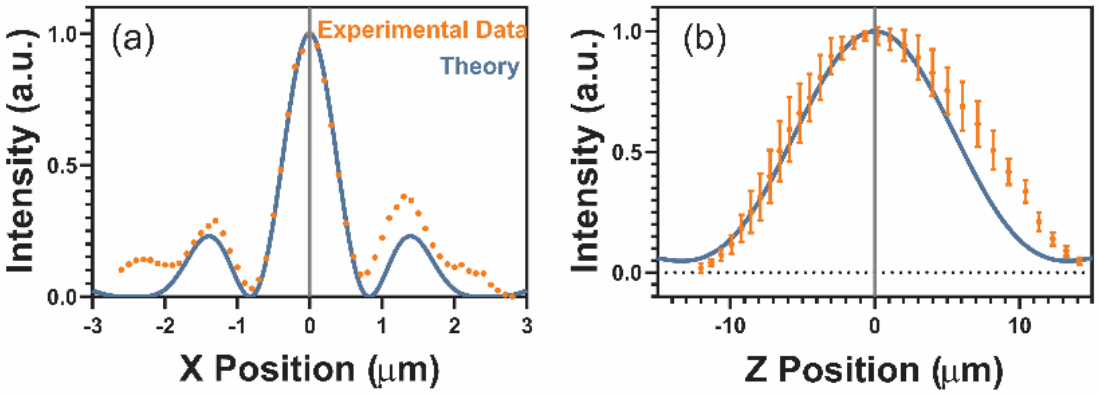

Figure 2.2: Profile of LBS. (a) Lateral profile of the LBS. A 100 nm fluorescent bead was stepped laterally in 100 nm increments by a piezo stage; intensity of the bead was measured in FIJI for each position. (b) Axial profile of LBS. 100 nm fluorescent beads were imaged as the LBS was stepped axially by ETL2 in 2 mA increments. Intensity of 7 beads was tracked across the scan in FIJI, error bars are standard deviations in intensity. Orange represents measured intensity from the fluorescent beads; blue represents a theoretical profile [203-205].

There are some distinct advantages and limitations to using an LBS as opposed to a Gaussian light sheet (GLS). As previously mentioned, the first advantage is that an LBS provides an extended depth of field for a given beam waist when compared to a GLS (Figure 2.3) [206]. This allows one to either obtain a longer light sheet or reduced the sheet thickness with less tradeoff than when using a GLS. It has recently been shown, however, that GLSs can obtain similar depth of fields for a given beam waist to square lattice light sheets [207]. However, the GLSs used in this work are fundamentally not Gaussian as light sheet profile as the sample is modulated by an aperture conjugate to the BFP as opposed to modulating the actual beam profile at the BFP. These light sheets are the effectively LBSs with an inner NA of 0. However, it is still quite intriguing that this intermediate GLS/LBS can obtain similar beam properties to that of a square lattice light sheet. The second major advantage of a LBS is that it has an inherent “self-healing” property [208]. That is, it can reconstruct itself beyond an obstruction. This occurs because the energy forming the light sheet is incident at an angle, so an obstruction at the front of the sheet does not occlude the energy from propagating past it and reforming the sheet behind the obstruction. This is particularly useful for imaging biological sample due to their inherent heterogeneity.

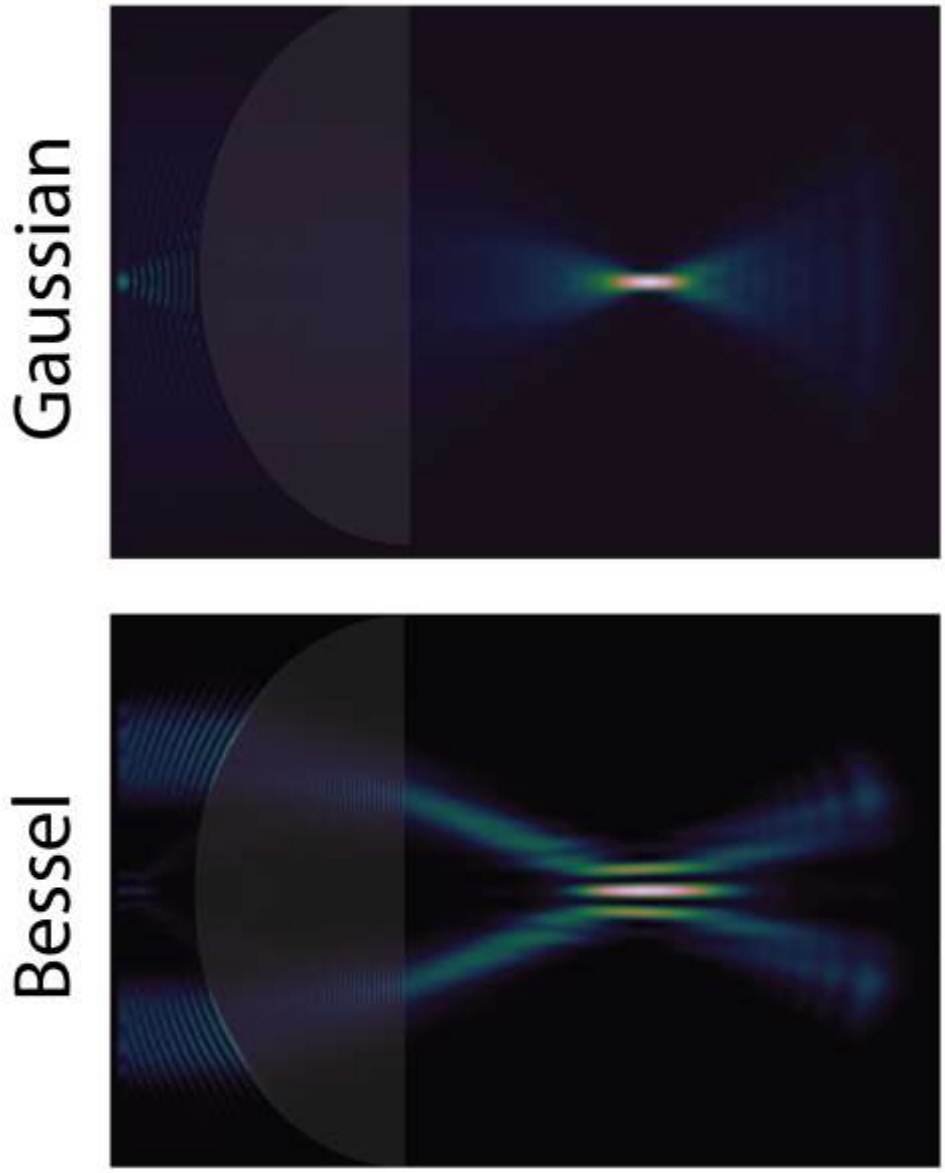

Figure 2.3: Simulation of Gaussian and Bessel light sheets. See also Video 2.1 and Video 2.2.

There are tradeoffs, however, when using an LBS as opposed to a GLS. First, we generate our LBS by passing a GLS through an annular aperture. This then blocks out the center of the GLS and subsequently a sizeable portion of the illumination light. For our system specifically, we estimate that we lose approximately 50% of the initial laser power at the annulus. This can be mitigated with high intensity lasers, though they come at an additional cost. Furthermore, an LBS is accompanied by concentric side lobes (Figure 2.2A, Figure 2.3), whereas a GLS is not. These side lobes illuminate the sample outside of the image plane of the detection objective, and therefore work against the fundamental concept of LSFM.

However, if the system is optimized such that the PSF of the detection objective matches in size the thickness of the central band of the LBS, these side lobes are sufficient damped in the total system PSF and therefore cause little background fluorescence. They will, however, still work to bleach regions outside of the plane of interest and reduce the overall intensity of the central band, which adds further issues. Whether or not to use an LBS is a system-dependent question, and there is no one answer for all microscopes. For our system, the trade-off of the additional side lobes and loss of light at the sample were worth the additional depth of field and self-healing properties and therefore we chose to implement an LBS.

2.3.2 Horizontal and Vertical Light Sheet Imaging of Chromatin

Modules 3 and 4 provide complete control of all three spatial positions of the illumination light while module 5 allows us to adjust the axial position of the imaging plane. We use a home-built LabView program that controls two NI DAQ boards (PCIe-6323 and PCI-6723). One controls voltages to the SM1 controller and ETL3 controller (TR-CL180, Gardasoft) while the other controls an acousto-optic tunable filter (AOTF:AOTnC-400.650-TN, Opto-Electronic) in our light engine to gate the laser light. We use the Optotune software to control the current applied to ETL2 which subsequently varies the optical power. We employed two LSFM methods, Horizontal Light Sheet (HLS) and Vertical Light Sheet (VLS), to image chromatin of cell nuclei (Figure 2.4). For both methods we introduced a small (180 μm) right-angle reflective prism (8531-607-1, Precision Optics) attached to a 6 degree-of-freedom mount, and lowered the mirror adjacent to the cell of interest [144]. For HLS imaging, the LBS reflected off the mirror and illuminated a single x-y plane. SM1, ETL2, and ETL3 were used to appropriately position the LBS and the imaging plane. For VLS imaging, the LBS propagated vertically out of the objective and through the cell, illuminating a single y-z slice. The objective was raised until the imaging plane intercepted the reflective optic. This rotated the imaging plane from x-y space to y-z space. As the objective was continually raised, the imaging plane stepped through the cell in X until it was aligned with the illuminated slice. Raising the objective lens outside of its traditional operating range can induce spherical aberration, so we have opted for a water immersion objective lens in order to minimize this impact. As a demonstration of these

techniques, we used both HLS and VLS to sequentially image orthogonal planes of a COS-7 cell nucleus stably expressing HaloTag-H2B labeled with Janelia Fluor 549 (JF549) (Figure 2.4(c,d)).

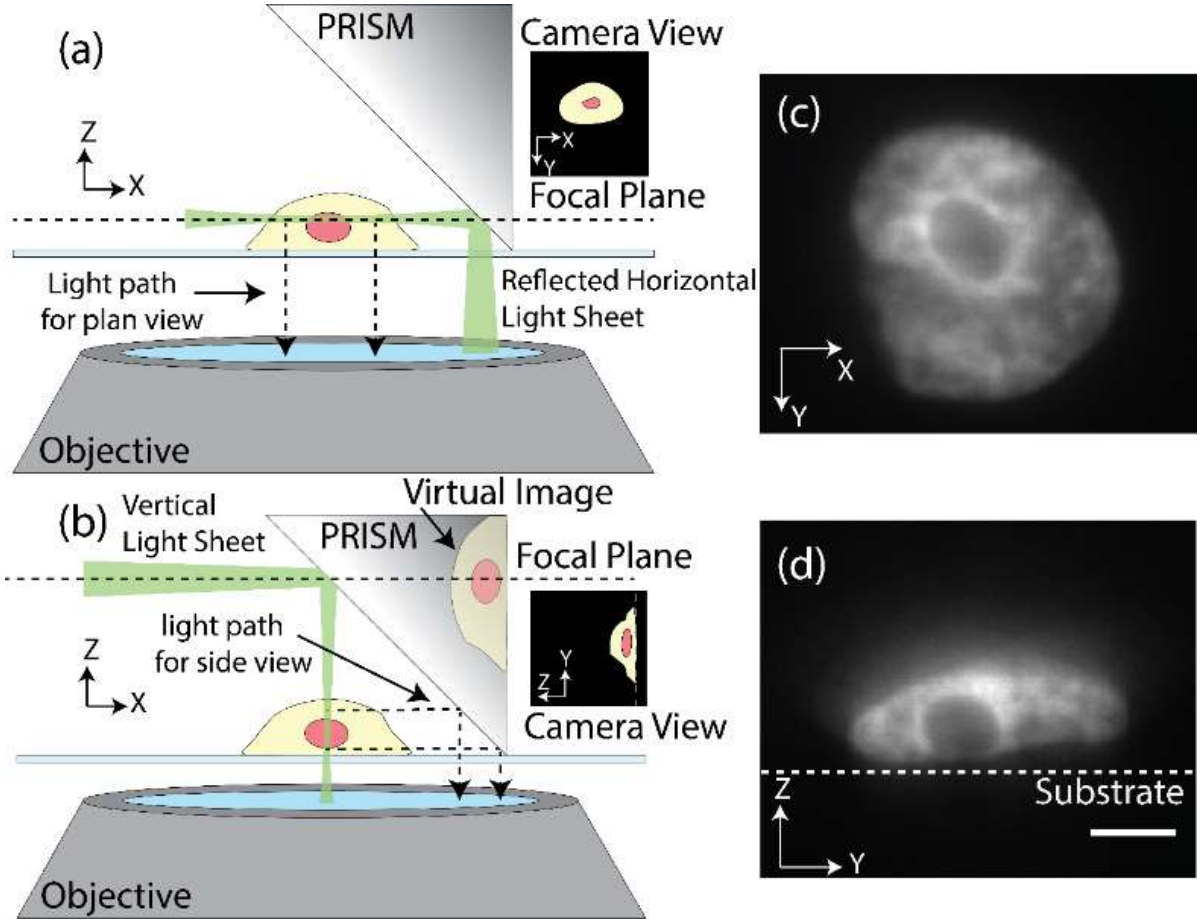

Figure 2.4: LSFM of orthogonal planes of heterochromatin and euchromatin. (a) Imaging setup for Horizontal Light Sheet. The light sheet emerges from the objective and is reflected by a right-angle prism. The image plane is matched (by module 5) to the plane of the reflected light sheet. (b) Imaging setup for Vertical Light Sheet. The light sheet emerges from the objective and creates a vertical slice through sample. The right-angle prism creates a virtual side-view image of the vertical slice. Horizontal (c) and vertical (d) light sheet images of the same COS-7 nucleus expressing HaloTag-H2B labeled with Janelia Fluor 549. Scale bar = 5 µm.

Transitioning from HLS to VLS is straightforward, fast, and can be done entirely through software. It is important to note that resolution can be affected by imaging in VLS as light collected is altered when imaging off of the prism [145]. Additionally, using an ETL for axial scanning of either the image plane or the illumination light will introduce additional spherical aberration; this can decrease the lateral and axial resolution by as much as a factor of two when using the full range of the ETL [200]. To transition from HLS to VLS requires movement of the image plane on the order of 50 µm, so one must understand the system's tradeoff between maximizing resolution and rapid transitions between HLS and VLS modes

using ETL3. Minimal adjustments of ETL3 (~10% of the full operating range) to maintain focus while in either HLS or VLS modes introduces minimal spherical aberration and negligibly impacts resolution.

Because of LSFM's ability to illuminate a single plane, we obtained images with low background and high signal-to-noise of orthogonal planes of the same nucleus. We observed that the light collection efficiency for a given illumination intensity and exposure time using HLS is approximately double that of using VLS. For highly sensitive imaging techniques such as FRET it is beneficial to use HLS imaging due to the larger signal-to-noise. However, AFM studies are better served with VLS imaging as it allows the user to take fast, high resolution images of the plane in which the AFM tip is applying force without the need for taking whole stacks [181, 209, 210]. Because of the lack of background fluorescence, we could discern heterochromatin (high H2B density) from euchromatin (low H2B density) within the nucleus. Specifically, we observed that a thin ring of heterochromatin surrounds the nucleolus. Visualizing chromatin structure is important in understanding chromosome territories and gene expression [90].

Several other variants of single-objective (so)LSFM exist and have proven useful for imaging live biological samples of varying scales. There are two primary variants of soLSFM: reflective-based soLSFM [167-169, 174, 179] and oblique plane illumination microscopy (OPIM) [170, 171, 175-178]. The former is akin to our HLS approach, wherein a reflective optic is located adjacent to the sample of interest and the single objective located beneath the sample captures the emitted light resulting from excitation with a horizontal light sheet. This technique has been implemented with a scanned beam approach [168] and a traditional Gaussian light sheet generated through a cylindrical lens approach to LSFM [179]. Furthermore, investigators have leveraged atomic force microscopy (AFM) cantilevers as the reflective optic in order to make reflective-based soLSFM compatible with multiwell plates [174]. The second class of soLSFM techniques is OPIM. The primary idea in OPIM is to illuminate the sample with a tilted light sheet from below (angles range typically between 30º - 45º), then use the same objective lens to capture the emitted photons. The emitted light is then propagated to a remote focusing unit which features two objective lens that are positioned at the same relative angle as the oblique light sheet is to the single objective at the sample. The first objective in the remote focusing unit re-images the light sheet at the sample, and the second objective captures this image as the proper alignment places the image plane of the second objective in the same plane as the reformed image. For volumetric imaging, either the sample

can be moved through the oblique light sheet [178] or the light sheet can be scanned through the sample with the resulting image being de-scanned by the same scanning mirror [175, 176]. The beauty of this approach is that neither the objective lens at the sample nor the objectives in the remote focusing unit need to physically move in order to capture volumetric images. Clever innovations in the remote focusing unit have allowed OPIM to be adapted to higher NA objective lenses [170, 171]. While reflective-based soLSFM and OPIM encompass a majority of soLSFM techniques, our VLS approach to soLSFM is entirely unique as it rotates the image plane itself with a reflective optic as opposed to rotating the plane of the light sheet or re-focusing remotely. This provides a unique view (side-view) that no other soLSFM method is able to image.

2.4 System Characterization

2.4.1 Steering Mirror and Tunable Lens Calibrations

As noted earlier, SM1 is conjugate to the BFP of the objective. Tilting SM1 translates the LBS in x-y at the sample plane. For volumetric imaging, we need to control only the translation of the LBS in the x direction (perpendicular to the long axis of the light sheet). We can then use a linear combination of the two voltage controls to SM1 to create a single voltage control parameter that translates the LBS in the x direction. To calibrate SM1, we used a fluorescent slide to visualize the LBS. We incrementally stepped the SM1 control voltage while taking an image at each step; the center of the LBS was determined for each image and plotted against its corresponding voltage. A line was fit to the resulting plot to determine a conversion of SM1 voltage to LBS translation (Figure 2.5(a)). Scanning SM1 allows us to translate the LBS laterally and collect volume images, and the calibration provides a means of calculating the voxel size. To calibrate ETL2, we again used a fluorescent slide to visualize the LBS. The objective lens was incrementally stepped and ETL3 was used to readjust image plane back to the coverslip. ETL2 was then used to lower the LBS back to the fluorescent substrate. This provided a calibration for how ETL2's current adjusts the axial position of the LBS (Figure 2.5(b)). Adjusting ETL2 ensures that the thinnest portion of the LBS is always located in our sample without manually adjusting the objective height. The maximum effective NA of the LBS is approximately 0.38, so utilizing ETL2 to axially scan the light sheet does not significantly compromise its structure. The Gardasoft controller for ETL3 is programmed to the

linear analog mode (0 V – 10 V) and outputs a current based on a closed-loop temperature feedback system. To calibrate ETL3, we place a grid (R1L3S3, Thorlabs) on the microscope and manually step the objective lens position. ETL3 is used to bring the grid back into focus, providing a calibration of ETL3 voltage with the imaging plane position (Figure 2.5(c)). Imaging plane location, light sheet position and AOTF are synchronized through an NI DAQ board.

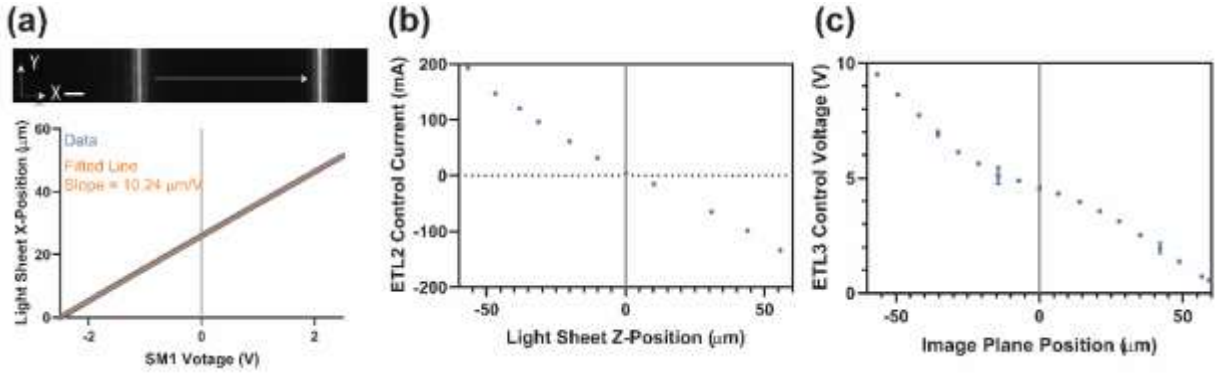

Figure 2.5: Calibration of SM1, ETL2, and ETL3. (a) Calibration of SM1 showing the light sheet x-position versus voltage applied to SM1 as well as a linear fit to this data. The slope of the linear fit provides us a conversion from SM1 voltage to scanning distance, allowing us to understand and properly set our voxel size during volume imaging. Scale bar = 5 μm. (b) Calibration of ETL2 showing the current applied to ETL2 versus the light sheet z-position. (c) Calibration of ETL3 showing the voltage applied to ETL3 versus the axial position of the image plane. Error bars for (b) and (c) are 95% confidence intervals, but are often smaller than the visualization of the data points.

For volumetric LSFM, both the image plane and LBS need to be stepped throughout the volume in sync. We used SM1 to step the LBS in increments laterally in the x-axis through the cell, and ETL3 was adjusted such that at each step the image was in focus. Every time the mirror was brought down next to a cell of interest, the spacing of the cell and mirror was different and the angle of the mirror relative to the substrate was slightly varied due to the mechanical micrometer control mechanism. For each cell, we then performed an initialization scan (Figure 2.6) yielding a lookup table of the ETL3 voltage value that provided the best focus for each LBS position in the volume scan. This initialization scan is done first by performing small sweeps of the ETL3 control voltage at a given LBS position. Image quality of the sample is assessed at each ETL3 control voltage through the Tenegrad method [165, 211], and a Gaussian is fit to the resulting data set (Figure 2.6(a)). This process is then repeated at several different LBS locations, and a linear interpolation fills in the parameter space between these locations (Figure 2.6(b)). This results in the aforementioned lookup table that is used for volumetric imaging.

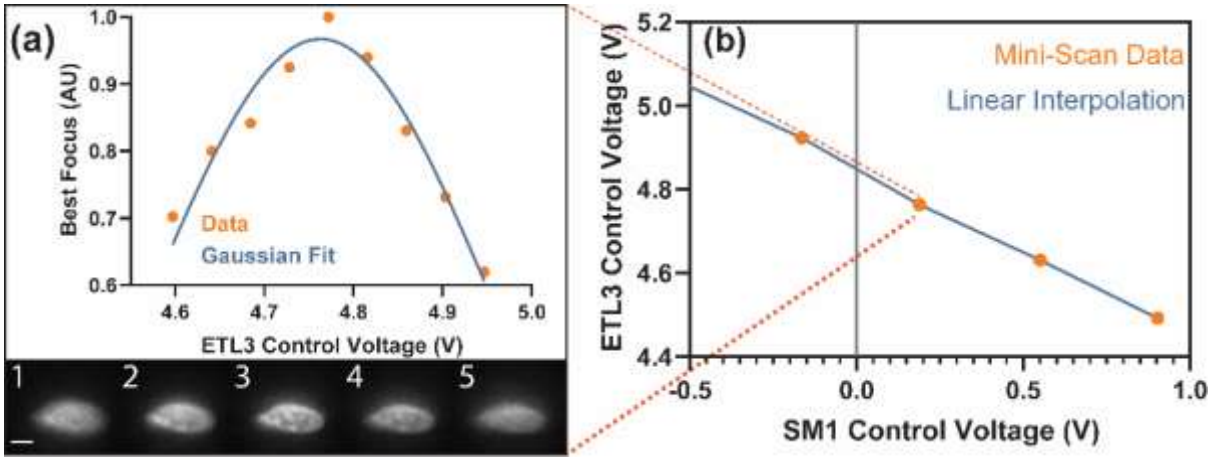

Figure 2.6: Initialization scan procedure for volumetric imaging. (a) A sample mini scan of a COS-7 nucleus expressing HaloTag-H2B labeled with Janelia Fluor 549 used in the initialization scan where the LBS is fixed to a specific location and the ETL3 voltage is varied about a suggested voltage of best focus. The Tenegrad method [165, 211] is used on each image from the mini scan to provide a metric for image quality. A Gaussian is fit to the mini-scan data to provide the optimal ETL3 voltage for a given light sheet position. (b) A sample lookup table that provides the best ETL3 voltage for a given light sheet position. Each orange data point is generated by a mini scan procedure. A linear interpolation is done between data points and is discretized based upon the number of slices per volume.

2.4.2 System Point Spread Function

In order to collect a side-view point spread function (PSF), we needed a sample that provided both fluorescent point particles as well as a fluorescent object to perform the initialization scan described above. Our sample of choice was a large (~10 μm) fluorescent, polyacrylamide (PA) sphere with a sparse coating of small, (~100 nm) fluorescent beads is a separate channel. The large PA sphere provide an appropriate object upon which to run an initialization scan, providing a lookup table converting ETL3 control voltages to SM1 control voltages. The lookup table was then used to collect side-view, volumetric images of the 100 nm fluorescent beads to obtain a PSF (Figure 2.7a).

Using the PSF theory previously determined [145] and the Rayleigh criterion for resolution, we calculate a x-axis resolution of 381 nm and a z-axis resolution of 574 nm with values based on the bead position with respect to the prism and substrate (Figure 2.7b). The expected axial (y-axis) PSF profile is calculated using these values then combined with the PSF profile of the Line Bessel sheet (Combined FWHM= 739 nm). Experimentally determined values are in excellent agreement with theory (Figure 2.7b,c). The distance where the PSF was taken represents the expected poorest imaging quality for

experimental conditions. Closer to the prism, x resolution is objective lens limited (res ~ 310 nm), and z resolution is ~ 400 nm. Typical cell distance to the prism is between 50 µm and 70 µm.

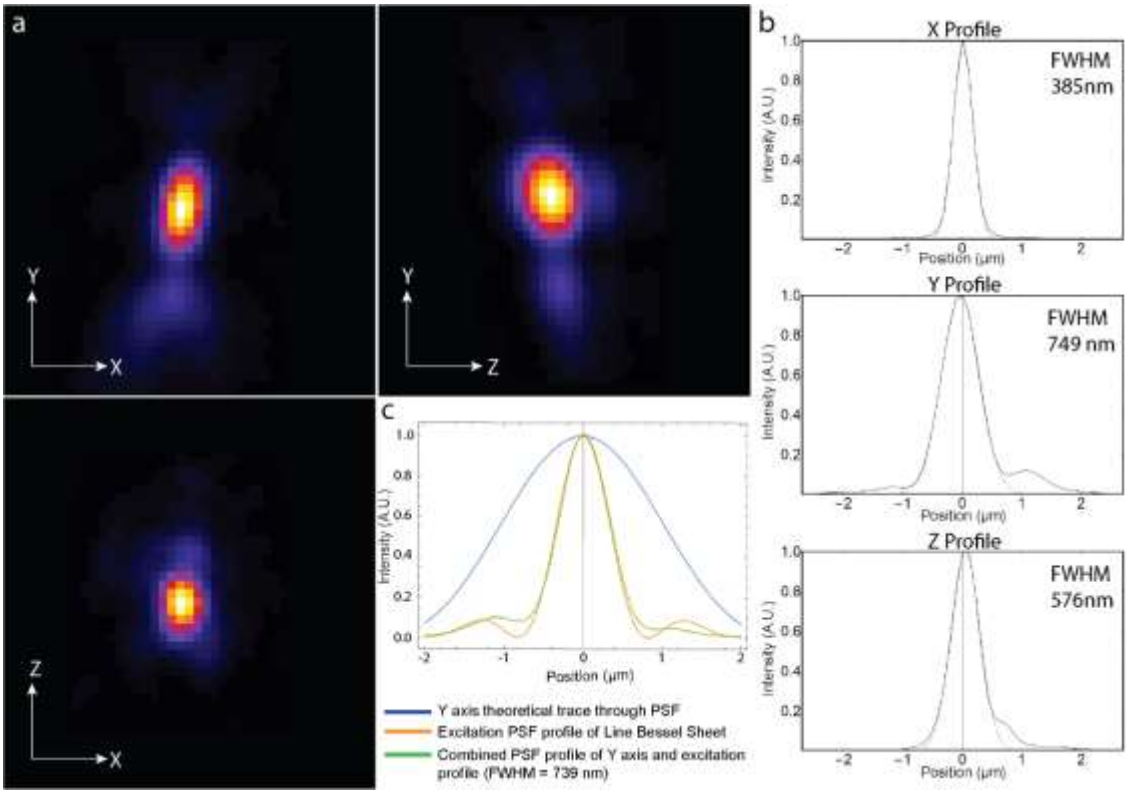

Figure 2.7: Point spread function of side view imaging. (a) Optical sections of the PSF in the x-y plane, the x-z (side view) plane, and the y-z plane. (b) The plotted profiles of each axes through the center of the PSF. (c) The theoretical calculated plot for the Y direction. The blue dotted lines in the profile plots are the gaussian fit to each plot from which the FWHM is determined. X is the direction parallel to the prism edge, Z is the direction from substrate to top of cell and Y is the light sheet stepping direction.

2.4.3 Detector Characterization

For our system, we obtained two detectors and sought to compare their quality and performance. To do so, we collected a photon transfer curve (PTC) following the protocol given in Waters and Wittmann [212]. A PTC is a log-log plot of camera noise versus camera signal, and it allows a user to understand the contribution of read noise, Poisson noise, and fixed pattern noise to the overall detector noise. The protocol, in short, calls for a uniform light source to illuminate the detector at increasing exposure times. As a cost-effective alternative to using an integrating sphere, a high-quality cell phone screen displaying a grey screen was used for even illumination (per the suggestion of the protocol). The two cameras used in the comparison are a Hamamatsu Orca Flash 4.0 v2+ (C11440-22CU-DEMO) and a Hamamatsu Orca

Flash 4.0 v3 (C13440-20CU-DEMO), both of which are scientific complementary metal–oxide–semiconductor (sCMOS) detectors. Figure 2.8 shows the PTC for each camera. It should be noted that the signal range over which the PTC was taken does not contain low enough signal to show the read-noise regime. These PTCs highlight mainly the contributions of Poisson and fixed pattern noise, which are the relevant contributors for the signals in our experiments. For single-molecule level experiments, however, the PTC should be extended to understand the read-noise regime as such experiments occur at very low signal levels.

Several immediate conclusions can be made directly from the PTCs of each camera. First, the v2+ shows higher levels of noise at all signal levels, meaning that when using the v3 less photons are needed to exceed a desired signal-to-noise level. As expected, the PTC in this regime is dominated by Poisson noise for both the v2+ and the v3. However, the fixed pattern noise in the v2+ does not following a single power-law relationship as it theoretically should (as shown in the v3 PTC). Instead, it shows a large bump in signals ranging from 100 – 1000 grey values. Finally, the v2+ shows a higher read noise than the v3. However, as previously discussed this is less of a problem for the experiments with which we are currently concerned.

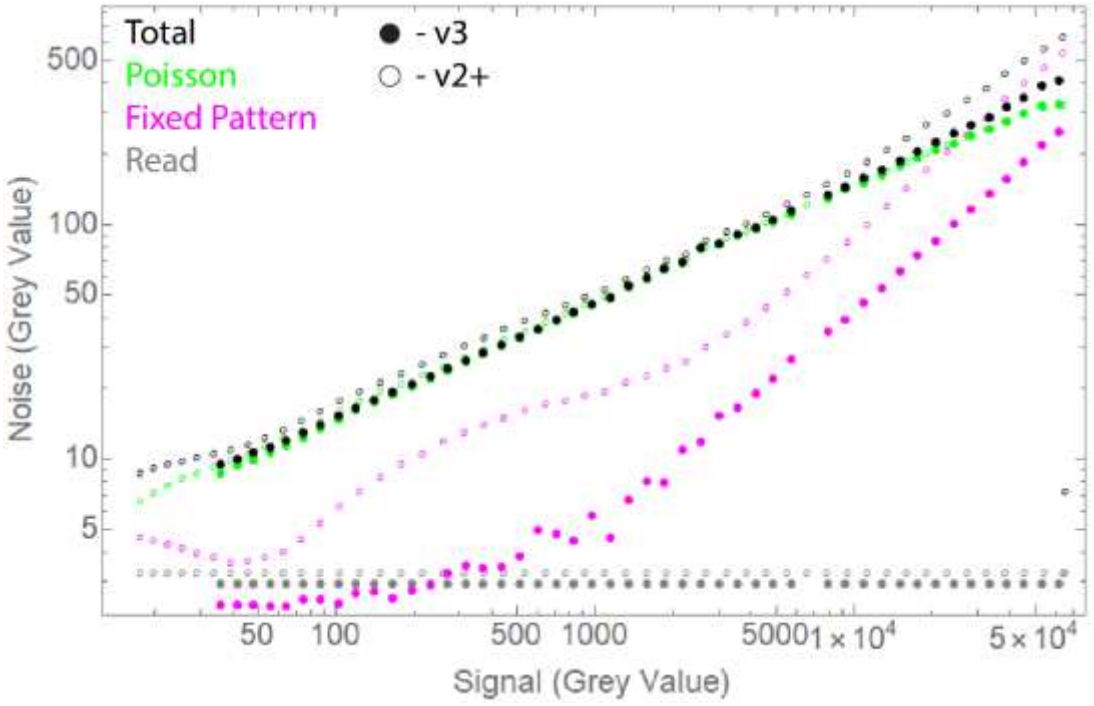

Figure 2.8: A photon transfer curve (PTC) over the Poisson and fixed-pattern noise regimes.

What the PTC does not do is immediately demonstrate is the quality of the images recorded on each detector. For this, we can look straight to the images collected for the PTC themselves. Figure 2.9A shows the fixed pattern noise for each detector (average intensity of 100 dark images). Figure 2.9B-D show comparative signal images from the PTC for low, medium, and high signals. Figure 2.9A highlights the characteristic vertical streaks associated with an sCMOS detector as well as the sharp horizonal line at the center of the detector which represents where the detector is split into two separate chips, each of which is read out separately. The v2+ fixed pattern noise (left) shows an intriguing circular artifact at the center of the chip, highlighting a potential defect in this detector. A similar circular structure can be seen for the low and medium signal images using the v2+, which is likely the source of the bump in the fixed pattern noise between 100 and 1000 grey values in the PTC (Figure 2.9B,C). At high signals (Figure 2.9D) the circular artifact is less apparent. However, a new artifact appears. Streaking across the top and right side of the v2+ image is clearly visible, unlike in the image from the v3. Such an artifact could seriously compromise quantitative and qualitative interpretation of microscopy data. In summary, the v3 shows lower noise levels (read and fixed pattern) and no detector-wide artifacts and is thus the more desirable camera for our purposes.

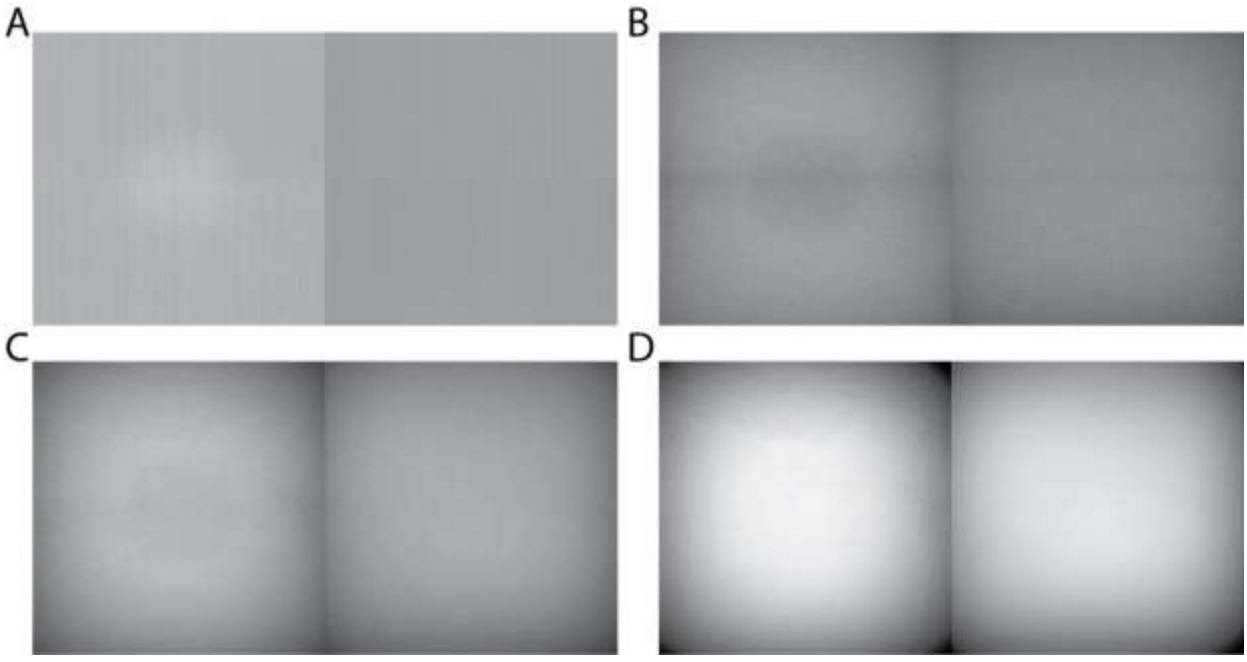

Figure 2.9: Side-by-side image comparison of v2+ and v3 sCMOS cameras. (A) Fixed-pattern noise. (B-D) Low, medium, and high signal image comparisons respectively. In (A – D), the left image is that of the v2+ and the right image is that of the v3.

2.5 Single-Cell, Light-Sheet Volumetric Imaging

This microscope design with LBS illumination is capable of fast (~1 s per single cell) volumetric imaging by incrementally stepping the light sheet across a sample and continuously matching the imaging plane to the position of the light sheet. In a single-objective system, it is slightly more complicated due to the coupling of the light sheet position and imaging plane. Even though both HLS and VLS can be used to take volume images, here we chose VLS because it requires one less degree of freedom (ETL2) to control through software than HLS. Implementation of combined HLS and VLS imaging would allow for multi-view fusion similar to that of the diSPIM [213], except in a single-objective system.

As an initial demonstration, we performed fast volume scans of RAW 264.7 macrophage cells stably expressing HaloTag-F-Tractin labeled with JF549 (Figure 2.10). Each slice was taken in 10 ms (5 ms exposure, 5 ms transition), and each volume consisted of 75 slices meaning that a single volume image was taken in 0.75 s. This is comparable to recent two-objective systems [159, 163, 166]. Because of the speed of our system, we were able to observe both formation and movement of filopodia on the timescale of several seconds. These timescales and dynamics are fundamental to processes such as phagocytosis and cell migration [214, 215], and hence our system is well suited to study mechanisms in which macrophages migrate and engulf foreign particles.

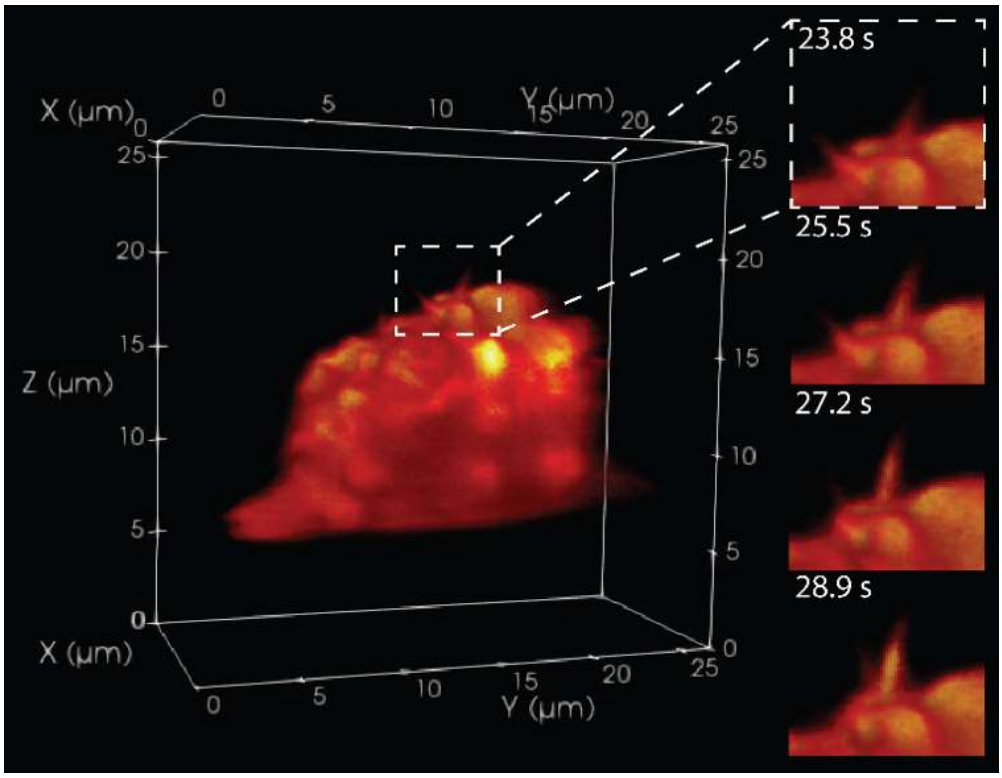

Figure 2.10: Vertical light sheet volume imaging showed filopodia formation and dynamics. Selected frame from a volumetric movie (Visualization L5) of a RAW 264.7 macrophage cell expressing HaloTag-F-tractin labeled with JF549. Each volume consists of 75 slices each taken in 10 ms (5 ms exposure, 5 ms transition time) for a 0.75 s total volume acquisition time with 100 ms delay between each volume. Total volume size is 12.5 µm x 26.7 µm x 25.9 µm, voxel size is 167 nm x 106 nm x 106 nm. We observed formation and movement of individual filopodium on second time scales. See also Video 2.3.

Our system is also capable of performing fast (~1 s per single cell volume), single-objective volumetric imaging in multiple channels. We first performed volumetric imaging of a live HeLa cell stably expressing vimentin-mEmerald and labeled with Lysotracker Deep Red (Figure 2.11a). This temporal resolution allowed us to visualize the 3D dynamics of lysosomes within the vimentin network on single-second timescales. This opens up the potential to study lysosome transport dynamics and their interaction with the cytoskeleton [216]. Recent reports show that the vimentin cytoskeleton plays a central role in regulating lysosome trafficking in autophagy [217].

To illustrate the ability of the system to visualize fine detail while scanning at a high frame rate, we fixed the mEmerald vimentin cells and stained them with AlexaFluor 594 phalloidin for F-actin. We then performed volumetric imaging as before, but with one half the axial step size (Figure 2.11b,c). A single-pixel line scan through the filopodia (Figure 2.11c) demonstrates the signal-to-background and feature resolution our system can achieve at this scan rate with a reasonable laser intensity for live-cell

studies. Two-color volumetric imaging paves the way for experiments to characterize the mechanobiological role of IFs in processes such as organelle motility [218, 219] and filopodia dynamics [220].

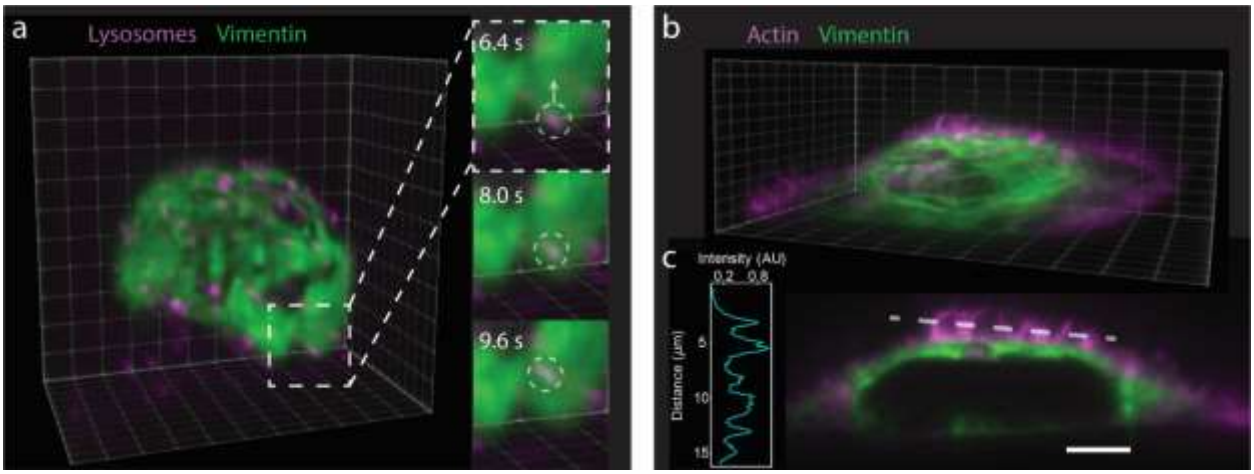

Figure 2.11: Volumetric imaging of vimentin cytoskeleton and lysosome movement. a, LSFM volumetric imaging of a live HeLa cell with labeled Lysotracker Red (magenta) and vimentin-mEmerald (green). Each volume consists of 75 slices per color acquired at 5 ms exposure time and 5 ms readout time; the total volume acquisition time is 1.5 s. A 100 ms delay is taken between volumes. Insets show dynamics of vesicles on the single-second timescale. Voxel size: 106 x 106 x 220 nm. Total volume: 29.3 x 26.3 x 16.5 µm. b, LSFM volumetric image of a fixed HeLa cell with labeled actin (AlexaFluor 568-Phalloidin - magenta) and vimentin-mEmerald (green). The volume consists of 300 slices per color acquired at 5 ms exposure time and 5 ms readout time; the total volume acquisition time is 6 s. Voxel size: 106 x 106 x 108 nm. Total volume: 52.6 x 19.1 x 32.4 µm. c, Selected side-view image from the volume data set shown in (b). A single-pixel line scan (dashed white line) through the actin channel shows we resolve individual filopodia at the above volume acquisition rate with adequate signal-to-noise (inset). Scale bar = 5 µm. See also Video 2.4 and Video 2.5.

2.6 Further Implementations and Modalities

The VIEW-MOD system is not restricted to just single-objective LSFM. In our previous work, we additionally demonstrated (1) widefield, TIRF, and variable angle (va)TIRF and (2) vaTIRF imaging combined with localized photo-activation [173]. Further novelty of this instrument, however, lies in its broad scope of applicability. We have outlined a table of various advanced microscopy techniques our system can implement as well as the required modules to do so (Table 2.1). Many of the available techniques involve scanning of different illumination patterns. By scanning the incident angle in vaTIRF, the penetration depth of the evanescent field is modified. Additionally stepping the imaging plane in sequence with the incident angle, one can axially section the range of the evanescent field and construct 3D renderings of near-surface interactions [221]. One could also adjust the incident angle such that it is

slightly below that of TIRF to achieve HILO microscopy [222]. Point illumination can be further extended by introducing two-photon microscopy, which allows for femtoliter focal volume precision [223]. Provided use of the proper laser and sample, our design can produce precise two-photon point illumination in 3D which allows for photoablation, photoactivation, and fluorescence recovery after photobleaching (FRAP) studies.

Our system has the ability to both laterally and axially scan a light sheet, which when combined with the rolling shutter functionality of an sCMOS camera can produce x-y or y-z images with minimal background [160, 224]. We also have the capability to create light sheets by dithering a focused beam at a higher frequency than the imaging rate. Our modules allow for precise shaping of the focused beam, meaning that a scanned beam could be tailored to image sub-cellular structures or multi-cell systems depending on the interest of the research group. Scanned beams could be used in our system for both x-y and y-z imaging as well as volumetric imaging similar to what we previously demonstrated [168]. Another LSFM application would be that of field synthesis [225]. By placing a mask at the location of ETL2, one could scan the illumination light with SM2 across the mask to generate time-average intensity profiles at the sample plane that match a variety of light sheets. Replacing ETL2, however, eliminates axial scanning of the light sheet. For the full benefit of the VIEW-MOD system and field synthesis, one may consider designing a separate field synthesis module. Finally, our system is capable of super-resolution imaging through either stochastic optical reconstruction microscopy (STORM) or photo activated localization microscopy (PALM) in conjugation with TIRF or LSFM. Both STORM and PALM rely upon on-off switching fluorophores and an illumination source with low background [226]. Provided the proper sample and software development (much of which is openly available), our microscope's TIRF and LSFM can be used for these super-resolution techniques.

Table 2.1: Expanded list of imaging modalities for VIEW-MOD. We provide an extensive, but not necessarily complete, list of imaging modalities in the scope of VIEW-MOD's capabilities. The modules required for each modality and are listed, only further software development would be required for implementation. *Module 1: Beam expansion and polarization modulation. Module 2: Beam shaping. Module 3: Beam steering. Module 4: Axial beam scanning. Module 5: Axial image plane scanning.

Imaging Modality	Description	Required Modules*	Reference
Single-Objective Light Sheet Fluorescence	As described above.	1-4 (2D), 5 (3D)	[173]

Microscopy (2D & 3D)			
Localized Point Illumination (2D & 3D)	As described in *Liu et al*.. This could be extended to control the z-position of the beam with use of module 5.	1-3, 4 (3D)	[173]
TIRF (variable angle or traditional)	As described in *Liu et al*.	1-3	[173]
Widefield Epifluorescence	As described in *Liu et al*.	1-3	[173]
Volumetric Imaging with vaTIRF	Varying the incident angle subsequently varies the penetration depth of the evanescent field. Scanning the incident angle in connection with the imaging plane allows for z-sectioning within the full range of the evanescent field. Image stacks can be taken and reconstructed to form volumetric images.	1-3,5	[221]
Laterally swept LSFM with rolling shutter	A light sheet propagates vertically from the objective lens and scans laterally either through the sample (y-z light sheet plane, x-y imaging plane) of across the prism (x-y light sheet plane, y-z imaging plane). The rolling shutter of a sCMOS camera is matched to the position of the light sheet as it is scanned to create high SNR images.	1-5	[224]
Single-Objective Scanned Beam LSFM (2D & 3D)	A focused beam is scanned at a higher frequency than the image acquisition rate to create a light sheet. This light sheet can be used similarly to as we have described in the main text.	1-4 (2D), 5 (3D)	[168]
Axially Swept LSFM with rolling shutter	A light sheet propagates vertically from the objective lens and scans laterally either through the sample (y-z light sheet and imaging plane) of across the prism (x-y light sheet and imaging plane). The rolling shutter of a sCMOS camera is matched to the position of the waist of the light sheet as it is scanned to create high SNR images.	1-4	[160]
Fluorescence Recovery After Photobleaching (FRAP)	A focused light beam of high intensity bleaches a localized section of a sample, and the sample is then imaged and the recovery of the fluorescent intensity at the location of the bleaching is monitored. This lets a user understand the timescale of diffusion of the fluorescent molecules in the sample.	1-4	[227]
2-Photon 3D Localized Excitation	With an appropriate laser and sample choice, our system can implement 2-photon microscopy wherein one could achieve a focal volume on the femtoliter	1-3, 4 (3D)	[223]

	order for the illumination light. This could be used to perform precisely localized photoactivation or laser ablation in 3D.		
HILO Microscopy	A beam is focused and translated laterally at the back focal plane of the objective such that the incident angle at the sample is just below that of TIRF, allowing a highly inclined beam to pass through the sample for improve signal-to-background over widefield.	1-3	[222]
STORM/PALM	STORM and PALM are super-resolution techniques that rely upon on-off switching of fluorophores. With the proper sample, our microscope design is capable of these techniques using either TIRF or LSFM.	1-4 (TIRF), 5 (LSFM)	[226]

2.7 Conclusions

It is essential for a microscopy system to both visualize and control the distribution and activity of target proteins. Optical systems are often designed around a single microscopy technique and even though such systems have drastically advanced our ability to investigate single cell dynamics, the focus on individual techniques can limit the scope of available research questions. Here, we present our VIEW-MOD system, capable of imaging in a myriad of modalities. This design is cost-effective and built upon a conventional inverted microscope with all commercially available components, making it easily implementable in any laboratory with the latter (Table 2.2). Furthermore, the open-source software can be expanded to include other techniques due to the complete control of illumination light and imaging plane location. In its current implementation, we have focused on single-objective LSFM. Specifically, we first showed 2D imaging of orthogonal planes of H2B-labeled nuclei. We further expanded to 3D imaging at timescales relevant for single-cell dynamics. This was shown both through imaging of filopodia dynamics in live macrophages as well as lysosome dynamics in live HeLa cells. Our previous work further demonstrates how the VIEW-MOD system can be used to implement widefield, TIRF, vaTIRF, and localized photoactivation [173]. This microscope design can be easily adapted to serve a user's needs, make use of the ever-growing number of light-sensitive tools being developed, and is minimally perturbing to normal cell physiology thus allowing great potential in opening new venues of research and answering important biological questions.

Table 2.2: Costs of the major components of the VIEW-MOD system.

Thorlabs			
Part Number	Description	Quantity	Subtotal
PAF-X-18-PC-A	FiberPort FC/PC f=18.4 mm 400 - 600 nm	1	525
CP08FP	FiberPort and LaserPort Adapter for 30 mm Cage System	1	28
BE052-A	Variable Optical Beam Expander 0.5X - 2X Zoom	1	814
GBE03-A	3X Achromatic Galilean Beam Expander	1	475
CCM1-PBS251/M	Polarizing Beamsplitter Cube	2	640
KCB1/M	Right-Angle Kinematic Mirror Mount	2	286
LA1986-A-ML	Ø1"Plano-Convex Lens, f = 125.0 mm	3	129
WPH05M-445	Ø1/2" Mounted Zero-Order Half-Wave Plate,	1	448
RSP1	Rotation Mount for Ø1" (25.4 mm) Optics	1	88
ACA254-200-A	Air-Spaced Achromatic Doublet, f= 200 mm	1	509
KCB2C/M	Right-Angle Kinematic Mirror Mount	2	338
AC254-125-B-ML	f=125 mm, Ø1" Achromatic Doublet	2	206
BB1-E02-10	Ø1" Broadband Dielectric Mirror, 10 Pack	1	675
LCC1111T-A	Temperature-Stabilized Half-Wave LC Retarder	1	1061
LCC25	Liquid Crystal Controller	1	1364
Rods, lens holders, posts, etc.			~2000
Optics In Motion LLC			
OIM 101	OIM 101 1” fast steering mirror	2	7020
Optotune			
el-16-40-TC-VIS-20D	Electric tunable lens with controller	3	2787
Gardasoft			
TR-CL180	TR-CL180 Industrial Lens Controller	1	550
National Instruments			
781045-01	PCIe-6323	2	1602
782536-01	SCB-68A Noise Rejecting, Shielded I/O Connector Block	2	594
192061-02	SHC68-68-EPM Shielded Cable	2	257
		Total	**22397**

2.8 Specific Materials and Methods

2.8.1 Cell Culture

Murine macrophage cells (RAW 264.7) were transfected with HaloTag-F-tractin gene using Fugene HD (Promega), and grown in phenol free DMEM F12 with 10% FBS. This cell line was developed by Megan Kern. Similarly, COS-7 cells (a gift from the Liu Lab at Janelia Research Campus) stably expressing HaloTag-H2B were grown in the same medium. For experiments, both cell types were plated sparsely on 55 kPa polyacrylamide (PA) gel pads that had been coated with fibronectin. After cells had spread on the gels, and 30 minutes before an experiment, a 2-5 µL of a 10-5 M solution of Janelia Fluor 549 (JF549) halo ligand (a gift from the Lavis Lab at Janelia Research Campus) in PBS was added to 200

µL of media in the cloning rings. The JF549 solution was then replaced twice with warmed media before imaging. Imaging was carried out in the same medium the cells were grown in.

Vimentin-/- HeLa cells stably expressing vimentin-mEmerald were generated as described [228]. In brief, the endogenous vimentin gene was deleted via CRISPR-Cas9 methods and a verified vimentin-/- clone was stably transduced with a lentiviral vimentin-mEmerald vector. Transduced cells were selected in 500 µg/ml G418 and sorted for uniform mEmerald expression via fluorescence-activated cell sorting. Cells were grown in DMEM-F12 media without phenol red. For experiments, cells were plated on collagen coated 55 kPa, thin (~10 µm) PA gels within 1 cm cloning cylinders (Corning, USA). The cloning cylinder was removed prior to imaging.

2.8.2 Polyacrylamide Gel Preparation

Gel pads were prepared on 40 mm circular #0 coverslips (Fisher Scientific) to minimize reflections from a glass surface onto the side view mirror. Coverglasses were UV cleaned and treated with APTES (Amino propyl triethoxy silane; 1% in toluene as vapor). 55 KPa gels were prepared from standard protocols, with the addition of 1% polyacrylic acid before polymerization. Once polymerization was initiated in a small volume of acrylamide with 10% APS, 10 µL was placed at the center of two coverglasses, and a 22 x 22 mm coverslip placed rapidly on top of each. These squares were treated with hexamethyldisilazane vapor after UV cleaning to develop a hydrophobic, non-adherent surface. A small weight was placed on the coverslip to promote spreading of the acrylamide in the few seconds before it gels.

After 5 minutes of polymerization, DI water was placed around the upper coverslip and a scalpel blade was used to gently pry up the upper coverslip. The gels were then allowed to dry slightly so that 1 cm cloning cylinders could be affixed to the gel with Dow High Vacuum grease. Then, 150 µL of either fibronectin (human; 10 µg/ml in PBS) or collagen (rat tail, 50 µg/ml in PBS) was placed within the cloning rings for 5 minutes before removal. The gels were allowed to dry for 10 minutes in a biosafety hood. The gels were then exposed to the bio-hood UV light for 5 minutes to sterilize them, and 200 µL of either PBS or medium was added until the cells were ready.

2.8.3 Polyacrylamide spheres for the point spread function

The PA spheres were generated by the methods as described [229], with some minor changes. We used the 3 µm SPG frits to extrude high stiffness PA gel into hexane at 300 RPM stirring. Beads were fixed overnight in AIBN as described [229], washed in fresh hexane, dried in air and resuspended into PBS with sonication to separate the beads. The spheres were 12-20 µm in diameter after resuspension, and were coated in a similar manner to the pads above. An aliquot of the PA beads was centrifuged in an Eppendorf tube (7000 RPM, 4 min), and resuspended in 10 mg/mL EDAC in pH 6 MES buffer and rotated for 15 min at room temperature. We centrifuged the beads to remove the EDAC as above, and resuspended them in 10 ug/mL alexafluor 488 goat anti mouse IgG (Invitrogen). After 30 min rotation, the beads were again centrifuged to remove unbound IgG, and resuspended in EDAC (10 mg/mL) with a 10^{-6} dilution of 0.1 µm red fluorescent microspheres (Invitrogen) in PBS. Beads were again rotated for 30 min and then pelleted, and resuspended in plain PBS. To attach the coated beads to a PA gel pad, low concentrations of beads were suspended onto the gels within the cloning cylinders, and again EDAC was added to 10 mg/ml final concentration. The IgG fluorescence was used to find the PA beads, and then an isolated red fluorescent bead was imaged for the PSF

2.8.4 Environmental Control

The specimen insulating chamber sits atop the circular sample coverslip. The specimen insulator made use of the Asylum Research petri dish heater and magnetic petri dish clamp while also allowing the prism to freely enter and exit the specimen space. A well that runs along the inside of the specimen insulator above and separate from the specimen media holds DI water to increase humidity of the chamber and discourage evaporation of the media. Additionally, the AFM head is equipped with an evaporation shield that caps the specimen insulating chamber. Once the chamber is enclosed a stable temperature environment (37^{o}C) can be maintained with minimal evaporation.

In addition to the petri dish heater, we used an objective heater (Thorlabs HK-100) with a PIV controller (Thorlabs TC200) to maintain the temperature at the sample location. Settings for both controllers were adjusted until the specimen reached the desired temperature, stability and gradient. The specimen

temperature was measured with an Omega thermocouple placed directly in a test media. 37.0°C was achieved with a 0.1°C gradient of the media from edge of the coverslip to the center of the coverslip.

2.8.5 Prism mounting, cleaning, and alignment

Right angle prisms (POC part 8531-607-1) were mounted onto a shaved glass capillary tube secured to a Thorlabs compact table clamp (Thorlabs CL3). A thin layer of UV polymerizing glue (Norland optical adhesive 81) was used to glue the bottom square side to the capillary tube, exposing the mirrored surface. The prism and capillary tube were then cured for 5 minutes. Prisms were rinsed with 70% ethanol and DI water after each use to remove any accumulated debris. If further cleaning was necessary, Red First Contact polymer cleaner (Photonic Cleaning, WI) was placed onto the surface of the prism, allowed to cure for 5 minutes, then peeled off with tweezers. Repeat cleanings were performed if needed.

A right-angle prism was secured to a thin capillary tube and mounted to the prism holder stage equipped with a tip, tilt, and rotation stage (TTR001, Thorlabs). The pitch, roll, and yaw adjustments to the prism were made before each experiment using a coverslip with fluorescent beads to align the light sheet with the prism. Using translation micrometers, the prism was positioned over but not touching the AFM cantilever and cell. The relative position of the prism and light sheet was adjusted such that ETL2 had enough working range to position the waist of the light sheet in the specimen while imaging in side-view. All pitch, roll, and yaw adjustments to the prism were done with the prism holder stage.

2.8.6 LSFM Imaging

COS-7 cells stably expressing HaloTag-H2B were labeled with JF549 and imaged with a 561 nm laser line (Coherent OBIS 561nm LS 150 mW). Images were acquired with a 200 ms exposure time for both HLS and VLS modes. Laser power at the sample plane was measured with a power meter (ThorLabs PM100D) to be 88 µW. RAW 264.7 cells stably expressing HaloTag-F-tractin were labeled with JF549 and imaged with a 561 nm laser line. Images were acquired with a 5 ms exposure time and 5 ms transition time, and each volume consisted of 75 images for a total volume acquisition time of 0.75 s. A delay of 100 ms was allowed between each volume image. Laser power at the sample plane was

measured to be 27 µW. Volume rendering were produced using ParaView 5.5.2 (Available at https://www.paraview.org/). No image processing was conducted asides from contrasting and mapping intensity to a color and opacity map as to properly visualize the 3D data set.

Live HeLa cells expressing vimentin-mEmerald were treated with 1 µM lysotracker dark red (Invitrogen, USA) for 10 min at 37 degrees, washed several times in fresh, equilibrated medium, and then placed on the AFM stage of the optical microscope. Indirect transmitted light was used to find a cell of interest and the prism was positioned next to the cell. Laser power at the sample for live cell imaging was 98 uW for 488 nm and 290 uW for 561 nm. To image F-actin with vimentin, the expressing cells were fixed in 4% formaldehyde for 5 min, stained with alexafluor 568 phalloidin (Invitrogen) for 30 min at 37 deg, washed with PBS, and imaged. Laser power at the sample for fixed cell imaging was 116 uW for 488 nm and 80 uW for 561 nm.

2.8.7 Plasmid Construction

pEGFP-C1 F-tractin-EGFP was a gift from Dyche Mullins (Addgene plasmid # 58473; http://n2t.net/addgene:58473; RRID:Addgene_58473). PiggyBac plasmids PB-rtTA and PB-miRE-tre-Puro were kindly provided by Mauro Calabrese (The University of North Carolina at Chapel Hill); PB-rtTA encodes reverse tetracycline-controlled transactivator (rtTA) and G418 resistant gene under UbC promoter46, and PB-miRE-tre-Hygro encodes a protein of interest and a hygromycin resistant gene under tetracycline-dependent and EF1 promoters, respectively. pF-tractin-Halo was first generated by cloning Halo-Tag cDNA (forward primer, agggggggctagcgctcgccaccatggcagaaatcggtactggctttc; reverse primer, cgaagcttgagctcgagatctagtcgactgaattcgcgttatcgc) between AgeI and BglII site of pEGFP-C1 F-tractin-EGFP using Gibson assembly (New England Biolabs, MA). Halo-F-tractin was then amplified using the primers (forward primer, tgaaccgtcagatcgcctggaccggtgccaccatggcgcgaccacgg; reverse primer, aggcacagtcgaaacgcattgtcgacttatggctcgccggaaatctcg), and cloned between AgeI and SalI sites of PB-miRE-tre-Hygro, yielding PB-tre-F-tractin-Halo-Hygro. Those plasmids were confirmed by sequencing before use. The primers were synthesized by Integrated DNA Technologies (CA) and sequences were performed by Genewiz (NJ).

CHAPTER 3: COMBINED ATOMIC FORCE MICROSCOPY AND LIGHT SHEET MICROSCOPY[2]

With an understanding of our unique light sheet microscope, it is next prudent to introduce our means of applying and measuring external forces. In Chapter 1, I described in brief how AFM has been used in the field of nuclear mechanics. Here, I dig deeper into the specifics of AFM and the ways in which it has been coupled with fluorescence microscopy. Next, I present our novel coupling of LSFM and AFM in a system we term AFM-LS. This system proves to be the first that is capable of simultaneous AFM force measurements with either direct LSFM imaging in the plane of applied force or volumetric LSFM imaging. Unlike traditional microscopes that physically move the objective lenses for volumetric imaging, our remote focusing strategy via ETLs described in Chapter 2 keeps the sample space still to minimize any coupling of the microscopy-induced vibrations and force measurements. This allows us to maintain ~10s of pN level force sensitivity. As examples, I demonstrate our AFM-LS system by visualizing membrane tether rupture (2D) and nucleoli translocation (3D). This system is uniquely poised to inform nuclear mechanics at a level previously unattainable, which I describe in full in Chapter 5.

3.1 An Introduction to Atomic Force Microscopy

Atomic Force Microscopy (AFM) is a powerful and widely used technique for studying mechanical properties of biological samples. AFM was originally developed as an imaging technology as the name suggests, and was later repurposed for use in mechanical studies. The premise of AFM is remarkably simple. A flexible cantilever is position over the sample of interest, or in our case a live cell, with one end of the cantilever fixed to a piezo motor and the other end left free to deflect (Figure 3.1). A super-luminescent diode (SLD) is reflected off of the back of the cantilever, and the reflected SLD is aimed at the center of a quadrant photodiode (QPD). The QPD measures the voltage in each quadrant separately. The piezo is used to lower the cantilever with nanometer precision towards the sample. As the cantilever

[2] Portions of this chapter are previously published in Nelsen, E., et al. (2020). "Combined Atomic Force Microscope and Volumetric Light Sheet System for Correlative Force and Fluorescence Mechanobiology Studies." Sci Rep **10**(1): 8133.

comes into contact with the sample, it starts to deflect. The change in angle of the cantilever subsequently changes the position of the SLD on the QPD (Figure 3.1). The difference between the voltage in the top two quadrants and the bottom two quadrants scales linearly with the deflection of the cantilever via a constant known as the deflection $InvOLS$ (inverse optical lever sensitivity). $InvOLS$, having units of distance per volt, provides the conversion from voltages, V, at the QPD to physical deflection of the cantilever, d, through the equation

$$d = InvOLS * (V_{top} - V_{bottom}) \tag{3.1}$$

To calibrate $InvOLS$, the general procedure is to lower the cantilever onto a glass coverslip. The cantilevers are many orders of magnitude softer than the glass, and therefore it can be assumed that the distance the piezo travels, Z, is equal to the deflection of the cantilever. The piezo distance is internally measured and the voltage difference is read off of the QPD, therefore the ratio of the two provides a calibration for $InvOLS$. To measure forces, we simply use Hooke's law given by

$$F = k * d \tag{3.2}$$

where F is the measured force and k is the spring constant of the cantilever. The spring constant of the cantilever is most commonly determined either through the thermal tune method [54] or the Sader method [55]. The amount that the sample is indented can be measured by

$$\delta = Z - d \tag{3.3}$$

Using the relationship between force and indentation, traditional AFM experiments will extract an elastic modulus from a given data set as a metric of the stiffness of the given sample.

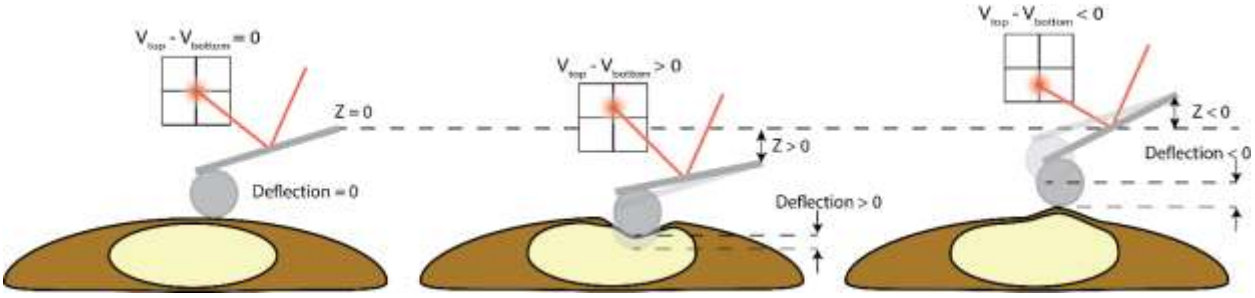

Figure 3.1: Schematic illustration of atomic force microscopy. (Left) A cantilever at the point of contact with a cell, deflection, z position, and voltage difference are set to zero. (Middle) Example of a compression measurement where a positive deflection, z position, and voltage difference are measured. (Right) Example of an adhesion measurement where negative deflection, z position, and voltage difference are measured.

A useful degree of freedom in AFM studies is the geometry of the AFM tip. Investigators have contrasted large bead tips (~10 μm) with sharp pyramidal tips to compare the bulk and local compressibility of nuclei respectively [48]. Such comparative studies have also shown that compression with pyramidal tips results in a much higher rate of nuclear rupture than compression with beaded (~4.5 μm) cantilevers, implying that nuclear membrane curvature is important for determining potential rupture sites [47]. Custom-manufactured tips have also been instrumental in furthering the field of nuclear mechanics. For example, custom, sharp cylindrical tips (3.4 μm x 130 nm) have been used to puncture the cell and nuclear membranes. This allowed for determination of separate elastic moduli of the cell membrane, cytoskeleton, and nucleus [25, 43]. Some investigators opt for tipless cantilevers to measure bulk strain [43] or increases in entropic pressure due to chromatin decondensation [50, 51]. Finally, AFM has also been used in an oscillatory mode where a user indented a cell to a desired force or indentation and then drive the cantilever at varied frequencies. This allowed for determination of frequency dependent elastic and viscous properties of the nucleus [42]. For a recent review of AFM-based cellular biophysics studies, we refer the reader to Krieg *et al* [56].

3.2 Combined AFM and Light Sheet Microscopy

As noted above, AFM is an extremely powerful tool for studying mechanical properties of biological samples. However, AFM is made more useful when coupled with the ability to simultaneously visualize the sample being probed. This harkens back to our discuss in Chapter 1 of measurements of force and cellular deformation. The AFM measures with high precision the stress applied to the sample; coupling with microscopy then provides the strain. Together, these two measurements allow one to extract mechanical properties. A standard means of doing this is to couple AFM with an inverted fluorescence microscope. Because the AFM head sits atop the sample, it is fairly straightforward to integrate epifluorescence techniques such as confocal microscopy or widefield illumination with AFM. In the context of cell nuclear mechanics, this has been done by several groups [22, 24, 25, 43, 47, 48]. While such techniques do provide an advancement to traditional AFM without simultaneous imaging, they are limited in their ability to better understand the dynamics of compression or extension experiments. The significant limitation is that epifluorescence techniques image the X-Y plane, however the AFM

compresses the sample in the Z plane. This means that the images being collected do not capture the plane of applied force. One solution to this is to collect 3D images during compression, however this comes at a cost of significantly reduced temporal resolution and spatial resolution in the Z direction. To remedy this, we combine our side-view LSFM system described in Chapter 2 with an AFM (Figure 3.2) [144, 145].

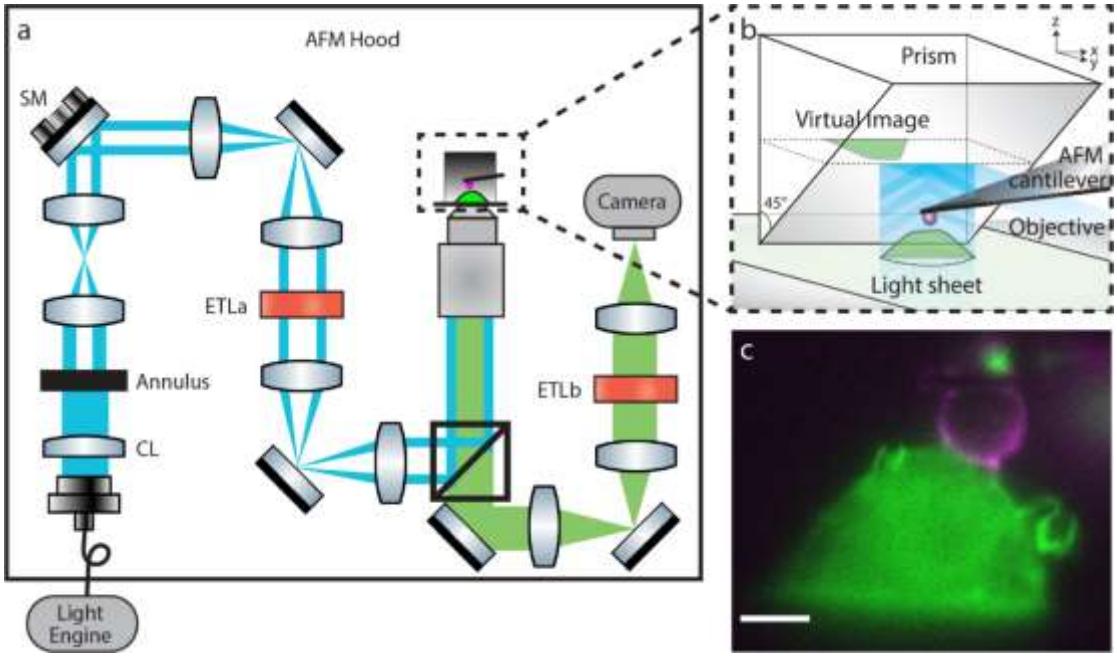

Figure 3.2: Schematic of the combined AFM and LSFM system. (a) Laser lines housed in our light engine are coupled into an optical fiber that passes into the AFM hood. A cylindrical lens focuses a sheet of light onto an annulus which is re-imaged to the back focal plane (BFP) of the objective to generate a Line Bessel Sheet. ETLa and ETLb control the axial position of the light sheet and image plane respectively. The steering mirror (SM), conjugate to the BFP of the objective, controls the position of the light sheet at the sample plane. (b) Schematic of the integration of the prism and AFM in the sample space. (c), Sideview LSFM image of a RAW 264.7 cell expressing HaloTag F-tractin labeled with Janelia Fluor 549 (green) and a polystyrene bead attached to an AFM cantilever coated with fluorescent IgG (magenta). Scale bar = 5 μm. Image captured by Evan Nelsen

Our specific implementation of the VIEW-MOD system described in Chapter 2 makes use of all 5 modules to generate an LBS that can be spatially controlled with an SM and ETL at the sample plane (Figure 3.2a). Additionally, we have axial scanning of the image plane through use of a second ETL (Figure 3.2a). At the sample space, the side-view imagine setup is unchanged from Chapter 2, however we additionally place an AFM cantilever oriented along the X direction between the cell of interest and the reflective prism (Figure 3.2b). The cantilever must be placed with extreme precision relative to the prism to prevent the prism from blocking the SLD from reaching the QPD. Once in place, this allows us to

collect 2D or 3D multicolor images during AFM compression with simultaneous 10 pN level force measurements. This unique tool situates our lab in a position to provide unprecedented insight into the mechanical properties of single cells and cellular mechanotransduction, with specific advantages and capabilities as listed below.

- ~5 ms 2D and ~1 s 3D multicolor LSFM imaging.
- Minimal phototoxicity and photobleaching
- Direct X-Z imaging of the plane of applied force.
- 10s pN – 100s nN force application range with ~10 pN sensitivity.
- High-NA detection objective enables high resolution imaging (385 x 749 x 576 nm X-Y-Z)

3.3 Noise Considerations and Limitations

One concern with coupled instruments is any compromise of the performance of one system due to the integration of a second system. Coupling of AFM and FM techniques can at times lead to crosstalk or coupling between the illumination light and the AFM signal [230]. Specifically, there are three main forms of coupling between the AFM and excitation light: radiation pressure, photothermal induced deflection, and cantilever/tip luminescence. Photothermal induced deflection is only an issue when there is a “bi-metallic” effect where one side of the cantilever is coated with a metal. Our cantilevers are identical on top and bottom surfaces and there should be no photothermal effect. Cantilever/tip luminescence is particularly important for excitation wavelengths above 800 nm, which is well above the wavelengths used in our system. Furthermore, this effect is primarily for multi-material cantilevers and the force response for laser powers that are an order of magnitude above ours is comparable to our noise level. The most relevant interaction for our system and cantilever is that of radiation pressure, wherein the photon flux from the illumination light causes an upwards deflection of the cantilever. For our AFM-LS experiments, our excitation power was nominally 10s of μW, which based upon previous literature lends to an effect below our measured noise floor. Additionally, there is reasonable concern that mechanical vibrations from the ETLs or SM could induce periodic noise into our measurements. To test this, we engaged a cantilever with a PA gel at a fixed z piezo position and examined the Fourier transform of the force time series both with and without the volume scanning optics on (Figure 3.3). This data was

collected at 2 kHz bandwidth for 65s. Given the parameters used for volumetric imaging, we expected noise at frequencies at 0.4 Hz, 25 Hz and 200 Hz. Contributions to the noise at 0.4 Hz and 200 Hz are seen when the volume scanning optics are engaged (Figure 3.3). However, they are on the order of single pN or less, which is an order of magnitude lower than the theoretical thermal noise floor of the cantilever.

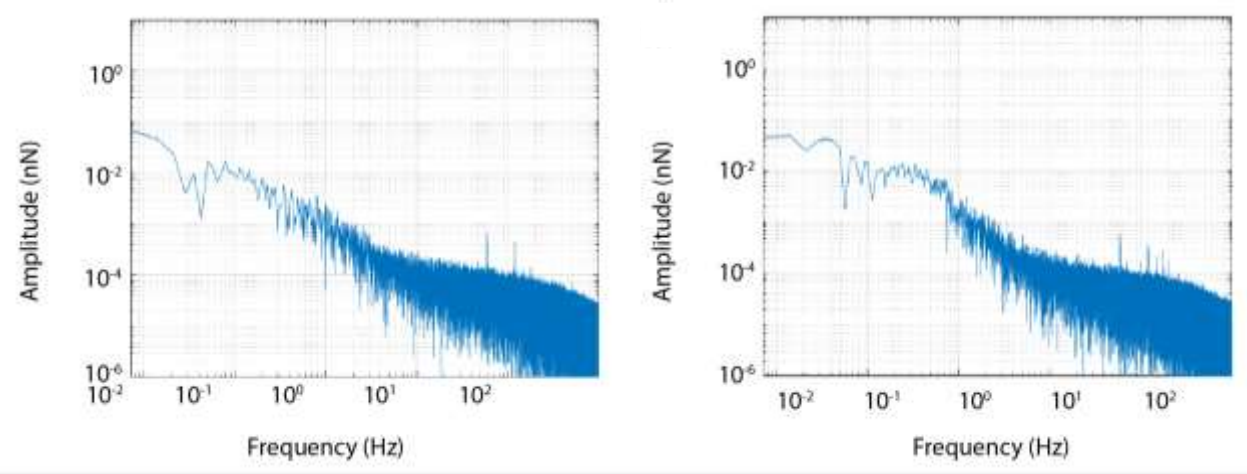

Figure 3.3: AFM-LS Noise Characterization. Fourier Transform of fixed z-position time series both with (left) and without (right) volume scanning optics running. The AFM cantilever was engaged with a gel substrate at 37ºC.

Although our system has a myriad of advantages detailed above and shown throughout this thesis, it is equally important to be conscious of the limitations of the AFM-LS system. Both AFM and LSFM have limitations in their own regards, but here was are interested in limitations that are specific to our system. The first limitation is regarding the use of the reflective prism to directly image an X-Z slice. Because the scale of the prism (180 μm) is comparable to the scale of a single cell (~50 μm), the amount of light collected off the prism is dependent upon the 3D position of the fluorophore emitting the light. In short, the PSF of our system is spatially dependent [145]. This means that both the intensity and the resolution vary throughout the full volume purely due to the change in position. Quantification of intensity then requires careful consideration before any sound conclusions may be drawn. Furthermore, the use of the reflective prism means that we must study only isolated cells (or a few cells in close contact). This limits the types of studies we may perform; for example, we cannot investigate confluent monolayers with the AFM-LS system.

Arguably more concerning, however, are the limitations resulting from the AFM tip interacting with the illumination light and emitted fluorescence. For a majority of our studies, we use a polystyrene bead which has a nominal index of refraction of ~1.6. Because the bead is not index matched to cells, which have a nominal index of refraction between ~1.3 – 1.5 [231], the bead can cause obstruction during 3D imaging. For example, sites of DNA damage – which appear as bright foci when labeled with 53BP1-mCherry – can seemingly disappear when the AFM tip is engaged due to this obstruction (Figure 3.4 Top). This is primarily an issue when using VLS imaging, however the index mismatch between the AFM tip and the cell also causes issues when imaging with HLS. The bead can act effectively as a ball lens in the HLS configuration, causing the light sheet to focus directly behind the bead (Figure 3.4 Middle). This can be quite problematic as it implies an intensity distribution that does not reflect the distribution of the fluorescently-tagged protein but rather the intensity profile of the illumination light. While this is easily detected when the sample is effectively volume labeled, such as when imaging YAP-EGFP (Figure 3.4 Middle), this could be harder to detect for more heterogenous samples. Finally, AFM-LS is subject to reflections off of the AFM tip. Again, this is easily visualized when imaging from the side with a homogeneous label such as NLS-GFP (Figure 3.4 Bottom). As the light sheet reflects off of the AFM Tip, is creates a bright band directly beneath the AFM tip. This causes significant difficulties in quantifying intensity values during compression experiments. Although these limitations and artifacts are significant and should be considered before designing an experiment that makes use of the AFM-LS system, they do not preclude neither the myriad of advantages that the AFM-LS provides nor the potential biophysical for which it allows investigation.

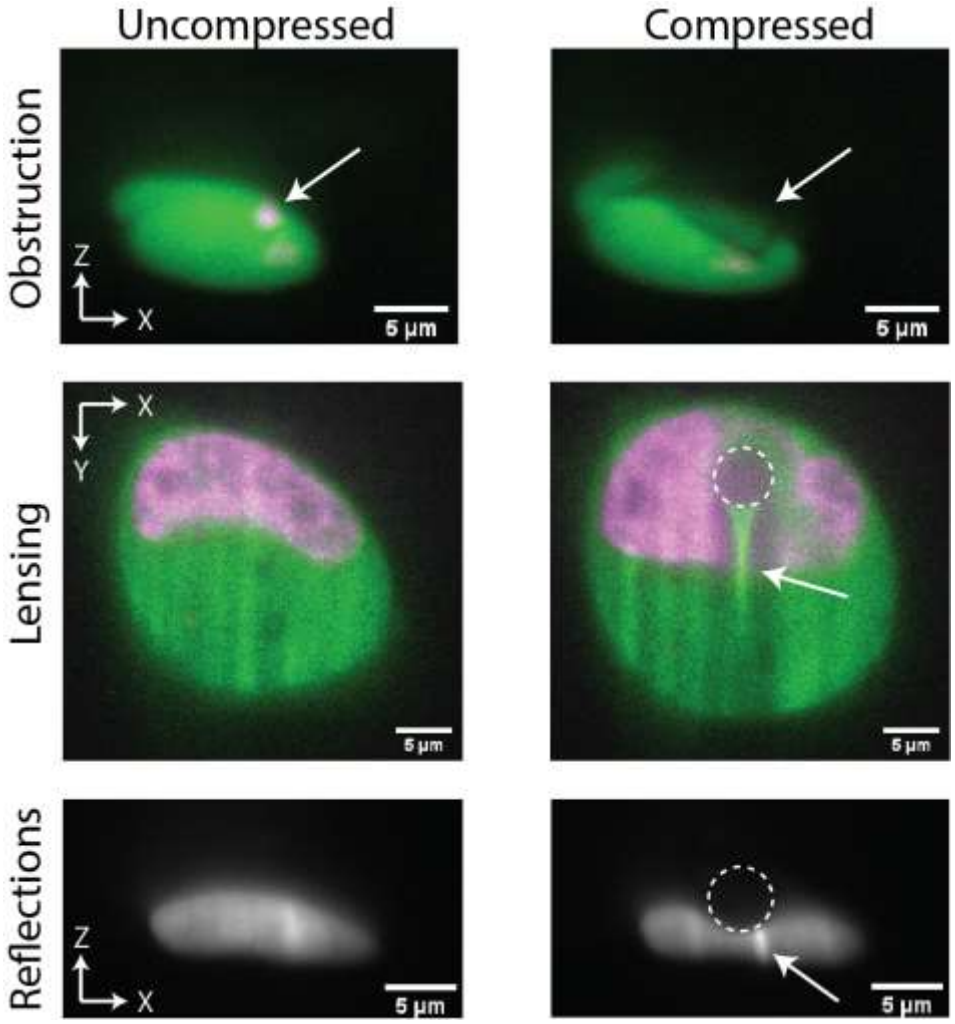

Figure 3.4: AFM-LS Artifacts. (Top) A live MDA-MB-231 cell expressing NLS-GFP (green) and 53BP1-mCherry (magenta) is compressed by an AFM tip while collecting simultaneous 3D images. Shown is a maximum intensity projection through the side-view image stack. Arrow points two where the AFM tip obstructs the emitted light from the 53BP1 focus. (Middle) A live SKOV3 cell stably expressing halotagged H2B labeled with JF585 (magenta) and transiently transfected with YAP-EGFP (green) is compressed with an AFM during HLS imaging. The light sheet is propagating in the positive-Y direction. During compression, the AFM tip (dashed circle) causes a lensing effect in the illumination light (arrow). (Bottom) A live MDA-MB-231 cell expressing NLS-GFP is compressed by an AFM tip while collecting VLS images. Reflections off of the AFM tip cause a bright, vertical stripe to appear (arrow) when the AFM tip is engaged with the cell.

3.4 2D AFM-LS: Membrane Tether Viscoelasticity

Using our AFM-LS system, we were able to compress live SKOV-3 cells stably expressing halotagged H2B and snaptagged KRAS-tail with the AFM will acquiring simultaneous, two-color, light-sheet fluorescence images (Figure 3.5). During the retraction portion of the experiment, we observed both the formation and breaking of membrane tethers. The AFM tip is a 6 µm carboxyl bead, so the binding

between the membrane and the AFM cantilever is non-specific. As a brief demonstration of the capabilities of the 2D AFM-LS experiment, we sought to quantify viscoelastic properties of these membrane tethers.

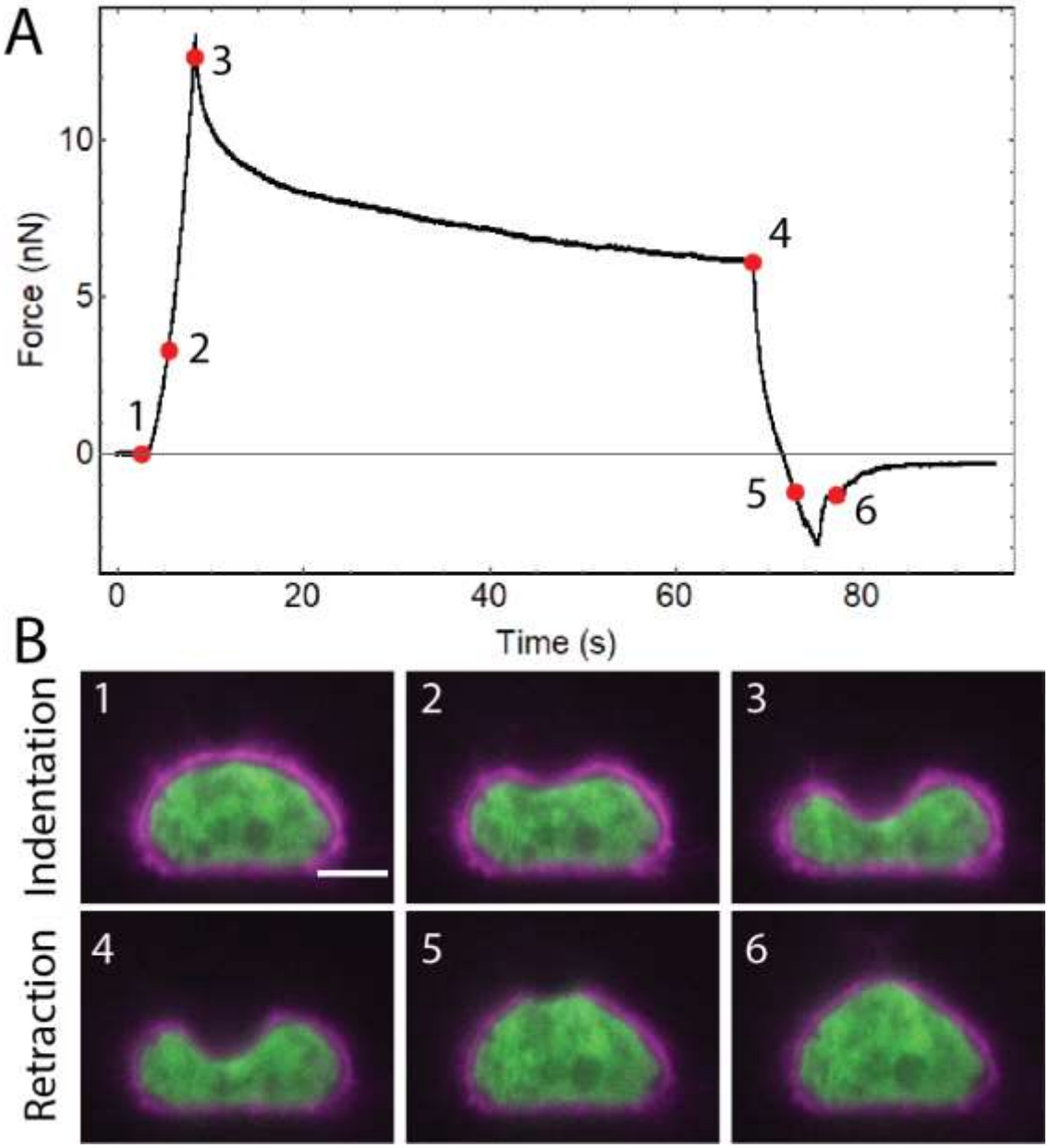

Figure 3.5: AFM-LS experiment on a live SKOV3 cell. (A) Force as measured by the AFM plotted against time. A positive force represents a compression of the cell; a negative force represents an adhesive force. (B) Side-view LSFM image sequences from an AFM-LS experiment. Numbers in each image correspond with the red dots in (A). Magenta – Kras-tail, green – H2B. Scale bar = 5 µm. See also Video 3.1.

Figure 3.6 (right) shows a time series in which a membrane tether ruptures. Also shown in Figure 3.6 (left) are plots of intensity in the tether, the change in cell height, and the force data recorded by the

AFM. The intensity data in the tether was calculated by selecting a rectangular region of interest over the tether and calculating the mean intensity as a time series. The calculate the change in cell height, the image was first blurred using a two-pixel Gaussian kernel, and then a line trace through the top of the cell was used to generate a kymograph. A Gaussian curve was fit to each time point in the kymograph to localized the position of the membrane as a function of time. The force data is recorded directly from the AFM. At this point in the experiment, the z piezo is fixed to a specific location and the tip of the cantilever is free to move. A negative force implies that the cantilever is being pulled down towards the cell, so as a tether releases, we expect a positive change in the recorded force. The tether releases at approximately 88.69 s, as seen in the fluorescence images as well as the tether intensity plot. The change in cell height due to the tether breaking is approximately 50 nm, and the force data can be seen to relax after the time at which the tether breaks.

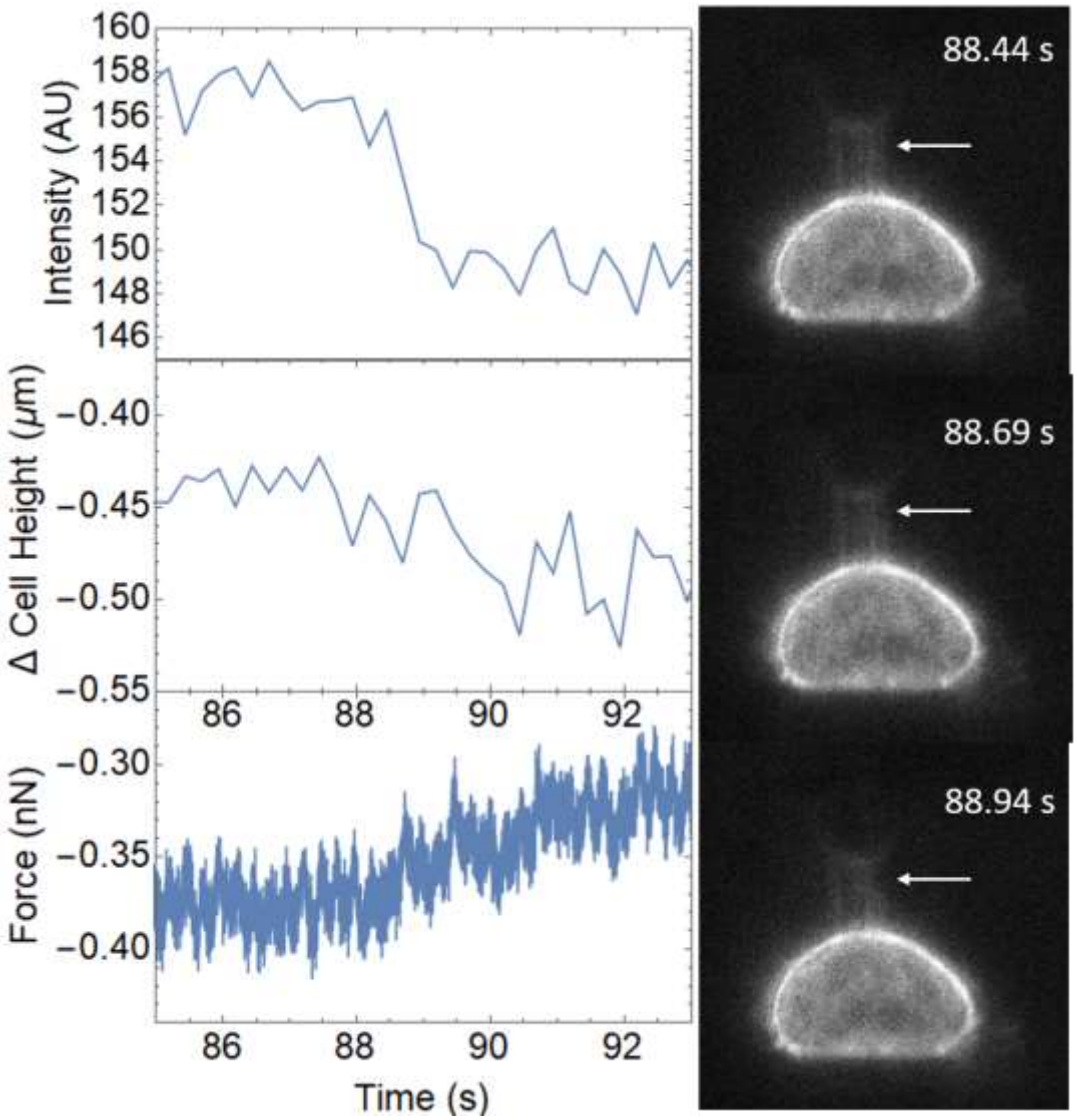

Figure 3.6: Membrane Tether Viscoelasticity. (Left) Time series of intensity in the membrane tether, change in cell height, and force as measured by the AFM during a membrane tether rupture event. (Right) A live SKOV3 cell expressing snaptagged KRAS-tail labeled with JF503. The arrow points to the location of a membrane tether breaking. See also Video 3.2.

To investigate the mechanics of membrane tethers, we modeled them as viscoelastic materials. The primary components of viscoelastic materials are springs and dashpots. Springs are governed by the equation

$$F = kx, \tag{3.4}$$

where F is the force across the spring, k is the spring constant, and x is the amount that the spring stretches. Dashpots are governed by the equation

$$F = \eta \dot{x}, \tag{3.5}$$

where η is the viscosity of the dashpot and $\dot{x}$ is the time derivative of the displacement. When placed in series, the total force across the two elements is equal to the force across any individual element and the total displacement across the system is the sum of the displacements across each element. When placed in parallel, the total displacement across the two elements is equal to the displacement across any individual element and the total force across the system is the sum of the forces across each element. To model a single tether, we chose to use a Standard Linear Solid (SLS) which consists of a spring and a dashpot in series, together in parallel with a second spring (Figure 3.7A). The relationship between the total displacement and total force across the system can be derived from the above equations and properties and is given by

$$F + \frac{\eta}{k_2}\dot{F} = k_1 x + \frac{\eta\,(k_1 + k_2)}{k_2}\,\dot{x}\,. \tag{3.6}$$

Because the total lengths of the tethers are on the order of 6 μm and the cell height changes only ~50 nm after a tether ruptures, we then approximate that the length of the tether is constant. With this assumption and the definition that $\tau = \eta/k_2$, we find that

$$F + \tau\,\dot{F} = k_1 x_0\,. \tag{3.7}$$

This differential equation can be solved for the force as a function of time, which is given by

$$F[t] = (F[0] - k_1 x_0)e^{-\frac{t}{\tau}} + k_1 x_0\,. \tag{3.8}$$

We next assume that each tether has the same mechanical properties, and so the full system can be modeled as N SLSs in parallel. Each tether then contributes the above equation to the total system, and so the total force measured by the AFM is given by

$$F_T[t] = (F_T[0] - N\,k_1 x_0)e^{-\frac{t}{\tau}} + N k_1 x_0\,. \tag{3.9}$$

Now, suppose at $t = t_0$ the system is in a steady state and a single tether breaks. Because the system was previously steady, $F_T[0] = N\,k_1 x_0$. The number of tethers instantaneously decreases by one, leaving the following equation that governs the force response immediately after the rupture event,

$$F_T[t] = k_1 x_0 e^{-\frac{t-t_0}{\tau}} + (N-1)k_1 x_0\,. \tag{3.10}$$

We may then use this equation to fit our force response; our fitting parameters are k_1, τ, and N which is restricted to integer values. Figure 3.7B shows the model fit to the data. This resulting fitting parameters were $k_1 = 15.4\ \mu N/m$, $\tau = 6.15\ s$, and $N = 4$, all of which are reasonable in regards to the current

literature [232-234]. Although this analysis is admittedly a for a single instance of membrane tether rupture, the framework could easily be applied to a population of data for rigorous statistical analysis. Furthermore, this example is sought to demonstrate the scope of applications for 2D AFM-LS, highlighting how we can couple high spatiotemporal resolution LSFM with AFM to extract mechanical properties of single cells.

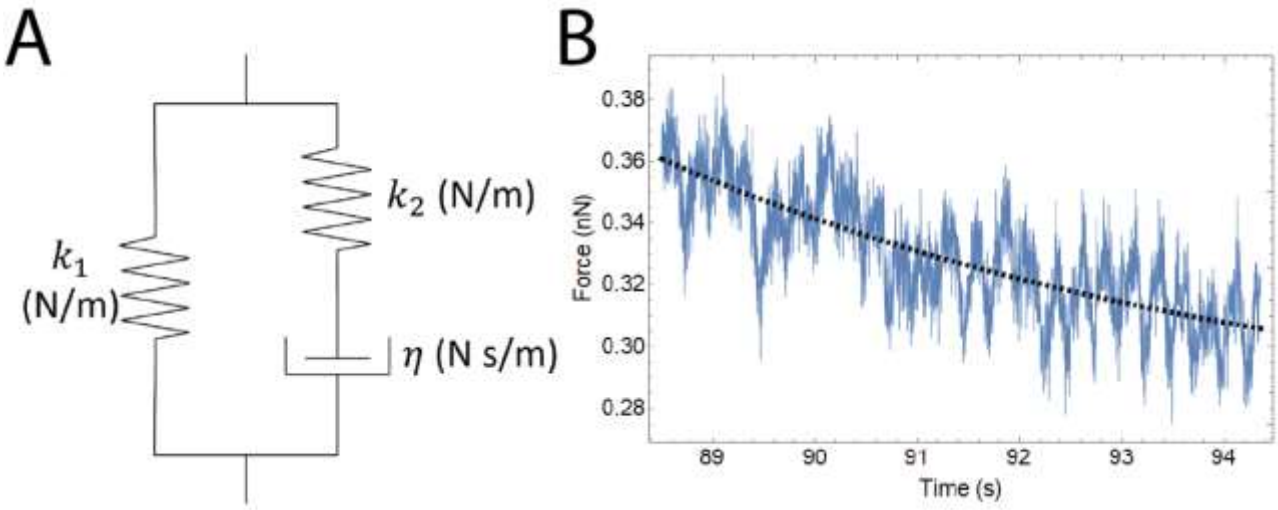

Figure 3.7: Viscoelastic Model of Membrane Tethers. (A) Schematic drawing of a standard linear solid (SLS). (B) Model fit to AFM force data during membrane tether rupture.

3.5 3D AFM-LS: Nucleolus translation

In the previous section, we have discussed an example of how 2D AFM-LS can inform mechanical properties of single cells. However, Chapter 2 has made clear that our VIEW-MOD system is capable of fast (order of seconds), multi-color, 3D images. Our AFM-LS system is also fully capable of integrating AFM with this 3D LSFM capabilities. As a demonstration of these capabilities, we have imaged the same cells described in the previous section (live, SKOV3 cells expressing halotagged H2B and snaptagged KRAS-tail) in 3D with simultaneous AFM compression (Figure 3.8). Each 3D image can be precisely correlated with the force data with ms temporal accuracy as the AFM software itself triggers the image acquisition. It should also be noted that there are no noticeable artifacts of the volumetric imaging on the AFM force data, unlike other techniques that require physically moving the objective lens which produce unphysical spikes in the AFM force data. To highlight our ability to track displacements of subnuclear structures, we decided to investigate the movement of nucleoli during compression.

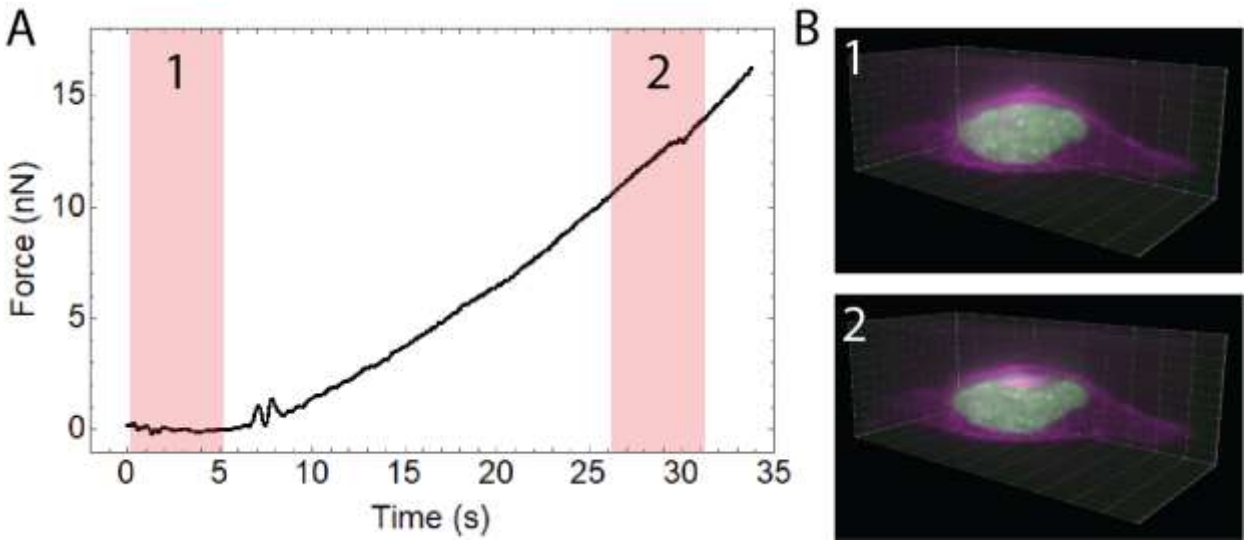

Figure 3.8: Simultaneous AFM and 3D LSFM. (A) Force versus time series as recorded by the AFM during indentation of a live SKOV3 cell. Red shaded regions correspond to the volume acquisition window for the corresponding images. (B) 3D renderings of the SKOV3 cell during AFM indentation. SKOV3 cells is stabling expressing halotagged H2B labeled with JF549 (green) and snaptagged KRAS-tail labeled with JF503 (magenta). Total image volume is 29.81 µm x 31.75 µm x 16.52 µm. Each image has an exposure time of 14 ms and readout time of 6 ms, with 127 images per channel per volume for a net volume acquisition time of 5.08 s. A 100 ms delay is taken between volumes. See also Video 3.3.

The nucleolus is the largest of several membraneless sub-nuclear bodies, forming phase-separated spheres with diameters of approximately several microns. This phase separation occurs primarily through electrostatic interactions as the proteins localized to the nucleolus are generally positively charged [235]. The nucleolus serves a variety of functions, both deemed canonical and non-canonical [236]. The canonical function is ribosome biogenesis – or more simply put the process of making ribosomes which later serve to synthesize proteins. Recently, non-canonical functions have been identified such as genome organization and DNA damage repair. Many of the proteins associated with canonical nucleolar functions are known to moonlight and serve additional purposes within the nucleus. Because of their roles in genome organization, we thought it to be relevant to observe their displacements during compression. We observed two nucleoli within the nucleus shown in Figure 3.8, identified their characteristic size and lack of histones. We then monitored their initial and final positions during the AFM compression is both X-Z (Figure 3.9) and X-Y space (Figure 3.10). By tracking the position of the center of each nucleolus to the nearest pixel, we observed that nucleolus 1 translated horizontally ~1.2 µm and had a net displacement of ~1.7 µm, while nucleolus 2 had an approximate horizontal displacement of ~1.4 µm and a net displacement of ~1.6 µm. The total indentation of the nucleus was measured to be

~3.1 μm, implying that roughly half of the net vertical indentation of the nucleus was translated into horizontal motion of the nucleoli. While this is again one example of nucleolar displacements due to AFM compression as opposed to a systematic study, it serves to highlight the capability of our system to simultaneously compress single cells, measure ~10 pN level forces, and image in multiple colors in 3D with high enough spatiotemporal resolution to track subnuclear bodies.

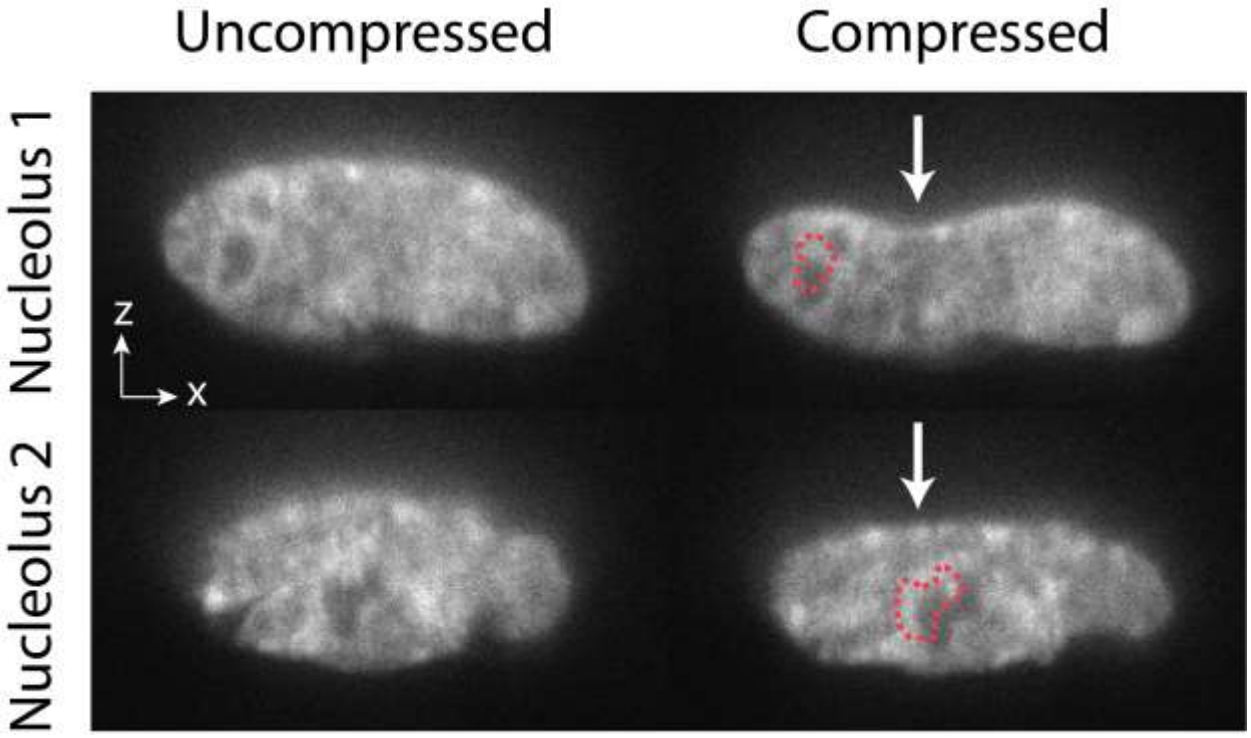

Figure 3.9: Side-view images of nucleolus displacement. Shown above are selected planes from a 3D AFM-LS experiment on a live SKOV3 cell stably expressing halotagged H2B labeled with JF549. Two nucleoli are observed to displace in X-Z space due to compression. Red dashed lines represent the initial position of the nucleolus before compression. White arrows represent approximate x-position of AFM indentation.

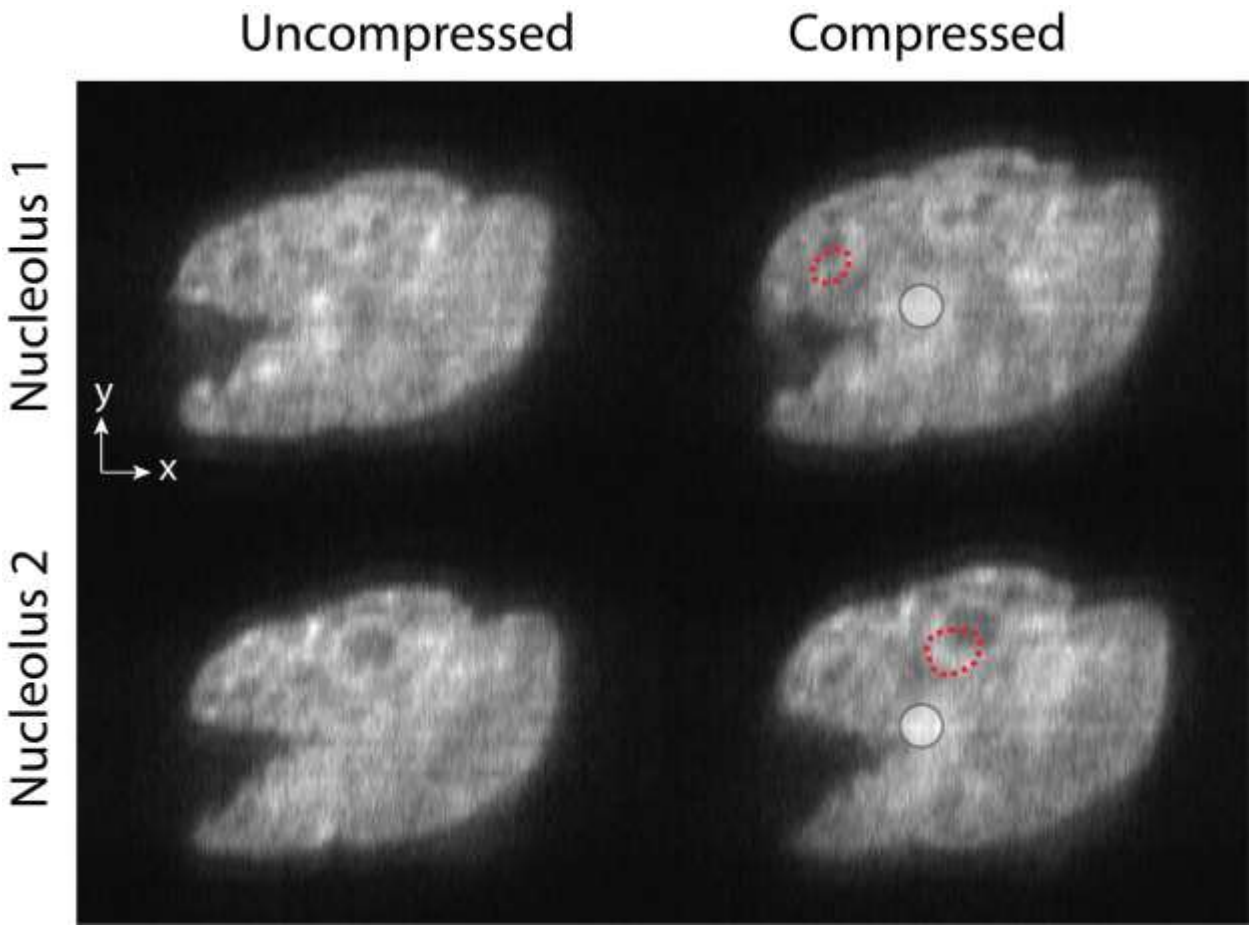

Figure 3.10: Plan-view images of nucleolus displacement (same cell as in Figure 3.9). Shown above are selected planes from a 3D AFM-LS experiment on a live SKOV3 cell stably expressing halotagged H2B labeled with JF549. Two nucleoli are observed to displace in X-Y space due to compression. Red dashed lines represent the initial position of the nucleolus before compression. White circles represent approximate x-y position of AFM compression.

3.6 Conclusions

Atomic Force Microscopy is a powerful tool for biophysicists to study mechanical forces at the single cell level. Featuring a dynamic range of 10s pN – 100s nN with ~10 pN level sensitivity, it allows one to measure phenomena ranging from single-molecule level forces to macroscopic cell compressive forces. However, one of the limiting factors of AFM is the ability to simultaneously visualize the sample as it is being deformed. Several investigators have sought to remedy this by coupling AFM with confocal or widefield microscopy. However, these techniques image in the plane orthogonal to applied force or require 3D reconstructions to image the plane of applied force. This leads to decreased spatiotemporal resolution, a high degree of photobleaching, and coupling of objective movement with the AFM force

data. Here, we describe out side-view AFM-LS system which features a micromirror designed to directly image the plane off applied force. Additionally, we employ a vertical light sheet which both minimizes photobleaching and improves optical sectioning by only illuminating the image plane. This system is the first to couple AFM force measurements with 2D and 3D multi-color LSFM. Though our AFM-LS system remedies several issues previously found with widefield/confocal AFM systems, it also features a suite of limitations primarily surrounding interactions with the AFM tip and the sample. As a demonstration of our system, we performed both 2D and 3D preliminary experiments that highlight specific capabilities. For the 2D experiments, we imaged membrane tether rupture and modeled this phenomenon using simple viscoelastic models. Such a problem requires high spatiotemporal imaging to directly visualize the tether rupturing along with force sensitivity in the range of 100 pN to sufficiently detect and model the forces associated with tether rupture. For the 3D demonstration, we imaged live SKOV3 cells in two channels (H2B and KRAS-tail) at a rate of 5.8 s per volume with simultaneous, synchronized AFM compression. By examining the H2B channel, we were able to track nucleoli movement during compression and quantify lateral and net displacements. Given its capabilities to gently image and mechanically probe single cells, our AFM-LS system is poised to investigate a range of biological questions not previously accessible through traditional methodologies.

3.7 Relevant Materials and Methods

3.7.1 Plasmid construction

LZ10 PBREBAC-H2BHalo was a gift from James Zhe Liu (Addgene plasmid #91564; http://n2t.net/addgene:91564; RRID: Addgene_91564) [237]. pR-pre-EGFP was a gift from Sergio Grinstein (Addgene plasmid # 17274 ; http://n2t.net/addgene:17274 ; RRID: Addgene_17274) [238]. Piggybac plasmid PB513Bm2 was made by removing copGFP from PB513B-1 (System Biosciences) by PCR-based mutagenesis. PBREBAC_H2BHalo and PB513Bm2 encode the G418 and puromycin resistant gene, respectively. The PB513Bm2_SNAP-KRas-tail vector was generated using PB513Bm2 as the backbone and SNAP_KRas-tail as the insert. Specifically, EGFP in pR-pre-EGFP was replaced with SNAP tag, then both pR-pre_SNAP_KRas-tail and PB513Bm2 were digested using NheI-HF and BamH1-HF restriction enzymes (New England Biolab, NEB). The products were purified using the QiaQUICK Gel

Extraction Kit protocol (Qiagen) and then ligated together using T4 DNA ligase (NEB) according to the manufacturer's instructions. Prior to use, the plasmid sequences were confirmed by sequencing using the CMV-Forward primer at Genewiz (NJ).

3.7.2 Generation of SKOV3 cell line and cell culture

SKOV3 cells were obtained from ATCC (HTB-77) and maintained in DMEM (Corning 15013CV) supplemented with 10% FBS (Sigma-Aldrich) and 1% GlutaMAX (Gibco). SKOV3 cells co-expressing H2B-Halo and SNAP_KRas-tail were generated through two consecutive transfections. We first produced a stable SKOV3 cell line expressing H2B-Halo to label the nucleus and then used those cells to produce a stable cell line expressing SNAP_KRas-tail to label the plasma membrane. The transfection was performed using Fugene HD transfection reagent (Promega) according to manufacturer's instructions. Briefly, SKOV3 cells were seeded onto a 6-well plate at 5x10^4 cells per well 24 hours prior to transfection. For each well, we used 6 ul of Fugene HD transfection reagent, 3 µg piggyBac transgene plasmid (LZ10 PBREBAC_H2BHalo or PB513Bm2_SNAP_KRastail) and 0.6 µg of piggyBac transposase plasmid (ratio at 5:1). After 24 hours transfection, the medium was replaced with the fresh culture medium and the cells were recovered for 24 hours. Stable transfectants were selected by gradually increasing antibiotics concentrations; geneticin (G418) at a concentration to 1 mg/ml for PB-Halo-H2B and Puromycin at a concentration to 2 µg/ml for PB513Bm2-SNAP-KRas-tail. SKOV3 cells were grown in DMEM F12 without phenol red (Gibco), 5% FBS (Sigma-Aldrich) and 1X antibiotic antimycotic (Gibco). On the day before experiments they were trypsinized and plated at low density on fibronectin-coated polyacrylamide gels. 10 µL of Janelia Fluor 549 and 503 was added 2 hours prior to experiments, and washed out immediately before cell were examined. This SKOV3 cell line was generated by Megan Kern.

3.7.3 Cantilever Preparation

Beaded cantilevers were generated by first drying nominally 6 µm diameter carboxylate beads onto a coverslip (17141-5, Polysciences, Inc); a small amount of UV-curable glue (NOA81, Norland Products) was spread onto the cover slip. A cantilever (Arrow TL1, Nanoworld) was mounted onto the AFM head (Ayslum Research MFP3D, Oxford Instruments), which was lowered over the aforementioned

coverslip. Using the manual height adjustment on the AFM, the cantilever was lowered first into the glue and then overtop of a bead. A UV flashlight was used to cure the glue for one minute; the cantilever was removed and set to cure for an additional five minutes. Once beaded, cantilevers were calibrated in media using the thermal tune method [53]; the nominal spring constant was 0.03 N/m.

3.7.4 AFM-LS Experimental Details

Cells prepared as described above were place onto the AFM-LS system in a custom, 3D-printed mount (uploaded as Thingiverse 2035546). Cells were kept in DMEM F12 with 15 mM HEPES without Phenol Red (Gibco) while on the microscope; this media is not C02 independent. An objective lens heater (Hk-100, Thorlabs, Inc, USA) with a PIV controller (TC200, Thorlabs, Inc.) and a heated scanning stage (900.062 MFP3D Scanner, Oxford Instruments) were used to keep the sample at 37ºC. Samples were kept on the AFM-LS system for no more than a couple hours to ensure viability; cells were observed to be viable throughout all experiments. The AFM headed with a calibrated cantilever was placed atop the sample and the cantilever was lowered over a cell of interest. Side-view imaging is achieved by placing a small (180 µm) mirror (8531-607-1, Precision Optics Corporation) adjacent to a cell of interest and raising the objective lens (UplanSAPO 60x/1.2 W, Olympus) until the image plane intersects the mirror. Details regarding mirror alignment and production are given in our previous work [172]. With the AFM in place, the mirror is placed next to the cell of interest such that the cantilever sits between the mirror and the cell. A vertical light sheet propagates out of the objective lens and an electrically tunable lens (ETL) was used to ensure the waist of the light sheet was in the cell. A second ETL is used in the detection path to dynamically adjust focus without moving the objective lens [239].

For AFM-LS experiments, force curves were taken at a loading rate of 1 µm/s (2D) or 250 nm/s (3D).The trigger point for the z-piezo movement was set such that the nucleus was compressed to approximately 2 µm. The z-piezo was then fixed in a closed-loop feedback mode for 60 s, after which the AFM retraced and continue recording data for an additional 15 s. Data from the AFM was recorded at a bandwidth of 2 kHz. A square wave from the AFM was sent to a DAQ board (PCIe-6323, National Instruments) which was used to synchronize both the camera (ORCAFlash4.0 V3, Hamamatsu) and laser light (OBIS-561-150-LS and OBIS-488-150-LS, Edmund Optics). For 2D AFM-LS experiments, each

channel (488 nm and 561 nm) had an exposure time of 100 ms and 25 ms was taken between each frame resulting in a two-color frame acquisition rate of 4 Hz. For 3D AFM-LS experiments, each frame had an exposure time of 14 ms and readout time of 6 ms, A 100 ms delay is taken between volumes.

CHAPTER 4: COMBINED SELECTIVE PLANE ILLUMINATION MICROSCOPY AND FRAP[3]

Chapters 2 and 3 established our means of studying nuclear mechanics. Next, I present our tool for measuring intranuclear dynamics. Cell nuclei depend upon transport and shuttling of proteins and small molecules across the nucleus and through the nuclear envelope to facilitate proper cell function. In understanding how these dynamic processes work, investigators have turned to single particle tracking, FCS, and FRAP for quantification of diffusive properties in nuclei. Here, I present a combination of selective plane illumination microscopy (SPIM) and FRAP that allows for *simultaneous* FRAP measurements for every pixel in a 2D image. I demonstrate SPIM-FRAP by generating 2D maps of diffusion coefficients, which can be correlated directly with chromatin structure to specifically show how intranuclear diffusion of NLS-GFP is heterogeneous and slowed in nucleoli. I also present a simulation of SPIM-FRAP that allows for conversions of FRAP recovery times to diffusion coefficients so that SPIM-FRAP experiments may be compared across methodologies. Finally, I use SPIM-FRAP to show how sites of DNA damage are more stable than the surround diffuse DNA damage protein. SPIM-FRAP is a novel method that will allow for a myriad of future nuclear dynamics studies that capture the *heterogeneous* nature of diffusive processes.

4.1 Measuring Intracellular Dynamics

Fluorescence Recovery After Photobleaching (FRAP) [89] is one of the most prevalent techniques for studying intracellular diffusion and protein dynamics. In brief, a region of interest of a fluorescently labeled sample is exposed to a high-intensity light source, thus photobleaching this specific region. Either through diffusion or (un)binding, the fluorescence of the bleached region recovers, allowing one to understand both the timescales of the recovery as well as the (im)mobile fraction. The widespread availability of both fluorescent proteins and point-scanning confocal microscopes has dramatically

[3] This chapter was previously published in Hobson, C. M., et al. (2020). "Combined Selective Plane Illumination Microscopy and FRAP Maps Intranuclear Diffusion of NLS-GFP." Biophys J **119**(3): 514-524.

increased the accessibility of performing FRAP experiments. The other most common technique for studying such dynamics is fluorescence correlation spectroscopy (FCS) [84]. FCS takes advantage of the fluorescence intensity fluctuations resulting from diffusion in and out of an excitation volume, and uses correlation analysis to extract quantitative measures of diffusion (i.e. the diffusion coefficient). FRAP and FCS have dramatically accelerated research in the realm of diffusions and protein dynamics.

The relative merits of FCS and FRAP are well documented. Both FRAP and FCS require precise knowledge of the illumination volume for an accurate measurement of the diffusion coefficient, often making absolute quantification difficult [240, 241]. Although, descriptions of relative changes of intracellular dynamics under various interventions are still readily possible. Beyond diffusion measurements, FRAP can measure immobile fractions, while FCS can measure absolute concentration and, in principle, faster dynamics than FRAP. As for limitations, FRAP can be sensitive to bleach correction, while FCS requires careful consideration of the concentration of the fluorescent protein of interest and has higher signal-to-noise requirements than FRAP [242]. However, the primary drawback of FRAP is the inability to distinguish heterogeneity of diffusion in a given sample. That is, each FRAP experiment produces one measurement for a given region of interest. Investigators have looked to FCS for studying such heterogeneous dynamics. By either iteratively performing FCS measurements across a cell of interest or using a selective plane illumination microscopy (SPIM) system coupled with FCS (SPIM-FCS), investigators have been able to generate 2D maps of intracellular diffusion [87, 88, 243-247]. These measurements require acquisition times on the order of minutes to create such maps, presumably due to the high signal-to-noise requirements of FCS. Here, we address these limitations of both FRAP and FCS by combining SPIM with FRAP (SPIM-FRAP) to generate the first simultaneous, FRAP-based, 2D maps of intranuclear diffusion.

SPIM systems, specifically single-objective implementations [168, 170, 171, 173], have become increasingly accessible to the biophysics community. Previous work has used a SPIM microscope to image after photobleaching with a focused beam [248]. Here, we use the light sheet to both photobleach and image our sample. By photobleaching a single plane that coincides with our image plane, we still allow for diffusion into the image plane from the rest of the 3D volume. Each pixel in our image then provides a simultaneous FRAP measurement. We demonstrate our SPIM-FRAP technique by mapping

the diffusion of NLS-GFP in MDA-MB-231 cells with improved temporal resolution over FCS-based techniques (SPIM-FRAP: 4 seconds, FCS-based: ~minutes) and the added spatial information compared to traditional FRAP. This decrease in acquisition time in not a feature of the specific experiment at hand, but rather is indicative of fundamental limitations of FCS and FRAP. For accurate FCS measurements, the acquisition time should be no less than $100\tau_D$, where τ_D is the relevant time scale given by $\tau_D = A_{eff}/4D$, A_{eff} is the effective area, and D is the diffusion coefficient [249]. Accurate FRAP measurements require only acquisition times of ~$10\tau_D$. the observed order of magnitude gain in acquisition time of SPIM-FRAP is then a fundamental feature of the technique itself. We further simulate SPIM-FRAP experiments to determine what degree of heterogeneity can be detected by our technique. To convert recovery times to diffusion coefficients, we generate a simulation of diffusion that accounts for diffusion during the bleach pulse. Both the diffusion coefficients we report are consistent with previous FRAP and FCS literature. We finally show that SPIM-FRAP can be applied to samples with larger heterogeneity than NLS-GFP by performing experiments on 53BP1-mCherry, a marker for DNA damage.

4.2 SPIM-FRAP Maps Intranuclear Heterogeneous Diffusion of NLS-GFP

SPIM-FRAP experiments were performed with a custom light sheet microscope (Figure 4.1A) by photobleaching a single plane of live MDA-MB-231 cells co-expressing either NLS-GFP and H2B-mCherry or NLS-GFP and 53BP1-mCherry. We then used the same light sheet at a reduced power to image the photobleached plane as the NLS-GFP intensity recovered via diffusion into the image plane (Figure 4.1B). Images were bleach corrected before analysis as described in the methods. The recovery images were minimally blurred in FIJI [250] with a single-pixel Gaussian blur prior to analysis. An exponential recovery (Eq. 4.1) was fit to the intensity of each pixel during the recovery portion of the time series (Figure 4.1D). From these data we can extract a characteristic recovery time, τ, and recovery percentage, $\frac{B}{I_{pre\,bleach} - I_{min}}$, for every pixel in the image plane (Figure 4.1C). This subsequently provides a 2D map of intranuclear diffusion of NLS-GFP. A single exponential recovery fits our data for diffusion of NLS-GFP well (Figure 4.1D) as $R^2 = 0.99973 \pm 0.00003$ (mean ± standard deviation) across all pixels in the data set shown in Figure 4.1. For dynamics where this is not the case, however, the function used to analyze the recovery for each pixel is interchangeable. That is, a double-exponential curve could be used

as opposed to Eq. 4.1 if it better suits the data set at hand. The total acquisition time for each experiment was ~4 seconds, providing an order-of-magnitude improvement to FCS-based techniques [87, 88, 243-247].

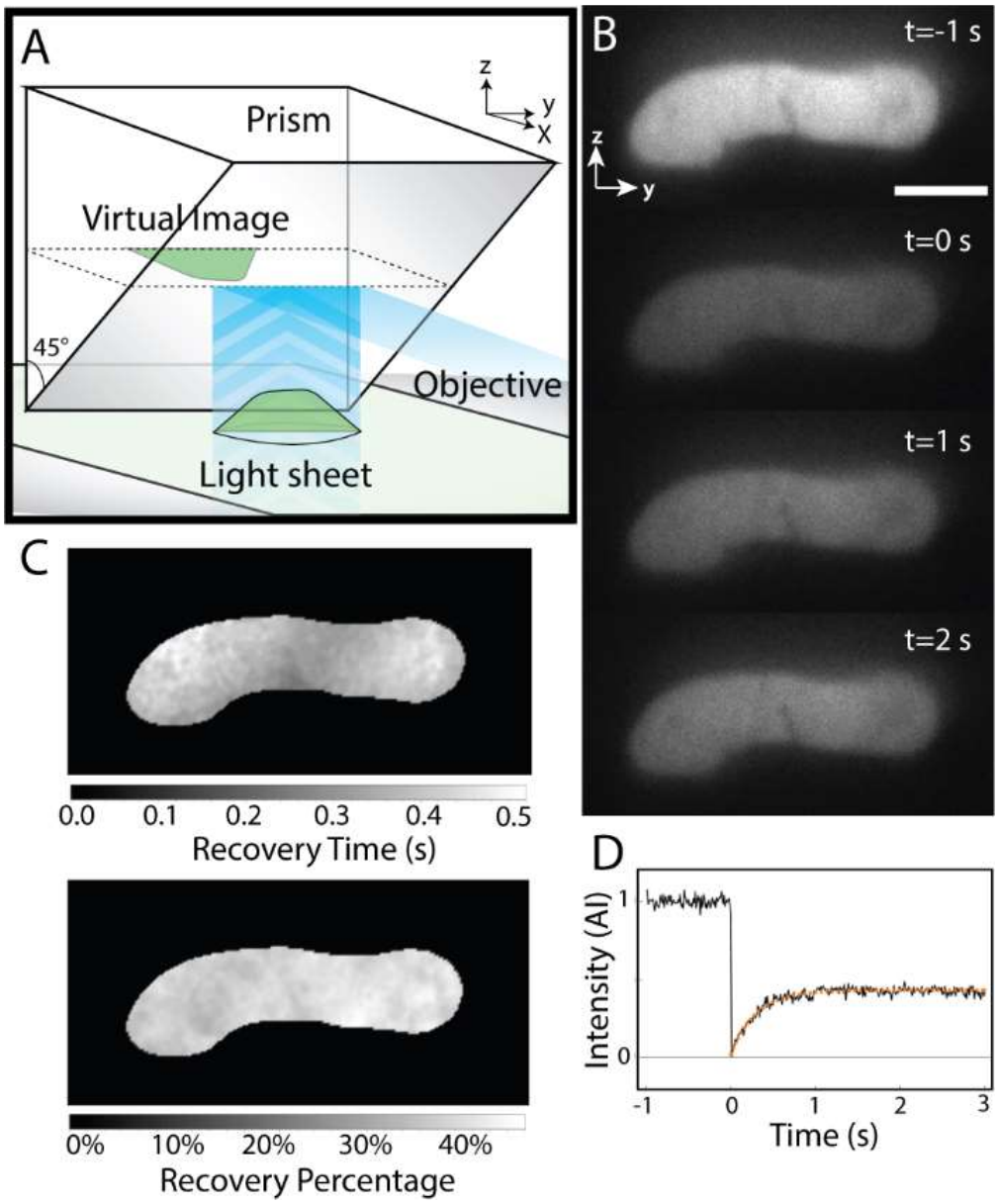

Figure 4.1: SPIM-FRAP generates simultaneous 2D maps of intranuclear NLS-GFP recovery times. (A) Schematic of our custom, single-objective SPIM microscope. (B) A side-view SPIM-FRAP image sequence of NLS-GFP showing the simultaneous recovery across the entire image plane (Movie S1). Scale bar = 5 μm. (C) 2D maps and histograms of NLS-GFP recovery times and recovery percentages for the SPIM-FRAP experiment shown in (B). (D) Time series of a single-pixel intensity of the image sequence shown in (B) after Gaussian blurring. The recovery is bleach corrected and the orange curve represents an exponential recovery fit. See also Video 4.1.Before drawing conclusions regarding the spatial distribution of τ, we sought to determine what our method is able to resolve. To study this, we generated a suite of

simulated SPIM-FRAP data sets (Figure 4.2). Simulations with a uniform recovery time showed that the addition of noise to the recovery curve broadened the distribution of measured recovery times, and that our 1-pixel Gaussian blur served to tighten this distribution at the cost of spatial resolution. Extracting τ for every pixel, then, does not necessarily mean that we have single-pixel resolution for discerning structure in recovery maps. Additionally, we simulated recovery with 5x5 (540x540 nm) pixel squares that were prescribed a 20% faster recovery time than the rest of the data set. Our analysis was still able to easily detect this structure. We then concluded that the short length scale (~2-3 pixels, ~216 – 324 nm) mottling structure is an artifact of the Gaussian blurring process coupled with noise in the image sequence. Thus, the lower bound on our spatial resolution with the current analysis protocol is on the order of ~500 nm. This is not necessarily the lower bound of SPIM-FRAP itself, but rather of SPIM-FRAP applied to this sample with our current analysis protocol. The large length-scale (> 5 pixels, 540 nm) heterogeneity in the experimental recovery time map, however, is not an artifact of the analysis. This implies there is a spatial dependency of intranuclear diffusion of NLS-GFP, consistent with FCS measurements [87]. This distribution was, in some instances, bimodal, which is suggestive of liquid-liquid phase separation. We verified that this heterogenous structure is reproducible by performing back-to-back SPIM-FRAP experiments on the same nucleus Figure 4.3A). We observed a positive correlation between the recovery time maps for the first and second experiment (Figure 4.3B); however, the magnitude of the recovery times seemed to fluctuate between measurements, potentially because the second experiment is not an exact replicate of the first experiment but rather a duplicated measurement in the same location with already-depleted signal.

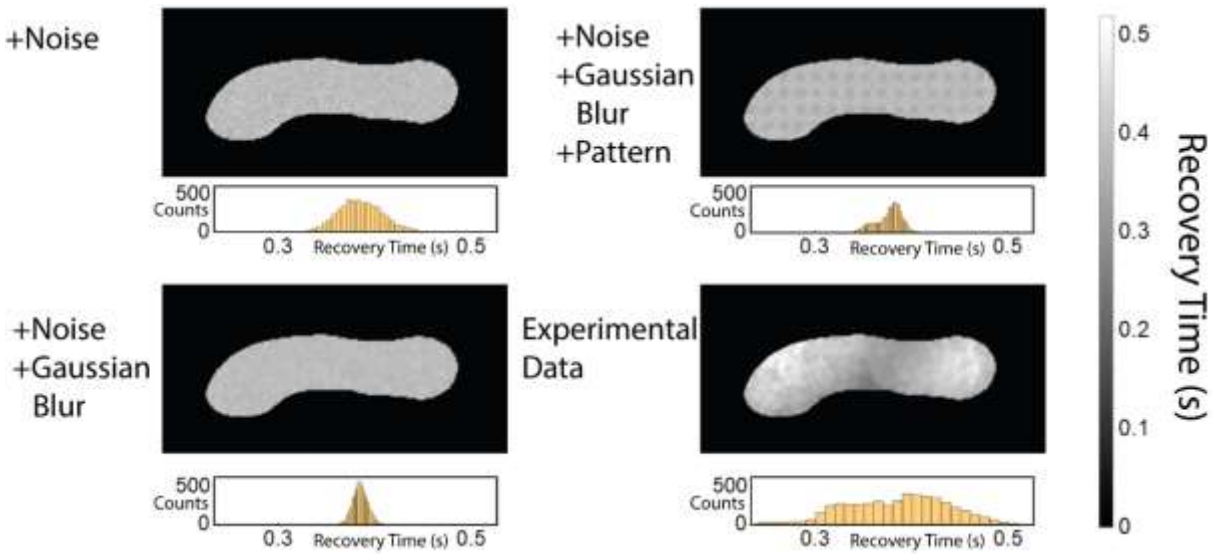

Figure 4.2: SPIM-FRAP simulated data sets. (Top, Left) Simulation with noise in the recovery curve. Ground truth is a uniform recovery time. (Bottom, Left) Simulation with noise in the recovery curve and Gaussian blurred before analysis. Ground truth is a uniform recovery time. (Top, Right) Simulation with noise in the recovery curve and Gaussian blurred before analysis. Ground truth is a 5x5 pixel array of recovery times that differ by 20%. (Bottom, Right) Experimental data set.

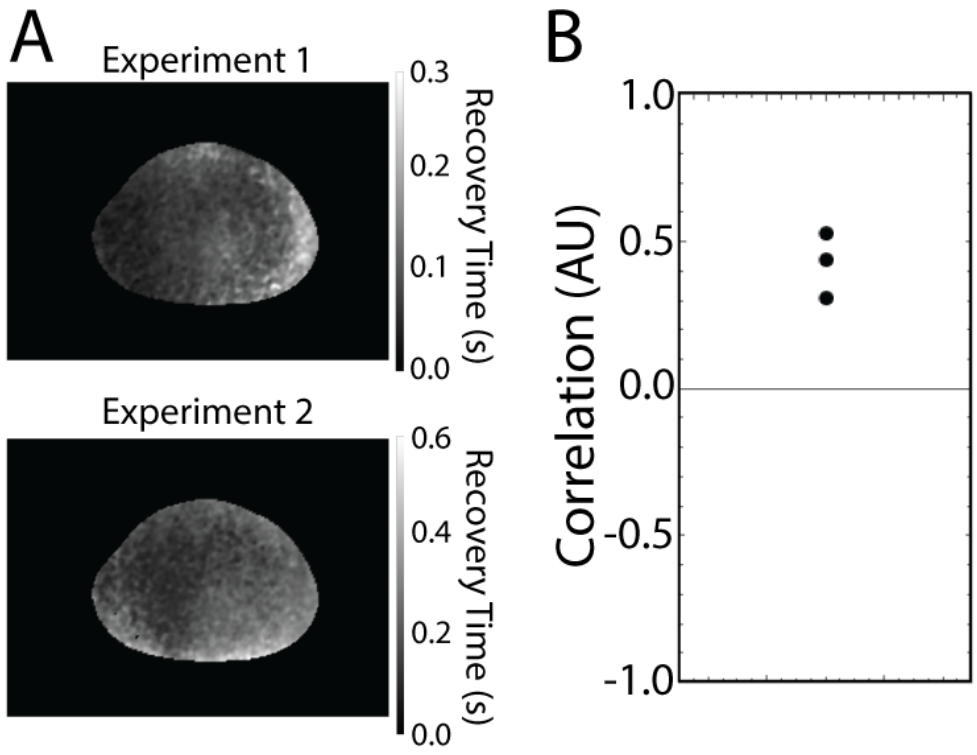

Figure 4.3: Repeated SPIM-FRAP experiments show positive correlations. (A) Recovery time map from SPIM-FRAP experiments of NLS-GFP. Experiment 1 and 2 are separated by 10 s. (B) Correlation coefficient of n=3 experiments between the recovery map from Experiment 1 and Experiment 2.

The source of the heterogeneous diffusion of NLS-GFP is presently unknown and warrants further studies. Intranuclear phase separated nucleoli have been shown to be more viscous than the surrounding nucleoplasm [243]. The observed heterogeneity in diffusion could then be indicative of liquid-liquid phase separation in the nucleus [251]. Alternatively, these data could suggest that the heterogeneity of the viscosity of the nucleoplasm is due to variations in concentration of macromolecules. This could have profound effects on nuclear mechanical properties and mechanotransduction [90]. Finally, binding of the NLS to RNA could be a source of varied diffusion [252]. Regardless of the origin, the observed spatial heterogeneity of intranuclear diffusion highlights that intranuclear transport is similarly heterogeneous on >~500 nm length scales. To understand the potential origin of this heterogeneity, we sought to correlate our diffusion measurements with nuclear structure.

4.3 Chromatin Does Not Inhibit Diffusion of NLS-GFP

Previous FCS literature has suggested that the diffusion of small molecules through the nucleus has little correlation with chromatin concentration [87]. Further work, however, reported through use of an FCS variant using pair Correlation Functions (pCF) that DNA does indeed play a role in hindering transport of small molecules [85]. SPIM-FRAP provides an opportunity to address such questions as it allows for correlation of recovery time maps with fluorescence images of other structures. By collecting a fluorescence image of H2B-mCherry prior to performing a SPIM-FRAP experiment of NLS-GFP on the same image plane (Figure 4.4A), we can explore any correlation between histone density and diffusion. For each cell examined (n=11), we plotted the normalized H2B intensity versus the measured recovery times per pixel (Figure 4.4B) and calculated the correlation coefficient (Figure 4.4C). We observed a large spread in the correlation coefficients with no significant difference from zero correlation. This implies, similar to previous work [87], that there is no immediate spatial correlation between histone density and intranuclear diffusion of NLS-GFP. However, this does not negate some of the more intricate theories regarding barriers to long-range diffusion and sudden bursts of motion across dense regions of DNA [85]. This also does not exclude the possibility of a correlation between diffusion of larger molecules and chromatin density, which could be studied by similar experiments using GFP-multimers. Additionally, SPIM-FRAP may not be able to detect a correlation on a length scale of ~100 nm.

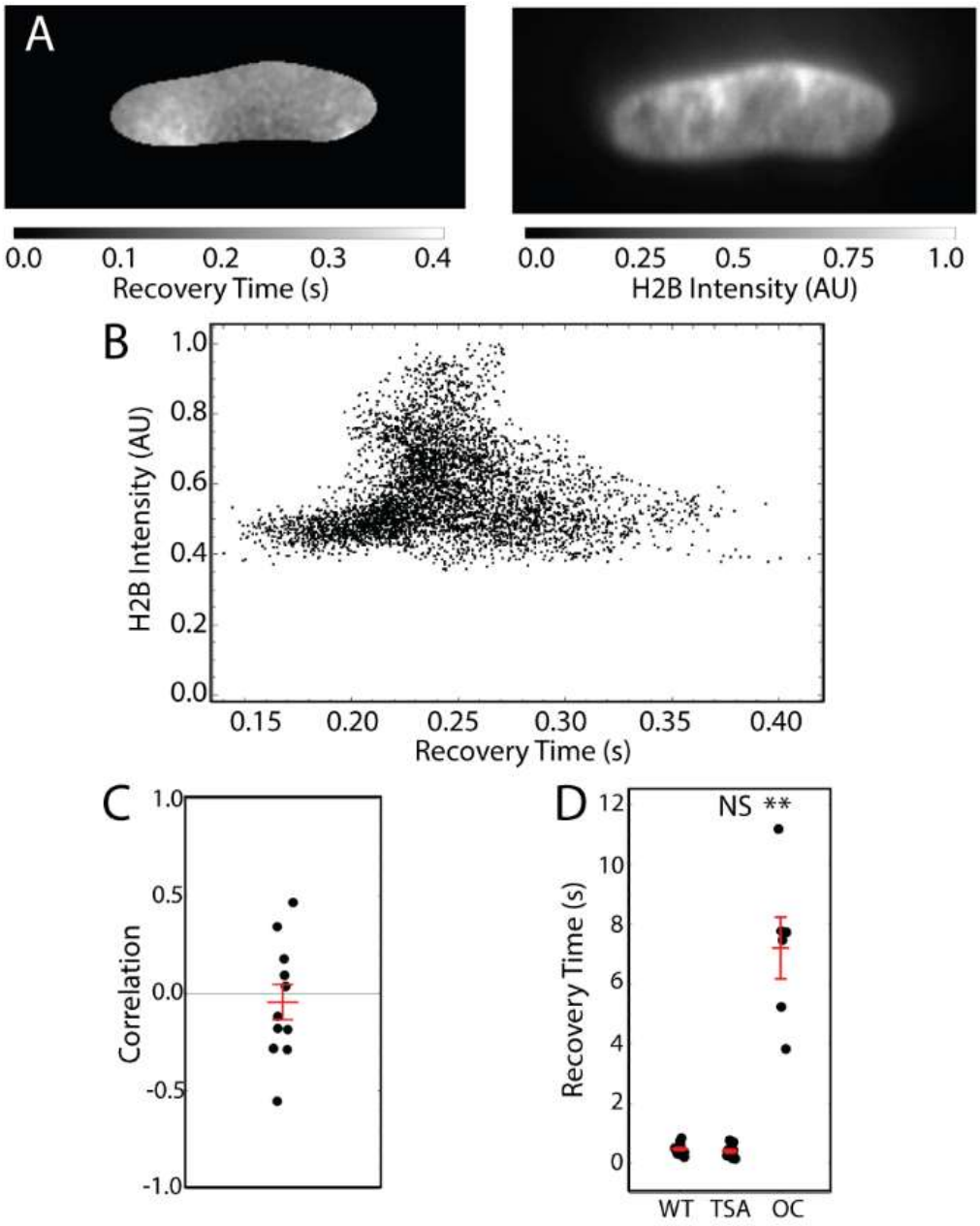

Figure 4.4: Chromatin Density does not inhibit diffusion of NLS-GFP. (A) SPIM-FRAP recovery time map for NLS-GFP and a corresponding image of H2B-mCherry. (B) A plot of normalized H2B intensity versus recovery time shows little correlation between chromatin structure and diffusion. (C) Correlation coefficients between recovery time and H2B intensity for N=11 nuclei show no significant correlation. (D) Peaks in recovery time for WT nuclei (n=9 cells, n=13 peaks), TSA-treated nuclei (n=10 cells, n=12 peaks), and osmotically-compressed (OC) nuclei (n=6 nuclei, n=6 peaks). A post-hoc Tukey test following a one-way ANOVA test gives no significant difference in recovery time between WT and TSA and gives $p<0.01$ (represented by **) between WT and OC. Red lines represent mean and SEM.

We further treated MDA-MB-231 cells co-expressing NLS-GFP and 53BP1-mCherry with

Trichostatin A (TSA) to decondense interphase chromatin levels [116] before performing SPIM-FRAP

experiments. The peak of each recovery time distribution was determined by fitting a Gaussian curve to the respective histogram; for bimodal distributions, two peak recovery times were extracted. We observed no significant difference in peak recovery times for WT and TSA-treated cells (Figure 4.4D). As a positive control, we also osmotically compressed (OC) nuclei by exchanging the media with a solution at 4 times the osmolarity. OC has been previously shown to slow intranuclear dynamics [253]. Similarly, we observed a significant increase in the recovery times for OC nuclei as compared to WT. This indicates that the lack of a difference between TSA and WT nuclei is not due to a lack of sensitivity, but rather that chromatin decompaction has no physical impact on diffusion of NLS-GFP. This is interesting, though not particularly surprising, in that the length-scale of changes in chromatin compaction is presumably much larger than the scale of NLS-GFP. Confinement effects due to chromatin compaction are then likely not prevalent for such small molecules, but may be of interest for transport of larger proteins.

4.4 Diffusion of NLS-GFP is Slowed in Nucleoli

It is well documented that nucleoli exhibit longer diffusion times than the surrounding nucleoplasm [243]. As a positive control for SPIM-FRAP, we wondered whether our technique would also detect differences in diffusion across the nucleolus. A representative example of our data is given in Figure 4.5A-C. Nucleoli are clearly identifiable in an H2B-mCherry image due to the absence of histones and sphericity (Figure 4.5A). We also observed similar regions of longer recovery times of NLS-GFP from the corresponding SPIM-FRAP experiments (Figure 4.5B). To quantify this apparent feature, we defined the nucleolus region based solely upon the H2B-mCherry image and subsequently separated the pixels in the corresponding pixel-by-pixel plot of H2B intensity versus recovery time into the nucleolus and nucleoplasm (Figure 4.5C). We observed a clear segregation in this phase space between the nucleolus and the nucleoplasm. This same trend of slowed diffusion in the nucleolus held true for n = 5 separate nuclei and SPIM-FRAP experiments (Figure 4.5D), showing that SPIM-FRAP is able to reproduce results regarding heterogeneous intranuclear diffusion from well-established techniques. However, SPIM-FRAP enables pair-wise comparisons of particular regions within a given cell as opposed to requiring population-based studies as with previous methods.

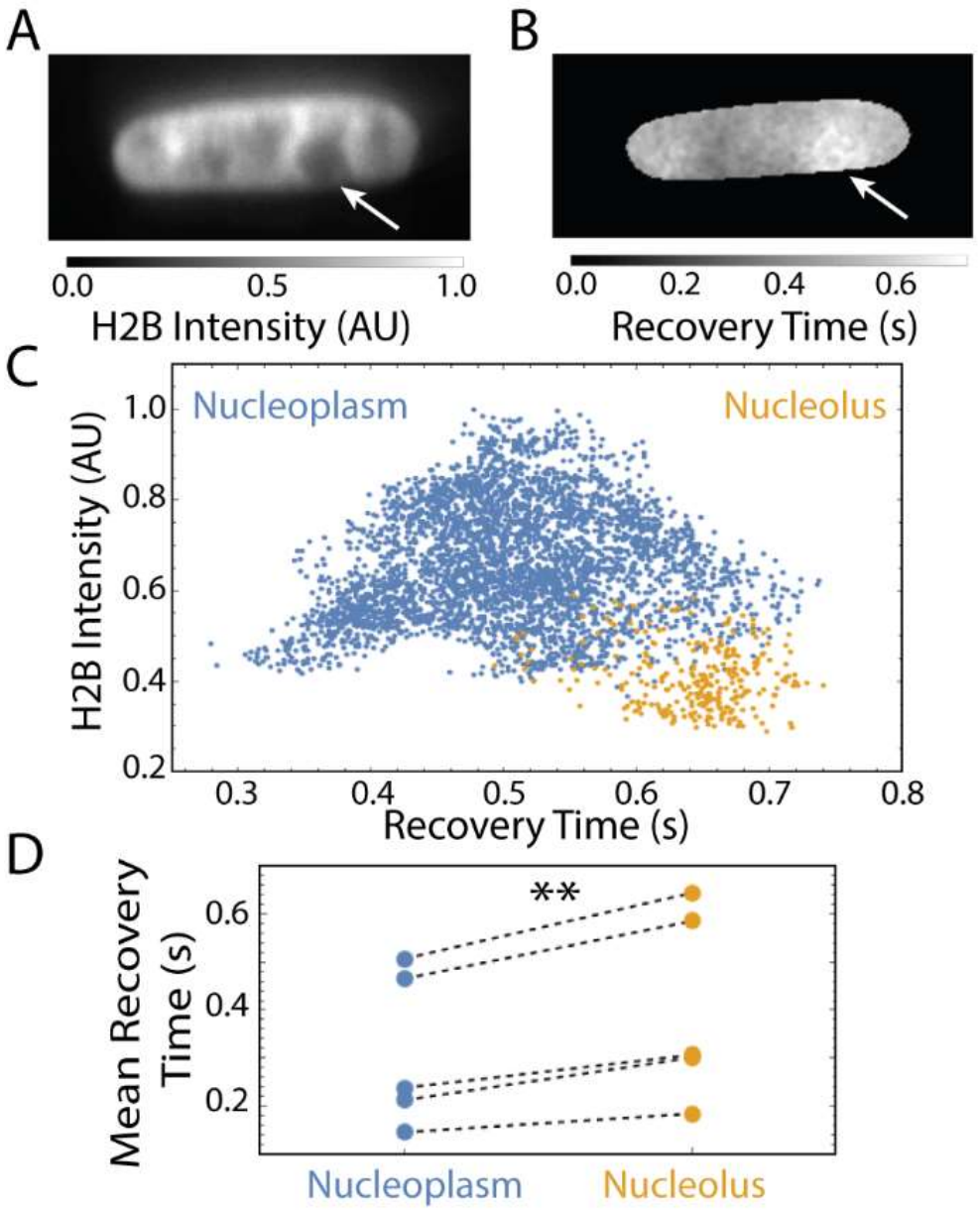

Figure 4.5: Diffusion of NLS-GFP is slowed inside of the nucleolus. (A) Image of H2B-mCherry; arrow points to a nucleolus. (B) The corresponding map of recovery times for NLS-GFP as measured by SPIM-FRAP. (C) A pixel-by-pixel plot of H2B intensity versus recovery time of NLS-GFP from a SPIM-FRAP experiment. Orange represents pixels deemed to be in the nucleolus based upon the H2B-mCherry image. Blue represents all other pixels. (D) Mean recovery times of NLS-GFP inside the nucleoplasm and the nucleolus (n=5 nuclei). Black dashed lines connect measurements in the same nucleus. ** represents $p<0.01$ for a Paired T-Test.

4.5 Diffusion Simulation Converts Recovery Times to Diffusion Coefficients

While recovery times provide a useful means of comparing two conditions in a given experiment, determination of the diffusion coefficient is far more useful for comparison of results across experiments

and techniques [242]. Extraction of diffusion coefficients from FRAP experiments requires careful modeling of the bleached geometry, and SPIM-FRAP is no exception. We therefore developed a simulation of diffusion during a SPIM-FRAP experiment (Figure 4.6). The primary assumption in our model is that diffusion in and out of the image plane is the dominant source of the recovery of the fluorescence signal. This simplifies the full 3D problem to a 1D approximation (Eq. 4.8). We used the theoretical profile of our Line Bessel Sheet to determine the region that will be photobleached. We additionally verified that we are bleaching a sheet consistent with this profile (Figure 4.7). Furthermore, the common assumption that the photobleach pulse is significantly shorter than the relevant time scale does not hold for our case ($\tau_D \approx 46$ ms for 1D diffusion where $\tau_D = l^2/2D$, $l = 675$ nm is the full width at half maximum of the light sheet and $D = 5\ \mu m^2/s$), so it was necessary that we account for diffusion into the region being photobleached during the photobleach pulse.

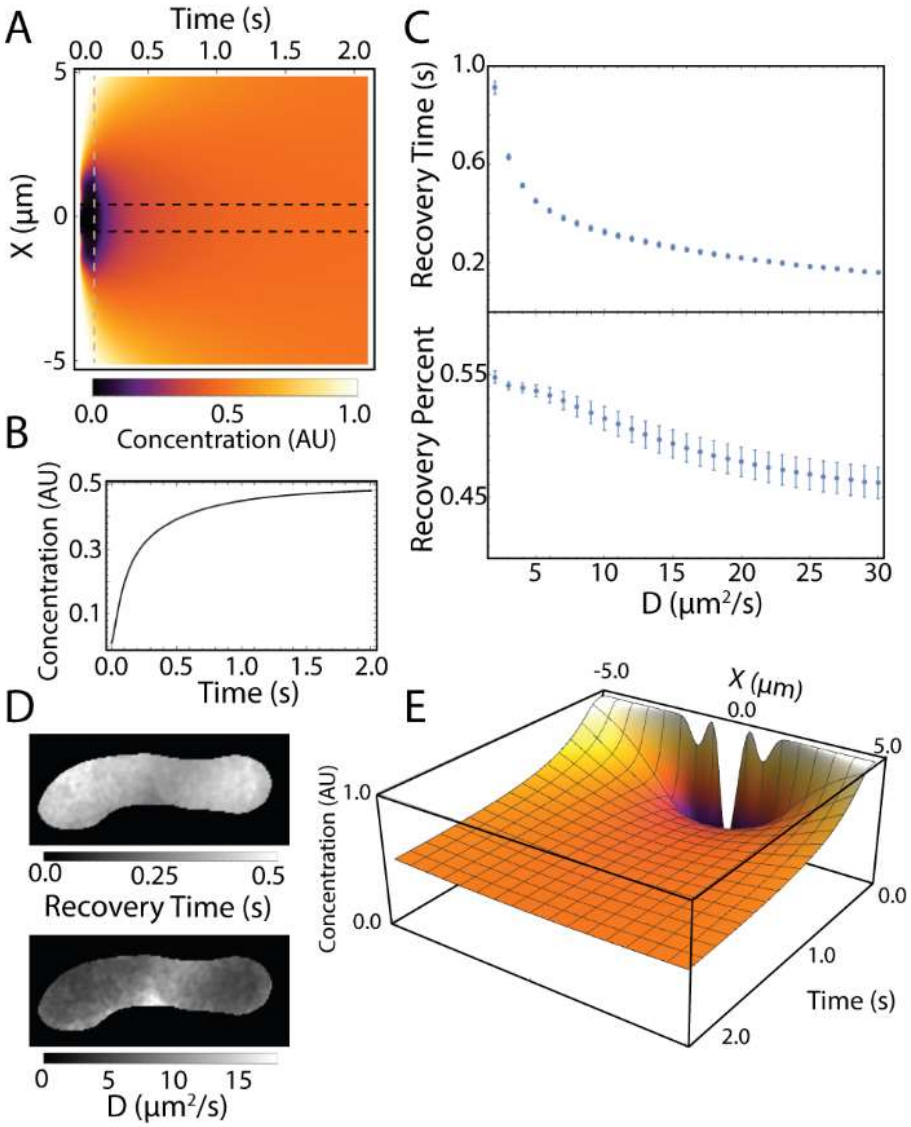

Figure 4.6: Diffusion simulation connects measured recovery times to diffusion coefficients. (A) Simulated diffusion for D=15 (um^2)/s. The grey dashed line represents when the light sheet turns off. Black dashed lines represent the region being integrated to determine recovery times. (B) Integrated concentration between the black dashed lines in (A) as a function of time (Movie S2). (C) Plot of recovery time versus diffusion coefficient for the simulated SPIM-FRAP diffusion process. Plot of recovery percentage versus diffusion coefficient for the simulated SPIM-FRAP diffusion process. Error bars represent standard errors for parameter fits. (D) An experimental map of recovery time for NLS-GFP and the corresponding map of D. (E) A 3D rendering of the diffusion simulation. At t=0, the initial concentration is the inverse of the light sheet profile. See also Video 4.2.

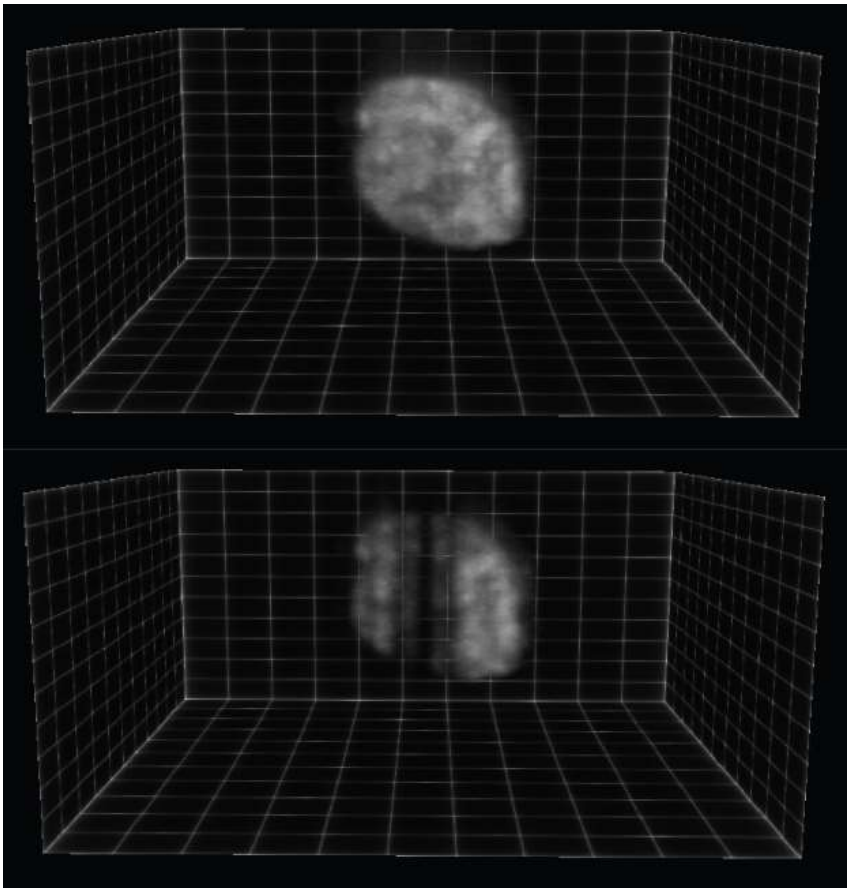

Figure 4.7: 3D rendering of a live MDA-MB-231 nucleus expressing H2B-mCherry both pre and post SPIM photobleaching. A clear 2D plane is bleached through the nucleus as well as small photobleaching of the concentric side lobes. Rendered in ClearVolume [254]. See also Video 4.3.

We performed this simulation across a sweep of diffusion coefficients, then fit Eq. 4.1 to the recovery of the simulation to determine the corresponding values of B and τ for a given diffusion coefficient (Figure 4.6C). The measured peak recovery times for WT cells range from 0.209 s to 0.832 s with a mean of 0.478 s. According to our simulation, this means we observed diffusion coefficients ranging from 2.22 μm^2/s to 21.6 μm^2/s with a mean of 4.52 μm^2/s. The simulated values of recovery percentage are also consistent with our experiments. We can use these results to convert experimental maps of τ to maps of D (Figure 4.6D). Previous literature on the intranuclear diffusion of small molecules gives diffusion coefficients ranging from approximately 4 μm^2/s to 50 μm^2/s [85-88, 246, 255-258]. For context, the diffusion coefficient of a GFP-sized inert particle in water is approximately 87 μm^2/s [259]. Our results then fall on the lower end of the previous reported values. This could potentially be due to factors regarding simulation, such as the principle assumptions, a dependence of D on the geometry of

the nucleus, or the specific bleach correction used in our analysis [242]. Alternatively, the slight discrepancy could be due to the addition of the nuclear localization sequence to the GFP molecule which subsequently changes RNA binding and molecular weight [252].

4.6 Recovery of 53BP1-mCherry is Slowed at Sites of DNA Damage

SPIM-FRAP has been clearly demonstrated to be a valid technique for studying diffusion of NLS-GFP, which is a relatively homogeneous sample. A majority of proteins of interest do not show this same level of homogeneity. To test whether SPIM-FRAP can be used to study the dynamics of structures which exhibit significant heterogeneity in the initial intensity distribution, we performed SPIM-FRAP experiments on live MDA-MB-231 cells expressing 53BP1-mCherry (Figure 4.8). 53BP1 is a marker for DNA damage [69]. It forms bright foci at sites of double-stranded DNA breaks and remains diffuse in the rest of the nucleus (Figure 4.8A). Previous literature suggests that 53BP1 foci are more stable than the surrounding diffuse 53BP1 [260, 261]. Similar to our experiments with NLS-GFP, we were able to extract maps of recovery times for 53BP1-mCherry from our SPIM-FRAP experiments (Figure 4.8B). Consistent with the previous literature [260, 261], we observe slower recovery at the sites of DNA damage (Figure 4.8C). Because the DNA damage foci recover slower than the surrounding diffuse protein, this implies that the foci are not limited by diffusion. Furthermore, we can infer that we are actually measuring the off-rate of binding at the sites of DNA damage. We segmented the nucleus by hand into regions of 53BP1-mCherry foci and diffuse 53BP1-mCherry. In principle, more than one focus can exist in a given image, however for our data we only observe one focus per image (Figure 4.8A). With this segmentation, we were able to quantify that the average recovery time for 53BP1-mCherry foci was larger than the diffuse 53BP1-mCherry for the two cells we examined (Figure 4.8E). As a second means of analysis, we segmented the nuclei into foci and diffuse regions prior to extracting recovery times as opposed to fitting Eq. 4.1 to each pixel before segmentation. We plotted the average, normalized intensity after photobleaching of the foci and diffuse regions and extracted recovery times by fitting Eq. 4.1 to these time series (Figure 4.8D). The recovery times for this coarse-grained approach agree well with the pixel-by-pixel analysis used previously Figure 4.8E). SPIM-FRAP is then not only a useful tool for studying diffusion of homogeneous

samples, but also for studying the dynamics of proteins that exhibit significant heterogeneity both in initial intensity distributions and the

recovery maps themselves.

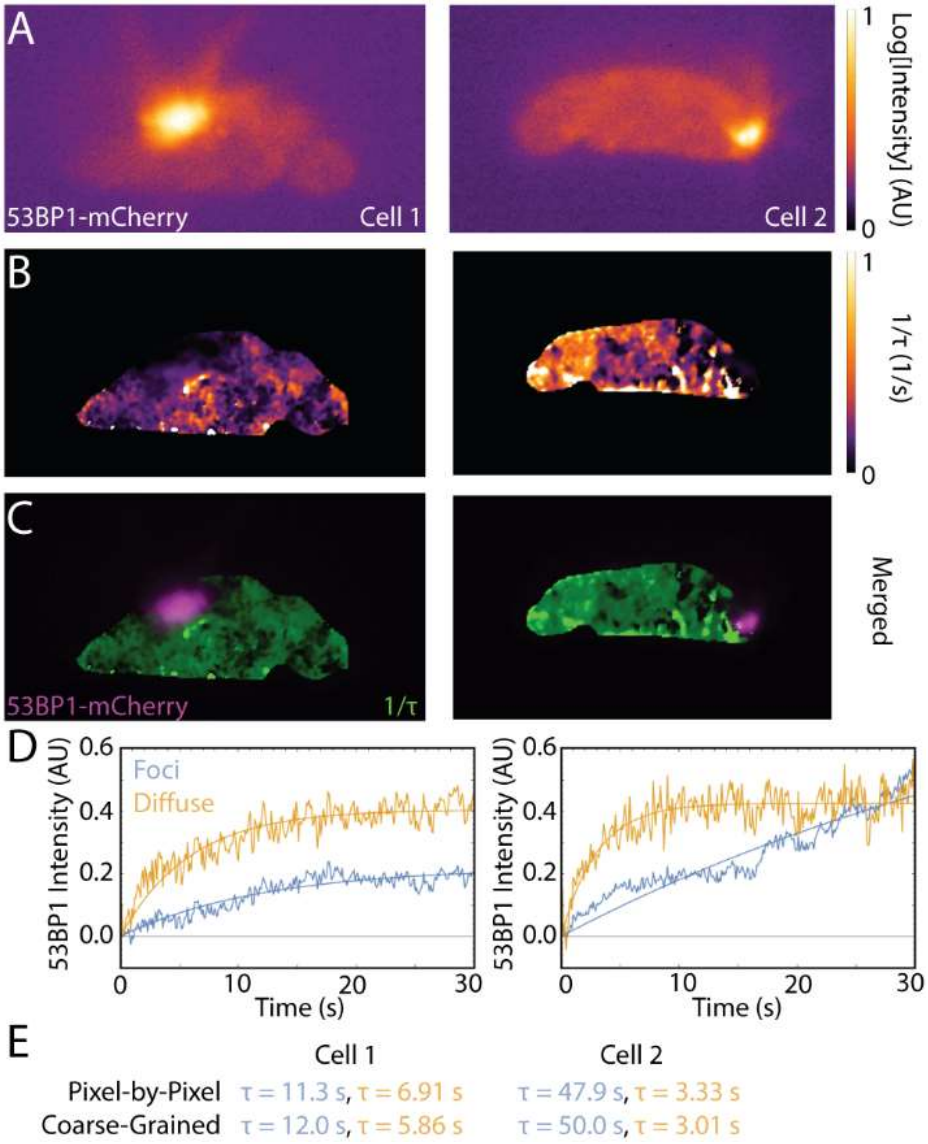

Figure 4.8: SPIM-FRAP of 53BP1-mCherry shows recovery is slowed at sites of DNA damage. (A) Side-view images of live MDA-MB-231 cells expressing 53BP1-mCherry, which is both diffusive in the nucleoplasm and concentrated at sites of DNA damage. (B) Maps of inverse recovery time for SPIM-FRAP of 53BP1-mCherry. (C) Merged maps of 53BP1-mCherry intensity and inverse recovery time. A correlation exists between the 53BP1 foci and longer recovery times. (D) A coarse-grained analysis of SPIM-FRAP shows the time series of 53BP1-mCherry after photobleaching. The second analysis also shows that recovery is slower in the 53BP1 foci. (E) A table of recovery times in the foci and diffuse 53BP1-mCherry as analyzed by pixel-by-pixel and coarse-grained methods.

4.7 Limitations of SPIM-FRAP

As with any advancement in methodology, there are accompanying limitations. One of the immediate drawbacks of SPIM-FRAP in its current implementation is in movement of the sample on the timescale of the recovery being measured. If the sample were to move into or out of plane, a false recovery would be detected (Figure 4.9). SPIM-FRAP with accompanying volumetric imaging can remedy this issue as one can monitor the bleached region even if it were to move in space; SPIM-FRAP with fixed plane imaging, however, is limited to measuring dynamics that are faster than cell morphodynamics and motility. Additionally, one must carefully consider the light sheet's depth-of-field, defined to be the length scale in the direction of propagation for which the light sheet has minimal dispersion. If the depth-of-field is comparable to the size of the sample, dispersion of the light could conflate the quantification. In our system, we are implementing a light sheet with a theoretical depth-of-field >10 μm [173] while the height of the nuclei is generally ~5 μm. Hence, our recovery maps do not show a systematic trend in the direction of propagation of the light sheet. Our vertical light sheet system allows us to utilize shorter light sheets. Investigators that use other geometries and types of light sheets must be cognizant of this upon implementation of SPIM-FRAP. That is, all the considerations associated with developing a SPIM system should also be accounted for when using SPIM-FRAP. Light sheets are also subject to striping artifacts (Figure 4.10), which could further complicate measurements or make them infeasible. Finally, the presented work presumes that the concentration of bright NLS-GFP fluorophores is effectively constant throughout the nucleus; this is not entirely the case. The distribution of NLS-GFP throughout the nuclear volume may not be constant, and this may have implications for our quantification. However, the variation of the distribution of NLS-GFP is far smaller than the variation induced by the photobleaching. This may not be true for all samples, and this should be considered in future experiments. Despite the aforementioned limitations of SPIM-FRAP, the benefits of resolving spatial heterogeneity with FRAP and the order of magnitude improvement of acquisition time relative to FCS prove useful for furthering the field of diffusion and protein dynamics.

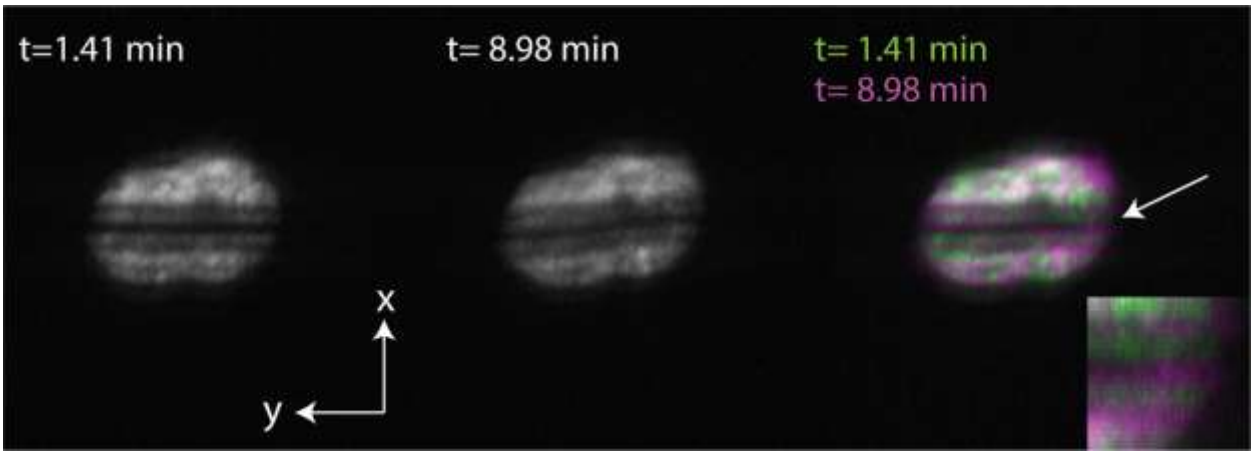

Figure 4.9: Maximum intensity projections of the reconstructed X-Y view of a live MDA-MB-231 nucleus expressing H2B-mCherry at different time points. *The* merged view shows the location of the bleached region moves in the x direction, which could conflate recovery measurements.

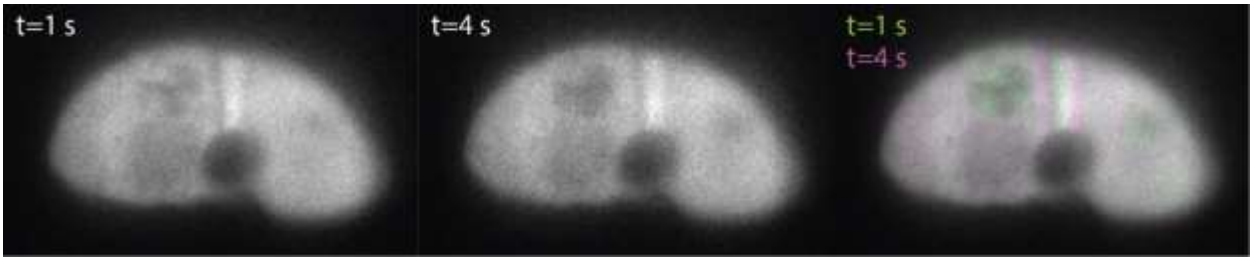

Figure 4.10: Selected images from an unsuccessful SPIM-FRAP experiment due to striping artifacts from the light sheet. The vertical stripe caused by the nucleolus shifts in time due to cell movement, making the recovery curves unusable.

4.8 Conclusions

We have presented a unique combination of SPIM and FRAP that proves useful for making simultaneous FRAP measurements for each pixel in a given 2D plane. This allows one to study heterogeneous diffusion and protein recovery on timescales ranging from milliseconds to hours. Such measurements were not previously accessible by traditional FRAP experiments and are an order of magnitude faster than FCS-based techniques. As with any development in methodology, SPIM-FRAP has limitations. However, we demonstrate that SPIM-FRAP can be used to track intranuclear diffusion of small molecules as well as the dynamics of DNA-damage repair proteins. The recovery times of NLS-GFP show heterogeneity across the whole nucleus that is uncorrelated with histone density. Intranuclear diffusion of NLS-GFP also seems to be independent of chromatin compaction levels, pointing to other possible sources of heterogeneous distribution such as intranuclear liquid-liquid phase separation,

variable concentration of macromolecules, or binding of NLS to RNA. However, the recovery times of NLS-GFP are well correlated with nucleoli and exhibit slowed diffusion in nucleoli relative to the nucleoplasm, likely due to phase separation between the two mediums. We have also shown through a 1D diffusion simulation that SPIM-FRAP produces diffusion coefficients that are consistent with previously reported values. Recovery time maps of 53BP1-mCherry were also able to show how DNA damage foci are more stable than diffuse repair proteins. SPIM-FRAP is poised to be immediately implemented on almost any light sheet microscope with minimal software development, making it a new tool for biologist to study not only the timescales and magnitudes of protein turnover and diffusion, but the spatial distributions as well.

4.9 Specific Materials and Methods

4.9.1 Cell Culture and Sample Preparation

Two MDA-MB-231 cell lines, transfected with NLS-GFP and either H2B-mCherry of 53BP1-mCherry, were generous gifts from the Lammerding Lab (Cornell University). Complete transfection protocols and reagents can be found in prior publication [69]. Cells were cultured in DMEM/F12 with 10% FBS (Sigma-Aldrich) and 1X antibiotic antimycotic (Gibco) without phenol red. The media has 15 mM Hepes buffer which helps stabilize the pH during experiments. One day before the experiment, 50-70% confluent cultures were trypsinized and plated on polyacrylamide gels such that only 1-3 cells were present per field of view at 60x magnification. Polyacrylamide gels were used in order to eliminate reflections during side-view imaging. Production details of PA gels are given in Chapter 2. PA gels were coated with rat tail collagen to ensure sufficient cell spreading.

For treatment with Trichostatin-A (TSA), TSA was dissolved to 10 mM in DMSO, and then serially diluted in PBS to 4 µM on the day of treatment. 10 µL of the 4 µM solution in PBS was then added to the cells as they were growing in 190 µL of media in 10 mm cloning cylinders, for a final concentration of 200 nM. Experiments were carried out 24-28 hours after drug addition. The 2×10^(-5) dilution of DMSO, giving 0.002% v/v final concentration was judged to be insignificant to the TSA effect. To challenge the cells with osmotic compression (OC), we prepared a solution of 1.8 osM sorbitol (Fisher Scientific) in our

DMEM/F12 medium, and added it 1:1 (v/v) to the cells on the microscope. This gave a 4-fold increase in osmolarity.

4.9.2 Image Acquisition and Analysis

Live MDA-MB-231 cells co-expressing either NLS-GFP and H2B-mCherry or NLS-GFP and 53BP1-mCherry were plated on 55 kPa polyacrylamide gels one day prior to examination on our custom light sheet microscope [173]. We utilized vertical light-sheet based illumination and side-view imaging via a reflective prism adjacent to a cell of interest to first collect side-view (Y-Z) light-sheet fluorescence images. For cells expressing H2B-mCherry, we first collected one image of the H2B at an exposure time of 200 ms. We then collected 100 images of the NLS with a 5 ms exposure time and 5 ms readout time (40 ms exposure and 10 ms readout for OC experiments because of the markedly slower recovery times). At this point, a single Y-Z sheet was bleached for 100 ms with high-intensity 488 nm light. Immediately after the vertical sheet was bleached, an additional 300 images of the NLS were collected at the same exposure and readout time. The laser power was measured to be 1.50 ± 0.03 mW for the bleach pulse and 53.3 ± 0.7 μW for the standard image acquisition. For SPIM-FRAP experiment of 53BP1-mCherry, the same protocol as above was executed with a 561 nm laser, a bleach time of 1 s, and an imaging rate of 10 Hz.

Image sequences were loaded into FIJI [250], and the first image was used to generate a mask of the nucleus as described in our previous work [14]. The image sequence was subsequently blurred using a 1-pixel Gaussian blur. All further analysis is performed in Wolfram Mathematica 11.2. The first 100 images were used to correct the time series for photobleaching via an exponential bleach correction. This photobleaching correction was applied to all images in the time series and was not performed on a pixel-by-pixel basis but rather uniformly across the whole image. There is potential for the photobleaching to be spatially dependent along the axial direction due to dispersion of the light sheet, however this effect is negligible in our work as our imaging conditions seek to minimize photobleaching and the depth of field of the light sheet is greater than the height of the nuclei. For each pixel in the mask of the nucleus, an exponential recovery curve of the

form

$$I(t) = A + B\left[1 - \mathrm{Exp}\left[-\frac{\mathrm{t}}{\tau}\right]\right] \quad (4.1)$$

was fit to the first 200 intensity values of that pixel immediately after the bleaching step. From each curve, we extracted both the characteristic recovery time, τ, as well as the recovery percentage, $\frac{B}{I_{pre\,bleach} - I_{min}}$.

Finally, we sought to verify the geometry of our photobleaching. To do so, we photobleached a single plane of a live MDA-MB-231 nucleus expressing H2B-mCherry. H2B has a recovery time on the order of hours for mammalian cells [262], so this sample was chosen such that we could observe the bleached region without concern for it recovering too quickly. After photobleaching a single plane, we collected volumetric images with our custom SPIM microscope (Figure 4.1). We observed a clear photobleached plane through the center of the nucleus as well as slight photobleaching from the concentric side lobes characteristic of a Line Bessel Sheet. These side lobes are accounted for in our diffusion simulation. We did not observe any significant bleaching outside of the light sheet region due to scattered light. This demonstrated that photobleaching with a light sheet, and subsequently SPIM-FRAP, is indeed a reliable and reproducible technique.

4.9.3 SPIM-FRAP Simulation

To validate our analysis protocol, we simulated SPIM-FRAP experiments based upon our experimental measurements (Figure 4.2). Simulated data sets were generated by first calculating the mean and standard deviation of both the recovery time and recovery percentage as well as the standard deviation of the plateaued recovery curve. For a given nucleus, the NLS image immediately after the bleach pulse was used as the starting image. Each pixel was prescribed an exponential recovery (Eq. 4.1) with a specified recovery time and recovery percentage based upon the mean of the experimental data. We simulated 3 conditions to isolate the contribution of each aspect of our analysis pipeline. First, we added noise to the simulated recovery based on the noise in the experimental data and fit an exponential recovery curve to each pixel. Next, we added a 1-pixel Gaussian blur along with the additional noise before fitting the recovery. Note that this serves to tighten the distribution of recovery times at the cost of spatial resolution. Finally, we added a predetermined spatial pattern of the recovery

times in the form of 5x5 pixel squares with recovery times 20% lower than the rest of the pixels. We were able to clearly discern this structure after the addition of noise and Gaussian blurring. That is, the prescribed 20% change is well above the noise floor of our technique. These simulations can be compared to the experimental data set to validate the heterogeneity present in the maps of recovery times.

4.9.4 Diffusion Simulation Theory

Traditionally, FRAP experiments use simple bleaching geometries and minimize bleaching times in order to use analytical models to convert recovery time to a diffusion coefficient [240]. Our light sheet microscope employs a Line Bessel Sheet (LBS), which features additional side lobes concentric to the main central lobe [173]. This prevents us from applying any model with a simplified geometry. Furthermore, our bleach time of 100 ms is on the order of the measured recovery time. This means that we must account for diffusion occurring during the bleach pulse itself. To understand how our measured recovery times corresponded to diffusion coefficients, we computationally modeled diffusion in our system. The full three-dimensional diffusion equation is given by

$$\frac{\partial \phi(\vec{r},t)}{\partial t} = \nabla \cdot [D(\phi,\vec{r})\, \nabla \phi(\vec{r},t)] \tag{4.2}$$

where $\phi(\vec{r},t)$ represents the concentration of bright molecules as a function of space and time, and $D(\phi,\vec{r})$ represents the diffusion coefficient as a function of concentration and space. We next describe the assumptions of the simulation and the justification for each assumption that is made.

Assumption 1: $D(\phi,\vec{r}) \approx D(\vec{r})$. Justification: First, the concentration of NLS-GFP in the nucleus is effectively uniform, so there is little variation in ϕ which subsequently means there is little change in D due to variation in ϕ. Additionally, the concentration is that of dark versus bright molecules. Whether or not the molecules are fluorescing has no physical bearing on the local diffusion coefficient and therefore $D(\vec{r})$ is effectively independent of ϕ. It is important to note that this assumption may not hold true for all experiments, and care should be taken in considering this assumption when implementing SPIM-FRAP simulations for other studies. By removing the dependence of D on ϕ, we find that

$$\frac{\partial \phi(\vec{r},t)}{\partial t} = \nabla \cdot [D(\vec{r})\, \nabla \phi(\vec{r},t)]. \tag{4.3}$$

Expanding $\nabla\phi(\vec{r},t)$ in Eq. 4.3 gives

$$\frac{\partial\phi(\vec{r},t)}{\partial t} = \nabla\cdot\left[D(\vec{r})\left[\partial_x\phi(\vec{r},t)\hat{x} + \partial_y\phi(\vec{r},t)\hat{y} + \partial_z\phi(\vec{r},t)\hat{z}\right]\right]. \tag{4.4}$$

Continuing to expand the right-hand side of Eq. 4.4 gives that

$$\frac{\partial\phi(\vec{r},t)}{\partial t} = \partial_x[D(\vec{r})\partial_x\phi(\vec{r},t)] + \partial_y\left[D(\vec{r})\partial_y\phi(\vec{r},t)\right] + \partial_z[D(\vec{r})\partial_z\phi(\vec{r},t)]. \tag{4.5}$$

Finally, further expansion of Eq. 4.5 yields

$$\begin{aligned}\frac{\partial\phi(\vec{r},t)}{\partial t} = {} & \partial_x D(\vec{r})\partial_x\phi(\vec{r},t) + \partial_y D(\vec{r})\partial_y\phi(\vec{r},t) + \partial_z D(\vec{r})\partial_z\phi(\vec{r},t) \\ & + D(\vec{r})\left[\partial_x^2 + \partial_y^2 + \partial_z^2\right]\phi(\vec{r},t).\end{aligned} \tag{4.6}$$

Assumption 2: $\partial_x D(\vec{r}) \approx \partial_y D(\vec{r}) \approx \partial_z D(\vec{r}) \approx 0$. Justification: We observe changes in the diffusion coefficient on the order of only a factor of two across the entire nucleus, meaning the local changes in the diffusion coefficient are negligible. By considering assumption 2 in Eq. 4.6, we find

$$\frac{\partial\phi(\vec{r},t)}{\partial t} = D(\vec{r})\left[\partial_x^2 + \partial_y^2 + \partial_z^2\right]\phi(\vec{r},t). \tag{4.7}$$

Assumption 3: $\partial_y\phi(\vec{r},t) \approx \partial_z\phi(\vec{r},t) \ll \partial_x\phi(\vec{r},t)$. Justification: The primary plane of symmetry being broken is that of the x direction because the bleached pattern forms a y-z sheet. Diffusion in the y and z directions will then cause a far smaller change in concentration than diffusion in the x direction. This may not hold true for samples with larger spatial heterogeneity than NLS-GFP, which would subsequently require more detailed modeling. Additionally, this assumption could be compromised if there is significant dispersion of the light sheet across the sample. Accounting for assumption 3 in Eq. 4.7 then gives

$$\frac{\partial\phi(\vec{r},t)}{\partial t} = D(\vec{r})\,\partial_x^2\phi(\vec{r},t). \tag{4.8}$$

Initial Conditions: $\phi(\vec{r},0) = 1 - LS(\vec{r})$ where $LS(\vec{r})$ represents the normalized, theoretical profile of the light sheet.

Bleaching Conditions: $\tilde{\phi}(\vec{r},0) = \phi(\vec{r},\delta t) * (1 - LS(\vec{r}))$. That is, Equation 4.8 was iteratively solved during the bleaching time and at each iteration the concentration was multiplied by the inverse profile of the light sheet. The new concentration profile was then used as the initial condition for the next iteration. It was assumed that the peak intensity of the light sheet was just sufficient to entirely bleach the sample. This was an assumption of the model and could be adjusted through multiplication by a scaling factor to either increase or decrease the effect of the light sheet during the bleaching phase. However, the observed

recovery percentages (Figure 4.1C) were consistent with the simulated recovery percentages (Figure 4.6C), and therefore the current scaling factor of 1 was appropriate for our simulation. The simulated bleaching also allowed for saturation.

Boundary/Normalization Conditions: $\int \phi(\vec{r}, t > t_B)dx = constant$. That is, once the bleaching has stopped, the total concentration of bright molecules remained constant.

CHAPTER 5: CELL NUCLEAR MECHANICS[4]

Chapters 2 and 3 described our VIEW-MOD and AFM-LS systems and the specific advantages it has in studying nuclear mechanobiology. In Chapter 5, I use this AFM-LS system to address two outstanding questions in the literature. How do chromatin and lamin A/C contribute *separately* in nuclear compression? Can DNA damage be incurred due to localized compression independent of nuclear rupture? I show here how chromatin and lamins dictate the force response at small and large indentations respectively, and further that chromatin – and not lamins – is relevant for regulating nuclear curvature during compression. Additionally, I show how AFM compression alone is sufficient to induce DNA damage in nuclei, contrary to previous work highlighting nuclear rupture as the predominant means of mechanically inducing DNA damage. Neither of these conclusions and studies were possible without the techniques previously describ3d, making this chapter a sufficient contribution to the literature in terms of both nuclear mechanobiology itself as well as the advantages of coupled advanced microscopy and force probes.

5.1 Introduction

The nucleus – which encapsulates and protects the entire genome – functions not only as the site of gene replication and transcription, but also as a fundamental mechanical constituent of the cell. As previously mentioned, altered nuclear mechanics and nuclear morphology have both been linked to various disease states ranging from Hutchinson-Gilford Progeria Syndrome (HGPS) [74, 136, 263] and Emery-Dreifuss muscular dystrophy [60, 263, 264] to breast cancer [263, 265]. Such diseased cells are often under stress either through external means such as cellular migration [5, 67] or intracellular forces like that of actin pre-stress [33], which has been shown to be sufficient to cause nuclear rupture [33, 266].

[4]Portions of this chapter are previously published in Hobson, C. M., et al. (2020). "Correlating nuclear morphology and external force with combined atomic force microscopy and light sheet imaging separates roles of chromatin and lamin A/C in nuclear mechanics." Mol Biol Cell: mbcE20010073 and Shah, P., et al. (2020). "Nuclear Deformation Causes DNA Damage by Increasing Replication Stress." Curr Biol.

Little work, however, has studied either the dynamic relationship between external forces and nuclear morphology or the role of nuclear mechanical constituents in this relationship. To fully understand the complex connections linking nuclear mechanics and morphology with disease and cellular function, we must first understand the intermediate relationship of how nuclear mechanical constituents resists external forces to maintain morphology.

Nuclear mechanics are primarily dictated by the nuclear lamina and chromatin, as well as indirectly influenced by the cytoskeleton [12]. The cytoskeleton protects the nucleus both through an actin cap [22, 31, 32] and a peri-nuclear cage of the intermediate filament vimentin [21, 24, 267]. The nuclear lamina, primarily lamin A/C, has consistently been shown to be a major mechanical constituent of the nucleus through constricted migration, micropipette aspiration, atomic force microscopy, micromanipulation, and other techniques [13, 18, 21, 23, 41, 44, 45, 60, 75, 76, 268]. Furthermore, understanding of chromatin's role as a mechanical element of the nucleus continues to be refined. Through examining swollen *Xenopus* oocyte nuclei, it was first thought that chromatin had little role in the mechanical properties of nuclei [75]. Additional work, however, revealed that chromatin indeed does contribute to nuclear stiffness, and that (de)compaction of chromatin leads to nuclear (softening) stiffening [13, 45, 48, 50, 51, 76, 83, 269-271]. The specific roles of chromatin and lamin A/C in nuclear mechanics have begun to be disentangled, as micromanipulation experiments have shown that chromatin dominates small extensions while lamin A/C dominates large extensions [13]. Both the mechanical constituents of the nucleus – the nuclear lamina and chromatin – as well as the cytoskeleton are paramount for protection of the genome and subsequently cellular function.

Directly related to the mechanical properties of nuclei is nuclear morphology; this is in general characterized by nuclear volume and nuclear surface area – or the more experimentally accessible 2D surrogates of nuclear cross-sectional area and nuclear perimeter respectively – as well as local curvature. Nuclear morphology also relates to nuclear abnormalities and/or blebs displayed across the spectrum of human disease [12]. However, here we are primarily concerned with morphology in regards to general nuclear shape. A variety of metrics have been used to quantify changes in nuclear morphology, such as area strain (percent change in projected cross-sectional area) [272] and 3D irregularity (ratio of excess volume of a fitted convex hull to nuclear volume) [265]. Aside from the previously noted connections to

disease, nuclear morphology has further been linked to levels of transcriptional activity as nuclei with reduced volume enter a more quiescent state [35]. Increases in the volume of nuclei either through swelling [125] or directed migration on patterned substrates [273] has been shown to decondense or dilate chromatin levels. Stretching of the nuclear surface area is thought to be a mechanism of nuclear mechanotransduction [94, 274]. Nuclear morphology is also characterized in part by local curvature; regions of high local curvature have been linked to nuclear rupture [47] and nuclear blebs [270, 275]. Nuclear morphology is directly related to both the mechanical integrity of the nucleus as well as nuclear and cellular function.

Previous work has used changes in nuclear morphology under force application as a metric for mechanical resistance [21, 22]; that is, smaller changes in nuclear morphology imply a stiffer nucleus. Nuclear morphology has also been used in studying stored elastic energy [265] and pressure gradients [276, 277]. Investigators have further developed an analytical model connecting nuclear morphology to external forces and mechanical properties for an idealized geometry [46]. However, a majority of work regarding nuclear mechanics is either agnostic to nuclear shape or focuses on a highly specific model of a single technique. For example of the former, atomic force microscopy (AFM) studies of nuclei have traditionally used a Hertzian contact mechanics model, which models the nucleus as a linearly elastic, isotropic, homogeneous material under small indentation [278]. Previous work, however, has shown the nucleus to be both nonlinear [13] and anisotropic [22]. While Hertzian analysis has brought to light many novel insights, it is limited by its ability to decouple contributions of specific structures. More intricate computational models have given direct insight into many mechanical techniques, including constricted migration [66], micropipette aspiration [279], magnetic bead twisting [59], plate compression [280], micromanipulation [13, 281], and atomic force microscopy [42]; however, their specificity inhibits extrapolation of their conclusions. There exists a need for an intermediate understanding of nuclear deformation that informs both the relative contributions of the various nuclear mechanical constituents as well as their roles in protecting against specific deformations to nuclear morphology.

Furthermore, there is a growing body of work that seeks to understand the coupling of mechanical forces and DNA damage. Previous reports using both AFM and constricted migration assays have shown conclusively that rupture of the nuclear envelope leads to DNA damage primarily through

cytoplasmic nucleases entering the nucleus and cleaving DNA [47, 67, 69, 71]. However, there are still outstanding questions regarding if nuclear rupture is entirely necessary for DNA damage to occur. One group has posed a model for such a process where segregation of mobile DNA damage repair proteins from the chromatin via nuclear constriction leads to DNA damage because of a shift in the balance of naturally occurring breaks and repairs [282]. This is backed by experimental evidence that such segregation of mobile proteins occurs in live cells [62]. Understanding the mechanisms – either chemical or mechanical – by which DNA damage can occur is crucial for understanding genetic mutations, cell migration, and cancer metastasis.

In this chapter, we address some of these open questions regarding the links between mechanics, morphology, and DNA damage through use of our combined atomic force microscope and side-view light sheet microscope (AFM-LS) [172]. Our approach allows us to visualize cells from the side (x-z cross section) with high spatiotemporal resolution during compression with an atomic force microscope. We use this technique to correlate changes in apparent SKOV3 nuclear volume and nuclear surface area with applied force to develop an empirical model for nuclear deformation, which has applications for assays beyond our own technique and is applicable to non-standard nuclear shapes. This allows us to disentangle the contributions of chromatin and lamin A/C to strain in nuclear volume and nuclear surface area, respectively, an insight not possible with previous AFM models and techniques. We also measure the dynamics of nuclear curvature under compression, and show that chromatin decompaction reduces curvature at the site of indentation; this indirectly shows the nucleus behaves as a two-material system. Furthermore, use our AFM-LS to study the role of compressive forces in DNA damage independent of nuclear rupture as well as characterize the mechanical properties of various cells lines in different stages of the cell cycle. In summary, we provide the first decoupling of the role of chromatin and lamin A/C in nuclear compression, new insight into the connection between external forces, nuclear mechanical constituents, and nuclear shape and curvature, and a highlights a novel mechanism of DNA damage.

5.2 Strain-Stiffening During Nuclear Compression

Our combined atomic force microscope and side-view light sheet fluorescence microscope (Figure 5.1A) allows visualization of the dynamics of cellular deformations in the plane of applied force while simultaneously monitoring the force response of the cell [172]. We have previously used this tool to show the existence of separate elastic moduli correlated with whole-cell and nuclear deformations [144]. We built on this previous work by studying the dynamics of nuclear morphology and the correlated force response under compression by AFM. We examined time series of side-view images of compressed, live SKOV3 cells stably expressing Halo-tagged histone 2B (H2B, green) and SNAP-tagged K-Ras-tail (magenta) labeled with Janelia Fluor (JF) 549 and 503 respectively (Figure 5.1B). Masks of nuclei were generated (see Materials and Methods) and used to extract both nuclear cross-sectional area ($NCSA$, blue) and apparent nuclear perimeter (NP, orange) as a function of indentation (Figure 5.1B). As in prior studies, we used $NCSA$ and NP as surrogates for nuclear volume and nuclear surface area respectively as the qualitative deformation of the nucleus is the same in any side-view orientation [125]. The AFM provided synchronized force data with approximately 20 pN resolution during the side-view image acquisition (Figure 5.1C). It should be noted that our measurements of apparent nuclear perimeter are not necessarily the same as measuring the perimeter of the nuclear envelope. The nucleus is not a closed system in general; the outer nuclear membrane is contiguous with the endoplasmic reticulum [283] and therefore could add length upon indentation. Furthermore, the nuclear envelope could have undulations that are smoothed out upon compression, similar to previously reported results [284, 285]. Our analysis of nuclear shape is then more aligned with the shape of the contents of the inner nuclear membrane – that is, primarily the nuclear lamina and the chromatin – which are the primary mechanical constituents of the nucleus. However, previously reported results show in micropipette aspiration studies that strain occurs in both the nuclear lamina in human embryonic stem cells [76] and the nuclear envelope in *Xenopus* oocyte nuclei [75].

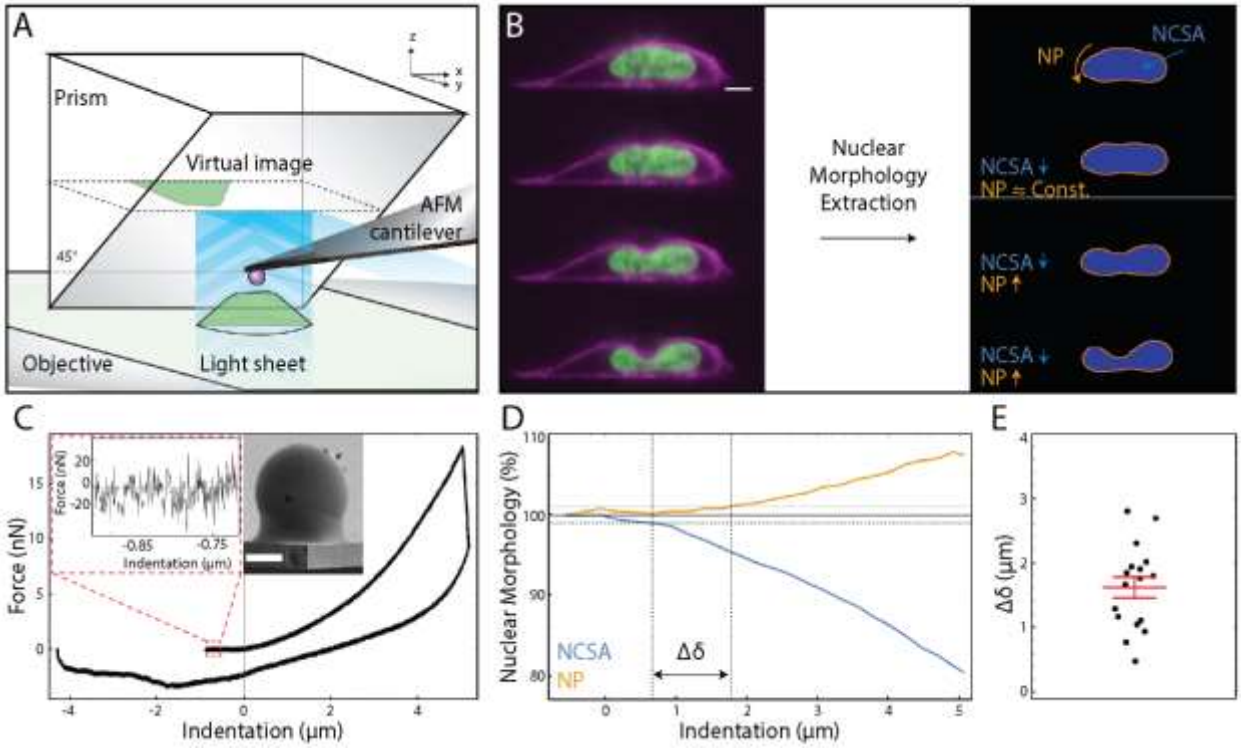

Figure 5.1: Combined atomic force microscopy and side-view light sheet microscopy (AFM-LS) extracts dynamics of nuclear morphology and applied force under whole-cell compression. (A) Cartoon schematic of our AFM-LS system. A full description is provided in our previous work. (B). A subset of fluorescence images collected by our AFM-LS during indentation of a live, SKOV3 cell (scale bar = 5 μm). The cell is stably expressing snaptagged KRas-tail (Magenta) and halotagged H2B (Green) labeled with Janelia Fluor 503 and 549 respectively. Custom workflow (see methods) allows for extraction of nuclear perimeter (NP) and nuclear cross-sectinoal area ($NCSA$). (C) Force versus indentation data for the previously displayed compression experiment. Left inset provides a scale for the noise in the force data. Right inset shows a scanning electron microscope image of a bead glued to the end of an AFM cantilever (see methods). Beads are nominally 6 μm in diameter; this bead was measured to be 5.4 μm in diameter (scale bar = 2 μm) (D) Nuclear morhpology as a percentage versus indentation for the previously displayed compression experiment. Orange and blue represent NP and $NCSA$ respectively. $\Delta\delta$ is defined to be the difference in indentation at which NP and $NCSA$ reach 1% change. (E) $\Delta\delta$ for n = 17 separate compression experiments. The red bar represents the standard error in the mean. See also Video 5.1.

We first observed that $NCSA$ and NP underwent strain at different levels of indentation (Figure 5.1D). We determined this difference in the onset of $NCSA$ strain and NP strain by linearly interpolating the $NCSA$ and NP indentation series and computing the difference in indentations at which $NCSA$ and NP reached 1% strain, denoted by $\Delta\delta$. This was chosen because 1% strain is a point reached in all data sets used in analysis and is far enough above the noise of the nuclear morphology data to confidently indicate a change. The onset of strain in $NCSA$ and NP differ by $\Delta\delta$ = 1.6 ± 0.7 μm (mean ± standard deviation of indentation), which is clearly greater than zero. This indicates the presence of two distinct and separate regimes for strain onset of nuclear surface area and nuclear volume (Figure 5.1E). Moreover, this implies

that the apparent nuclear surface area to volume ratio does not follow one simple scaling relationship under AFM compression. Whether the outer nuclear membrane itself is adding length, smoothing out undulations, or physically stretching, however, is not distinguished.

Nuclear volume has been shown to be directly correlated with transcriptional activity. In one study, NIH3T3 mouse fibroblasts cultured on fibronectin patterned coverslips were uniformly compressed with an additional weighted coverslip. This resulted both in an increase in chromatin condensation as well as a decrease in nuclear volume, both of which correlated with the subsequent reduction in transcriptional activity [35]. Separately, a migration assay has been used to show that transcription activity is altered as a result of introducing a constriction to the migration pathway [286], which can decrease nuclear volume. Through showing chromatin is partially responsible for resisting nuclear volume strain and coupling this result with previous studies regarding nuclear volume and function, we conjecture that the mechanical properties of chromatin aid in regulating its own condensation and transcriptional activity. We further see that the nucleus is susceptible to volume changes at low levels of indentation, meaning these downstream effects of volume change can occur as a result of intracellular forces.

Stretching of the nuclear surface, however, has different implications for nuclear function and mechanotransduction [94]. The nucleus is a mechanosensor that can covert mechanical signals at the cell surface into chemical responses [90]. This physical connection from integrins to the nucleus through the cytoskeleton, the LINC complex, and the nucleus was first shown by pulling fibronectin-coated micropipettes attached to the cell surface [26]. It was later shown that by twisting fibronectin-coated magnetic beads attached to the cell surface, one could induce stretching of chromatin and subsequent upregulation of transcription activity [29]. The distribution of stresses along the nuclear lamina is believed to be the primary mechanism responsible for such responses [94], which has led to the hypothesis of stretch-activation along the nuclear envelope [274]. By connecting expression levels of lamin A/C to resistances to change in nuclear surface area and consequently the nuclear stretch modulus, we have shown the relevance of lamin A/C to mechanoresponses governed by stretches in the nuclear envelope. Interestingly, we observe such nuclear surface area stretches only at large deformations. This implies that the nuclear lamina is relevant primarily for processes such as cellular migration or joint compression, and

that the mechanoresponses associated with nuclear envelope stretches are not likely to happen outside of such processes that cause macroscopic, whole-cell deformations.

5.3 Scaling Relationships Between Nuclear Morphology and Applied Force

Previous research has shown both a two-regime force response upon stretching nuclei with flexible micropipettes [13] as well as the necessity of a term accounting for the stretching of nuclear surface area to explain non-linear osmolarity of the nucleus [277]. This work and our results showing distinct indentations thresholds for nuclear volume and surface area strain led us to hypothesize the existence of a two-regime force response resulting from separate forces associated with changes in nuclear volume and nuclear surface area.

To test this hypothesis, we first examined the scaling relationship between applied force from the AFM, F_{AFM}, and $\Delta NCSA$ ($NCSA_{Max}$ - $NCSA$); note that $\Delta NCSA$ is positive for a decrease in $NCSA$. We observed a clear, two-regime force response wherein applied force scales with $\Delta NCSA$ to different powers in each regime (Figure 5.2A). This phenomenon was seen in all but one cell examined (n=17 cells examined total). To determine the scaling relationships between external force and $\Delta NCSA$, we fit two separate power law relationships between force and $\Delta NCSA$ – one before and one after the transition point. The transition point between fitting regimes was allowed to vary to minimize error in the power law fits in both regimes. The exact transition point was determined to be the point at which the two power law relationships intersect.

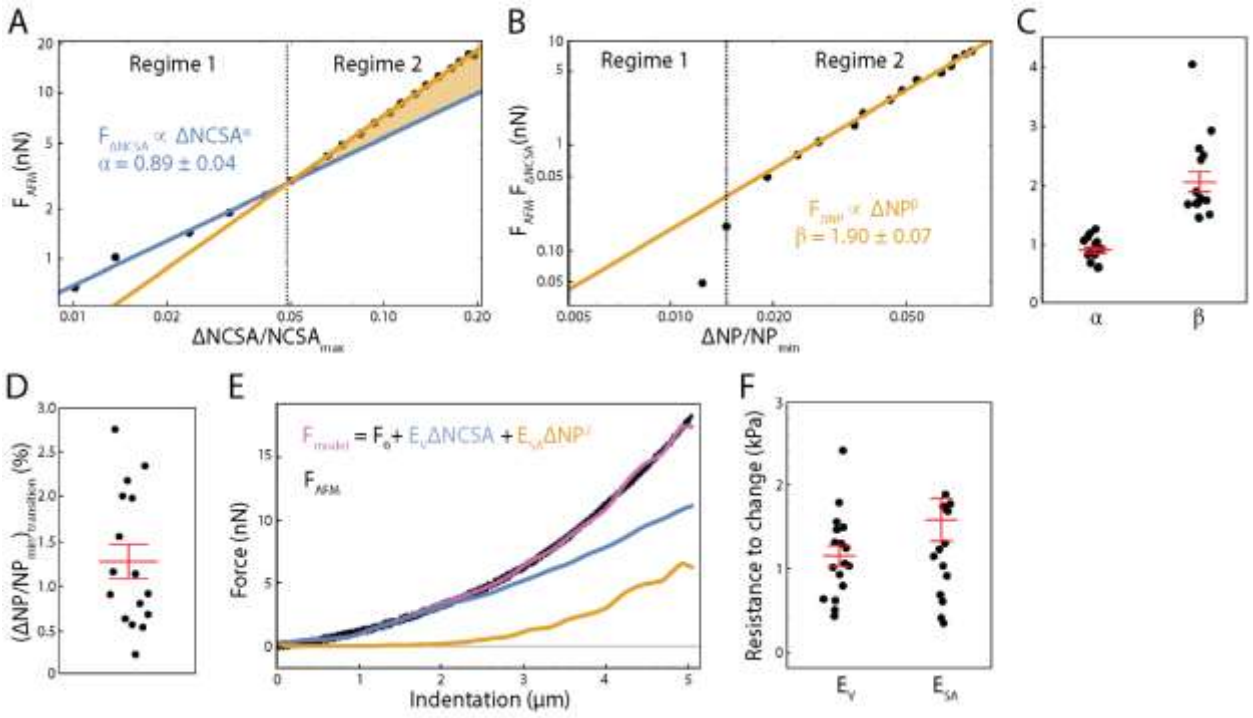

Figure 5.2: Correlating nuclear morphology and applied force informs an emperical model for strain stiffening response. (A) Force as recorded by the AFM versus change in $NCSA$ plotted on a log-log scale. Two distinct power-law regimes are observed. (B) Force as recorded by the AFM minus the force response in regime 1 plotted against changed in NP on a log-log scale, showing a single power law relationship in regime 2. (C) α, the exponent for $F_{\Delta NCSA}$, and β, the exponent for $F_{\Delta NP}$, as determinded for n = 16 cells. Red bars represent mean and SEM. (D) The strain in NP at the transition point between regime 1 and regime 2 as determined for n = 16 cells. Red bars represent mean and SEM. (E) An emperical model for nuclear deformation as shown over force versus indentation. We display our full emperical model (magenta), the individual contributions required to deform the nuclear volume and surface area (blue, orange respectively), and the AFM data over the full indentaiton. (F) Resistance to nuclear volume change, E_{V}, and resistance to nuclear surface area change, E_{SA}, as determined for n = 17 cells. Red bars represent mean and SEM.

Knowing that at small indentations we only observed strain in $NCSA$ (constant nuclear surface area) indicates that regime 1 immediately provided us a scaling relationship between external force and $\Delta NCSA$. That is, we defined a force associated with $\Delta NCSA$ given by $F_{\Delta NCSA} \propto \Delta NCSA^{\alpha}$ (Blue line, Figure 5.2A). Under the assumption that the aforementioned relationship was unchanged during indentation, we subtracted $F_{\Delta NCSA}$ from F_{AFM} to isolate the additional force response resulting from strain in NP (Yellow shaded region, Figure 5.2A). We then plotted this additional force response against ΔNP ($NP - NP_{Min}$) where we observed a constant power law relationship in regime 2 (Yellow line, Figure 5.2B). We then defined a separate force required to stretch the nuclear surface area given by $F_{\Delta NP} \propto \Delta NP^{\beta}$. Performing

this analysis on n=16 cells allowed us to determine that $\alpha = 0.9 \pm 0.2$ and $\beta = 2.1 \pm 0.7$ (mean ± standard deviation, Figure 5.2C).

Previous work, however, has modeled the nucleus as having a strain-dependent elastic modulus [42], which could provide an alternate explanation of the origin of the two-regime phenomenon we have observed. To differentiate the two explanations, we examined the transition point as a function of ΔNP. The transition point between the two regimes corresponded to 1.2% ± 0.8% (mean ± standard deviation) change in NP (Figure 5.2D), meaning the force response in regime 1 correlated only with strain in $NCSA$ while the force response in regime 2 correlated with both strain in $NCSA$ and NP. This correlation between the onset of regime 2 and the onset of strain in ΔNP provided support to our hypothesis that the two regimes are a result of separate forces required to deform the volume and surface area of the nucleus. With the combination of this result and our determination of the specific scaling relationships between applied force and both $\Delta NCSA$ and ΔNP, we then posed the following empirically-determined model to correlate nuclear deformation with applied force.

$$F = F_0 + E_V(\Delta NCSA) + E_{SA}(\Delta NP)^2 \tag{5.1}$$

Here, F_0 represents any force response accumulated prior to deformation of the nucleus. Our interpretation is that F_0 is a result of compressing the space between the plasma membrane and nuclear membrane, comprised of the cytosol and cytoskeleton. E_V and E_{SA} are the effective mechanical resistance the cell provides to changes in nuclear volume and nuclear surface area respectively, as represented by $NCSA$ and NP. These resistances are composed of contributions from not only the nucleus, but also from the cytosol, internal pressure gradients, the cytoskeleton, the actin cortex, and other cellular structures. However, the nucleus has been shown to be the stiffest sub-cellular structure and also encompasses a majority of the strain during compression, implying that E_V and E_{SA} are primarily dictated by the mechanical properties of the nucleus. Our results are consistent in that F_0 is on the order of 100 pN, implying there is minimal force response prior to deformation of the nucleus. They also inherently include viscous contributions as there is no time scale built directly into our model and our AFM measurements are not fully quasistatic (Figure 5.3). Indenting at higher (lower) rates would then increase (decrease) our

measured values of E_V and E_{SA}. While not studied here, this decomposition provides the opportunity to study the relative viscous contributions associated with strain in $NCSA$ and NP. A single value of E_V and E_{SA} are determined by fitting the Equation 1 to the entire indentation of each cell (Figure 5.2E and F). Furthermore, this model and observe two-regime force response holds true for nuclei lacking pre-tension, as determined by performing the same experiment on more rounded cells induced by a reduction of adhesion to the substrate (Figure 5.4).

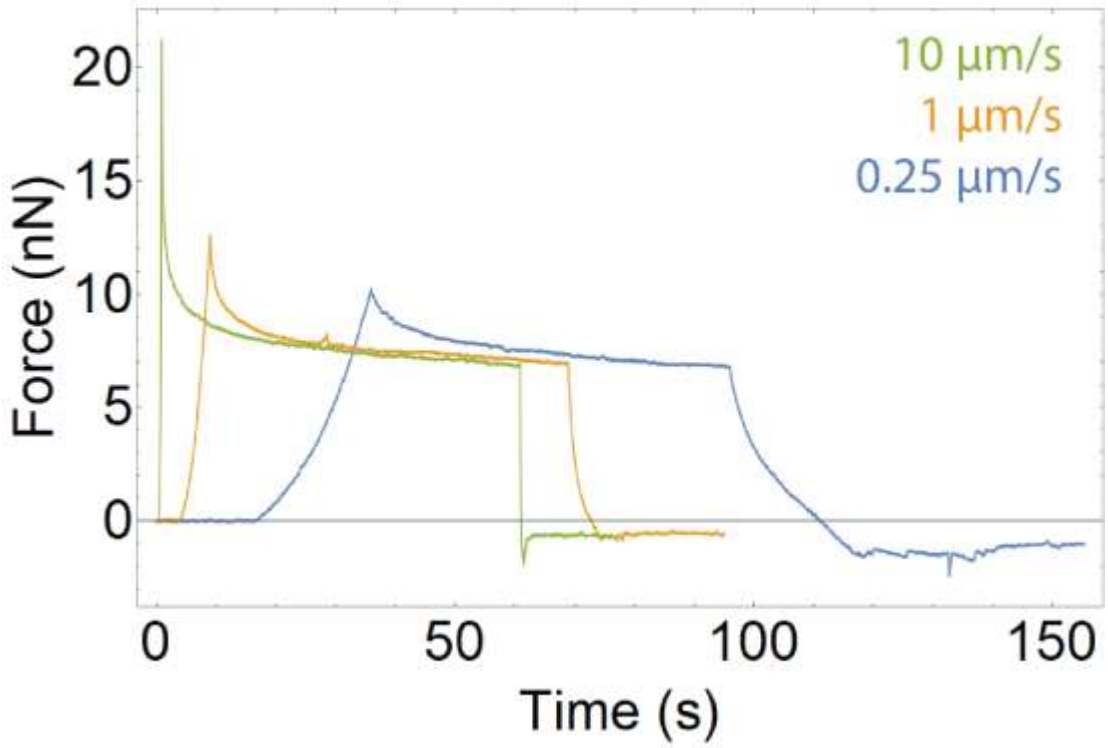

Figure 5.3: Force versus time plot for three different AFM indentation and retraction rates (10 µm/s – Green, 1 µm/s – Orange, 0.25 µm/s – Blue). All AFM parameters asides from the indentation and retraction rate remained constant. For each compression, the cantilever was lowered a prescribed distance at the given rate, and then the z piezo was held fixed for 60 seconds. The cantilever then retracted at the same rate and the z piezo was help fixed for 15 seconds. Viscous relaxation is present for all rates of indenation, as seen by the decay during the 60 second dwell.

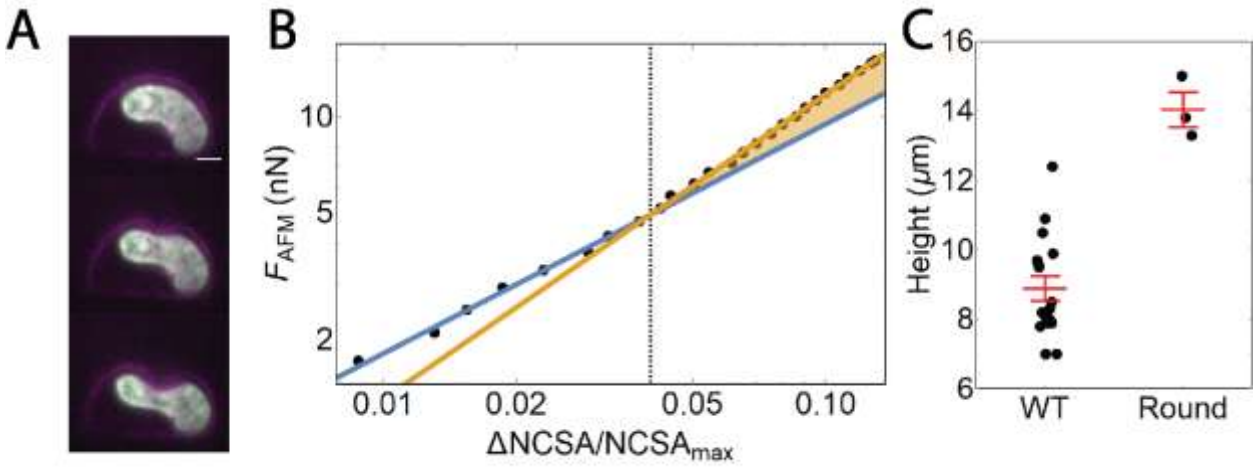

Figure 5.4: Cells with reduced adhesions and nuclear tension exhibit two-regime force response. (A) A subset of fluorescence images collected by our AFM-LS during indentation of a live, SKOV3 cell (scale bar = 5 μm). The cell is stably expressing snaptagged KRas-tail (Magenta) and halotagged H2B (Green) labeled with Janelia Fluor 503 and 549 respectively. (B) Force as recorded by the AFM versus change in $NCSA$ plotted on a log-log scale. Two distinct power-law regimes are observed for all rounded cells (n=3). (C) A comparision of cell height for WT and rounded cells. Red bars represent mean and SEM.

We find that for SKOV3 cells, E_{SA} is approximately 1.36 times greater than E_V, implying these nuclei are more susceptible to strain in volume than in surface area. This can be compared to the Hertz model [278] and the height-corrected Hertz model [287], both of which fail to model the force response over the entirety of the indentation (Figure 5.5). It is also important to note that Hertzian analysis specifies probe and target geometries, and assumes homogeneity and linearity. Our approach, however, makes no prior assumption regarding such geometries and is simply empirical. Moreover, Hertzian analysis is restricted to small indentations as the approximation of contact area breaks down at high strain. Accounting for the eventual plateau of contact area leads to a linear force-indentation relationship, which further underestimates the true force response. Our technique, however, moves beyond this limitation as we make no specific model of contact area and instead examine the empirically-determined scaling relationships between shape and force. Our model was constructed across small and large indentations, and is therefore applicable in both scenarios. Our approach also allows us to decouple resistances to specific types of nuclear strain as opposed to providing a single metric of stiffness for the entirety of the nucleus. This complements and improves on earlier analytic modeling efforts [46] in that we have empirically determined a relationship between force and morphology that accounts for contributions of both the bulk compressibility and surface tension without assuming a predefined geometry.

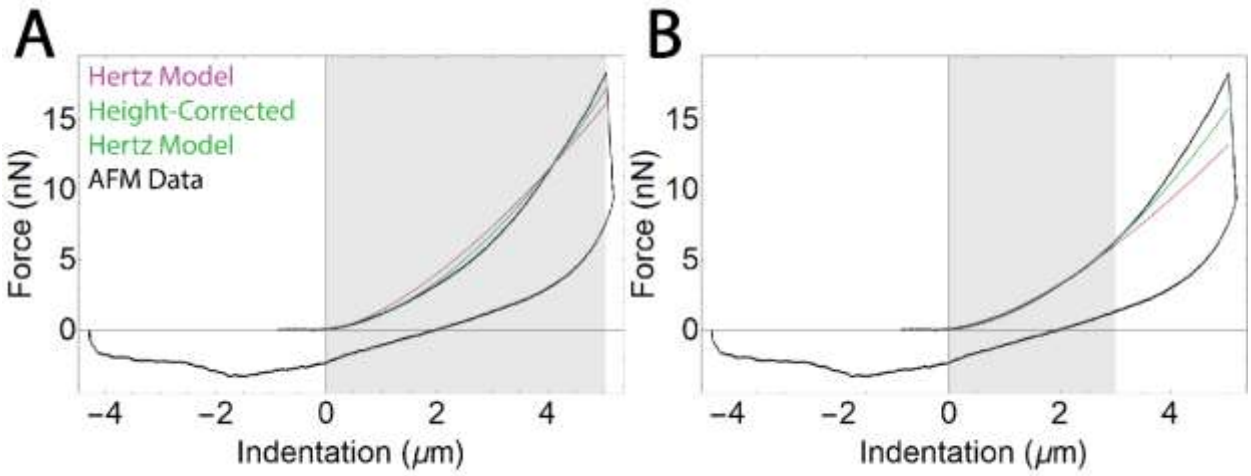

Figure 5.5: Force versus indentation plots showing the fits of both the Hertz model (Purple) and the height-corrected Hertz model (Green) over the entire indentation (A) and over the first 3 μm of indentation (B). The gray region represents the portion of data to which the model was fit, which for (B) corresponds to the nominal bead radius of 3 μm. Fitting to the entire indentation shows that neither model accurately represents the data set. Fitting to the early portion of the indentation shows that both models are applicable for low indentations, but underestimate the force response at high indentations. This is suggestive that an additional mechanism for force response is needed to match the experimental data.

A further alternative model is a polynomial in indentation ($F_{AFM} = a + b\,\delta + c\,\delta^n$) that has been reported to fit AFM indentation of the simple red blood cell when adherent [288]. Here, the linear term is representative of the membrane tension and the higher order term ($n \approx 2 - 3$) reflects membrane dilation. This work also observed a strain-stiffening effect; however, this stiffening occurs at forces of order 100 pN and indentations of order 100 nm. We also observe similar stiffening at low forces (Figure 5.6), along with an additional stiffening at forces of order 1 nN and indentations of order 1 μm (Figure 5.2A, Figure 5.6). Our work focuses exclusively on the latter stiffening effect seen at higher forces, for which this alternative approach does not explain. Our scaling relationships for the low-force stiffening do not precisely match that of this alternative mode, but this may be explained by their use of conical AFM tips as compared to our spherical AFM tips. A full model of AFM indentation may then first apply this polynomial approach at quite small forces and indentations, and our empirical approach at large forces and indentations.

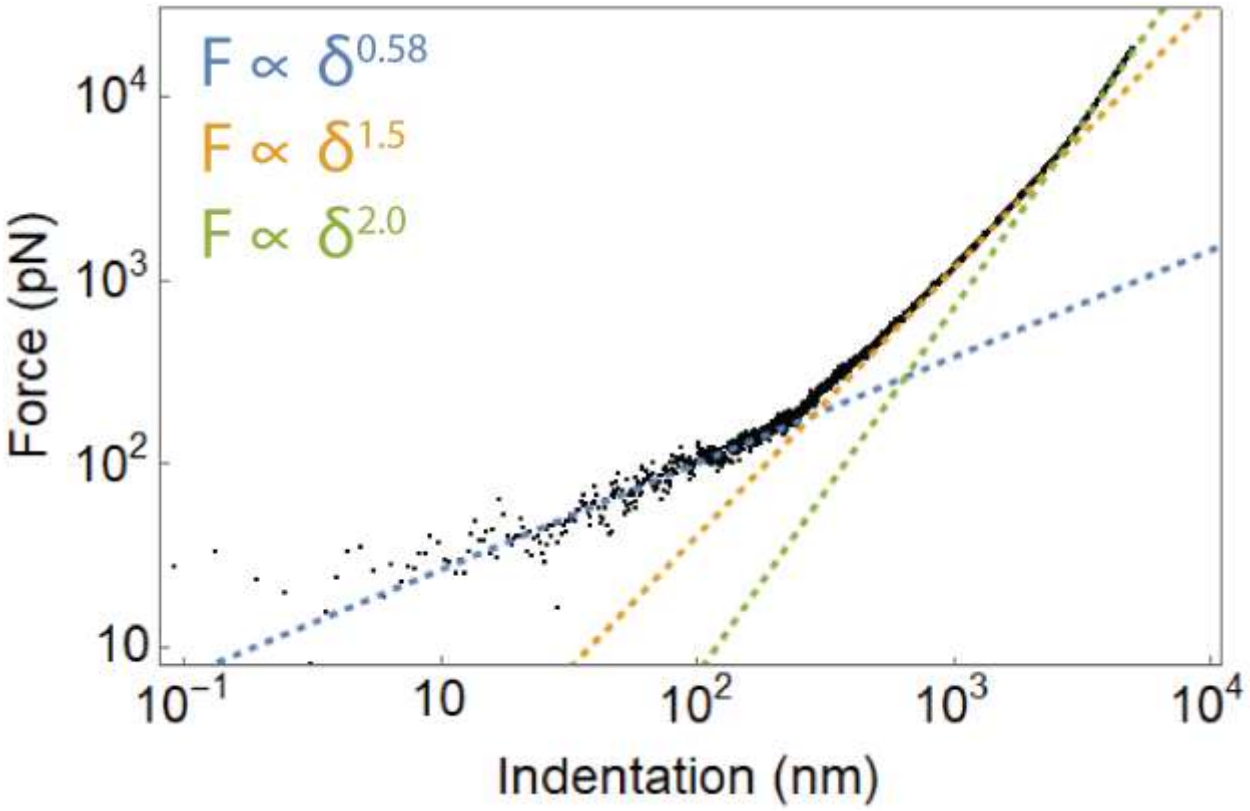

Figure 5.6: Log-Log plot of force versus indentation shows multiple stiffening regimes. We observe three separate scaling relationships over the entire indentation; a power law relationship was fit to each regime to highlight the stiffening effects. The specific scaling relationship for each regime is provided for this specific data set.

Our AFM-LS technique does not systematically examine a specifically oriented vertical slice as the distribution of polarity amongst the cells is seemingly random. One potential failure of the proposed model and technique would be a dependence of E_V and E_{SA} on the initial morphology of the nucleus or the orientation in which we image the nucleus from the side. To examine this, we determined both E_{NCSA} and E_{NP} for n = 17 cells and plotted E_V and E_{SA} against initial values of $NCSA$ and NP (Figure 5.7). We performed a Pearson's correlation test between E_V, E_{SA} and $NCSA$, NP. No significant correlation was observed between either E_V or E_{SA} and $NCSA$ or NP, implying that the resistances to nuclear morphology changes determined by our model are not systematically dependent on either the scale of the nucleus or the specific side-view orientation in which we visualized the nucleus. Our approach is then robust to initial cell orientation or initial nuclear size.

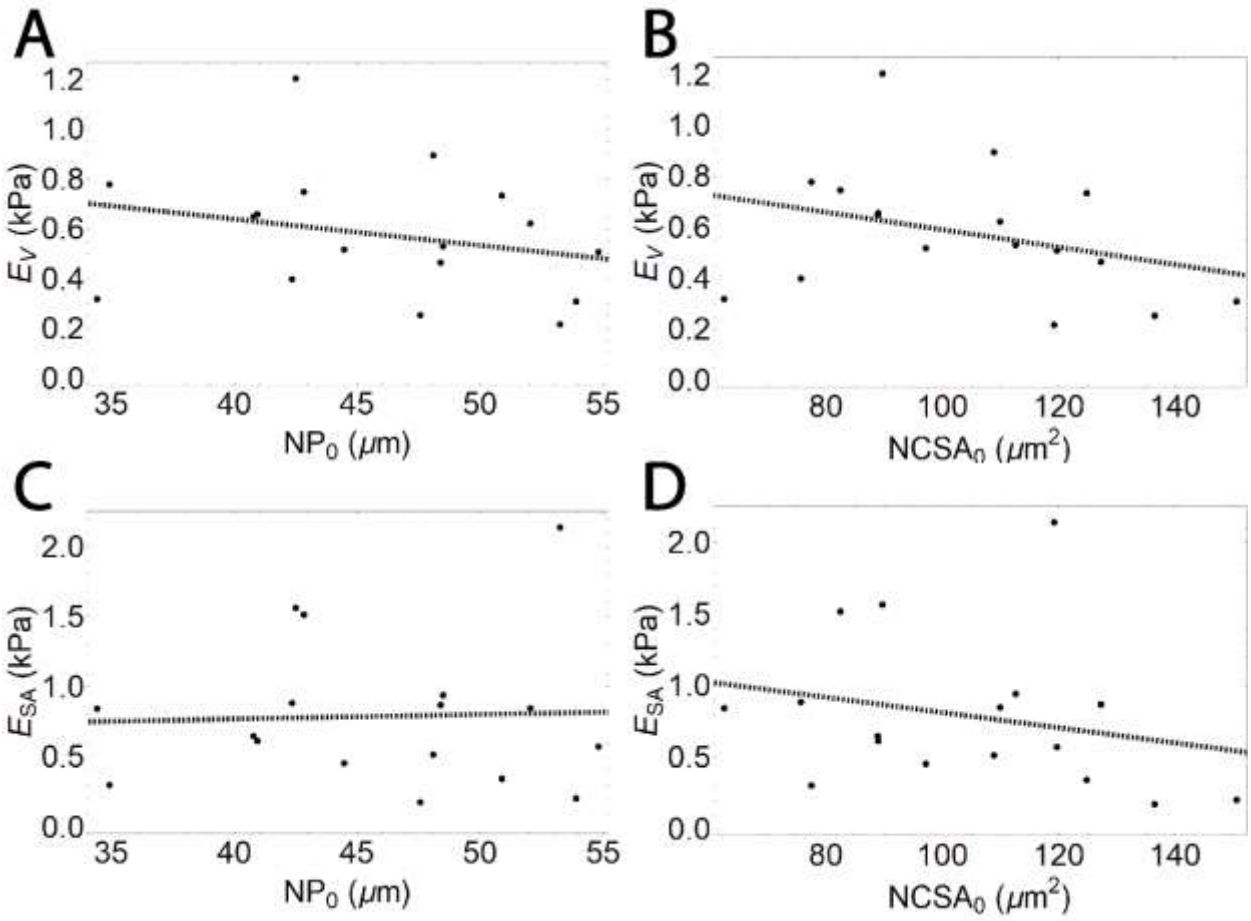

Figure 5.7: There is no significant correlation between initial nuclear morphology and E_V or E_{SA}. Plots of (A) E_V versus NP_0, (B) E_V versus $NCSA_0$, (C) E_{SA} versus NP_0, (D)E_{SA} versus $NCSA_0$, as well as best fit lines (dashed). A Pearson's correlation test for each relationship shows no significant correlation.

Our combined AFM-LS approach to studying nuclear mechanics first showed the existence of two regimes of deformation: one at low levels of indentation (regime 1) and one at high levels of indentation (regime 2). In regime 1, we observed only changes in nuclear volume; in regime 2, we observed changes in both nuclear volume and apparent surface area. This allowed us to extract scaling relationships between applied external forces and changes in nuclear morphology, leading to an empirical model of nuclear deformation characterized by two fitting parameters: E_V and E_{SA} (Figure 5.2). These fitting parameters provide a metric of resistance to nuclear volume change and nuclear surface area change, respectively, but further are directly proportional to the elastic modulus of the nucleus and the nuclear stretch modulus.

Often missing from current studies, are measurements of the external stress a nucleus experiences throughout a given experiment. Such measurements could provide additional context for interpreting why certain phenomena may be occurring. For example, constricted migration assays how allowed investigators to study how deficiencies in the nuclear lamina lead to increased migration rates [5, 67, 78], higher rates of nuclear rupture [69], and increases in plastic damage [63, 66, 67], all of which are relevant for understanding disease states and cellular function. Our work provides a means of estimating the external force applied to a nucleus simply through measuring nuclear morphology in the plane of applied force. Clear limitations exist for applying this model, such as complex 3D nuclear strains; however, some common assays for studying nuclear dynamics could benefit for our model.

5.4 Chromatin and Lamin A/C Separately Resist Bulk and Surface Deformations

Chromatin and lamin A/C have been shown to be the primary mechanical constituents of nuclei; recent work has shown that during micromanipulation extension of isolated nuclei chromatin dominates small-scale extensions while lamin A/C governs large-scale extensions [13]. It remains untested if similar phenomena hold true for compression-based deformations of nuclei in intact cells. We hypothesized that in AFM indentations chromatin in part dictates the resistance to nuclear volume change while lamin A/C separately resists changes in nuclear surface area. Such a measurement was not previously attainable without AFM-LS.

To test this hypothesis, we first treated our SKOV3 cells with a 200 nM concentration of Trichostatin A (TSA) for 24 hours prior to performing AFM compression with side-view imaging experiments. TSA decompacts chromatin by increasing euchromatin marker histone tail acetylation (Figure 5.8) [116]. We extracted nuclear morphology dynamics under compression and fit Equation 1 to the corresponding force data to extract E_V and E_{SA}. We observed a significant 40% decrease in E_V upon TSA treatment ($p<0.05$ from a t-test), but no significant difference in E_{SA} (Figure 5.9A and B).

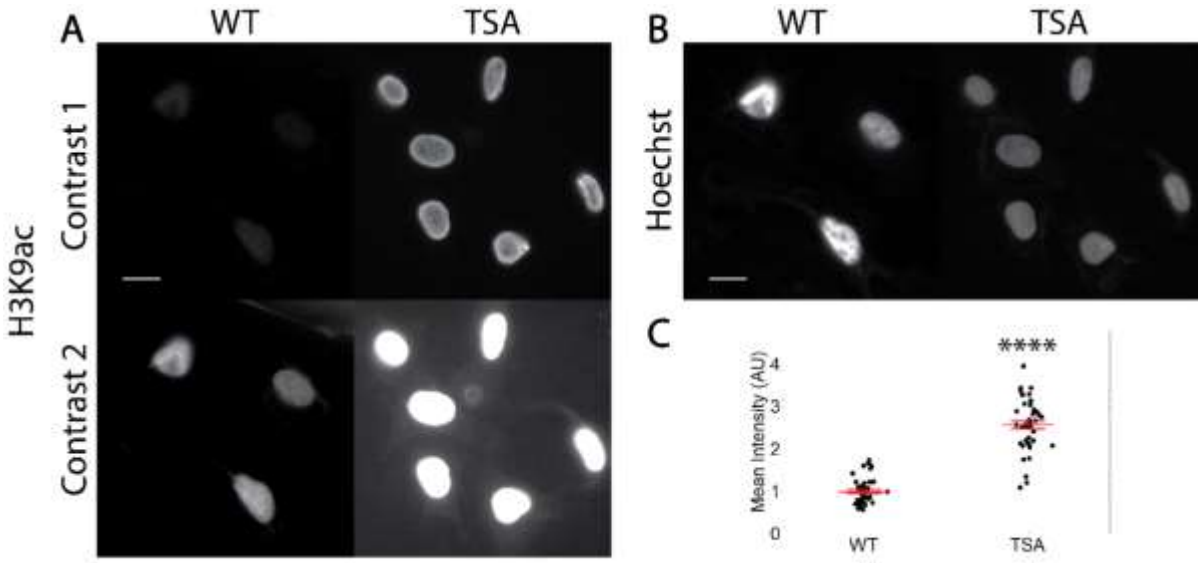

Figure 5.8: Immunofluorescence validation of TSA treatment. (A) Representative fluorescence images of H3K9ac in both WT and TSA treated cells. Images are shown at two different contrast levels (scale bar = 20 μm). (B) Representative fluorescence images of Hoechst in both WT and TSA treated cells (scale bar = 20 μm). (C) Mean intensity of H3K9ac for WT (n = 43) and TSA treated (n = 41) cells shows a significant increase in decondensed chromatin for TSA treated cells. **** represents $p < 0.0001$ for a t-test. Red lines represent mean and standard error. Images acquired by Tim O'Brien.

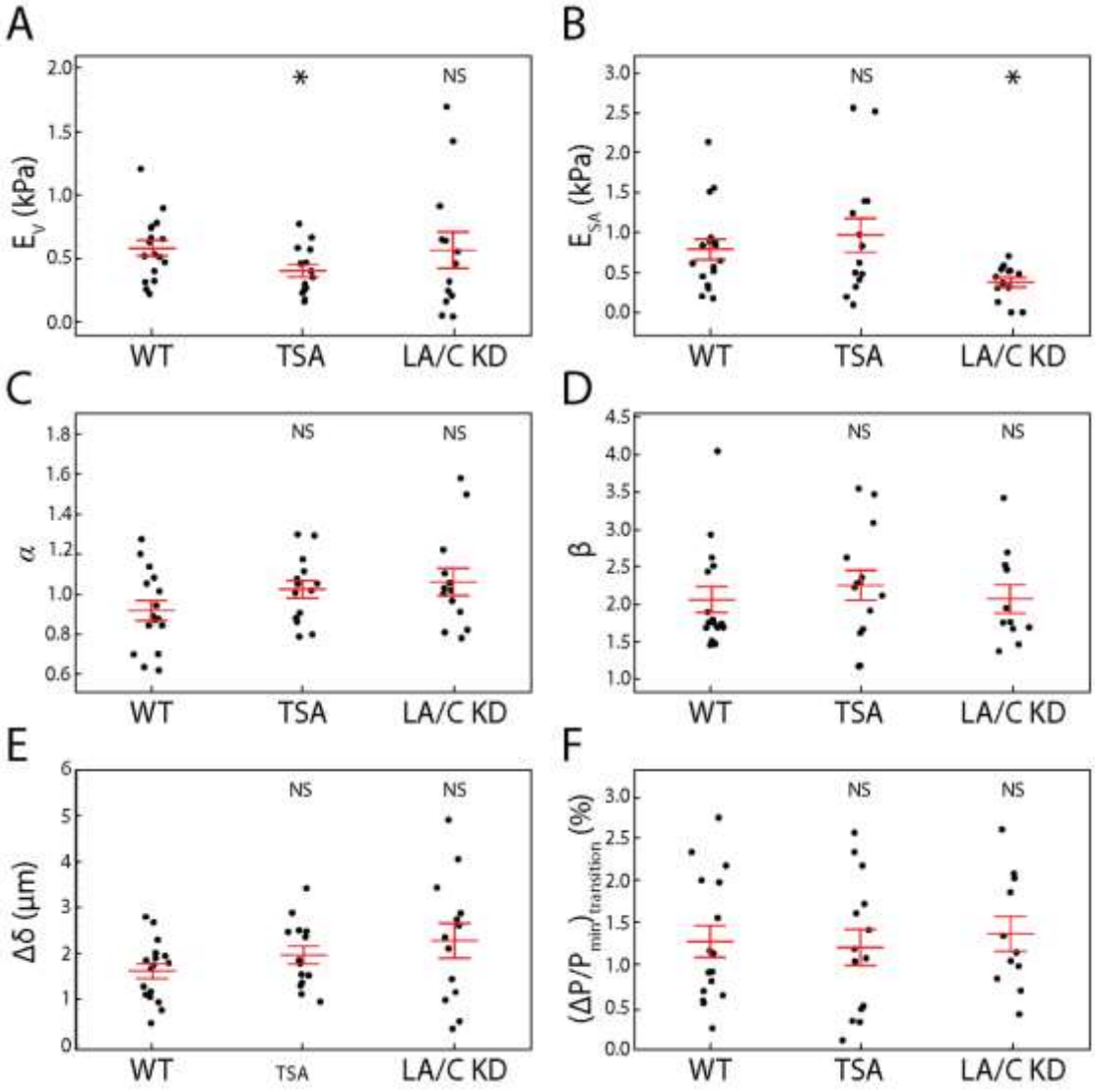

Figure 5.9: Chromatin decompaction and lamin A/C depletion weaken resistance to volume and surface area changes respectively, while behaving similar to the empirical model. (A) Resistance to nuclear volume change, E_{V}, is decreased by TSA but unchanged by LA/C KD. n = 17, 14, 13 for WT, TSA, LA/C KD. (B) Resistance to nuclear surface area change, E_{SA}, is unchanged by TSA but decreased by LA/C KD. n = 17, 14, 13 for WT, TSA, LA/C KD. (C) α, the exponent for $F_{\Delta NCSA}$, is unchanged by TSA and LA/C KD. n = 16, 14, 13 for WT, TSA, LA/C KD. (D) β, the exponent for $F_{\Delta NP}$, is unchanged by TSA and LA/C KD. n = 16, 14, 11 for WT, TSA, LA/C KD. (E) The difference in indentation at the onset of change in NP and NCSA is unchanged by TSA and LA/C KD. n = 17, 14, 13 for WT, TSA, LA/C KD. (F) The strain in NP at the transition point between regime 1 and regime 2 is unchanged by TSA and LA/C KD. n = 16, 14, 11 for WT, TSA, LA/C KD. Red bars represent mean and SEM. NS – not significant. * - $p < 0.05$.

Furthermore, we transfected our SKOV3 cell line with siRNA to halt production of new lamin A/C (LA/C KD, Figure 5.10). We then performed AFM-LS experiments 4-6 days post transfection and extracted E_V and E_{SA} as previously described. We observed a significant 50% decrease in E_{SA} ($p<0.05$ for a t-test), yet no significant change in E_V (Figure 5.9A and B). This means both that chromatin resists

strain in nuclear volume while lamin A/C separately resist strain in surface area. Furthermore, this indicates that chromatin does not resist nuclear surface area stretching nor does lamin A/C resist deformation in nuclear volume. Because strain in nuclear volume and nuclear surface area occur at different indentation scales (Figure 5.1), we have also shown that chromatin and lamin A/C provide mechanical resistance at short and long indentations respectively.

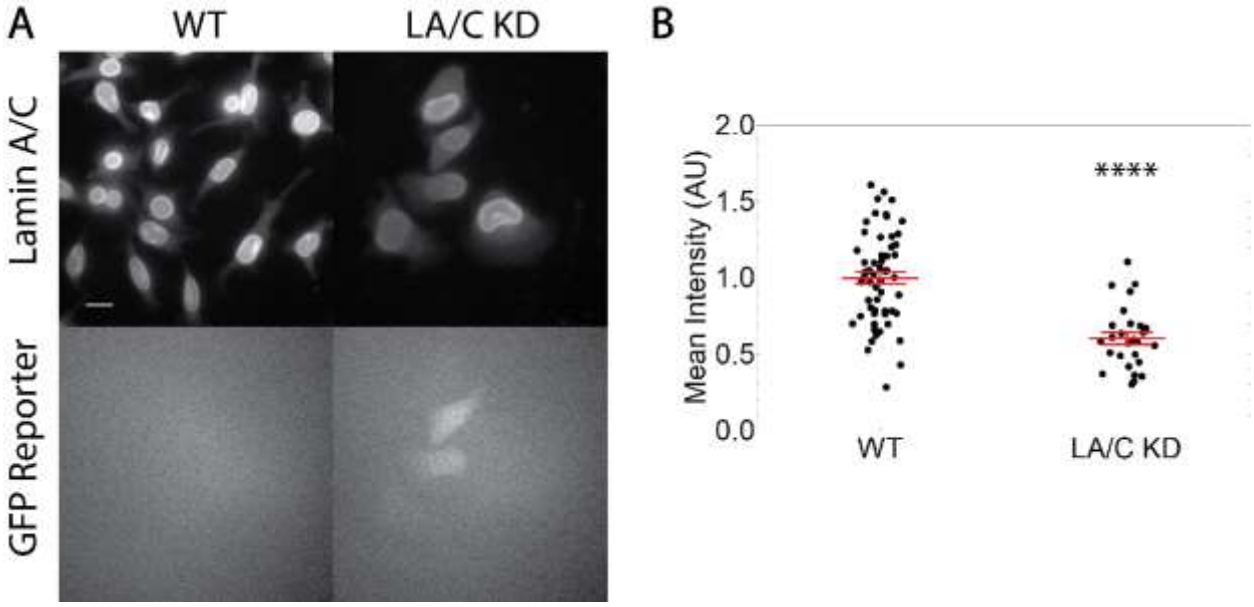

Figure 5.10: Immunofluorescence validation of lamin A/C knock down. (A) Representative fluorescence images of lamin A/C and the GFP reporter in both WT and LA/C KD cells (scale bar = 20 μm). (B) Mean intensity of lamin A/C for WT (n = 58) and LA/C KD (n = 27) cells shows a significant decrease in lamin expression for LA/C KD cells. **** represents $p < 0.0001$ for a t-test. Red lines represent mean and standard error. Images acquired by Tim O'Brien.

An alternative explanation for the decreases in E_V and E_{SA} seen upon TSA treatment and LA/C KD respectively is that our proposed empirical model (Equation 1) is no longer valid after these treatments. More specifically, we could be observing changes in E_V and E_{SA} that are actually representative of changes in the scaling relationships between force and nuclear morphology themselves; that is, α and β could be dependent on chromatin compaction and lamin A/C expression. To address is explanation, we performed the analysis previously described to extract α and β from both the TSA-treated and LA/C KD samples. We found no significant change in either α or β (Figure 5.9C and D), meaning the previously determined scaling relationships between nuclear morphology and applied force are unchanged. Because these scaling relationships remain constant, our observed changes in E_V and E_{SA}

are indicative of changes in the nucleus' ability to resist strain in nuclear volume and nuclear surface area.

Furthermore, we observed no significant difference in $\Delta\delta$ (Figure 5.9E) or the strain in NP at the transition point (Figure 5.9F). This implies that the existence of the strain-stiffening effect is more closely related to nuclear geometry and the manner of deformation than the relative stiffnesses associated with the volume and surface area of the nucleus. This result is supported by previous findings in micromanipulation studies [281]. The lack of changes in scaling (α and β) and transition (indentation and strain) solidifies our conclusions regarding the role of chromatin and lamin A/C in separately resisting strain in nuclear volume and surface area respectively.

With our approach we were able to separate deformations of nuclear volume and nuclear surface area and tease apart how the mechanical constituents of the nucleus are responsible for each class of deformation. Specifically, we showed through disruption of histone-histone interactions via TSA treatment that chromatin resists strain in nuclear volume, but not in the nuclear surface area. We also showed through a knockdown of lamin A/C that the nuclear lamina resists strain in the nuclear surface area, but not in the nuclear volume. This further implies that chromatin dictates the mechanics of small indentations, whereas lamin A/C is relevant for large indentations. Additionally, through our FEA modeling we find that alterations in chromatin compaction and lamin A/C expression directly alter the nuclear elastic and stretch moduli respectively. These findings are in agreement with work showing that stretching of isolated nuclei via micromanipulation with micropipettes yields a two-regime force response where chromatin regulates the low-deformation regime and lamin A/C regulates the high-deformation regime [13]. These results help to provide a guide for AFM experiments in that small indentation measurements will likely probe only the mechanical properties of the chromatin, and large indentation measurements will need additional compensation beyond standard contact mechanics models to account for stretching of the nuclear lamina.

Previous research has also shown that in micropipette aspiration studies, the mechanics of swollen nuclei are dominated by the nuclear lamina whereas the mechanics of shrunken nuclei are governed in part by chromatin [45]. This result that shifting the primary load-bearing structure from chromatin to the nuclear lamina via swelling is consistent with our results as swelling would pre-stretch

the nuclear surface area, thus eliminating regime 1 entirely and leaving only the lamina-dominated regime 2. Studies of osmolarity have also shown similar phenomena that can be explained by our model. Cell volume and inverse osmolarity follow a linear relationship, which can be modeled by the Boyle Van't Hoff relation [289]. Nuclei, however, have been shown to deviate from this linear relationship at large swelling volumes. To match this behavior, an additional term modeling nuclear membrane tension which is proportional to the nuclear surface area must be added [277], consistent with our findings.

AFM studies of mechanical properties have historically been used to study small-deformation mechanical properties because of the limitations of the analytical models applied to resulting data. Using cantilevers with large (10 μm) diameter beads positioned above the nucleus, force-indentation curves were collected on HT1080 fibrosarcoma cells for relatively low indentations (~1 μm). The Hertz model was fit to the force-indentation curves to extract an elastic modulus. They showed that TSA treatment resulted in nuclear softening [48]. This is consistent with our results showing that TSA treatment reduces E_V, which is the primary resistance at low indentations and proportional to the elastic modulus of the nucleus. A separate AFM study on isolated *Xenopus* oocytes revealed not only that increases in lamin A resulted in nuclear stiffening, but that the force-indentation curves become more linear as a function of lamin A expression levels [44]; a linear force-indentation curve is representative of a pressurized shell [290]. They were able to extract a nuclear membrane tension by fitting the end of the force indentation curve to a linear relationship, and it is crucial to note that they indented nuclei up to approximately 10 μm. By fitting the end of the force-indentation curves for large indentations, they effectively extracted the mechanical properties of regime 2. Our results are then consistent in that we also showed a dependency of E_{SA} on lamin A/C expression; this implies that lower levels of lamin A/C reduces the nuclear stretch modulus at large nuclear deformations.

Our work provides a synthesis of these previous studies, helping to piece together separate results into a single, cohesive explanation for the force response of the nucleus. Previous AFM studies using Hertzian analysis could only observe when nuclei became softer or stiffer under a given treatment. That is, chromatin decondensation and lamin A/C knockdowns show an apparently identical softening response (decrease in elastic modulus) under Hertzian analysis [48, 291], despite having distinctly different roles in nuclear compression as shown here. With knowledge of both the length scales of

deformation for which chromatin and lamin A/C are relevant as well as the specific morphological deformations against which they protect, we can progress forward to understanding their relative contributions in disease and function.

5.5 Nuclear Curvature During Compression

Recent studies have connected nuclear curvature to locations of nuclear rupture and subsequent DNA damage. Through AFM compression with both 4.5 μm diameter beaded cantilevers and sharp tip cantilevers (diameter < 0.1 μm), a correlation between indentation with high-curvature probes and nuclear rupture was reported [47]. Similarly, nuclear blebs induced by increases of euchromatin were shown to systematically form at the pole of the major axis, which is the site of highest curvature [270]. We then sought to study the roles of chromatin and lamin A/C in nuclear curvature dynamics during AFM compression.

Nuclear curvature, defined as the inverse of the radius of a best-fit circle, was extracted for each point in the discretized perimeter of the nucleus for every image collected during the indentation. Prior to compression, the nucleus shows two peaks corresponding to the ends of the oval-shaped nucleus (Figure 5.11A). Once compressed, the nucleus shows a new, clearly defined peak at approximately 10 μm; this peak corresponds to the new curvature formed as a result of indentation with the AFM (Figure 5.11B). By fitting a Gaussian curve to this peak for each frame in the indentation (Figure 5.11C), we can study how curvature changes as a function of indentation; specifically, we extract maximum curvature at the site of indentation. We observed that in the regime over which nuclear curvature changes, there is a linear relationship between maximum nuclear curvature and indentation (Figure 5.11D). Eventually the maximum nuclear curvature plateaus as it cannot exceed that of the AFM probe.

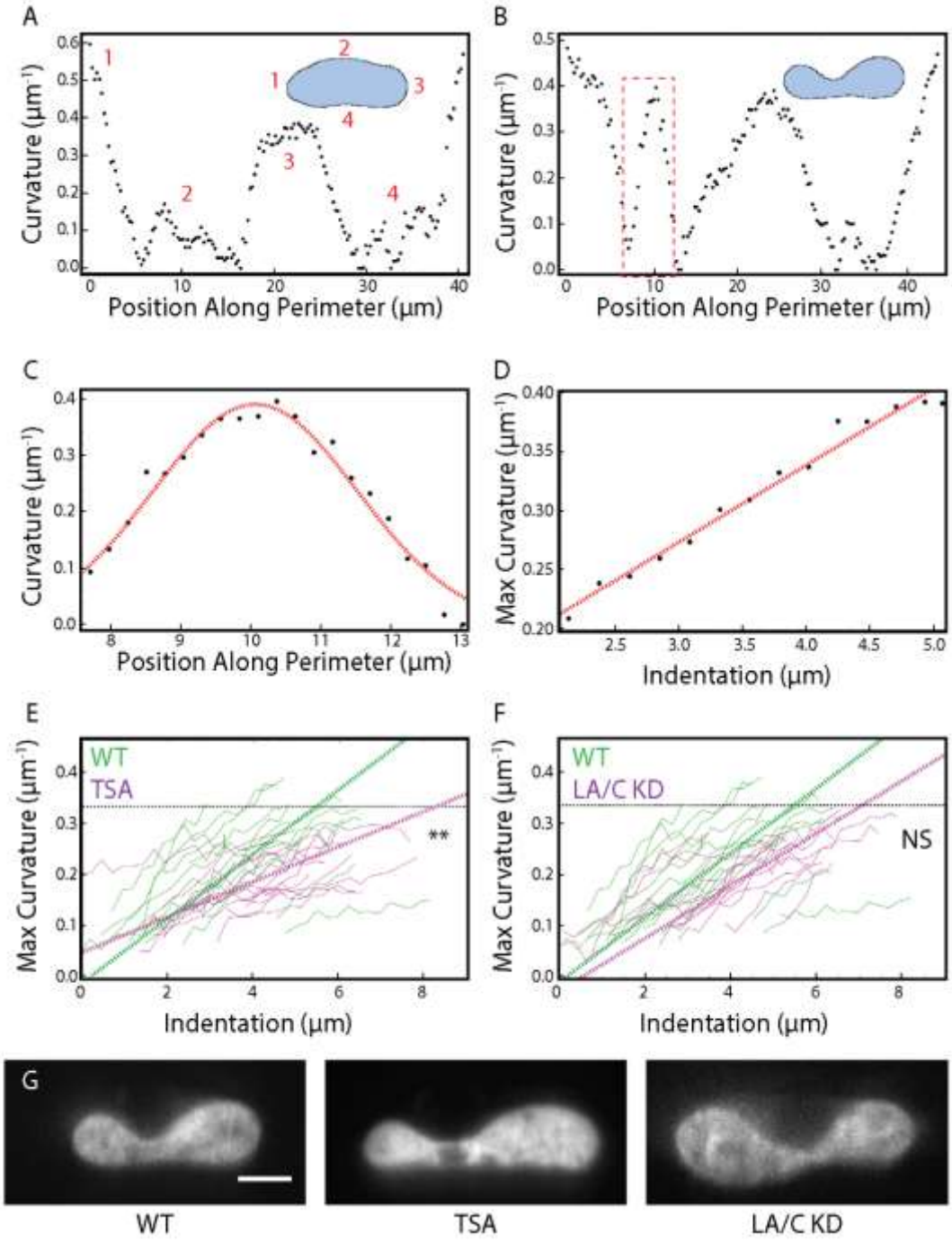

Figure 5.11: Dynamic nuclear curvature analysis during AFM indentation. (A) Nuclear curvature versus position along perimeter for an undeformed nucleus. The inset displays the mask of the nucleus and the discritization of the perimeter. (B) Nuclear curvature versus position along perimeter for a deformed nucleus. The inset displays the mask of the nucleus and the discretization of the perimeter. Note the additional peak centered around 10 μm representing the site of indentation. (C) A Gaussian fit to the peak at the site of indentation extracts maximum curvature under the AFM bead (red dashed box in (B)). (D) Maximum curvature plotted during the entire indentation. A linear fit is performed for the region of changing curvature. (E) Maximum curvature as a function of indentation plotted for n = 14 WT cells and n = 14 TSA treated cells. ** represnts $p < 0.01$ for a t-test comparing the mean slope of maximum curvature versus

indentation. (F) Maximum curvature as a function of indentation plotted for n = 14 WT cells and n = 13 LA/C KD cells. Black dashed line represents curvature of the AFM bead. NS represnts no significance for a t-test comparing the mean slope of maximum curvature versus indentation. (G) Representative images of SKOV3 nuclei (H2B) under maximum compression with various treatments. Scale bar = 5 μm. See also Video 5.2.

Maximum nuclear curvature was plotted against indentation and compared between perturbation and control WT nuclei (Figure 5.11E-G). We discovered a significant decrease ($p<0.01$ for a t-test) between the mean slope of maximum curvature versus indentation for TSA treated cells. This implies that larger indentations are necessary to induce that same of amount of nuclear curvature in TSA treated cells as compared to WT cells. Contrary to chromatin decompacted cells, we observed no significant change in the mean slope of maximum curvature versus indentation for LA/C KD cells as compared to WT cells; this could be due to either a minimal contribution of lamin A/C to nuclear curvature or an inability to detect the changes in nuclear curvature due to the geometry of our assay or the degree of knockdown of lamin A/C. While not studied here, our ability to monitor dynamics of nuclear curvature under compression will facilitate further studies of both varied deformation geometries and increased of chromatin compaction and lamin A/C levels.

We observed that chromatin decondensation through TSA treatment resulted in less nuclear curvature during indentation as compared to WT, whereas LA/C KD nuclei showed no change in curvature under compression in our assay. We hypothesize that this is due to a change in the relative resistances to nuclear volume and nuclear surface area strains that we have previously shown. By decreasing the bulk resistance, the energy necessary to deform the nuclear volume relative to the nuclear surface area decreases. Minimization of energy cost then implies that the nucleus will undergo larger volume changes and smaller surface area changes. Decreased nuclear curvature is one means by which the nucleus could accommodate larger volume changes with less stretching of the nuclear surface area. Our hypothesis for the decreased rate of curvature change in TSA treated cells would lead us hypothesize that LA/C KD cells would show a higher rate of curvature change, or that overexpression of lamin A/C would mimic the behavior of TSA treated nuclei. Our observation of no significant change could either be due to a lack of correlation between lamin A/C and nuclear curvature, or more likely due to the geometry of the AFM probe and minimal knockdown of lamin A/C levels limit our ability to observe the affect LA/C KD would have on nuclear curvature. Regardless, the dependence of nuclear curvature on chromatin compaction levels clearly shows that the nucleus behaves as a two-material system. For a

simple elastic solid, the curvature at the site of indentation is independent of the Young's modulus, a second material is necessary to observe altered deformation patterns by changing the material properties. This further confirms that both chromatin and lamin A/C contribute to nuclear stiffness in compression.

The relevance of nuclear curvature has primarily been linked to rupture of the nuclear envelope as well as development of nuclear blebs. Previous work has examined the correlation between nuclear curvature and nuclear envelope rupture through AFM [47]. U2OS cells were compressed with a constant force using both sharp (diameter < 0.1 μm) tips and 4.5 μm beads. Nuclear rupture was shown to be significantly more frequent when using the sharp tip as detected by mislocalization of YFP-NLS into the cytoplasm. Similarly, a constricted migration assay has revealed that it is rather the nuclear curvature, as opposed to tension, that is relevant for nuclear envelope rupture [72]. Nuclear blebs have also been shown to systematically form at sites of high curvature [270, 275] and are prone to rupture [108]. Specifically, chromatin decompaction alone was sufficient to induce an increase in nuclear blebs [270]. Nuclear curvature is then highly relevant for understanding the mechanical integrity of nuclei, as loss of nuclear compartmentalization due to rupture causes nuclear dysfunction which may contribute to human disease [12, 292]. Our work suggests that lamin A/C may not be important for nuclear curvature. However, a valid alternate hypothesis is that the geometry of our bead limits our ability to detect the effect of the lamin A/C KD on nuclear curvature. We have clearly shown, however, that the state of compaction of chromatin has a direct link to the nuclear curvature, and we hypothesize that this is due to the altered, relative contributions of the nuclear elastic modulus and nuclear stretch modulus.

Our results regarding the dynamics of nuclear curvature under indentation also provide insight into how nuclear mechanotransduction may be altered through chromatin decompaction. We show that the nucleus develops less curvature during indentation for TSA treated cells, simultaneously implying that there is less stretching of the nuclear envelope. As previously noted, stretching of the nuclear lamina is thought to be a fundamental mechanism of nuclear mechnotransduction [94]. The state of compaction of chromatin may then indirectly alter transcription or the function of stretch activated channels [274] if the nucleus is undergoing external stress, as we have shown the distribution of strain to be dependent on chromatin compaction.

5.6 DNA Damage and Nuclear Compression

5.6.1 AFM-LS Shows Deformation-Induced DNA Damage

Several studies shown that as cell migrate through constricted environments, the confinement can result in nuclear blebbing which subsequently leads to an increase in DNA damage [62, 69, 71]. Additionally, chromatin decompaction has been shown to increase nuclear blebbing and DNA damage independent on lamins [270]. Recent work, however, has suggested that chromatin compaction is dynamically regulated in order to prevent DNA damage, and that negating the cell's ability to regulate chromatin compaction can lead to increases in DNA damage during mechanical perturbation independent of rupture to the nuclear envelope [6]. We then sought to study using AFM-LS if mechanical perturbation alone is sufficient to cause an increase in DNA damage independent of nuclear rupture.

To study this question, we used our AFM-LS system to compress live MDA-MB-231 nuclei co-expressing NLS-GFP and 53BP1-mCherry to a height of approximately 2 μm (Figure 5.12A, Figure 5.13). During compression, we collected two-color volumetric images allowing us to monitor both DNA damage foci (53BP1-mCherry) and nuclear rupture (NLS-GFP leaking into the cytoplasm). As a control, we also performed experiments under identical conditions, however the AFM tip was only brought into contact with the cell surface (Figure 5.12A). MDA-MB-231 cells showed a significant increase in DNA damage independent of nuclear rupture when compressed as compared to when not compressed (Figure 5.12B). These results were used to validate a broader study primarily using microfluidic devices to force cells into constricted environments to study DNA damage independent of nuclear rupture [142].

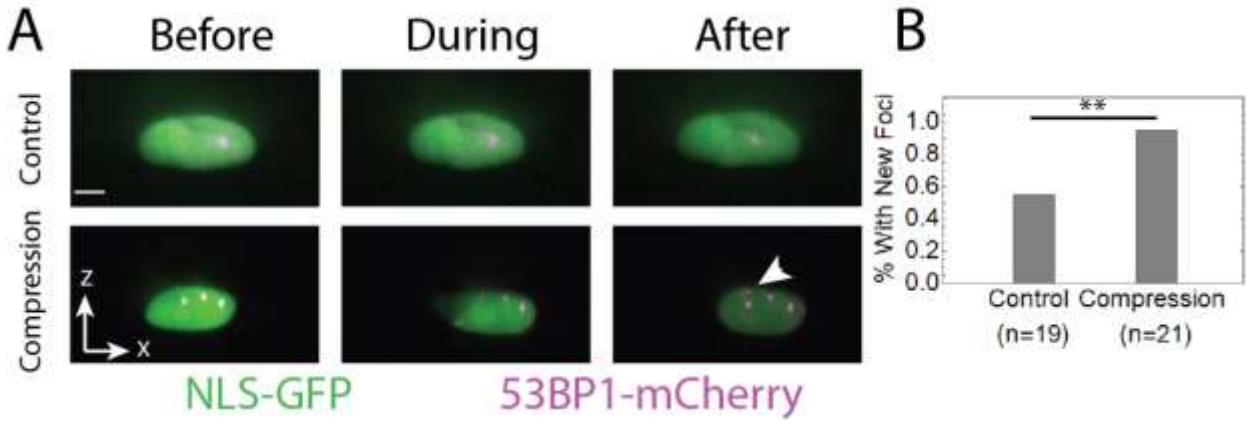

Figure 5.12: AFM-LS shows compression alone is sufficient to induce DNA damage. (A) Representative image sequences (side-view maximum intensity projections) of control and compressed nuclei before, during, and after compression with the AFM. The white arrow points to a new site of DNA damage observed

in the compressed condition. Scale bar = 5 µm. (B) Percentage of nuclei with new DNA damage foci for control (n=19) and compressed (n=21) nuclei. ** represents p<0.01 for a Fischer's Exact.

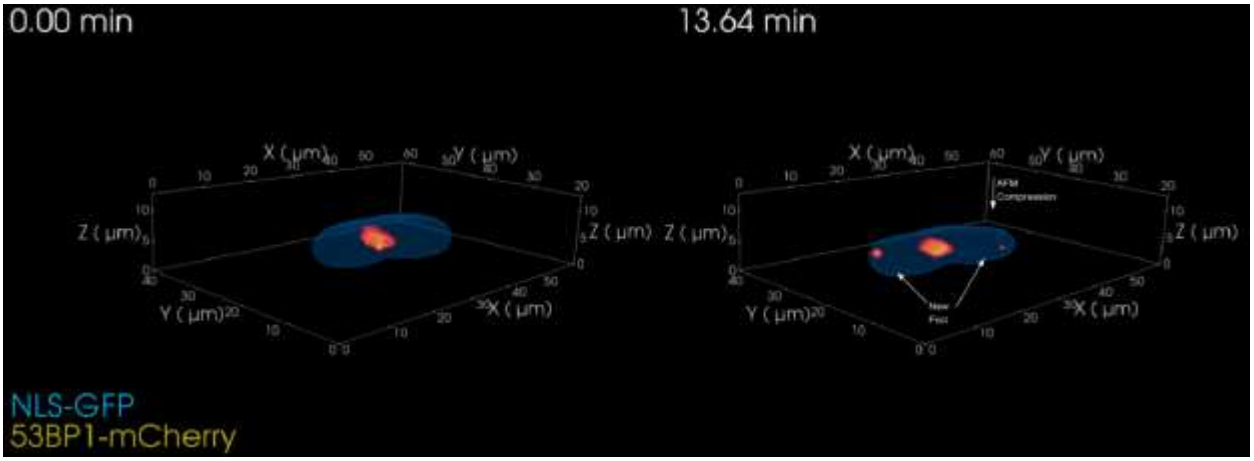

Figure 5.13: 3D rending of a live MDA-MB-231 nucleus under compression. AFM compression alone induces two new DNA damage foci without rupture of the nuclear envelope. See also Video 5.3 and Video 5.4.

5.6.2 Comparison of Mechanical Properties of HT1080 and MDA-MB-231 Nuclei

It was shown that the increase in DNA damage due to deformation alone was cell-type-specific phenomenon. For example, the HT1080 fibrosarcoma cell line was more prone to rupture-induced DNA damage as opposed to the MDA-MB-231 breast cancer cell line, which was more prone to deformation-induced DNA damage [142]. We sought to see if there existed any differences in the mechanical properties of these two cells lines as a potential explanation of this behavior (Figure 5.14). We began by performing AFM-LS experiments (Figure 5.14A) and using Eq. 5.1 to extract E_V and E_{SA} for each cell line (MDA-MB-231: n = 17, HT1080: n = 15)) (Figure 5.14B). We observed no significant change in E_V between HT1080 and MDA-MB-231 nuclei (Figure 5.14C). However, E_{SA} was significantly lower in MDA-MB-231 nuclei when compared to HT1080 nuclei (Figure 5.14D). This implies that the chromatin-dominated bulk resistance in similar between the two cell lines, however the lamin-dominated resistance to stretching of the nuclear surface is lower in MDA-MB-231 nuclei [14]. MDA-MB-231 nuclei have been shown directly to have lower lamin A/C levels when compared to HT1080 cells [142], so these results are in direct agreement with our Lamin A/C KD experiments shown above. Interestingly, lower lamin levels and nuclear envelope tension has been shown to minimize the cells ability to protect the nucleus from

DNA damage under strain application [6]. This may explain why MDA-MB-231 nuclei are more susceptible to DNA damage independent of nuclear rupture than HT1080 nuclei.

Furthermore, it was shown that deformation-induced DNA damage occurred primarily in the S/G2 phase of the cell cycle [142]. We then used traditional AFM with Hertzian contact mechanics to compare to measure the stiffness of nuclei in HT1080 and MDA-MB-231 cells while simultaneously monitoring cell cycle with a FUCCI reporter (Figure 5.14F), which labels cells in red during G0/G1 phase and in green during S/G2 phase [293]. Unsurprisingly, we overserved the MDA-MB-231 nuclei were softer than HT1080 nuclei regardless of cell cycle. Additionally, we saw no dependence of nuclear stiffness on cell cycle for either cell line. Finally, we sought to quantify nuclear curvature during indentation as nuclear curvature has been previously linked to nuclear rupture [47, 270]. We observed no change in the dynamics of nuclear curvature during indentation (Figure 5.14F,G), which is consistent with our previous resulting showing that LAC K/D nuclei have similar curvature dynamics to WT nuclei [14].

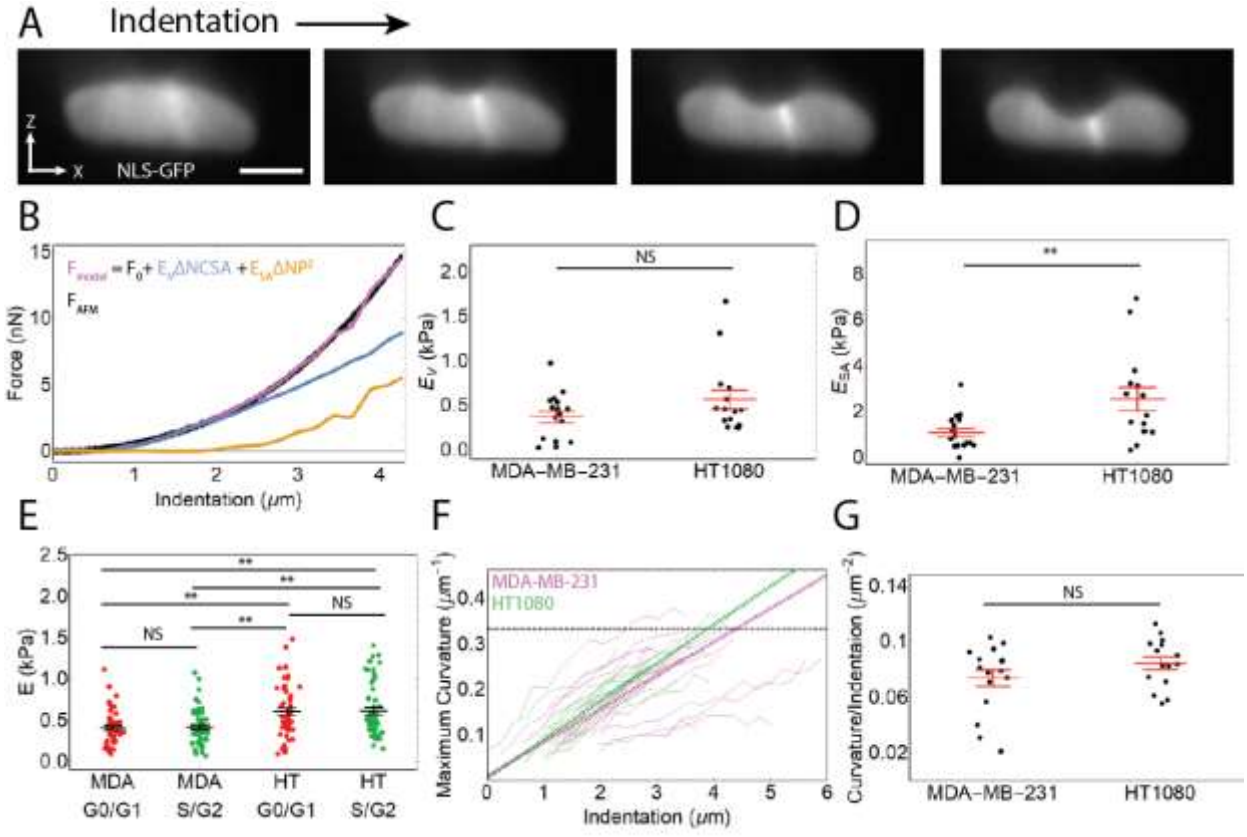

Figure 5.14: Mechanical comparison of MDA-MB-231 and HT1080 cells. (A) A representative time series of an AFM-LS compression experiment. Shown are side-view images of an MDA-MB-231 nucleus expressing NLS-GFP, indentation with the AFM increases from right to left. Scale bar = 5 um. (B) A

representative force versus indentation curve with our model fit as previously described. (C,D) E_V and E_{SA} as determined by fitting our model to force versus indentation curves. No significant difference in E_V is observed between MDA-MB-231 nuclei and HT1080 nuclei (NS: p>0.1 for an unpaired, two-tailed T-Test). A significant decrease in E_{SA} is observed for MDA-MB-231 nuclei as compared to HT1080 nuclei **: (p<0.01 for an unpaired, two-tailed T-Test). (E) AFM with Hertzian contact analysis for MDA-MB-231 and HT1080 cells expressing a FUCCI reporter for cell cycle (NS: not significant, **: p<0.01 for an ANOVA with post-hoc Tukey test). (F) Maximum nuclear curvature at the site of compression plotted versus indentation during AFM-LS experiments. Solid lines represent single cells, dashed lines represent average behavior. Black dashed line represents the curvature of the AFM bead. (G) The slope of maximum nuclear curvature versus indentation compared between MDA-MB-231 and HT1080 nuclei. No significant difference is observed between the two cell lines (unpaired, two-tailed T-Test).

5.7 Conclusions

The nucleus is not simply a passive rheological sub-cellular component, but rather an active body that dynamically regulates cell fate and function in response to mechanical stress. Before understanding nuclear mechanotransduction, however, one must first understand nuclear mechanics. Here, we used our novel AFM-LS system to study the intricate relationship between compression forces and nuclear morphology. Nuclear compression leads to a two-phase force response, with the first phase governed by nuclear volume loss and the second phase signifying the onset of nuclear surface stretching. Chromatin and lamin A/C were shown to dictate the two phases respectively. We also were able to study nuclear curvature dynamically during compression. Chromatin decompaction altered these curvature dynamics, however surprisingly lamin A/C KD had no effect on nuclear curvature. Both curvature and stretching of the nuclear surface are highly relevant for stretch-activated nuclear mechanotransduction, so the work shown here helps inform the length scales at which nuclear stretching occur and the subnuclear components that regulate stretching and curvature.

The nucleus also houses and protects the entire genome, and alterations to the chromatin can lead to a variety of disease states. DNA damage – or specifically breaks in the double helix structure – can lead to genomic instability and are thought to relate to mutations. Previously, nuclear rupture was thought to be the primary mechanism for inducing DNA damage during cancer metastasis. However, here we shown that compression alone is sufficient to induce DNA damage independent of nuclear rupture in MDA-MB-231 cells. This phenomenon is cell-line dependent and HT1080 fibrosarcoma cells do not show this phenomenon [142]. We then sought to compare the mechanical properties of these two cells lines and found that MDA-MB-231 nuclei are more susceptible to stretching of the nuclear surface which may

be a mechanism by which they are susceptible to DNA damage without rupture. We further saw that there is no dependency of nuclear mechanical properties on cell cycle. These results highlight that rupture is not always necessary to cause genomic instability, however one must be careful in developing future studies surrounding this as this phenomenon is cell-line dependent.

5.8 Specific Materials and Methods

5.8.1 Cell culture

SKOV3 cells were grown in DMEM F12 without phenol red (Gibco), 5% FBS (Sigma-Aldrich) and 1X antibiotic antimycotic (Gibco). On the day before experiments they were trypsinized and plated at low density on fibronectin-coated polyacrylamide gels. 10 µL of Janelia Fluor 549 and 503 was added 2 hours prior to experiments, and washed out immediately before cell were examined. Janelia Fluor 503 was not used in Lamin A/C KD cells as to not conflate the GFP reporter signal. MDA-MB-231 and HT1080 cells were cultured in DMEM/F12 media without phenol red supplemented with 10% FBS (Sigma-Aldrich), 1× antimycotic (Gibco) and 15mM HEPES. A day before the experiment, 50-70% confluent cultures were trypsinized and plated on polyacrylamide gels (stiffness of 55 kPa) coated with collagen

5.8.2 Combined atomic force microscopy and side-view light sheet microscopy

The intricate details our AFM-LS system, both regarding the optical design and integration of the atomic force microscope, are described in our previous work [172, 239] and above in the previous sections. Beaded cantilevers (Figure 5.1C) were generated as described in Chapter 3. Cells prepared as described above were place onto the AFM-LS system for no more than a couple hours to ensure viability; cells were observed to be viable throughout all experiments. Details of the prism alignment and AFM-LS setup are also given in Chapter 3.

For nuclear mechanics experiments, force curves were taken at a loading rate of 1 µm/s unless otherwise stated. The trigger point for the z-piezo movement was set such that the nucleus was compressed to approximately 2 µm. The z-piezo was then fixed in a closed-loop feedback mode for 60 s, after which the AFM retraced and continue recording data for an additional 15 s. Data from the AFM was recorded at a bandwidth of 2 kHz. A square wave from the AFM was sent to a DAQ board (PCIe-6323,

National Instruments) which was used to synchronize both the camera (ORCAFlash4.0 V3, Hamamatsu) and laser light (OBIS-561-150-LS and OBIS-488-150-LS, Edmund Optics). For compression of SKOV3 cells, each channel (488 nm and 561 nm) had an exposure time of 100 ms and 25 ms was taken between each frame resulting in a two-color frame acquisition rate of 4 Hz. For MDA-MB-231 and HT1080 cells, a single channel (488 nm) was imaged with a 200 ms exposure time and 50 ms readout time for an acquisition rate of 4 Hz. Custom software was designed for the synchronization process and image acquisition.

For DNA damage experiments, Volumetric images were acquired before, during and after compression. Cells were compressed to an approximate height of 2 μm by lowering the cantilever at the rate of 250 nm/s. For control cells, the cantilever was lowered to indent the cell only a few hundred nanometers. Images were acquired for 20 minutes with compression before retracting the cantilever at the rate of 250 nm/s. Cells were imaged for 5 minutes after retraction as well.

5.8.3 Nuclear morphology extraction and curvature analysis

All nuclear morphology extraction was performed in FIJI [250] using side-view fluorescence images of H2B. A rolling-ball background subtraction was performed with a radius dependent on the size of the nucleus (~50 – 150 pixels). A Gaussian blur was then performed with a kernel size of 2 pixels based upon the full-width half max (FWHM) of the system's point spread function (PSF). The FeatureJ Edges plugin (http://imagescience.org/meijering/software/featurej/) was used to determine the outline of the nucleus during compression; this outline was thresholded to generate a binary image. The binary outline was then dilated several pixels (2 – 5 pixels, depending on the initial image quality) to form a continuous boundary, after which the boundary was filled to generate a mask. The mask was eroded by the same amount as the initial dilation to form the final mask of the nucleus. FIJI's "analyze particles" feature was used to extract the cross-sectional area and perimeter of the nucleus throughout the AFM compression.

All curvature analysis was performed in Mathematica 11.2 (https://github.com/alihashmiii/curvatureMeasure). Masks of nuclei were imported and the mask boundary was discretized such that each discrete point was separated from the next by approximately 250 nm

based upon the FWHM of the PSF of our system. For each point on the perimeter, a circle was fit to that point and the adjacent points within one fourth of the circumference of the AFM bead on either side. Curvature was defined to be the inverse of the radius of the fitted circle; a curvature of 0 represents a flat line. To dynamically track the maximum curvature at the site of indentation, a Gaussian curve was fit to the curvature versus boundary point data in the region where the nucleus was indented.

5.8.4 Treatments of SKOV3 cells

For treatment with Trichostatin-A (TSA), TSA was dissolved to 10 mM in DMSO, and then serially diluted in PBS to 4 µM on day of treatment. 10 µL of a 4 µM solution in PBS was then added to 190 µL of media in 10 mm cloning cylinders, for a final concentration of 200 nM. Experiments were carried out 24-28 hours after drug addition. The 2×10^{-5} dilution of DMSO, giving 0.002% v/v final concentration was judged to be insignificant to the TSA effect. A full description of our knockdown of Lamin A/C is available in our previous work [13] Briefly, DNA for the interfering RNA was transfected using Fugene HD. The media was changed regularly after the first 2-day treatment. Cells were plated on days 3, 4, and 5, and used on days 4, 5, and 6 respectively. Two cells were excluded from the lamin A/C sample because they showed sever plastic damage, a phenomenon previously observed in the literature [66, 76] but not present in any other cell of the study (Figure 5.15).

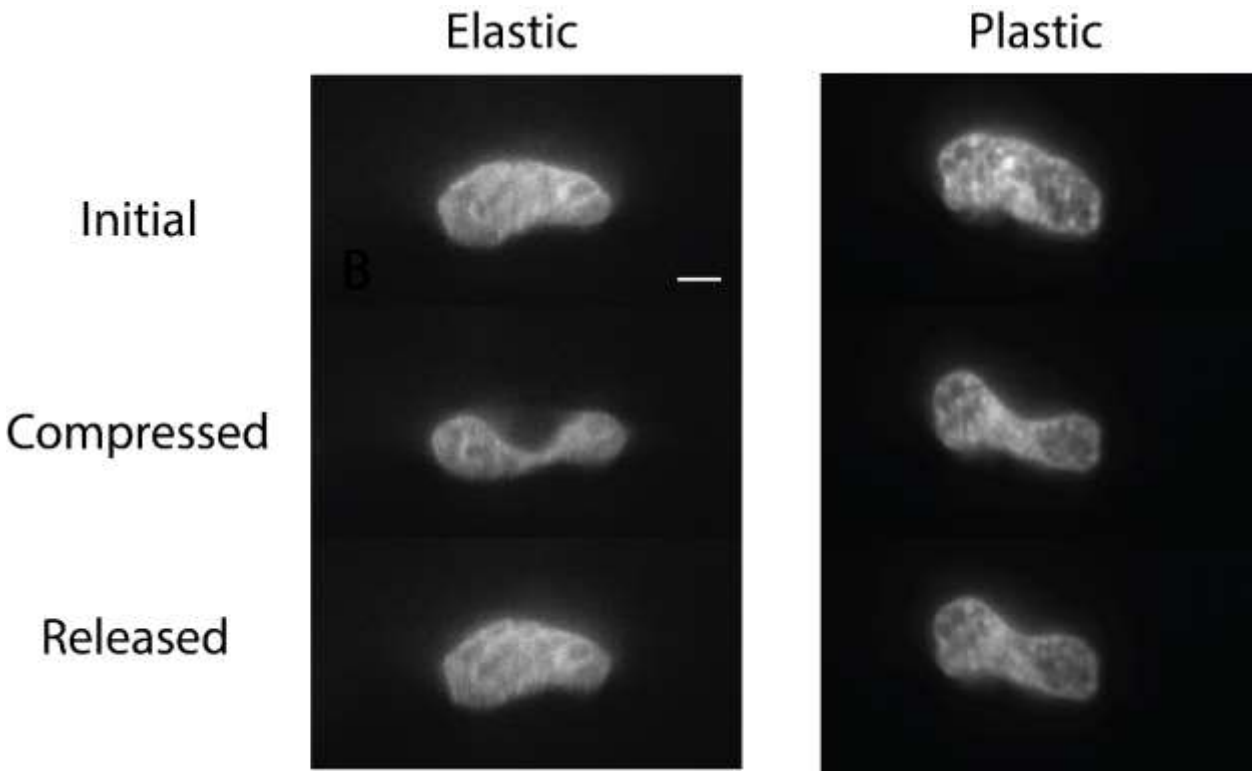

Figure 5.15: Side-view image series for AFM compression of live SKOV3 stably expressing halotagged H2B labeled with Janlia Fluor 549. These cells were compressed 6 days post-transfection of siRNA to halt production lamin A/C. One nucleus (left) shows elastic behavior, while the second nucleus (right) shows plastic damage. Scale bar = 5 µm.

5.8.5 Immunofluorescence

To test whether the TSA treatment was effective at inhibiting histone deactylation, we plated cells as described and treated half with TSA as described, and half with a sham pipetting of PBS. At 24 hours, cells were fixed in 4% formaldehyde, permeabilized with .25% Triton x-100, washed and incubated with rabbit monoclonal antibody to acetyl histone H3 (Acetyl-Histone H3 (Lys9) (C5B11) Rabbit mAb #9649, Cell Signaling Technology), 1/400 dilution with 1 mg/mL BSA as blocker, overnight. After primary antibody incubation, cells were washed 3 times, and incubated with Alexafluor 488 goat anti-rabbit IgG (Invitrogen), and 1/1000 dilution of Hoechst 33342 DNA stain for 1 hour. After washing, cells were imaged at 150 ms exposure with 405 nm and 488 nm excitation light (Objective lens: Plan Apo 60x/1.20 W, Nikon) (Figure 5.8A and B).

To test whether the knockdown was successful, we fixed and stained parallel samples with Lamin A/C Antibody (E-1) (sc-376248, Santa Cruz Biotechnology) as described above, but used a Goat anti

Mouse secondary antibody (Alexafluor 568, Invitrogen). Cells plated in parallel were stained with the same solutions and were imaged at 100 ms exposure with 488 nm and 568 nm excitation light (Objective lens: UPlanFL N 40x/1.3 Oil, Olympus) (Figure 5.10A).

After the collection of immunofluorescence images, nuclei were manually segmented in FIJI [250]. For the TSA verification, mean intensity of the H3K9ac marker was calculated for all nuclei (n = 43 for WT, n = 41 for TSA). A t-test shows a significant relative increase in H3K9ac of approximately 250% for TSA treated cells as compared to WT cells (Figure 5.8C). For the Lamin A/C KD verification, mean intensity of lamin was quantified for cells expressing the GFP reporter in LA/C KD nuclei (n = 27) and for all WT nuclei (n = 58). A t-test shows a significant relative reduction in lamin expression for LA/C KD nuclei of approximately 40% as compared to WT nuclei (Figure 5.10B). Note that LA/C KD nuclei appear to have a slightly larger spread area as compared to WT nuclei, which is consistent with previous findings [32].

5.8.6 AFM and Hertzian Analysis

HT1080 and MDA-MB-231 cells expressing a FUCCI reporter were cultured and prepared as stated in the previous AFM-LS section. However, cells were plated directly on collagen-coated coverslips as opposed to collagen-coated PA gels. Epifluorescence was used to first determine if a cell of interest was in S/G2 or G0/G1 phase. Next, a beaded (6 µm diameter) cantilever was positioned directly over top of the cell nucleus. Force curves were acquired at an approach velocity of 1 µm/s with data being acquired at 2 kHz bandwidth. Three replicates were performed for each cell line, resulting in a total of n = 51, 51, 50, 50 for HT1080 cells in S/G2 and G0/G1 phases and MDA-MB-231 cells in S/G2 and G0/G1 phases respectively. To extract the apparent elastic modulus from the force versus indentation data, the Hertz equation for contact between an elastic sphere and an infinite half-space was used and is given as follows

$$F = \frac{4}{3}\frac{E}{1-\nu^2}\sqrt{R\,\delta^3} \tag{5.2}$$

Here, F represents the force as is measured by the AFM, ν is the Poisson ratio which is set to 0.5 for this analysis, R is the radius of the indenter, δ is the indentation, and E is the elastic modulus. Custom Matlab software was used to extract E from the first 1.5 µm of indentation for each force curve. Contact points

were determined algorithmically via a golden-section search method. Results were analyzed by performing an ANOVA with post-hoc Tukey test.

CHAPTER 6: MECHANICAL MODELS OF CELL NUCLEAR MECHANICS[5]

In Figure 1.1 I alluded to the importance of iterative feedback between mechanical models of cell nuclei and physical measurement through force probes and microscopy. Mechanical models can serve either to validate conclusions drawn from experimental data or to provide predictions that guide future experiments. In any case, the importance of mechanical modeling in nuclear mechanobiology has been grossly underappreciated, with purely experimental studies garnering the majority of attention as modeling studies fall aside. In an effort to draw appreciation to the benefits that mechanical modeling can serve the community, Chapter 6 provides a review different classes of models, the ways in which nuclear mechanical constituents are treated in the models, and the physiologically-relevant problems these models address. Furthermore, I develop my own continuum model for AFM compression experiments as a means of validating my experimental conclusions from Chapter 5. While theory and simulation often take a back seat to beautiful images and experimental data, I hope to tip that narrative slightly towards equilibrium through this chapter.

6.1 Introduction

The cell nucleus is not only the site of transcriptional activity and DNA replication in eukaryotic cells, but its mechanical properties additionally serve to both protect the genome and transfer mechanical signals from the extracellular environment to the chromatin. The nuclear lamina, which forms a protein meshwork along the underside of the nuclear envelope, is one of the primary mechanical constituents of the nucleus. A variety of disease states ranging from heart disease [294] to premature aging called progeria [295] are associated with defects in the nuclear lamina. These and many other diseases, such as cancer [296-299], are known to be associated with both altered nuclear morphology and mechanical

[5] Portions of this chapter are previously published in Hobson, C. M. and A. D. Stephens (2020). "Modeling of Cell Nuclear Mechanics: Classes, Components, and Applications." Cells **9**(7). and Hobson, C. M., et al. (2020). "Correlating nuclear morphology and external force with combined atomic force microscopy and light sheet imaging separates roles of chromatin and lamin A/C in nuclear mechanics." Mol Biol Cell: mbcE20010073.

properties, which are then known to increase nuclear blebbing, nuclear rupture, DNA damage, and cellular invasiveness. Mechanical modelling of cell nuclei has become a growing area of research for the last decade because of the physical nature of these processes. The purpose of this chapter is to introduce mechanical modeling to a broad audience as well as discuss a variety of current and future applications of mechanical modeling regarding cell nuclei. In this chapter, we outline the primary classes of mechanical models along with their advantages and limitations. Additionally, we detail the current experimental understanding of the mechanical constituents of the nucleus, including the cytoskeleton, lamins, and chromatin, as well as the ways in which they have been modeled. Subsequently, we discuss the importance of mechanical models in interpreting experimental data across different assays. Finally, we detail how mechanical models have been used to further our collective understanding of biologically relevant processes such as nuclear blebbing and rupture, as well as lay out areas of nuclear mechanics in need of additional modeling. Given the extensive role of the nucleus in cellular function and the association of mutations in the genes that encode the nuclear lamins with disease, mechanical modeling has and will continue to serve a vital role in interpreting current results and providing predictions to guide new experiments.

6.2 Classifications of Mechanical Models

Broadly speaking, mechanical models of nuclei can be broken down into three categories: (i) schematic models, (ii) continuum mechanics (CM) models, and (iii) molecular dynamics (MD) simulations (Figure 1). Schematic models are not necessarily specific to nuclei as they are often unable to account for geometry and separate components, whereas CM and MD models are designed to be nucleus-specific with accurate geometries and separate roles of nuclear constituents. Other approaches and techniques exist, however a majority of the mechanical models of cell nuclei fall into the aforementioned three categories. Each of these classes have a unique set of advantages and limitations reviewed below and summarized in Table 6.1. One model type is not necessarily better than another, but rather different. The level of specificity and type of a model should be dictated by the phenomena that wish to be studied.

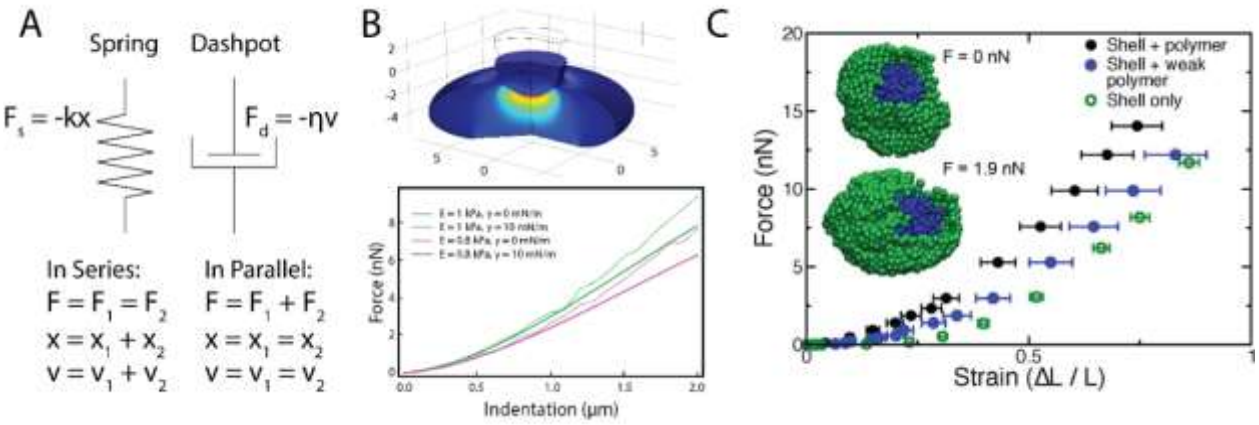

Figure 6.1: Classes of mechanical models. (A) Common components for 1D viscoelastic schematic models where F is the force across a given element, k is the spring constant, η is the viscosity, x is displacement, and v is velocity. (B) A CM model of atomic force microscopy where the nucleus is treated as an elastic solid surrounded by a thin, elastic shell. The axes represent distance in μm. Force versus indentation data shows strain stiffening during compression where the small indentation regime is dictated by the elastic solid and the large indentation regime is dominated by stretching of the elastic shell. Reprinted with permission for *Hobson et al.* (2020) [14]. (C) An MD simulation of micromanipulation of an isolated nucleus. The nucleus is modeled to have a crosslinked polymeric interior that is linked to a polymeric shell. The presence of the polymer interior dictates the initial force response while the shell results in a strain-stiffening response during long extension. Reprinted with permission from *Stephens et al.* (2017) [13].

Table 6.1: A summary of the primary advantages and limitations of the three classes of models.

Model Type	**Advantages**	**Limitations**
Schematic	- Easily solved analytically - Provides a simple equation or set of equations to fit to a given data set - Effective at detecting global changes in mechanical properties - Effective at studying limiting cases where certain structures dominate the system's response	- Not specific to nuclei, but rather applied to nuclear mechanics data - Require unrealistic assumptions regarding homogeneity, dimensionality, and geometry (1D) - Limited in their ability to separate contributions of specific nuclear structures
Continuum Mechanics (CM)	- Can be solved either computationally or analytically - Allow for realistic nuclear geometries - Ability to prescribe different mechanical properties to each structure being modeled - Successful at studying assay-specific nuclear deformations	- Assume each material to be continuous, thus limiting the ability to model polymeric structures or variations in protein concentration - Mechanical properties for each material are prescribed a priori as opposed to being emergent
Molecular Dynamics (MD)	- Quasi molecular-scale modeling of nuclear constituents give a more accurate representation of the polymeric structures	- Computationally intensive due to quasi molecular-scale modeling - Accurate knowledge of interactions between monomers is required

	- Ability to prescribe strength and number of bonds in a given material and between materials - Global material properties are emergent from local, molecular interactions	- Prescribing complex geometries is more difficult than in CM models

6.2.1 Schematic Models

Schematic models are those which use simple combinations of springs and dashpots to provide one-dimensional relationships between stress, strain, and time. A spring has a force response that is proportional to extension or compression while a dashpot has a force response that is proportional to the rate of extension or compression (Figure 6.1A). The primary benefit of schematic models is that, once solved, they provide a set of exact equations to be fit to a given data set. Because of their inherent simplicity, schematic models are extremely successful in detecting changes in mechanical properties due to biological intervention. A classic example is the Jeffreys model which features a spring and a dashpot in parallel, together in series with a second dashpot. This model, when applied to micropipette aspiration data collected on MEFs, has been used to show how lamin A/C-deficient nuclei have reduced viscosity and elasticity [300]. Similarly, a standard linear solid model which features a spring and dashpot in series together in parallel with a second spring has been used to show isolated chondrocyte nuclei are stiffer and more viscous than intact chondrocytes [79]. Schematic models are also quite successful at studying limiting cases: that is, cases where certain structures or phenomena dominate the entire system, allowing for the system's response to be distilled into simple elements such as springs and dashpots. The primary advantages of schematic models are then their ease of use and accessibility, their ability to detect changes in mechanical properties under different conditions, and their success in studying limiting cases.

Schematic models also have a suite of limitations when applied to nuclear mechanics. Exact solutions to physical problems characteristic of these models typically require idealized conditions and sweeping assumptions that almost certainly do not hold true for biophysical problems. Cell nuclei have been shown to be anisotropic [22], heterogeneous [301], and strain stiffening in both compression [14] and extension [13]; this directly invalidates these key assumptions. One must then be cautious in interpreting the absolute magnitude of the mechanical properties determined by such schematic models

as their assumptions are often not met. Other common assumptions surround nuclear geometry and structure, where in schematic models the nucleus is often assumed to be a one-dimensional object that glosses over the intricacies of the chromatin, lamins, and their connections. Revisiting the aforementioned example of the Jeffreys model, the investigators showed a significant decrease in all parameters associated with the model when comparing lamin A/C-deficient MEFs to healthy MEFs. This means the model was not successful in distinguishing the specific role of lamin A/C in nuclear mechanics as it could not be associated with a specific element of the model being applied. Simply put, schematic models make it difficult to determine differential contributions of nuclear components. Along these lines, schematic models are generally not specific to cell nuclei; that is, each element in the model is not necessarily equated to a mechanical constituent of the nucleus. Schematic models are rather just applied to data taken on cell nuclei. Schematic models provide an approachable and easy-to-use means of characterizing changes in mechanical properties and studying limiting cases or dominant phenomena. However, users must be wary of the assumptions made in their derivation when considering their results.

6.2.2 Contiuum Mechanics (CM) Models

CM models are those which assume that the materials being modeled are continuous as opposed to discretized particles (Figure 6.1B). These models can either be solved analytically or computationally. The former generally requires more stringent assumptions while the latter allows for additional flexibility and specificity. A classic example of an analytically-solved CM model is the Hertz contact mechanics model which presumes contact between two linearly elastic, homogeneous, isotropic solids under small indentations [278], which is an idealistic approximation of a nucleus under compression. The Hertz model has been used extensively and successfully in atomic force microscopy (AFM) studies to highlight the importance of chromatin compaction and lamin A/C in the mechanical integrity of nuclei [48, 302]. However, computationally solving CM models through means such as finite element analysis (FEA) allows investigators to circumvent some of assumptions of analytically-solved CM models at the cost of computational intensity. For example, computationally-solved CM models of AFM have allowed investigators to move beyond the Hertz model and study the separate roles of lamins and chromatin, more accurate nuclear geometries, and viscous contributions [14, 42, 303, 304]. The first benefit of this

approach is in the flexibility of the geometry of the system. The investigator can not only set up the model to more accurately describe the geometry of the nucleus being studied, but also vary this geometry to understand the dependence of the mechanical response on the geometry itself. An example is one of the foundation studies of nuclear mechanics which modeled plate compression of spread, rounded, and isolated nuclei [280]. Furthermore, an additional advantage is the ability to prescribe layers to a system, each with different mechanical properties. This is a simple way to model, for example, the inner and outer nuclear membranes as well as the nuclear lamina separately with little added complexity for the user [279, 303]. Additionally, each of these layers can be prescribed a separate constitutive law based on the current understanding of the literature. Finally, CM models are quite advantageous for modeling specific assays because of their ability to quickly and precisely set up the geometry of a system.

There are limitations, however, to using CM models. The first of these is that CM models assume that each material and layer is continuous. More specifically, CM models do not model polymeric systems or motion of individual proteins, but instead smooth over the complex filamentous nature of, for example, the nuclear lamina and treats it as a continuous solid shell. This is an inherent limitation in that CM models do not account for the true physical structure of the constituents of the nucleus, such as the meshwork nature of the nuclear lamina [305-307]. Furthermore, CM models require that you know and prescribe the mechanical properties of each material a priori. This is in contrast to a simulation for which the mechanical properties are emergent. CM models are then advantageous for prescribing realistic geometries and easily modeling multiple layers with different material properties. However, they are limited in that they require a priori assumptions of the material properties of the system and cannot model non-continuous materials.

6.2.3 Molecular Dynamics (MD)

The final class of models are MD simulations (Figure 6.1C). In these MD simulations, nuclei are discretized on a quasi-microscopic level. Individual molecules can be linked together through specified interactions – such as a spring-like force – to form polymeric chains with motion subject to Newton's laws. The polymers can then be organized to form structures such as chromatin fibers or the nuclear lamina, and subsequently be subjected to external forces. The first advantage of MD simulations is that they can

provide a more accurate structural representation as both chromatin and the nuclear lamina are effectively polymer networks [305, 307-309]. Furthermore, these models allow the investigator to prescribe both the location and strength of the bonds between nuclear substructures. For example, one recent study has investigated the role of the bond strength between the cytoskeleton and the nucleus in regulating nuclear shape fluctuations [310]. A third unique advantage of MD simulations is that the mechanical response is often emergent and not prescribed. That is, the investigator will define the specific interactions between monomers to form polymers as well as the number of polymers and the interactions between them, but the simulation will then reveal the mechanical response of this polymer meshwork. This has been used to show that nuclei exhibit strain stiffening in micromanipulation experiments without needing to prescribe any strain-stiffening phenomena directly into the model itself [13, 281]. Similar to CM models, MD simulations allow investigators to easily prescribe multiple materials with varied interactions.

As with the previous techniques, MD simulations also have a set of limitations. First, MD simulations are limited in their accessibility to the broader biological community. They often require extensive computational power and expertise to design effective and realistic MD simulations. An additional limitation is that they are often coarse-grained simulations. That is, there is often a loss of structural detail in both the chromatin and lamin networks. Coarse-graining the model then means that tuning the strength and number of interactions between monomers is non-trivial and not necessarily indicative of the true molecular-scale interactions. They are also limited in their ability to study how varying the material properties of a specific nuclear substructure alters the mechanical response. In an MD simulation, one can alter that interactions between monomers, but not specifically change the overall material properties as easily as in CM models. MD simulations then provide a means of modeling the polymeric nature of the nuclear substructures as well as allow for emergent phenomena to be discovered, but they are limited in overall accessibility and the need for precise knowledge of quasi-molecular-scale interactions.

6.3 Nuclear Mechanical Constituents and How They Are Modeled

While the cell nucleus is a beautifully complex system, its mechanical response is in general dependent on 3 things: the cytoskeleton, the nuclear lamina, and the chromatin (Figure 6.2). These structures are themselves composed of multiple constituents, each of which are dynamic with intricate molecular-scale interactions [93, 311, 312]. Additionally, these structures are not independent. They form a mechanical and biochemical pathway from integrin receptors to the nuclear interior, capable of propagating forces on the cell surface to the DNA and subsequently altering transcription [26, 28, 29]. Mechanical modeling, however, has not yet reached this full level of detail and often takes a coarse-grained approach to studying their respective roles. Here, we review the current understanding of the mechanical roles of these three structures based on experimental data and how they have subsequently been treated in nucleus-specific CM models and MD simulations (Table 6.2) [12].

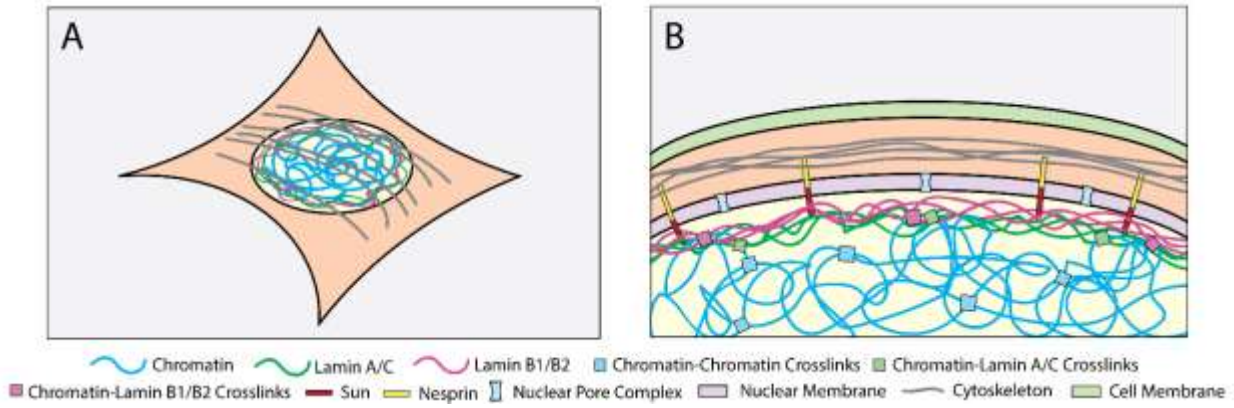

Figure 6.2: Schematic view of the cell nucleus. (A) A schematic of a whole cell. (B) A close-up, cross-section schematic of the ventral half of the cell drawn in (A). The proteins, structures, and interactions are a subset of the full system, but are historically those which are relevant to consider when developing a mechanical model for nuclei.

Table 6.2: Summary of nucleus-specific mechanical models. Column 1 provides the class of model. CM-A: analytically-solved continuum mechanics model. CM-C: computationally-solved continuum mechanics model. MD – Molecular dynamics model.

Assay or Phenomenon	**Cytoskeletal Component**	**Lamins Component**	**Chromatin Component**	**Simulation Conclusions**	**Reference**
AFM (CM-C)	N/A	Elastic Shell	Elastic Solid	- Nuclei exhibit strain stiffening in AFM	Hobson, C., M. …

				- Chromatin resists volume changes at small indentations - Lamin A/C resists surface area changes causing strain stiffening at large indentations	Superfine, R. [14]
AFM (CM-C)	N/A	Elastic Shell	Viscoelastic Solid	- Including the nuclear envelope is necessary to recapitulate the magnitude and shape of experimental force versus indentation curves on cells - Force response is sensitive to elasticity of “nucleoplasm” - Force response is highly dependent on probe angle	Vaziri, A., … Mofrad, M. R. K. [303]
AFM (CM-C)	N/A	N/A	Poroelastic	- Nuclei exhibit depth-dependent relaxation rates, consistent with poroelastic materials	Wei, F., … Li, G. [304]
AFM (CM-C)	N/A	Elastic Shell	Elastic Solid (radially-decaying Elastic Modulus)	- A radially-decaying elastic modulus recapitulates experimentally-determined depth-dependent elastic moduli. - Presence of nuclear lamina adds an overall increase of stiffness	Lherbette, M., … Schaap, I. A. T. [42]
Micropipette Aspiration (CM-C)	N/A	Elastic Shell	Viscoelastic Solid	- Micropipette aspiration measurements are highly sensitive to the stiffness of the nuclear lamina	Vaziri, A., Mofrad, M. R. K. [279]
Micromanipulation (MD)	N/A	Polymer Shell	Confined Polymer	- Nuclear lamina buckles with lack of chromatin - Chromatin provides the short extension force response - Lamin determines strain stiffening due to the geometry of the nucleus during long extension - Two regime force response requires both chromatin-chromatin and chromatin-lamin tethers	Banigan, E. J., … Marko, J. F. [281] Stephens, A. D., … Marko, J. F. [13]
Plate Compression (CM-A)	N/A	Elastic Shell	Viscoelastoplastic	- Lower stiffness of the nuclear lamina increases nuclear plasticity - Increased stiffness of the “nucleoplasm” increases nuclear plasticity	Deveraux, S., … Aubry, D. [313]

Plate Compression (CM-C)	Hyperelastic	N/A	Hyperelastic	- Force response is dependent on cell and nuclear geometry, with spread cells appearing stiffer than round cells, both of which appear stiffer than isolated nuclei	Caille, N., … Meister, J. J. [280]
Actin Compression (CM-A)	Uniform Compressive Plate	Elastic Shell	N/A	- Provide equations linking nuclear shape to applied force and elastic modulus	Balakrishnan, S., … Ananthasuresh, G. K. [46]
Substrate Stretching and the Actin Cap (CM-C)	Shear deformable beams	N/A	Elastic Solid	- Stress concentrates along the edges of the nucleus in absence of actin cap - Absence of actin cap increases nuclear stress	Kim, J. K., … Kim, D. H.[32]
Constricted Migration (CM-A)	N/A	(i) Elastic Shell (ii) N/A	(i) Inviscid Fluid (ii) Elastic Solid	- Provide relationship between mechanical properties and active processes for migration - There exists a critical pore radius for which a cell can enter based upon nucleus stiffness and the ability to form adhesions	Giverso, C., … Prezisosi, L. [314]
Constricted Migration (CM-C)	Driving Force for Migration	Hyperelastic Shell	Poroelastic	- Resistance to transmigration is dependent on ECM stiffness, pore size, and lamin A/C stiffness - Lower lamin A/C stiffness results in increased nuclear plastic damage - Model predicts buckling of the lamina, nuclear rupture, and volume loss	Cao, X., … Shenoy, V. B. [66]
Constricted Migration (CM-C)	N/A	N/A	Hyperelastic Solid	- There exists a critical force a cell must overcome to enter a constricted pore - The critical force increases as the pore size decreases and/or the stiffness of the environment increases - Decreases in the stiffness of the nucleus decrease the critical force	Heo, S., … Mauck R. L. [315]
Constricted Migrati	Driving Force for Migration, Viscoelastic	Viscoelastic Shell	Elastoplastic	- Nuclear softening increases invasiveness - Nuclear stiffening increases plastic damage of the nucleus	Mukherjee, A., … Sen, S. [316]

on (CM-C)				- Constricted migration leads to kinking of the nuclear membrane	
Nuclear Blebbing (MD)	N/A	Two-Polymer Shell	N/A	- Retraction of blebs with only A-type lamins follow a double-exponential decay - Retraction of blebs with A- and B-type lamins follow an exponential decay - One-component blebs can stabilize in the blebbed state	Wren, N. S., … Dahl, K. N. [317]
Shape Fluctuations and Nuclear Blebbing (MD)	Point particles connected to lamina via springs	Polymer Shell	Confined Polymer	- Tethering between chromatin and nuclear lamina is necessary for bleb formation - Stiffness of connection between the nucleus and cytoskeleton correlates with nuclear shape fluctuations	Lionetti, M. C., … La Porta, C. A. M. [310]
Nuclear Blebbing (CM-C)	N/A	Two-Material Elastic Shell	N/A	- Larger mesh size of A-type lamins relative to B-type lamins is required to form nuclear blebs	Funkhouser, C. M., … Olvera de la Cruz, M. [318]
Nuclear Rupture and Chromatin Herniation (CM-A)	N/A	Viscoelastic Shell	Semi-Flexible Polymer	- Rupture site radius increases exponentially to a critical value before closing linearly in time. - Increased viscosity of the nuclear lamina minimizes rupture radius - Chromatin herniations are exponentially sensitive to rupture radius	Deviri, D., … Safran, S. A. [319]
Nuclear Rupture (CM-A)	N/A	Elastic layer with and without nuclear pore complexes	N/A	- Develops scaling laws between hole nucleation rate and strain on the lamina for homogenous and heterogeneous lamina layers. - Predicts that increased lamin density correlates with a transition from homogenous to heterogeneous nucleation mechanisms	Deviri, D., … Safran, S. A. [320]
Nuclear Rupture (CM-C)	Fluid	N/A	Fluid	- Rate of outflow of nuclear contents correlates with the diameter of the rupture site	Zhang, Q., … Lele T. P. [272]
DNA Damag	N/A	N/A	Elastic-Fluid	- Separation of repair proteins from the chromatin resulting in delayed repair is sufficient to	Bennett, R. R., … Liu, A. J. [282]

e (CM-A)				recapitulate experimental observation of increased DNA damage in constricted migration	
Cell Detachment and Attachment (CM-C)	Compressive Plate	Hyperelastic Shell	N/A	- Higher pressure and thinner nuclear lamina increase wrinkling of detached nuclei - Nuclear volume decreases upon detachment	Kim, D. H., … Sun, S. X. [276]
Cell Spreading, Geometric Constraints* (CM-C)	Provide Compressive Stress	Stiffening filamentous network	Elastic Solid	- Cell geometry alters local stresses which regulate nuclear architecture and mechanics - A 3-way feedback mechanism between the nucleus, the cytoskeleton, and adhesions recapitulates experimental results regarding cell geometric constraints and can predict implications of cytoskeletal disruptions	Alisafaei, F., … Shenoy, V. B. [129]
Cell Spreading (CM-C)	Compressive contractile network	Elastic Shell	Elastic Solid	- Cell spreading is necessary and sufficient to drive nuclear flattening	Li, Y., … Dickinson, R. B. [321]

*This work features several different models for which a full description is outside the scope of this table.

6.3.1 Cytoskeleton

The cytoskeleton primarily consists of actin, microtubules, and intermediate filaments. Arguably the most important of these constituents for nuclear integrity and mechanics are actin and vimentin intermediate filaments. In spread cells, actin has been experimentally shown to form a perinuclear cap that is important for mechanosensation, cell migration, and nuclear shape [31, 36, 321, 322]. Additionally, Arp2/3-driven actin polymerization has been shown to disrupt the nuclear lamina and facilitate constricted migration [323]. The cytoskeleton also serves an antagonistic rule as both actin and microtubules can deform the nucleus [266, 324, 325]. The literature regarding actin and the actual mechanical properties of the nucleus are seemingly conflicting, likely due to extension- versus compression-based force measurements and the aforementioned antagonistic behavior. Single and dual micromanipulation extension studies have concluded that actin is not critical for protecting against nuclear shape change

under external force [21] or *in vivo* or *ex vivo* single nucleus force measurements [13]. AFM studies with sharp probes compressing nuclei, however, concluded actin depolymerization reduces nuclear elasticity and viscosity [25]. Vimentin – an intermediate filament shown to be itself strain stiffening [326, 327] – forms a perinuclear cage [328]. This cage has been experimentally shown to maintain nuclear positioning and deformation in the cell through single micromanipulation studies [21], AFM [24], and constricted migration assays [329].

Despite these significant contributions of the cytoskeleton to nuclear integrity, a majority of mechanical models consider only isolated nuclei, in which vimentin does not contribute to nuclear mechanics [13]. The models that consider the cytoskeleton often seek to model its role as either a compressive element in nuclear flattening [32, 46, 129, 321] or a mechanism of facilitating constricted migration [66, 316]. Only one mechanical model has studied the role of vimentin in AFM simulation; vimentin was modeled as a cage-like structure and simply shown to resist nuclear deformations [129]. There is then a need in the current literature surrounding mechanical models that include the cytoskeleton as a relevant structure to elucidate its specific role in either inducing or protecting nuclear strain and deformation.

6.3.2 Lamins

The second mechanical constituent of the nucleus is the nuclear lamina. Here, we provide a review of the nuclear lamina as well as the ways it has been mechanically modeled. The nuclear lamina forms a thin protein meshwork along the inside of the nuclear envelope and consists of two primary types: A- and B-type lamins [330]. A-type lamins consist of lamin A and C; B-type lamins consist of lamin B1 and B2. The nuclear lamina is of particular interest in nuclear modeling because it is a major mechanical component of the nucleus [60] and thus has roles in nuclear morphology [32], bleb formation [330], and nuclear rupture [331] especially during migration [62, 69, 71]. Early micropipette aspiration experiments showed the relevance of the nuclear lamina to the elastic response of nuclei [75]. Lamins' storied role in nuclear mechanics has led to its inclusion in most mechanical models. Most commonly (and simply), the nuclear lamina has been modeled as a linear elastic shell, either infinitely thin [14] or with some finite thickness [42, 46, 279, 303, 313, 314]. This serves primarily to capture the mechanical resistance from

stretching of the nuclear lamina, but may oversimplify key experimental findings. Lamin B1 has itself been experimentally shown to be strain stiffening [332]. Along these lines, lamin A/C and B1/B2 have been shown to have a low persistence length suggesting they are easy to bend but hard to stretch like idealized worm like chain models [307]. Simulations using a hyperelastic shell model for the nuclear lamina employed by some investigators [66, 276] are then more applicable for modeling this behavior as it captures the nonlinear force response at high strains. There is further experimental evidence that the nuclear lamina has a viscous response on relevant timescales [41, 76, 333]; various groups have sought to model this by treating the nuclear lamina as a viscoelastic material as opposed to purely elastic [316, 319]. Outside of continuum theory, the lamina has been modeled as a meshwork of polymers [13, 129, 281, 310, 317], providing a more physical representation of the true structure visualized and detailed by super-resolution microscopy studies [305, 306] and cryo-electron tomography [307]. Such modeling allows for studying the implications of altered mesh sizes, fiber stiffness, and bond strengths, which are parameters not easily accessible through experimentation or continuum modeling. Because of its clearly demonstrated importance in nuclear integrity, the nuclear lamina is an essential component of any nuclear mechanical model.

The majority of the previously mentioned techniques of modeling the nuclear lamina treat it as a single-material system; this is not the case. As previously noted, the nuclear lamina consists of both A- and B-type lamins, which serve distinct roles both in nuclear mechanics and nuclear function. It was originally thought that only lamin A/C was relevant for nuclear mechanics [18], and that lamin B1 was more so associated with proper orientation of the nucleus relative to the cell body [334]. However, it was later shown that in micropipette aspiration experiments that the ratio of A-type to B-type lamins was positively correlated with nuclear stiffness [41]. Additional work has shown that when nuclei with already low levels of lamin A/C are experimentally depleted of lamin B1, nuclei become stiffer in both micropipette aspiration [78] and micromanipulation experiments [13]. Furthermore, viscoelastic studies have suggested that lamin A/C could be the primary viscous contribution and lamin B1/B2 could be the primary elastic contribution to mechanical response [41, 67]. Although, there is no mechanical modeling to back these conclusions. Recent work has also shown that lamin B2 mimics the role of lamin A/C in that decreasing levels of lamin B2 induces nuclear softening and increases migration [335]. The distinctions

between lamin A and C as well as lamin B1 and B2 provide an additional level of depth to be researched. Not only do they serve separate mechanical purposes, but they also are post-translationally modified differentially and spatially separated as well. While both lamin A/C and B1/B2 are post-translationally farnesylated, lamin A/C is further processed to lose the farnesyl group and lamin B1/B2 maintains it [336]. This differential farnesylation is believed to underlie the reason lamin B1/B2 resides approximately 10-20 nm closer to the nuclear periphery as determined by super resolution microscopy methods [17]. To date, few models have sought to account for the different types of lamins. A polymer-based model [317] and a CM model [318] have worked to capture this by treating lamin A/C and lamin B1/B2 as distinct materials to study bleb formation. However, there are little-to-no mechanical models that treat lamin A/C and lamin B1/B2 as separate materials with different viscoelastic properties in the common assays such as AFM and micropipette aspiration. For a complete model of the complexity of the nuclear lamina, one would need to account for each trait detailed here – elasticity, strain stiffening, viscosity, polymeric structure, separation of lamin A/C and lamin B1/B2 – as well as the variation in density of lamin A/C and lamin B1/B2 around the nuclear surface.

6.3.3 Chromatin

Chromatin is the final mechanical constituent of the nucleus. Initial micropipette aspiration studies of isolated *Xenopus* oocyte nuclei concluded that chromatin had little role in the mechanical properties of nuclei [75]. Later research, however, has concluded otherwise, specifically showing that the compaction levels of chromatin are directly related to nuclear stiffness and dominate small deformations [6, 13, 14, 48, 76, 269, 337]. Early models of nuclear mechanics consistently refer to the nuclear interior as the “nucleoplasm” [279, 303]; this term inaccurately portrays the nuclear interior as purely fluid-like. Experimentally, the chromatin has been observed to have an elastic response which is inconsistent with pure fluid-like behavior. The simplest model of the chromatin is then a purely elastic solid, which captures only the elastic response and ignores the viscous contribution from the surrounding fluid [14, 129]. An improved approach is taken by other groups where the chromatin and the surrounding fluid are more appropriately modeled as viscoelastic [279, 303, 313, 316], which is consistent with experimental observations in intranuclear protein mobility [83] and micropipette aspiration [45, 79, 300]. A further

alternative approach is the poroelastic model of chromatin. [66, 304]. A poroelastic material accounts for viscous flow through defined pore sizes, similar to flow of the surrounding medium through the chromatin. Such materials are characterized by a strain-dependent viscous response, which has been observed in AFM studies [304]. This builds on purely viscoelastic treatments as it can inform how the compaction state of chromatin, and the subsequently altered pore size, could have an influence on the viscous response as well as the elastic response Increased viscosity has also been shown to be a signature of high-risk leukemia cells [338]. These viscous contributions from bulk nuclear deformation must be carefully considered as they may not be present for physiologically relevant timescales of approximately 10s of nm/s [339, 340]. Outside of continuum theory, the chromatin has been modeled as a confined polymeric system tethered to itself and the nuclear surface [281, 310]. With the recent developments regarding the mechanical role of chromatin, it is crucial that it be accurately modeled in studies of nuclear mechanics moving forward.

6.4 Modeling of Assays for Studying Nuclear Mechanics

One purpose of mechanical modelling in informing how changes in nuclear mechanics can be measured by experimental techniques. Most experimental studies use a simple schematic model to extract material properties from a given data set. This approach can be quite useful in understanding the dominant response in a given system, yet it glosses over the intricacies of each assay. Additional computational modeling provides this added insight of the assays used to probe nuclear mechanical properties. Such modeling has been done for almost all experimental techniques, including AFM [14, 303, 341], micropipette aspiration [279], micromanipulation [13, 281], constricted migration [66, 314, 316], substrate stretching [32], plate compression [280, 313], and magnetic bead twisting [59]. A majority of these computational models are CM models because of the ease of defining a geometry consistent with the assay. Results of these models often show discrepancies from their schematic counterparts, generally providing a more accurate representation of the experimental data.

6.4.1 Modeling Resolves Contrasting Experimental Results Across Assays

Each assay mechanically probes the nucleus in different ways; mechanical models are especially useful in determining how a given assay may be more or less sensitive to specific nuclear structures, time scales, or length scales. For example, one group developed nearly identical CM models of micropipette aspiration and AFM with conical tips, both modeling an isolated nucleus consisting of the outer and inner nuclear membranes, the nuclear lamina, and the "nucleoplasm" [279, 303]. Their simulations showed that micropipette aspiration is highly sensitive to changes in the stiffness of the nuclear lamina relative to the "nucleoplasm" [279]. Their AFM simulations, however, were quite sensitive to changes in the elasticity of the "nucleoplasm" [303], or more appropriately the chromatin filling the nucleus. This provides insight into why early micropipette aspiration measurements did not see chromatin as a relevant mechanical constituent [75] until the chromatin was condensed drastically via divalent ions [76], whereas AFM studies have clearly shown the relevance of chromatin to the elastic response of nuclei [14, 48]. These simulations showed that the intranuclear strain is dependent on the geometry by which the nucleus is deformed, which subsequently leads to more specified probing of the lamina in micropipette aspiration. Similar geometry dependence has been shown for simulated micromanipulation [281]. This highlights further how and specifically why conclusions made with one assay may not necessarily transpire directly to another assay. Such comparative modelling of assays could help clarify the seemingly conflicting experimental results of the mechanical role of actin previously noted where clear differences are seen between extensional and compressive measurements [13, 21, 25]. Mechanical models are paramount for providing more informed conclusions about one's experimental data and are likely to clarify the origin of conflicting results as different perspectives rather than right versus wrong.

6.4.2 Emergent Mechanical Phenomena from Complementary Experimental Assays – Strain Stiffening

Models of nuclear mechanics assays have also been useful in explaining emergent experimental findings. A specific example regards the relative contributions of the nuclear lamina and chromatin. We previously described how both the nuclear lamina and chromatin contribute to the mechanical response of nuclei. Micromanipulation experiments of isolated nuclei were able to separate their respective roles. They showed the existence of a two-regime force response where the low-strain regime (< 3 μm) is

dominated by chromatin and the high-strain regime (>3 μm), specifically strain stiffening, was dominated by the nuclear lamina. The investigators developed an MD simulation of a polymer shell (lamina) filled with a cross-linked polymeric interior (chromatin) that recapitulated the experimental results of both strain stiffening as well as predicted buckling of the lamina in the absence of chromatin [13, 281]. Our results build upon this work by showing similar strain-stiffening results in AFM compression. To validate our conclusions and connect our results to mechanical properties, we developed a simple computational model of AFM indentation experiments. As the nucleus is the stiffest sub-cellular structure and the focus of our analysis, we chose to model only deformation of the nucleus. We constructed an axisymmetric finite element analysis (FEA) model featuring a stiff, spherical, polystyrene indenter and an ellipsoidal nucleus (Figure 6.3A). Previous research has examined FEA models of AFM [341, 342], yet to our knowledge none have examined the relationship of nuclear morphology and force. The nucleus in our model features two separate materials: an infinitely thin, elastic membrane with a stretch modulus (γ) wrapped around an elastic solid with an elastic modulus (E). This then does not account for the interaction between the outer nuclear membrane and the endoplasmic reticulum, and instead models primary the closed system of the nuclear lamina and chromatin. The model assumes quasistatic behavior.

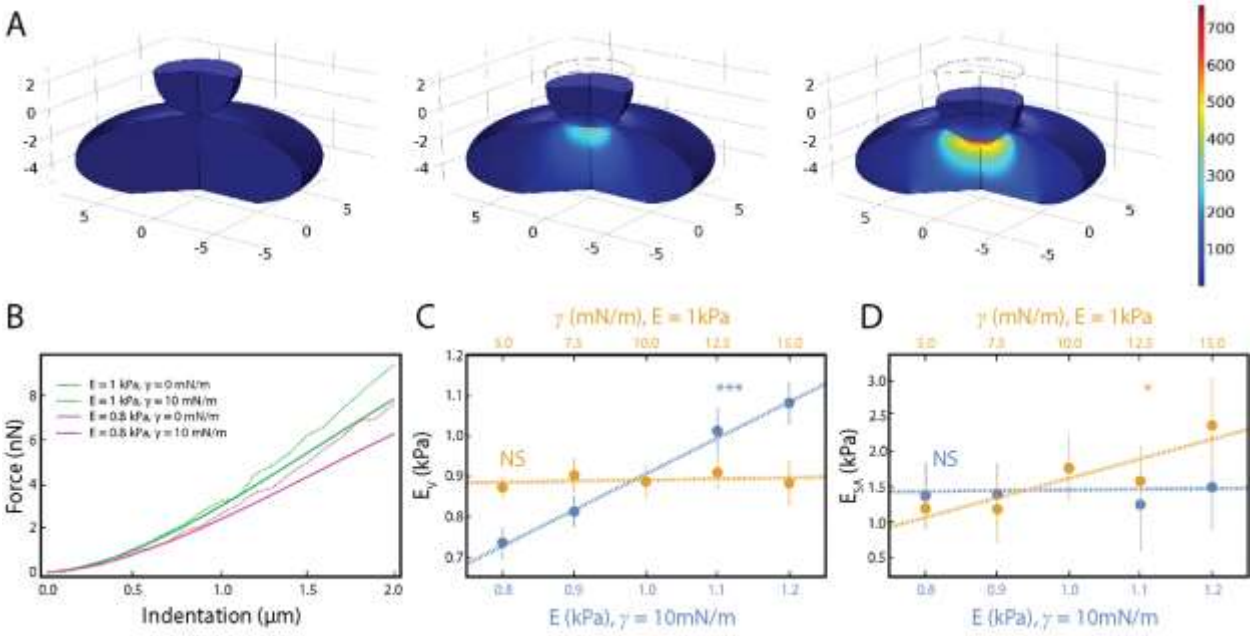

Figure 6.3: Finite Element Analysis (FEA) model of AFM indentation. (A) Selected frames from a finite element analysis simulation of a nucleus undercompression. The nucleus has an elastic modulus, E, and a separate stretch modulus, γ. (B). Force versus indentation shown for varied E and γ. (C). Resistance to nuclear volume change, E_V, plotted against variations in both E and γ. A significant correlation (p<0.001)

is seen between E_V and E, but no significant correlation is seen between E_V and γ. (D). Resistance to nuclear surface area change, E_{SA}, plotted against variations in both E and γ. A significant correlation ($p<0.05$) between E_{SA} and γ is seen, but no significant correlation is seen between E_{SA} and E. See also Video 6.1.

We simulated AFM indentation with varied values of E and γ and examined the qualitative changes in the force-indentation curves (Figure 6.3B). We found that varying the elastic modulus leads to softening over the entirety of the indentation. However, variations in the stretch modulus of the elastic layer led to altered behavior only at larger indentations (> 0.5 μm). This corresponds directly with our observation from our AFM-LS experiments. We showed that decondensation of chromatin and knockdown of lamin A/C lead to decreases in E_V and E_{SA} respectively, and E_V provides resistance over the entire indentation while E_{SA} provides the additional resistance at larger indentations.

Observing the same qualitative behavior in the force-indentation curves provided motivation to correlate the material properties of the FEA model (E, γ) with E_V and E_{SA}. To do so, we performed identical analysis for extracting E_V and E_{SA} as previously described on our FEA model data. By varying either E or γ while keeping the other constant, we were able to study these correlations. We examined correlations between E_V (Figure 6.3C) and E_{SA} (Figure 6.3D) with E (blue) and γ (orange). We observed a significant, linear correlation between E_V and E as well as E_{SA} and γ; no significant correlation was observed between either E_V and γ or E_{SA} and E. This shows that our resistances to nuclear volume change and nuclear surface area change (E_V and E_{SA}) are indicative of material properties of the nucleus. Specifically, E_V is a representative measure of the elastic modulus of the nucleus and E_{SA} is a representative measure of the nuclear stretch modulus. We then find that our measured mean E_V of 0.58 kPa corresponds to E = 0.63 kPa and our measured mean E_{SA} of 0.79 kPa corresponds to γ = 2.5 mN/m, both of which are consistent with the current literature for Young's modulus measurements of the nucleus and stretch modulus of the nuclear membrane respectively [24, 25, 43-45, 50, 51, 75]. Furthermore, we varied the size of our model nucleus and found that E_V and E_{SA} are independent of initial nuclear size (Figure S8), similar to our results from experiments (Figure 6.4).

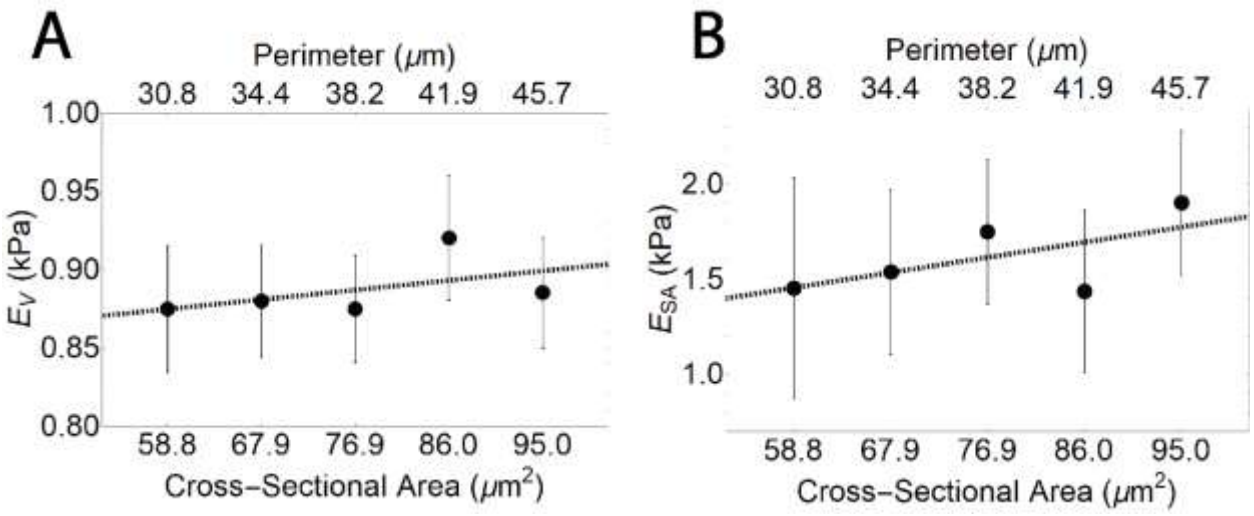

Figure 6.4: E_V and E_{SA} extracted from FEA model are independent of initial nuclear morphology. Plots of E_V (A) and E_{SA} (B) versus nuclearly morphology as well as best fit lines. A Pearson's correlation test gives no significant correlation between E_V or E_{SA} and initial nuclear morphology.

All finite element analysis (FEA) modeling was performed in COMSOL Multiphysics 5.2a. The geometry was defined in 2D under axisymmetric assumptions. The AFM tip was modeled to be an elastic sphere of radius 3 μm with an elastic modulus of 3.5 GPa and Poisson ratio of 0.3. The nucleus was modeled to be an elastic ellipsoid with a long axis radius of 8.5 μm and a short axis radius of 3 μm. The bottom 1.5 μm of the ellipsoid was truncated and set to be a fixed constraint. The nucleus had a Poisson ratio of 0.3 and an elastic modulus varied about 1 kPa. The nucleus was wrapped in a thin elastic layer governed by a total spring constant which varied about 10 mN/m. The thin elastic layer also changes the boundary condition between the nucleus and AFM tip such that forces on either side of the boundary are equal in magnitude and opposite in direction, but the displacements on the either side of the boundary are no longer coupled. To simulate indentation, the AFM tip was incrementally stepped a total distance of 2 μm in steps of 0.1 μm. At each step, the MUMPS solver was used to solve for the displacement and stress along the mesh. A surface integral on the AFM tip provided the reactionary force at each indentation step; nuclear morphology was also extracted at each indentation step. All analysis was performed under that assumption of quasistatic behavior; that is, no time-dependence was accounted for in our FEA model. The equation governing the behavior of elastic solids is given by

$$0 = \nabla \cdot \mathbf{S} + \overrightarrow{F_V} \tag{2}$$

where $\mathbf{S}$ is the stress tensor and $\overrightarrow{F_V}$ is the volume force. The equation governing the thin elastic layer is given by

$$\boldsymbol{S} \cdot \vec{n} = -\frac{\gamma}{A}\vec{u} \tag{3}$$

where $\boldsymbol{S}$ is the stress tensor, $\vec{n}$ is the vector normal to the surface, γ is the stretch modulus, A is the contact area, and $\vec{u}$ is the displacement field.

In both instances of micromanipulation and AFM, the mechanical models explained that geometry alone is sufficient to induce strain stiffening; non-linear material properties are not necessary. They additionally provided a means of simulating the effects of knocking down lamin A/C as well as decompacting chromatin, providing support to the conclusions that chromatin dominates small nuclear strains while the lamina provides strain stiffening at large nuclear strains. Finally, lamin strain-stiffening is supported by many experiments including *in vitro* filament stretching [332], short persistence length measurements [307], nuclear morphology during cell seeding [321], nuclear stress stiffening [76], and non-linear nuclear osmotic properties [277]. Observing emergent phenomena in nuclear mechanics must be solidified and backed by accurate mechanical models that validate the source of these phenomena. Here, lamin-based nuclear strain stiffening has been supported both by complementary experimental techniques of extension (micromanipulation) and compression (AFM), but also by complementary MD simulations and CM modeling respectively.

6.5 Applications of Mechanical Models to Biologically Relevant Processes

Mechanical models have historically been useful in informing our collective understanding of a variety of biological processes. Here, we review the major topics for which these models have proven useful for understanding key biological processes. These topics include cellular migration, nuclear blebbing, nuclear rupture, and cell spreading and detachment. Specifically, we detail the major experimental observations and conclusions as well as how mechanical models have been used to explain these conclusions and predict phenomena to be observed in future experiments.

6.5.1 Constricted Cellular Migration

During processes such as cancer metastasis and immune response, cells migrate through tight constrictions resulting in extreme levels of strain, where lamin mechanics dominate. The cell nucleus – and more specifically the nuclear lamina stiffness – was experimentally shown to provide the rate-limiting step in such migration [5, 67]. Softer nuclei, due to lower levels of lamin A/C, have been previously correlated to increased migration efficiency, potentially providing a connection because successful metastasis and altered mechanical properties [67]. Alternatively, recent experimental work has shown also that nuclei treated with Trichostatin A (TSA) to decondense chromatin and subsequently induce nuclear softening leads to slower migration rates [343] but increased successful constricted migration [315]. This is not immediately intuitive as we traditionally understand migration speed to correlate with successful migration. However, decreased compaction could limit the ability of the nucleus to propagate the force necessary to traverse a constriction [344]. It is additionally known that active processes condense chromatin at the induction of cell migration [126]. Finally, the significant external stress on the nucleus during migration has experimentally been shown to cause nuclear rupture and subsequent DNA damage [62, 69, 71] as well as plastic deformation [66, 67]. The physiological relevance of constricted migration combined with the role of mechanical properties in its efficiency make it well suited to be studied by mechanical modeling.

Both mechanical [314, 316] and chemomechanical [66] models have been developed to better understand constricted migration. A crucial result shown in simulation is that decreasing the stiffness of the nuclear lamina allows for increased migration rates, which is consistent with the previously mentioned experimental data. While this does not appear immediately profound, this modeling result highlights that it is actually the mechanical properties of the nuclear lamina that limit migration. While this does not preclude a role for a downstream active response to lowered levels of lamin A/C, this shows that the mechanical properties alone are sufficient to explain the experimental observations. Similarly, modeling concludes that lower nuclear lamina stiffness is sufficient to increase nuclear plasticity [66, 316]. Recent modeling work has begun to study the role of chromatin's material properties on migration, showing through simulation that reducing the stiffness of chromatin decreases the amount of force the cell must generate to enter a constriction [315]. No modeling, however, has studied why chromatin decompaction

serves to slow constricted migration speed. Some modeling has been done to understand the feedback mechanisms that regulate nuclear morphology and chromatin condensation levels [129]; however, no such modeling has been applied to constricted migration. Additionally, these models allow for predictions to be made; one such example is that nuclei undergo volume loss during constricted migration [66], which could have significant implications regarding chromosome territories and transcription as nuclear volume loss has been experimentally shown to lead the nucleus into a transcriptionally quiescent state [35]. While this has yet to be observed in migration assays, nuclear volume loss has recently been shown for similar magnitudes of compression in AFM experiments [14] and plate-compression assays [35]. Mechanical modeling of constricted migration has been crucial for confirming that nuclear mechanical properties in part govern successful migration, but further simulations could inform additional subtleties regarding the role of chromatin.

6.5.2 Nuclear Blebbing and Rupture

Nuclear blebs are defined to be abnormal protrusion from the nuclear surface. Formation of such blebs has been a prominent topic of recent research as they are often associated with a variety of disease states such as leukemia [345], prostate cancer [296], cervical cancer [297], breast cancer [298, 299], progeria/advanced aging, and muscular dystrophy [295]. Depletion or mutation of lamins were the first and most prominent experimental change that cause nuclear blebbing and ruptures. There is conflicting research regarding the composition of the nuclear lamina within nuclear blebs. Early work had defined blebs to be enriched only with lamin A/C and lacking of lamin B1/B2 [330]. However, a recent study has shown the existence of a bimodal distribution wherein approximately half of the blebbed population lacks lamin B1/B2 in the bleb while the other half has lamin B1/B2 in the bleb [270]. The rate of bleb formation has been experimentally shown to increase with lamin B1 deficiencies [346]; recent research has also shown that nuclear blebs can proceed solely from chromatin decompaction and weakened chromatin-based nuclear mechanics, independent of changes to lamins [270, 337, 347]. Further experimental work has shown that the increase in entropic pressure from chromatin decompaction is sufficient not only to induce blebs, but to rupture nuclei [50, 51]. Little is known, however,

on the exact mechanism by which blebs form. Given their association with disease and nuclear rupture, bleb formation and stability are relevant phenomena to investigate through mechanical modeling.

To study nuclear blebs through mechanical models, investigators have modeled the nuclear lamina as a two-material system, allowing them to separate the roles of lamin A/C and lamin B1/B2 in bleb formation [317, 318]. In the earlier study, the lamin A/C and lamin B1/B2 were treated as separate polymeric systems tethered together by a series of connectors. The investigators were more interested in understanding dynamics of blebs as opposed to mechanisms of formation. Blebs consisting of either both lamin A/C and B1/B2 or just lamin A were artificially induced with no physiological mechanisms prescribed. It was shown that blebs enriched in just lamin A/C were more mechanically stable, suggesting that the physical separation of lamin A/C and lamin B1/B2 and the strength of their connections govern the stability of blebs. This model is also consistent with the reduction of αII-spectrin causing nuclear blebs of only one component [348]. The latter model used a CM approach wherein they modeled the nuclear lamina as a shell with each spatial location corresponding to a location of enriched in either lamin A/C or lamin B1/B2 [318]. They modeled bleb formation by considering the preferred nuclear shape due to minimization of bending and stretching energy as a function of the relative amount of lamin A/C to lamin B1/B2 as well as the mesh sizes of each structure. It was assumed in the model that A- and B-type lamins have different preferred curvatures and mesh sizes. Their model showed that a difference in mesh sizes between lamin A/C and lamin B1/B2 was necessary for forming a blebbed system. Both of these models of nuclear blebs predated the recent research regarding the role of chromatin in bleb formation; neither model considered chromatin in their simulations. While these models have provided solid initial steps in understand the mechanics of blebs, they do not exactly recapitulate experimental findings. A recent model, however, has considered chromatin's role in bleb formation [310]. They showed specifically through simulation that tethering of the chromatin to the nuclear lamina at lamin associated domains was necessary to induce blebbing. However, this model does not separate A- and B-type lamins and therefore cannot shed light on their roles in bleb formation. There is then room to build upon these works to further understand the mechanisms by which blebs form and their mechanical properties.

The formation of blebs can often lead to nuclear rupture, which is believed to be associated with nuclear dysfunction. Such rupture events are often associated with cellular migration [62, 69, 71],

however it also is known to occur as a result of actin-based confinement [266]. Furthermore, recent work has shown that local tensile [272] and compressive forces [47] are sufficient to rupture nuclei as well. Such rupture events provide a chance for cytoplasmic contents to mislocalize into the nucleus, and vice versa [349]. With flow across the nuclear envelope no longer regulated by the generally-selective nuclear pore complex [350], a variety of groups have observed an increase in double-stand DNA breaks [62, 69, 71, 108]. This has obvious implications for proper nuclear and cellular function, and is worthy of deeper mechanical analysis and simulations to understand the basis.

Nuclear rupture itself has also been the subject of recent mechanical models [272, 319, 320]. One analytical approach considers two limiting cases where the nuclear interior is treated either as a semi-flexible polymer that forms a channel to the rupture site or as a simple viscous fluid. Interestingly, their conclusions regarding the dynamics of the rupture hole were qualitatively similar for both cases. Their model showed that upon rupture, the size of the hole increases exponentially to a maximal radius before closing linearly in time. Furthermore, their model concluded both that chromatin herniations are exponentially sensitive to the radius of the rupture site, and that increased viscosity of the nuclear lamina reduces this rupture radius thus minimizing chromatin herniation [319]. This highlights that the material properties of the nuclear lamina are relevant for limiting the size of the rupture site and subsequently the magnitude of the chromatin herniation. Building on this earlier work, a second analytically-solved CM model was developed to study nucleation mechanisms of blebs in the nuclear lamina. They used an energetics approach to study how the inclusions of nuclear pore complexes (NPCs) alters the scaling relationships between hole nucleation rate and strain in the lamina. They were able to predict that increasing the density of the lamina induces a transition from homogeneous nucleation (no NPCs) to heterogeneous nucleation (with NPCs), which could be validated with further experiments. A separate CM model of diffusion of EGFP-NLS at local nuclear rupture sites has helped inform that the magnitude of a local nuclear stress is directly related to the size of the rupture size [272], which subsequently governs the rate of mislocalization of nuclear contents to the cytoplasm. Finally, a recent model sought to distinguish whether the DNA damage associated with nuclear rupture and specifically constricted migration is due to mechanical stress or could be explained separation of repair proteins from the chromatin. Through treating the nucleus as an elastic-fluid system wherein the fluid surrounding the chromatin can be

squeezed out of the nucleus, their model showed that outflow of mobile repair proteins due to the constricted migration was sufficient to explain the experimental data on increased damage sites [282]. Recent experimental work has shown similarly that nuclear deformation alone can cause increased DNA damage [142]. In their model, nuclear rupture was assumed to merely delay the ability of the repair factors to return to their original locations. This profound result infers that mechanically-induced separation of repair factors from damage sites could be more important for increases in DNA damage than the actual mechanical stresses themselves. It is clear then that mechanical models have shaped the collective understanding of the dynamics and causes of nuclear rupture and DNA damage, specifically that the scale of the rupture site is dependent on the material properties of the lamina which has consequences for the amount outflow of nuclear contents into the cytoplasm. Although, chromatin and its mechanical properties also influence nuclear rupture and DNA damage [351]. Additional mechanical modeling is needed along with experiments to fully understand how nuclear rupture occurs and effects nuclear functions and leads to DNA damage.

6.5.3 Cell Spreading and Detachment

As cells adhere to substrates, they begin to spread and subsequently flatten nuclei; the stiffness of the underlying substrate regulates how much cells are able to spread [37]. Experimental data shows both that nuclear height and surface roughness are reduced in spread cells; lamin A/C deficiencies subsequently re-introduce nuclear surface roughness in spread cells [32]. This nuclear flattening has also been shown to be dependent of the geometry upon which cells can spread [35], and recent experimental work suggests that the movement of cell boundaries is sufficient to shape the nucleus during this process [265, 273]. Additionally, it was observed that upon removal from the cell body, nuclear shape was unchanged [265]. Such permanent changes to cell geometry ultimately alter chromatin organization and subsequently cellular function [352].

Several mechanical models have been constructed to understand how nuclear morphology changes as cell adhere or detach from substrates [276, 321] and how cell geometric constraints alter nuclear morphology as well [129]. In an analytical model presuming the nucleus to be a pressurized sphere with an elastic shell under uniform plate compression representative of the actin cap [32],

investigators derived equations linking nuclear volume and surface area to the magnitude of external force and the elastic modulus [46]. Although, this model clearly neglects the previously detailed role of the chromatin in this process. In one simulation, the nuclear lamina is treated as a neo-Hookean (hyperelastic) material of finite thickness and there existed a pressure differences across the nuclear envelope. Their model showed that nuclei undergo significant volume loss and wrinkling after detachment consistent with experimentation. Both the volume loss and wrinkling were dependent on the thickness of the nuclear lamina and the magnitude of the pressure gradient. This highlights the role of the nuclear lamina and pressure in regulating nuclear shape. A separate study focused more on nuclear morphology during cell spreading [321]. It was shown that in general, nuclei extend their surface area during spreading up until it begins to stretch; volume remained mostly constant during the spreading process. This is consistent with a strain-stiffening response that results from the lamina becoming taut and stretching [13, 14]. Their simulations showed how nuclear flattening could occur without actomyosin activity or bundles, microtubules, the LINC complex, or intermediate filaments; this is consistent with the experimental observations claiming that the movement of cell boundaries is sufficient to shape the nucleus. Finally, a recent model has sought to study the feedback mechanisms between cell adhesions, the cytoskeleton, and the nucleus [129]. Their model was able to show that this three-way feedback system recapitulated the experimental results of the dependence of nuclear flattening on cell geometry. Cell spreading is a phenomenon often studied purely through observation; mechanical modeling has been fundamental in explaining the roles of cell boundaries and pressure in the manner by which the nucleus is shaped during this process.

6.6 Outlook on Mechanical Models

Although investigators have been mechanically modeling cell nuclei for over fifteen years, there are still several open areas of research where models could be useful. In this concluding section, we outline several facets of nuclear mechanics where sufficient mechanical models are lacking. These topics include the roles of tethers between chromatin and the nuclear lamina, the role of links between the cytoskeleton and the nucleus, and the separation of lamin A/C and lamin B1/B2. A myriad of intricate connections exists between the chromatin, lamina, and the cytoskeleton; we have focused our description

on a subset of these connections we feel to be of particular biophysical relevance. Additional problems warrant further studies and modeling, specifically how cell type and mechanosensation of the environment may modulate nuclear mechanical properties. However, we have chosen to focus this section on connections between the nuclear mechanical constituents as opposed the aforementioned additional considerations. Each of these areas of research prove to be relevant for understanding laminopathies and cellular function; mechanical modeling then can inform a more complete understanding of these intricacies.

6.6.1 Lamin-Chromatin Connections

As previously described, the nuclear lamina and the chromatin are the two dominant nuclear structures regarding mechanical stability. The chromatin and nuclear periphery are mechanically tethered together; this tethering has been experimentally shown to be relevant for nuclear stability [271]. In mechanical modeling, such tethering could be presented as a boundary condition between the chromatin and nuclear lamina in CM models or as a physical link in MD simulations. A majority of CM models assume this boundary condition to be a no-slip condition, meaning relative motion of the chromatin and lamina at the boundary is not allowed. It is unclear, however, how valid this assumption is as laminopathies and lamin deficiencies disrupt lamin-associated domains (LADs) [353, 354] and potentially invalidate such assumptions. One recent study has begun to investigate such questions with mechanical modeling [310]. Their mechanical model required that lamin-chromatin tethers are localized along lamin domain boundaries to form nuclear blebs and abnormal nuclear morphologies. Additionally, these connections are necessary for modeling strain stiffening in micromanipulation [281]. There is little-to-no work, however, on how such variations in the boundary conditions may present itself in common assays such as AFM or micropipette aspiration. For example, an experimental micropipette aspiration study observed an increase in chromatin mobility when lamin A/C was knocked down in human A549 cells [76]; distinguishing whether this is, in part, due to a reduction in tethering of the chromatin to the nuclear lamina could be achieved through mechanical modeling with varied boundary conditions. Mechanical models with tunable chromatin-lamin tethering could then prove highly useful for furthering our understanding of laminopathies.

6.6.2 Lamin-Cytoskeleton Connections

The second subsection of nuclear mechanics that is lacking sufficient modeling is in the role of mechanical links between the cytoskeleton and the nuclear lamina. Numerous proteins exist amongst these connections. One subset of these proteins is known formally as the Linker of the Nucleoskeleton and Cytoskeleton (LINC) Complex, and consists primarily of nesprins and SUN proteins that link that cytoskeleton to the outer nuclear membrane and the inner nuclear membrane to the nuclear lamina respectively [355]. Experiments have demonstrated the importance of the LINC complex for transferring mechanical signals from the cell surface to chromatin [26, 356], which subsequently can lead to altered transcriptional activity due to chromatin stretching [29]. Laminopathies have been shown to disrupt this connection [357, 358], which subsequently alters a cell's ability to process mechanical signals. Models of the cytoskeleton have predominantly focused on the cytoskeleton as a means of facilitating cellular migration [66, 316]; little work, however, has sought to model the mechanical implications of disrupting these connections. Effective models could then inform how laminopathies alter nuclear mechanics and mechanotransduction.

6.6.3 Separate but Interacting Lamin A/C vs B1/B2 Meshworks

The final area well-suited for additional modeling is the distinction of A- and B-type lamins in the mechanical response of cell nuclei. As discussed previously, A- and B-type lamins serve distinct mechanical roles. More specifically, it has been experimentally shown that decreasing expression of lamin B1 and increasing expression of lamin A/C both result in nuclear stiffening; this implies the ratio of lamin A/C to lamin B1 to be a proper metric of nuclear stiffness [13, 78], in agreement with landmark initial findings [41]. Additionally, experiments suggest that lamin A may govern the viscous response while lamin B could dictate the elastic response [41, 67]. However, only mechanical models of nuclear blebbing have sought to distinguish A- and B-type lamins [317, 318]. There have no detailed mechanical models to date that explicitly explore these separate roles for common force measurement assays such as AFM, micromanipulation, or micropipette aspiration. Such models would inform our understanding of why the experimental results detailed above have been observed. Given the myriad of diseases associated with mutations in the nuclear lamina and the clearly made experimental distinctions between the isoforms, to

not begin distinguishing between A- and B-type lamins in mechanical models would be to place fundamental limitation on the intersection between mechanics and disease.

6.7 Conclusions

The final area well-suited for additional modeling is the distinction of A- and B-type lamins in the mechanical response of cell nuclei. As discussed previously, A- and B-type lamins serve distinct mechanical roles. More specifically, it has been experimentally shown that decreasing expression of lamin B1 and increasing expression of lamin A/C both result in nuclear stiffening; this implies the ratio of lamin A/C to lamin B1 to be a proper metric of nuclear stiffness [13, 78], in agreement with landmark initial findings [41]. Additionally, experiments suggest that lamin A may govern the viscous response while lamin B could dictate the elastic response [41, 67]. However, only mechanical models of nuclear blebbing have sought to distinguish A- and B-type lamins [317, 318]. There have no detailed mechanical models to date that explicitly explore these separate roles for common force measurement assays such as AFM, micromanipulation, or micropipette aspiration. Such models would inform our understanding of why the experimental results detailed above have been observed. Given the myriad of diseases associated with mutations in the nuclear lamina and the clearly made experimental distinctions between the isoforms, to not begin distinguishing between A- and B-type lamins in mechanical models would be to place fundamental limitation on the intersection between mechanics and disease.

CHAPTER 7: FUTURE DIRECTIONS

The previous chapters consist almost exclusively of published data and their accompanying analyses. Over the duration of my research, however, I have also collected a wide array of preliminary data that is suggestive of promising new research directions. In Chapter 7, I describe some of the most exciting and engaging preliminary data as well as my thoughts and hypotheses. The conclusions and analysis are meant to be speculative in hopes of spurring on further efforts in the realm of method development and nuclear mechanics.

7.1 Chromatin Mechanics and Nuclear Compression

7.1.1 Dynamics of Intranuclear Strain

Chromatin is increasingly appreciated as an important mechanical and rheological element of the cell nucleus [12, 351]. Specifically, it is well-documented that chromatin dominates the mechanical response of the cell nucleus for low-strain regimes in both compression- and extension-based measurements [13, 14]. However, these measurements targeted only the global force response of the nucleus as opposed to the local distribution of strains in the chromatin due to external force application. Given that recent studies have revealed how local chromatin strain upregulates transcriptional activity at the site of strain [29, 123], it is crucial to understand not only the global force response of the nucleus but also how those forces are distributed throughout the chromatin. Previous studies have sought to quantify intranuclear strain distributions [28, 121], however they are lacking in data addressing how strain *dynamically* changes throughout the application of stress. Our unique AFM-LS system provides us the perfect method to gain novel insights into intranuclear strain over a range of deformation length scales.

To begin investigating intranuclear strain distributions, we used AFM-LS data previously collected as described in Chapter 5 on live SKOV3 nuclei. We next made use of a previously published image analysis tool, BioFlow [359], which presumes a simple fluid-like system and uses optical flow-based methods to calculate displacement fields between adjacent images in a time series. We performed this

analysis on both WT and LA/C KD data (Figure 7.1). The first overall observation is that the displacement fields are not consistent with that of a linearly elastic solid, which is somewhat unsurprising given the previously noted results in Chapter 5. Interestingly, there appears to be a symmetry breaking phenomenon within the WT displacement field data. At low deformations, the displacement field appears symmetric around the AFM tip. At large displacements, however, this symmetry appears to break and give way to large-scale lateral displacement of the chromatin. This correlates well with the previous results on strain stiffening at different length scales of nuclear deformation. We hypothesize that this symmetry breaking phenomenon is a consistent feature of the displacement fields at large deformations. On the contrary, the LA/C KD displacement field data shows significant lateral motion of the chromatin throughout the entirety of the indentation. It is known that the nuclear lamina is physically tethered to the chromatin at lamin-associated domains (LADs), and we hypothesize that in knocking down lamin A/C these physical connections are disrupted. This is analogous to altering the boundary conditions of the chromatin – without these linkages, chromatin is allowed to slip. Additionally, we hypothesize the disruption of the LINC complex would yield similar alterations to chromatin displacements as in lamin A/C KD.

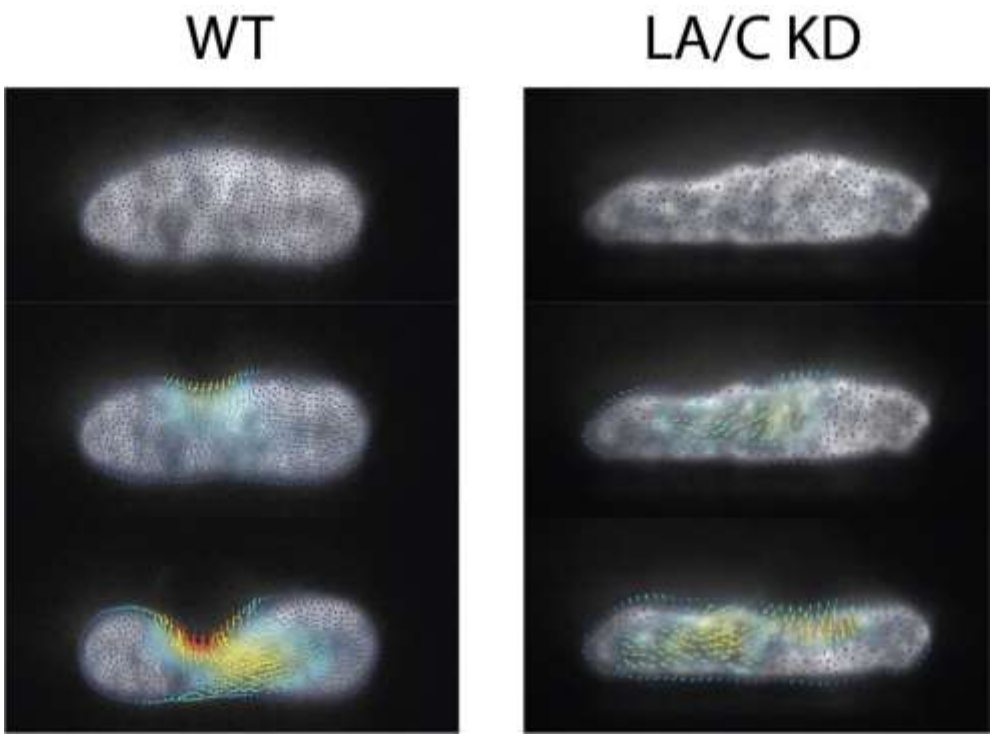

Figure 7.1: Chromatin displacement analysis with AFM-LS. Side-view images of live WT (left) and LA/C KD (right) SKOV3 cells with halotagged H2B labeled with JF 549 during AFM compression. Displacement maps are overlayed with the raw fluorescence data. See also Video 7.1 and Video 7.2.

7.1.2 Local Plasticity of Chromatin

Intranuclear displacements themselves are not the only topic of interest, but also whether or not these displacements are reversible. When chromatin does not return its original state after removal of the physical perturbation, this is known as plastic damage**.** Plastic damage can occur within the nucleus at several tiers of its hierarchical structure. At the largest length scale, the shape of the nucleus can be plastically damaged due to external forces as observed in micropipette aspiration [76] and constricted migration assays [66]. It has been further posited and observed that the shape of the cell nucleus mimics the shape of the cell boundaries [265, 273, 360]. Looking further into the nucleus at the individual chromosome level, it has been observed that individual chromosomes have altered positions and volumes when cells are either mechanically stressed [120] or plated on substrates of varied geometries [130]. Coincidently, alterations in nuclear architecture are associated with various cancers across all levels of the chromatin hierarchy, ranging from the single nucleosome to chromosome territories [137].

While the aforementioned studies have observed nuclear plasticity, there are still many outstanding questions regarding the relationships between the magnitude and duration of external stress and the degree of global and local nuclear plasticity. Systematically studying these relationships will reveal the physiological scenarios in which nuclei are susceptible to plastic damage and subsequent genomic alterations.

As was noted in Chapter 5, we have observed global nuclear plastic damage due to AFM compression in LA/C KD nuclei. However, we have arguably more intriguing results when cells are treated with Latrunculin B to depolymerize actin filaments (Figure 7.2). As opposed to more global nuclear shape change, we observed local chromatin damage at the site of compression. The chromatin appears to pinch in on itself and does not recover with the cell membrane during the relaxation phase after retraction of the AFM tip. Note here that relaxation refers to when the AFM tip is no longer engaged with the cells. This highlights that actin depolymerization may inhibit the connections between the cell surface and the nucleus. We hypothesize that the degree of damage is dependent on both the magnitude of the force being applied as well as the duration over the which the force is held upon the nucleus. Follow up studies on this phenomenon could investigate this parameter space both for WT nuclei as well as nuclei treated with drugs and RNAs to mimic disease states such as cancers or laminopathies. The nucleus is organization in highly non-random manner, so understanding the conditions in which force can permanently alter this organization is crucial. The fact that we have observed this in conditions where the cytoskeleton is disrupted proves an exciting path for further research.

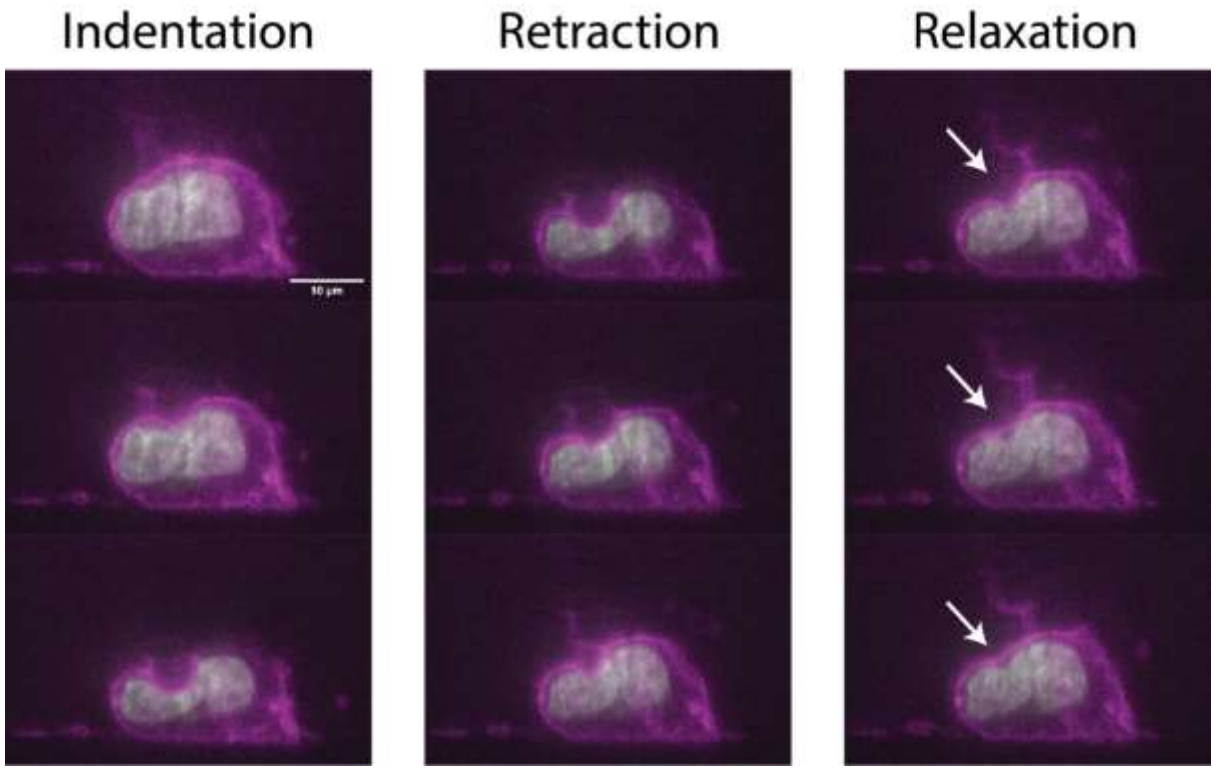

Figure 7.2: Nuclear plasticity due to compression and actin depolymerization. Side-view images of live SKOV3 cells with halotagged H2B (green) and snaptagged KRAS-tai (magenta)l labeled with JF549 and JF503 respectively during indentation (left), retraction (middle), and relaxation (right). Relaxation here refers to the period of time after the AFM tip has released from the cell surface. The cell was treated with Latrunculin B to depolymerize actin. White arrows point to site of local chromatin plasticity. See also Video 7.3.

While the preliminary results mentioned above highlight more local damage than as mentioned in Chapter 5, there is still the question of measuring small, internal rearrangements of chromatin within the nucleus that may be independent of changes to global nuclear shape. To study this, we leverage the stability of fluorescently-labeled histones. Recall from our previous discussions in Chapter 4 that in mammalian cells, H2B recovers after photobleaching on a timescale on the order of hours. This means that if a certain area of H2B is bleached, it will remain dark during a short experiment performed immediately after the photobleaching. With this in mind, we introduce a new method known as orthogonal plane photobleaching (OPP), wherein we convert our system to temporary operate in HLS mode and use the light sheet to photobleach a horizontal plane in the fluorescently-labeled H2B. After this is completed, we return to VLS mode for a side-view AFM-LS compression experiment (Figure 7.3A). The benefit of this method is that we have a known and distinct structure to track both in terms of shape and intensity. If the intensity of the photobleached line increases dramatically after compression, we may infer that some

previously unbleached histones have now entered the region that was previously entirely dark. This implies that compression would have led to local spatial overlap of chromatin and thus plastic damage or viscosity on a much more local scale than global nuclear shape change. To test this, we plotted a vertical line profile directly underneath the site of compression in our OPP experiment (Figure 7.3B). During the compression, we see both that the dip in intensity that corresponds to the photobleached plane both increases in intensity overall, shifts downward, and somewhat plateaus – that is, it shows less of a dip in intensity than before. This means that during compression, we see some intermingling of chromatin. However, after the compression is released, we observe a near identical line trace as before compression, meaning that there was no sustained damage to the chromatin. It should also be noted that OPP is not simply a method for detecting local changes in concentration, it may also be used as a means of tracking strain. If one could monitor both the position and width of the photobleached line (or plane, in the case of 3D experiments) as a function of space and time during compression, this would provide a means of quantifying local stains and displacements. While we have not developed the software as of yet to perform such functions, a realization of such an experiment is not far away.

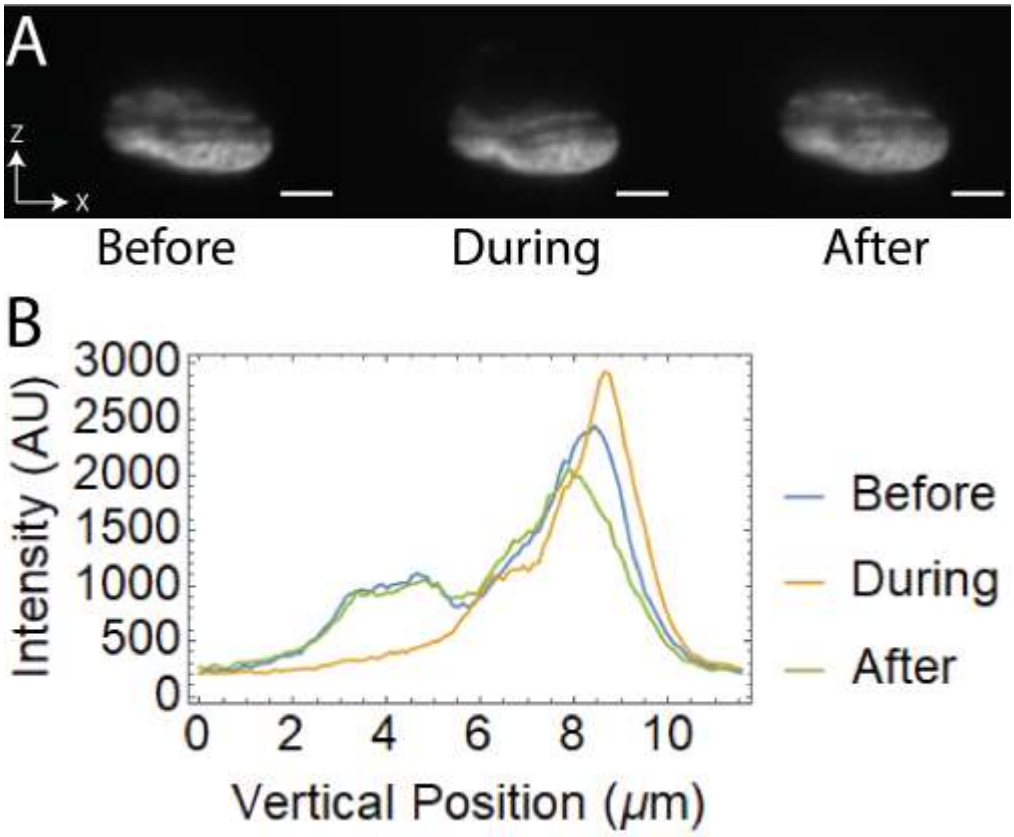

Figure 7.3: Orthogonal Plane Photobleaching (OPP) as a means of studying chromatin plasticity. (A) Side-view images of a live SKOV3 cell nucleus expressing halotagged H2B labeled with JF549 before, during, and after compression (scale bar = 5 μm). Prior to imaging, the VIEW-MOD system was operated in HLS mode to photobleach a horizontal plane through the center of the nucleus. (B). Plot of intensity of a vertical line trace through the nucleus from (A) directly under the site of compression before, during, and after AFM indentation. Note this line trace is taken from the top of the image, and thus a vertical position of 0 μm refers to the top of the image. See also Video 7.4.

7.2 Intranuclear Dynamics and Mobility: Combined AFM-LS and SPIM-FRAP

The nucleus relies on efficient and effective transport of proteins and small molecules to properly function. Spatiotemporal modifications of transport in response to external mechanical factors may be a significant mechanotransductive effect. However, the role of crowding and strain in the nucleus on the diffusion of nuclear proteins depends on a complex set of factors including environmental mesh size and binding. Each of these may be affected by strain. The nuclear interior is a complex and active environment filled with polymeric DNA, surrounding nucleoplasm, and a myriad of proteins and subnuclear bodies. Taken together, this complexity turns a relatively simple problem of diffusion into a far

more intricate and detailed phenomenon. With our unique AFM-LS and SPIM-FRAP methodologies, we are poised to begin studying such processes.

We began by performing back-to-back SPIM-FRAP experiments (as described in Chapter 4) before and after AFM compression on a given MDA-MB-231 nucleus labeled with NLS GFP (Figure 7.4A). This allowed us to quantify the timescales of diffusion across the entire image plane of the nucleus with and without physical constrictions. Furthermore, we could normalize the recovery times of the region being compressed to the regions not being compressed in order to account for any artifacts associated with repeated experiments. We observed that compression seemingly led to and increased rate of diffusion at the site of compression relative to the uncompressed regions (Figure 7.4B). This initially may seem contradictory, as a constriction would, at lowest order, crowd the environment and slow diffusion. However, the nucleus is not this simple. It has been previously shown that physical constrictions can actually segregate larger mobile proteins away from the chromatin [62]. That is, at the constriction there is an increase in chromatin density and a decrease in large mobile repair proteins. We have previously observed that diffusion of NLS-GFP is independent of chromatin compaction levels [361], and so we hypothesize that the constriction via AFM compression actually reduces the concentration of mobile proteins thus allowing small proteins such as NLS-GFP to diffuse more freely. This further leads us to hypothesize that large proteins, such as DNA repair proteins like 53BP1, would indeed show slowed diffusion at sites of constriction, and that really this is a size-dependent phenomenon. This initial result proves quite interesting, and opens up further questions. Combining SPIM-FRAP and AFM serves as a useful tool for studying the complex nature of confinement and dynamics within the nucleus.

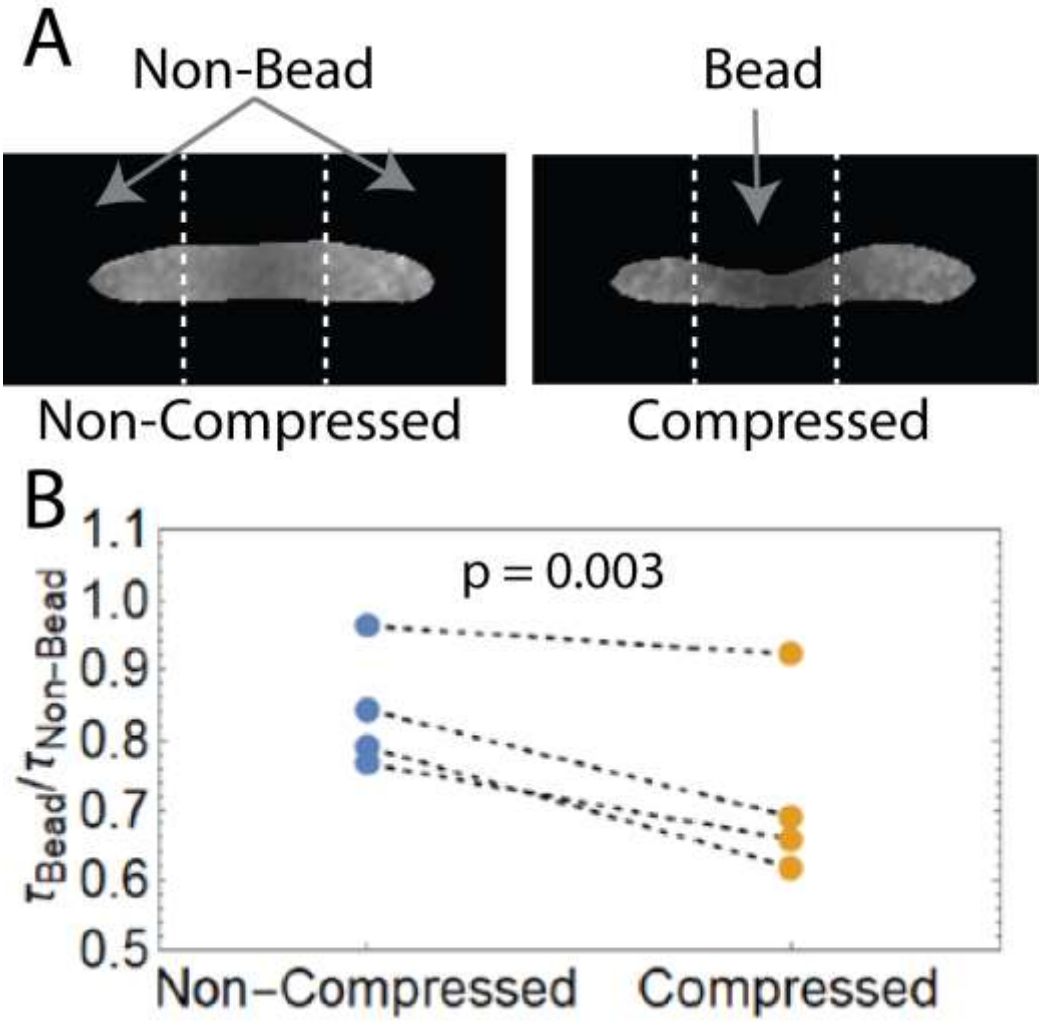

Figure 7.4: Combined AFM-LS and SPIM-FRAP to study intranuclear diffusion in physically constrained environments. (A) Side-view maps of FRAP recovery time (black to white represents increasingly long recovery time) from a SPIM-FRAP experiment on live MDA-MB-231 nuclei expressing NLS-GFP. SPIM-FRAP experiments were performed back-to-back on the same nucleus before and after compression with AFM. The dashed lines segment the region under the AFM tip (bead) and outside the AFM tip (non-bead). (B) Comparison of the ratio of recovery times in the bead and non-bead regions before and after AFM compression. A paired T Test gives a p value of 0.003.

7.3 Mechanotransduction at the Nuclear Surface

7.3.1 Nucleocytoplasmic Shutting of YAP

It is well documented that external force applied to the nucleus induces transport of transcription factors (YAP/TAZ [99-103], MKL [109], NF-κB [110], and MRTF [111]), enzymes regulating histone acetylation [112, 113], and calcium [106, 107]. However, the precise mechanism by which stretching of the nuclear envelope mediates such transport is unknown [274]. Two competing hypotheses can explain

this nucleocytoplasmic shutting. The first hypothesis is that external force triggers a global nuclear response that opens all nuclear pores along the nuclear envelope, thus allowing for increased transport. The second hypothesis is that *mechanical strain itself* is sufficient to open a nuclear pore. That is, only the nuclear pores in regions of local strain will be opened, and the transport across the nuclear envelop will be concentrated at regions of high strain in the nuclear surface. These hypotheses have yet to be rigorously tested, and leave an opening in the field for further exploration.

To begin testing these competing hypotheses, we study YAP translocation due to AFM compression (Figure 7.5). A YAP-eGFP plasmid (Addgene 17843) was streaked onto a Kanamycin bacteria plate and kept at 37 C overnight. Individual colonies were then picked and grown in LB broth (Luria-Bertani) with 100 μg/ml Kanamycin and shaken at 37 C for 18 hours. We then performed a Miniprep for DNA purification (Qiagen 27104). Finally, we used a nanodrop spectrophotometer to calculate the exact DNA concentration. With the purified DNA in hand, we transiently transfected SKOV3 cells with YAP-eGFP by first diluting the DNA into Opti-MEM to a concentration of 0.02 μg/ml. 2 μl of Fugene HD (1 μg/ml) was then added to 48 μl of the Opti-MEM and DNA mixture. The final mixture was added to individual wells in a 6 well plate before imaging approximately 24 hours later. By performing AFM-LS experiments, we were able to show for a single cell that compression led to a dramatic increase in nuclear-to-cytoplasmic YAP localization (Figure 7.5). Images were collected once every second during compression. Intriguingly, the magnitude of our YAP ratio and the amount of change induced by AFM compression was strikingly similar to previous results [99]. With the baseline information that the assay was working, we then sought to determine specifically where the changes in YAP concentration were occurring. For this analysis, we investigated the same time series, but subtracted off the intensity of the image immediately after compression (Figure 7.6). Also, a 2-pixel Gaussian blur was used to smooth the data. We first observed a decrease in YAP outside the nucleus and a coinciding increase in YAP inside the nucleus near the site of strain in the nuclear envelope. Though we are not directly observing strain in the nuclear envelope in this experiment, additional data of AFM-LS compression with fluorescently-labeled lamin A/C points towards consistent strain in the nuclear envelope around the AFM tip. We are thus inferring that the same holds true for this experiment. We then observed a steady decrease in the pool of YAP outside the nucleus. This points towards the hypothesis that only the nuclear pores that are

under strain are active in this process, however more data would be necessary to draw a definitive conclusion.

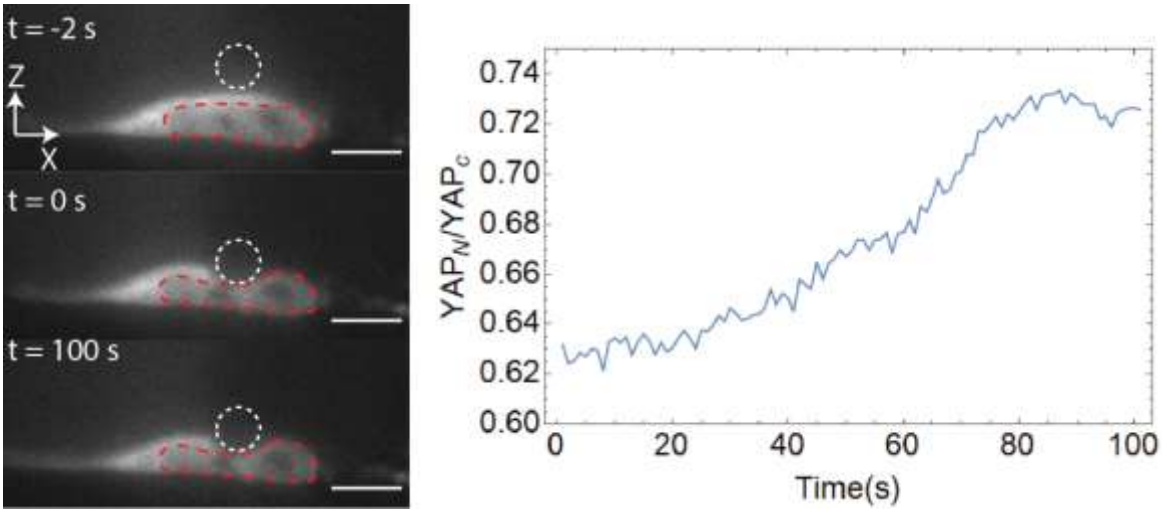

Figure 7.5: AFM compression causes YAP nuclear translocation. (Left) Side-view images of a live SKOV3 cell transiently transfected with YAP-eGFP during AFM compression. The red dashed line represents a manual segmentation of the nucleus. The white dashed line represents the AFM tip. Scale bar = 10 μm. (Right) A time series of the ratio of nuclear-to-cytoplasmic YAP intensity shows a dramatic increase at the time of compression (t=0 s).

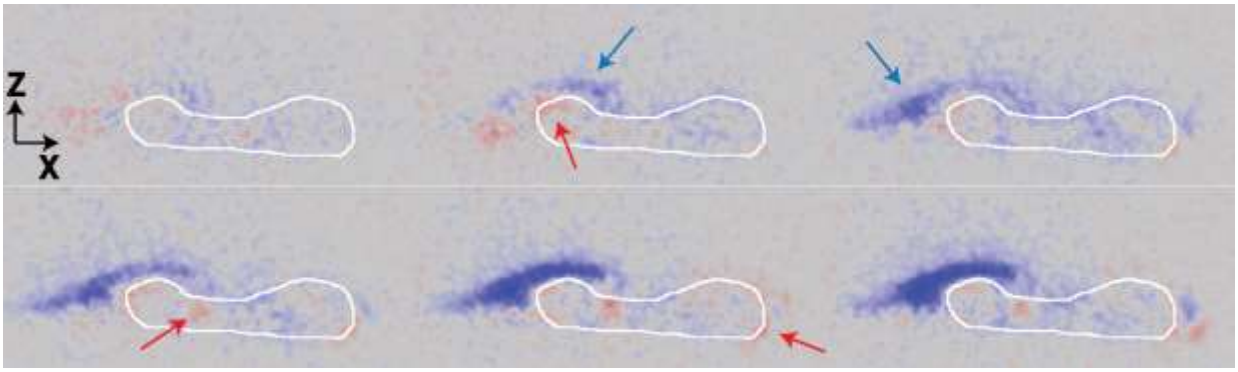

Figure 7.6: Difference imaging of YAP. Side-view images of a live SKOV3 cell transiently transfected with YAP-eGFP during AFM compression, with the t = 0 image subtracted from the given images. Blue to gray to red color scale represents a negative to zero to positive change in YAP intensity from t = 0. Blue and Red arrows highlight regions of local loss or gain of YAP respectively. See also Video 7.5.

7.3.2 Strain and Turnover in the Nuclear Lamina

The nuclear lamina is a meshwork of type V intermediate filaments that reside along the underside of the inner nuclear membrane. Comprised of both A- and B-type lamins, the nuclear lamina is known to provide structural integrity to the cell nucleus, primarily during large-scale compressions and extensions [13, 14]. Furthermore, the nuclear lamina is known to be mechanosensitive [41, 275, 284].

Specifically, recent work has begun examining how stretching of the nuclear surface can control actomyosin contractility [362, 363]. Laminopathies – disease characterized by mutations of the *LMNA*, *LMB1*, and *LMB1* genes that encode A- and B-type lamins [16] – can alter these mechanoresponses [93].

We sought to begin studying mechanotransduction in the nuclear lamina first by performing AFM-LS compression experiments on live cells with fluorescently-labeled lamins. Live MDA-MB-231 cells generously given by the Lammerding Lab at Cornell University featured CRISPR knockin mNeonGreen-lamin were used for these experiments. We first investigated a rounded cell with wrinkling in the nuclear lamina, and indeed observed that under compression the nuclear lamina begins to unfold (Figure 7.7). Interesting, recent studies have pointed to the role of wrinkling in the nuclear envelop in nuclear mechanotransduction [364]. Next, we performed AFM-LS experiments both in 2D (Figure 7.8) and in 3D (Figure 7.9) upon well-spread cells which featured an unruffled nuclear lamina. We observed that the nuclear lamina does appear to stretch at the site of compression, implying that that our assay is well suited to provided deformations that may induce nuclear mechanotransduction at the nuclear lamina.

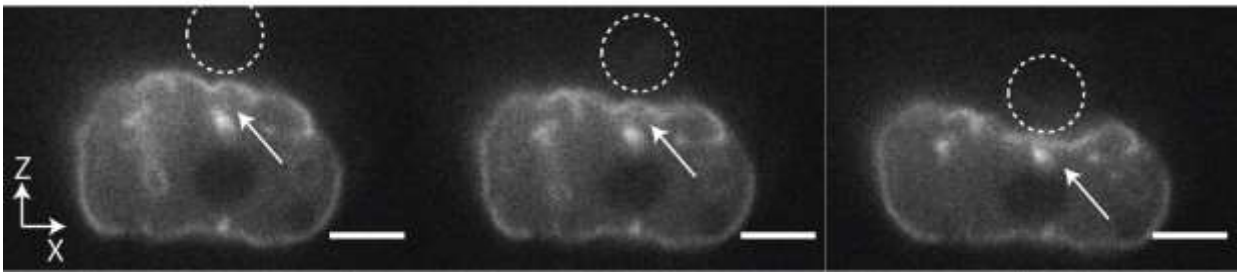

Figure 7.7. AFM-LS experiment on a rounded cell with fluorescent lamin A/C. Scale bar = 5 μm. This given cell is a live MDA-MB-231 cell with CRISPR knockin mNeonGreen-lamin. White arrow points to local unruffling of the nuclear lamina. See also Video 7.6.

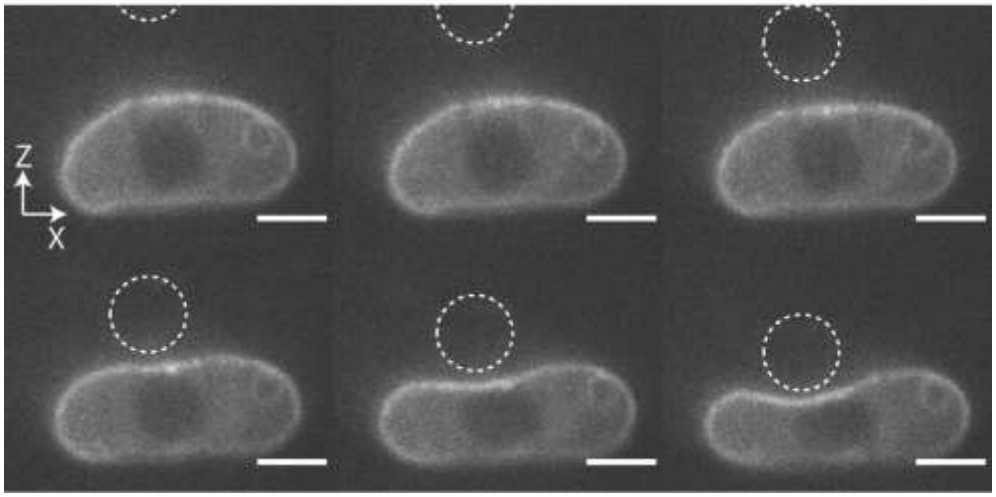

Figure 7.8: AFM-LS experiment on a spread cell with fluorescent lamin A/C. Scale bar = 5 μm. This given cell is a live MDA-MB-231 cell with CRISPR knockin mNeonGreen-lamin. See also Video 7.7.

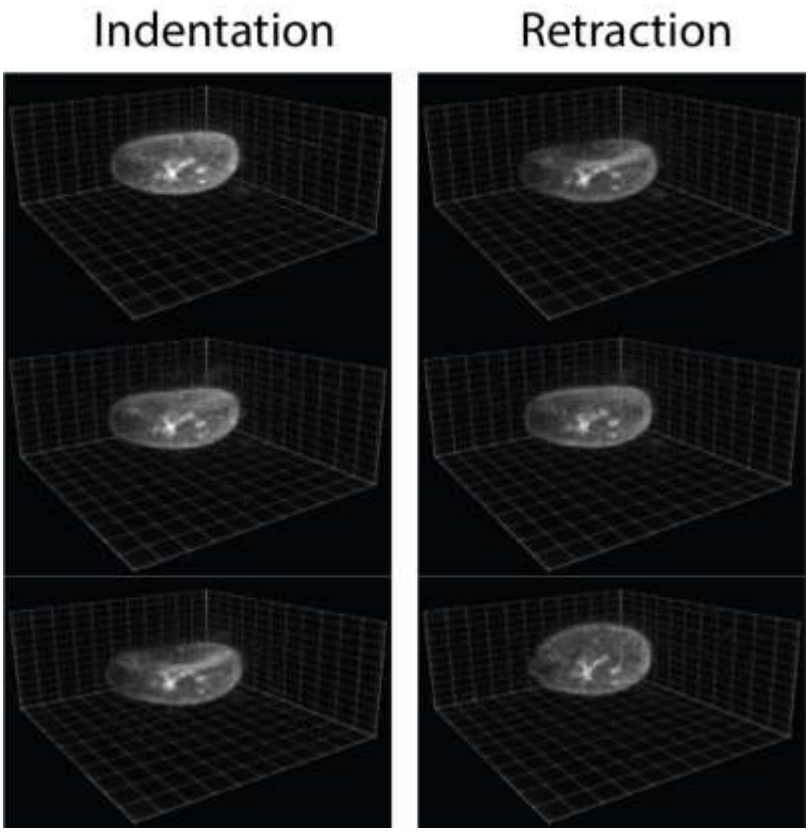

Figure 7.9: 3D AFM-LS experiment on a spread cell with fluorescent lamin A/C. This given cell is a live MDA-MB-231 cell with CRISPR knockin mNeonGreen-lamin. Raw images have been blurred with a 1-pixel Gaussian blur prior to rending in ClearVolume. Voxel size: 108 nm x 108 nm x 250 nm. Total volume: 21.2 μm x 45.4 μm x 36.3 μm. Images were acquired with an exposure time of 20 ms and a readout time of 10

ms for a total volume acquisition time of 4.35 s. A 100 ms delay was taken between volumes. See also Video 7.8.

One potential effect we sought to investigate is the turnover of nuclear lamins due to strain. It has been previously documented use a combination of AFM and FRAP that turnover of actin is slowed upon increasing compressive force [365]. We hypothesized that a similar effect may be present in the nuclear lamina. We then performed simultaneous AFM compression and SPIM-FRAP on one of the aforementioned cells, subsequently quantifying recovery times of lamins along the edge of the nucleus at the nuclear lamina (Figure 7.10). Our preliminary results suggest that there may indeed be a similar phenomenon at play as with actin in that we saw apparent slowed turnover of lamins around the AFM tip, but not elsewhere along the nuclear surface. Further studies could quantify this across numerous cells and provide correlations between the magnitude of strain and the relative change in lamin turnover.

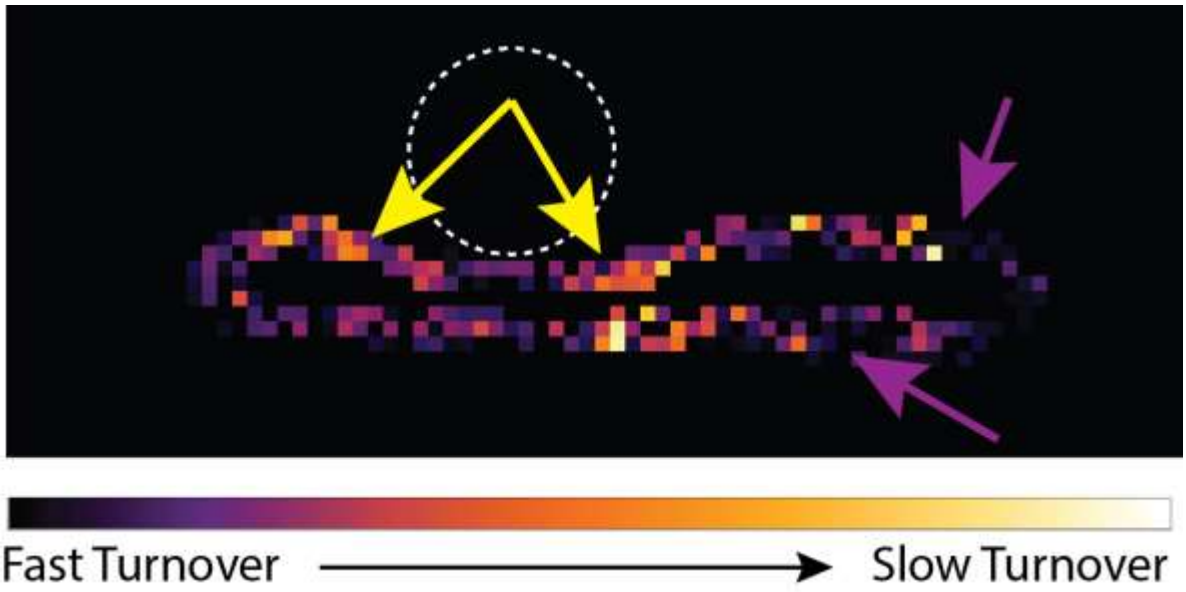

Figure 7.10: Combined AFM-LS and SPIM-FRAP to study stretch-activated lamin A/C turnover. A live MDA-MB-231 cell nucleus with CRISPR knockin mNeonGreen-lamin is compressed with an AFM prior to performing a SPIM-FRAP experiment. Yellow and purple arrows point to sites of slow and fast turnover along the nuclear lamina respectively.

APPENDIX A: SUPPLEMENTAL VIDEO CAPTIONS

All supplemental videos for this work can be found at this google drive link. Additionally, each video is hyperlinked below and at each associated figure, though the quality of these videos is compromised due to compression. For full quality videos, download them directly from the google drive link above.

Video 2.1: Propagation of a Gaussian through a simple lens.

Video 2.2: Propagation of an approximated Bessel-Gauss beam through a simple lens.

Video 2.3: Volumetric movie playing both forwards and then backwards of a live, RAW 264.7 cell expressing HaloTag-F-Tractin labeled with JF549. Various angles are shown with different planes slicing through the volume over the course of the movie to show the internal structure.

Video 2.4: LSFM volumetric imaging of a live HeLa cell with labeled Lysotracker Red (magenta) and vimentin-mEmerald (green). Each volume consists of 75 slices per color acquired at 5 ms exposure time and 5 ms readout time; the total volume acquisition time is 1.5 s. A 100 ms delay is taken between volumes. Insets show dynamics of vesicles on the single-second timescale. Voxel size: 106 x 106 x 220 nm. Total volume: 29.3 x 26.3 x 16.5 µm.

Video 2.5: LSFM volumetric image of a fixed HeLa cell with labeled actin (AlexaFluor 568-Phalloidin - magenta) and vimentin-mEmerald (green). The volume consists of 300 slices per color acquired at 5 ms exposure time and 5 ms readout time; the total volume acquisition time is 6 s. Voxel size: 106 x 106 x 108 nm. Total volume: 52.6 x 19.1 x 32.4 µm.

Video 3.1: Side-view LSFM movie from an AFM-LS experiment. Magenta – Kras-tail, green – H2B. Scale bar = 5 µm.

Video 3.2: Side-view LSFM movie during AFM-LS retraction. Arrow points towards membrane tether rupture site.

Video 3.3: 3D rendering of the SKOV3 cell during AFM indentation. SKOV3 cells is stabling expressing halotagged H2B labeled with JF549 (green) and snaptagged KRAS-tail labeled with JF503 (magenta). Total image volume is 29.81 μm x 31.75 μm x 16.52 μm. Each image has an exposure time of 14 ms and readout time of 6 ms, with 127 images per channel per volume for a net volume acquisition time of 5.08 s. A 100 ms delay is taken between volumes.

Video 4.1: A side-view SPIM-FRAP image sequence of NLS-GFP showing the simultaneous recovery across the entire image plane.

Video 4.2: A time series of the1D diffusion simulation, showing how concentration develops dynamically as a function of time.

Video 4.3: 3D rendering of a live MDA-MB-231 nucleus expressing H2B-mCherry both pre and post SPIM photobleaching. A clear 2D plane is bleached through the nucleus as well as small photobleaching of the concentric side lobes. See Movie S3 for additional views.

Video 5.1: Combined side-view light sheet microscopy and atomic force microscopy. (Left) Force versus time series during AFM indentation. Red line indicates current frame. (Right) Side-view images of a live SKOV3 cell under compression. Green – halotagged-H2B labeled with Janelia Fluor 549. Magenta – snaptagged-Kras Tail labeled with Janelia Fluor 503. Scale bar = 5 μm.

Video 5.2: Dynamic curvature analysis curing AFM compression. (Left) Nuclear curvature versus position along perimeter of the nucleus during AFM compression. Note the formation of a peak at approximately 10 μm throughout the compression. (Right) Side-view images of a live SKOV3 cell under compression.

Green – halotagged-H2B labeled with Janelia Fluor 549. Magenta – snaptagged-Kras Tail labeled with Janelia Fluor 503. Scale bar = 5 μm.

Video 5.3: Representative example of MDA-MB-231 cell co-expressing NLS-GFP (blue) and 53BP1-mCherry (yellow) subjected to external compression to a height of 2 μm with an AFM tip. DNA damage formation can be seen by occurrence of new 53BP1-mCherry foci. Scale bar: 5 μm.

Video 5.4: Representative example of MDA-MB-231 cell co-expressing NLS-GFP (blue) and 53BP1-mCherry (yellow) in which the AFM tip is only brought in gentle contact with the cell surface without causing nuclear deformation. In this case, no new DNA damage is formed, and only pre-existing 53BP1-mCherry foci are visible. Scale bar: 5 μm.

Video 6.1: Finite element analysis simulation of AFM compression. Grid lines indicate distance in μm. Color map indicates von Mises stress in Pa.

Video 7.1: Side-view movie of live WT SKOV3 cell with halotagged H2B labeled with JF 549 during AFM compression. Displacement maps are overlayed with the raw fluorescence data.

Video 7.2: Side-view movie of live LA/C KD SKOV3 cell with halotagged H2B labeled with JF 549 during AFM compression. Displacement maps are overlayed with the raw fluorescence data.

Video 7.3: Side-view movie of a live SKOV3 cell with halotagged H2B (green) and snaptagged KRAS-tail (magenta) labeled with JF549 and JF503. The cell was treated with Latrunculin B to depolymerize actin.

Video 7.4: Side-view movie of a live SKOV3 cell nucleus expressing halotagged H2B labeled with JF549 (scale bar = 5 μm). Prior to imaging, the VIEW-MOD system was operated in HLS mode to photobleach a horizontal plane through the center of the nucleus.

Video 7.5: Side-view images of a live SKOV3 cell transiently transfected with YAP-eGFP during AFM compression, with the t = 0 image subtracted from the given images. Blue to gray to red color scale represents a negative to zero to positive change in YAP intensity from t = 0.

Video 7.6: AFM-LS experiment on a rounded cell with fluorescent lamin A/C. Scale bar = 5 μm. This given cell is a live MDA-MB-231 cell with CRISPR knockin mNeonGreen-lamin.

Video 7.7: AFM-LS experiment on a spread cell with fluorescent lamin A/C. Scale bar = 5 μm. This given cell is a live MDA-MB-231 cell with CRISPR knockin mNeonGreen-lamin.

Video 7.8: 3D AFM-LS experiment on a spread cell with fluorescent lamin A/C. This given cell is a live MDA-MB-231 cell with CRISPR knockin mNeonGreen-lamin. Raw images have been blurred with a 1-pixel Gaussian blur prior to rending in ClearVolume. Voxel size: 108 nm x 108 nm x 250 nm. Total volume: 21.2 μm x 45.4 μm x 36.3 μm. Images were acquired with an exposure time of 20 ms and a readout time of 10 ms for a total volume acquisition time of 4.35 s. A 100 ms delay was taken between volumes.

APPENDIX B: SOFTWARE AVAILABILITY

SPIM-FRAP Analysis and Hardware Control – Written by Rasheeq Azad, Chad Hobson, and Joe Hsiao

https://github.com/hobsonc11/SPIM-FRAP

VIEW-MOD Hardware Control – Written by Joe Hsiao and Chad Hobson

https://github.com/hobsonc11/VIEW-MOD-Control

https://github.com/CISMM/lightsheet-volume-scan

Image Texture Analysis – Written by Melissa Kissling

https://github.com/hobsonc11/Texture-Analysis

Image Curvature Analysis – Written by Ali Hashmi, not in conjunction with this dissertation

https://github.com/alihashmiii/curvatureMeasure

Electromagnetic FDTD Simulator – Written by Floris Laporte, not in conjunction with this dissertation

https://github.com/flaport/fdtd

REFERENCES

1. Harris, A.K., P. Wild, and D. Stopak, *Silicone rubber substrata: a new wrinkle in the study of cell locomotion.* Science, 1980. **208**(4440): p. 177-9.

2. Engler, A.J., et al., *Matrix elasticity directs stem cell lineage specification.* Cell, 2006. **126**(4): p. 677-89.

3. Swaminathan, V., et al., *Mechanical stiffness grades metastatic potential in patient tumor cells and in cancer cell lines.* Cancer Res, 2011. **71**(15): p. 5075-80.

4. Alam, S.G., et al., *The nucleus is an intracellular propagator of tensile forces in NIH 3T3 fibroblasts.* J Cell Sci, 2015. **128**(10): p. 1901-11.

5. Davidson, P.M., et al., *Nuclear deformability constitutes a rate-limiting step during cell migration in 3-D environments.* Cell Mol Bioeng, 2014. **7**(3): p. 293-306.

6. Nava, M.M., et al., *Heterochromatin-Driven Nuclear Softening Protects the Genome against Mechanical Stress-Induced Damage.* Cell, 2020.

7. Isermann, P. and J. Lammerding, *Nuclear mechanics and mechanotransduction in health and disease.* Curr Biol, 2013. **23**(24): p. R1113-21.

8. Davidson, P.M. and J. Lammerding, *Broken nuclei--lamins, nuclear mechanics, and disease.* Trends Cell Biol, 2014. **24**(4): p. 247-56.

9. Hobson, C.M. and A.D. Stephens, *Modeling of Cell Nuclear Mechanics: Classes, Components, and Applications.* Cells, 2020. **9**(7).

10. Lang, I., M. Scholz, and R. Peters, *Molecular mobility and nucleocytoplasmic flux in hepatoma cells.* J Cell Biol, 1986. **102**(4): p. 1183-90.

11. Venkatesh, S. and J.L. Workman, *Histone exchange, chromatin structure and the regulation of transcription.* Nat Rev Mol Cell Biol, 2015. **16**(3): p. 178-89.

12. Stephens, A.D., E.J. Banigan, and J.F. Marko, *Chromatin's physical properties shape the nucleus and its functions.* Curr Opin Cell Biol, 2019. **58**: p. 76-84.

13. Stephens, A.D., et al., *Chromatin and lamin A determine two different mechanical response regimes of the cell nucleus.* Mol Biol Cell, 2017. **28**(14): p. 1984-1996.

14. Hobson, C.M., et al., *Correlating nuclear morphology and external force with combined atomic force microscopy and light sheet imaging separates roles of chromatin and lamin A/C in nuclear mechanics.* Mol Biol Cell, 2020.

15. Maurer, M. and J. Lammerding, *The Driving Force: Nuclear Mechanotransduction in Cellular Function, Fate, and Disease.* Annu Rev Biomed Eng, 2019. **21**: p. 443-468.

16. Worman, H.J., *Nuclear lamins and laminopathies.* J Pathol, 2012. **226**(2): p. 316-25.

17. Nmezi, B., et al., *Concentric organization of A- and B-type lamins predicts their distinct roles in the spatial organization and stability of the nuclear lamina.* Proc Natl Acad Sci U S A, 2019. **116**(10): p. 4307-4315.

18. Lammerding, J., et al., *Lamins A and C but not lamin B1 regulate nuclear mechanics.* J Biol Chem, 2006. **281**(35): p. 25768-80.

19. Hetzer, M.W., *The nuclear envelope.* Cold Spring Harb Perspect Biol, 2010. **2**(3): p. a000539.

20. Mejat, A. and T. Misteli, *LINC complexes in health and disease.* Nucleus, 2010. **1**(1): p. 40-52.

21. Neelam, S., et al., *Direct force probe reveals the mechanics of nuclear homeostasis in the mammalian cell.* Proc Natl Acad Sci U S A, 2015. **112**(18): p. 5720-5.

22. Haase, K., et al., *Extracellular Forces Cause the Nucleus to Deform in a Highly Controlled Anisotropic Manner.* Scientific Reports, 2016. **6**.

23. Hanson, L., et al., *Vertical nanopillars for in situ probing of nuclear mechanics in adherent cells.* Nature Nanotechnology, 2015. **10**(6): p. 554-U92.

24. Rosso, G., I. Liashkovich, and V. Shahin, *In Situ Investigation of Interrelationships Between Morphology and Biomechanics of Endothelial and Glial Cells and their Nuclei.* Adv Sci (Weinh), 2019. **6**(1): p. 1801638.

25. Wang, X., et al., *Mechanical stability of the cell nucleus - roles played by the cytoskeleton in nuclear deformation and strain recovery.* Journal of Cell Science, 2018. **131**(13).

26. Maniotis, A.J., C.S. Chen, and D.E. Ingber, *Demonstration of mechanical connections between integrins, cytoskeletal filaments, and nucleoplasm that stabilize nuclear structure.* Proc Natl Acad Sci U S A, 1997. **94**(3): p. 849-54.

27. Wang, N., J.P. Butler, and D.E. Ingber, *Mechanotransduction across the cell surface and through the cytoskeleton.* Science, 1993. **260**(5111): p. 1124-7.

28. Hu, S., et al., *Prestress mediates force propagation into the nucleus.* Biochem Biophys Res Commun, 2005. **329**(2): p. 423-8.

29. Tajik, A., et al., *Transcription upregulation via force-induced direct stretching of chromatin.* Nat Mater, 2016. **15**(12): p. 1287-1296.

30. Wu, J., et al., *Actomyosin pulls to advance the nucleus in a migrating tissue cell.* Biophys J, 2014. **106**(1): p. 7-15.

31. Khatau, S.B., et al., *A perinuclear actin cap regulates nuclear shape.* Proceedings of the National Academy of Sciences of the United States of America, 2009. **106**(45): p. 19017-19022.

32. Kim, J.K., et al., *Nuclear lamin A/C harnesses the perinuclear apical actin cables to protect nuclear morphology (vol 8, 2017).* Nature Communications, 2018. **9**.

33. Lammerding, J. and K. Wolf, *Nuclear envelope rupture: Actin fibers are putting the squeeze on the nucleus.* J Cell Biol, 2016. **215**(1): p. 5-8.

34. Makhija, E., D.S. Jokhun, and G.V. Shivashankar, *Nuclear deformability and telomere dynamics are regulated by cell geometric constraints.* Proc Natl Acad Sci U S A, 2016. **113**(1): p. E32-40.

35. Damodaran, K., et al., *Compressive force induces reversible chromatin condensation and cell geometry dependent transcriptional response.* Mol Biol Cell, 2018: p. mbcE18040256.

36. Kim, D.H., S. Cho, and D. Wirtz, *Tight coupling between nucleus and cell migration through the perinuclear actin cap.* Journal of Cell Science, 2014. **127**(11): p. 2528-2541.

37. Lovett, D.B., et al., *Modulation of Nuclear Shape by Substrate Rigidity.* Cell Mol Bioeng, 2013. **6**(2): p. 230-238.

38. Chancellor, T.J., et al., *Actomyosin tension exerted on the nucleus through nesprin-1 connections influences endothelial cell adhesion, migration, and cyclic strain-induced reorientation.* Biophys J, 2010. **99**(1): p. 115-23.

39. Cabianca, D.S. and S.M. Gasser, *Spatial segregation of heterochromatin: Uncovering functionality in a multicellular organism.* Nucleus, 2016. **7**(3): p. 301-7.

40. Solovei, I., et al., *Nuclear architecture of rod photoreceptor cells adapts to vision in mammalian evolution.* Cell, 2009. **137**(2): p. 356-68.

41. Swift, J., et al., *Nuclear lamin-A scales with tissue stiffness and enhances matrix-directed differentiation.* Science, 2013. **341**(6149): p. 1240104.

42. Lherbette, M., et al., *Atomic Force Microscopy microrheology reveals large structural inhomogeneities in single cellnuclei.* Scientific Reports, 2017. **7**.

43. Liu, H.J., et al., *In Situ Mechanical Characterization of the Cell Nucleus by Atomic Force Microscopy.* Acs Nano, 2014. **8**(4): p. 3821-3828.

44. Schape, J., et al., *Influence of Lamin A on the Mechanical Properties of Amphibian Oocyte Nuclei Measured by Atomic Force Microscopy.* Biophysical Journal, 2009. **96**(10): p. 4319-4325.

45. Dahl, K.N., et al., *Power-law rheology of isolated nuclei with deformation mapping of nuclear substructures.* Biophys J, 2005. **89**(4): p. 2855-64.

46. Balakrishnan, S., et al., *A Nondimensional Model Reveals Alterations in Nuclear Mechanics upon Hepatitis C Virus Replication.* Biophysical Journal, 2019. **116**(7): p. 1328-1339.

47. Xia, Y., et al., *Nuclear rupture at sites of high curvature compromises retention of DNA repair factors.* J Cell Biol, 2018. **217**(11): p. 3796-3808.

48. Krause, M., J. te Riet, and K. Wolf, *Probing the compressibility of tumor cell nuclei by combined atomic force-confocal microscopy.* Physical Biology, 2013. **10**(6).

49. Beicker, K., et al., *Vertical Light Sheet Enhanced Side-View Imaging for AFM Cell Mechanics Studies.* Scientific Reports, 2018. **8**.

50. Neubert, E., et al., *Chromatin swelling drives neutrophil extracellular trap release.* Nature Communications, 2018. **9**.

51. Mazumder, A., et al., *Dynamics of chromatin decondensation reveals the structural integrity of a mechanically prestressed nucleus.* Biophys J, 2008. **95**(6): p. 3028-35.

52. Ali, M.R.K., et al., *Nuclear Membrane-Targeted Gold Nanoparticles Inhibit Cancer Cell Migration and Invasion.* Acs Nano, 2017. **11**(4): p. 3716-3726.

53. Gavara, N., *A beginner's guide to atomic force microscopy probing for cell mechanics.* Microsc Res Tech, 2017. **80**(1): p. 75-84.

54. Hutter, J.L. and J. Bechhoefer, *Calibration of Atomic-Force Microscope Tips.* Review of Scientific Instruments, 1993. **64**(7): p. 1868-1873.

55. Sader, J.E., et al., *Method for the Calibration of Atomic-Force Microscope Cantilevers.* Review of Scientific Instruments, 1995. **66**(7): p. 3789-3798.

56. Krieg, M., et al., *Atomic force microscopy-based mechanobiology.* Nature Reviews Physics, 2019. **1**(1): p. 41-57.

57. Keenen, M.M., et al., *HP1 proteins compact DNA into mechanically and positionally stable phase separated domains.* bioRxiv, 2020.

58. Guilluy, C., et al., *Isolated nuclei adapt to force and reveal a mechanotransduction pathway in the nucleus.* Nature Cell Biology, 2014. **16**(4): p. 376-+.

59. Karcher, H., et al., *A three-dimensional viscoelastic model for cell deformation with experimental verification.* Biophys J, 2003. **85**(5): p. 3336-49.

60. Lammerding, J., et al., *Lamin A/C deficiency causes defective nuclear mechanics and mechanotransduction.* J Clin Invest, 2004. **113**(3): p. 370-8.

61. Neuman, K.C. and A. Nagy, *Single-molecule force spectroscopy: optical tweezers, magnetic tweezers and atomic force microscopy.* Nat Methods, 2008. **5**(6): p. 491-505.

62. Irianto, J., et al., *Nuclear constriction segregates mobile nuclear proteins away from chromatin.* Mol Biol Cell, 2016. **27**(25): p. 4011-4020.

63. Davidson, P.M., et al., *Design of a microfluidic device to quantify dynamic intra-nuclear deformation during cell migration through confining environments.* Integr Biol (Camb), 2015. **7**(12): p. 1534-46.

64. Xia, Y., C.R. Pfeifer, and D.E. Discher, *Nuclear mechanics during and after constricted migration.* Acta Mechanica Sinica, 2019. **35**(2): p. 299-308.

65. Rowat, A.C., et al., *Nuclear envelope composition determines the ability of neutrophil-type cells to passage through micron-scale constrictions.* J Biol Chem, 2013. **288**(12): p. 8610-8.

66. Cao, X., et al., *A Chemomechanical Model for Nuclear Morphology and Stresses during Cell Transendothelial Migration.* Biophysical Journal, 2016. **111**(7): p. 1541-1552.

67. Harada, T., et al., *Nuclear lamin stiffness is a barrier to 3D migration, but softness can limit survival.* J Cell Biol, 2014. **204**(5): p. 669-82.

68. Irianto, J., et al., *DNA Damage Follows Repair Factor Depletion and Portends Genome Variation in Cancer Cells after Pore Migration.* Curr Biol, 2017. **27**(2): p. 210-223.

69. Denais, C.M., et al., *Nuclear envelope rupture and repair during cancer cell migration.* Science, 2016. **352**(6283): p. 353-8.

70. Elacqua, J.J., A.L. McGregor, and J. Lammerding, *Automated analysis of cell migration and nuclear envelope rupture in confined environments.* PLoS One, 2018. **13**(4): p. e0195664.

71. Raab, M., et al., *ESCRT III repairs nuclear envelope ruptures during cell migration to limit DNA damage and cell death.* Science, 2016. **352**(6283): p. 359-362.

72. Xia, Y., et al., *Rescue of DNA damage after constricted migration reveals a mechano-regulated threshold for cell cycle.* J Cell Biol, 2019.

73. Rowat, A.C., J. Lammerding, and J.H. Ipsen, *Mechanical properties of the cell nucleus and the effect of emerin deficiency.* Biophys J, 2006. **91**(12): p. 4649-64.

74. Dahl, K.N., et al., *Distinct structural and mechanical properties of the nuclear lamina in Hutchinson-Gilford progeria syndrome.* Proceedings of the National Academy of Sciences of the United States of America, 2006. **103**(27): p. 10271-10276.

75. Dahl, K.N., et al., *The nuclear envelope lamina network has elasticity and a compressibility limit suggestive of a molecular shock absorber.* J Cell Sci, 2004. **117**(Pt 20): p. 4779-86.

76. Pajerowski, J.D., et al., *Physical plasticity of the nucleus in stem cell differentiation.* Proc Natl Acad Sci U S A, 2007. **104**(40): p. 15619-24.

77. Buxboim, A., I.L. Ivanovska, and D.E. Discher, *Matrix elasticity, cytoskeletal forces and physics of the nucleus: how deeply do cells 'feel' outside and in?* J Cell Sci, 2010. **123**(Pt 3): p. 297-308.

78. Shin, J.W., et al., *Lamins regulate cell trafficking and lineage maturation of adult human hematopoietic cells.* Proc Natl Acad Sci U S A, 2013. **110**(47): p. 18892-7.

79. Guilak, F., J.R. Tedrow, and R. Burgkart, *Viscoelastic properties of the cell nucleus.* Biochem Biophys Res Commun, 2000. **269**(3): p. 781-6.

80. Irianto, J., et al., *As a Nucleus Enters a Small Pore, Chromatin Stretches and Maintains Integrity, Even with DNA Breaks.* Biophys J, 2017. **112**(3): p. 446-449.

81. Wirtz, D., *Particle-tracking microrheology of living cells: principles and applications.* Annu Rev Biophys, 2009. **38**: p. 301-26.

82. Tseng, Y., et al., *Micro-organization and visco-elasticity of the interphase nucleus revealed by particle nanotracking.* J Cell Sci, 2004. **117**(Pt 10): p. 2159-67.

83. Erdel, F., M. Baum, and K. Rippe, *The viscoelastic properties of chromatin and the nucleoplasm revealed by scale-dependent protein mobility.* Journal of Physics-Condensed Matter, 2015. **27**(6).

84. Magde, D., E.L. Elson, and W.W. Webb, *Fluorescence correlation spectroscopy. II. An experimental realization.* Biopolymers, 1974. **13**(1): p. 29-61.

85. Hinde, E., et al., *In vivo pair correlation analysis of EGFP intranuclear diffusion reveals DNA-dependent molecular flow.* Proc Natl Acad Sci U S A, 2010. **107**(38): p. 16560-5.

86. Politz, J.C., et al., *Intranuclear diffusion and hybridization state of oligonucleotides measured by fluorescence correlation spectroscopy in living cells.* Proc Natl Acad Sci U S A, 1998. **95**(11): p. 6043-8.

87. Dross, N., et al., *Mapping eGFP oligomer mobility in living cell nuclei.* PLoS One, 2009. **4**(4): p. e5041.

88. Capoulade, J., et al., *Quantitative fluorescence imaging of protein diffusion and interaction in living cells.* Nat Biotechnol, 2011. **29**(9): p. 835-9.

89. Axelrod, D., et al., *Mobility measurement by analysis of fluorescence photobleaching recovery kinetics.* Biophys J, 1976. **16**(9): p. 1055-69.

90. Kirby, T.J. and J. Lammerding, *Emerging views of the nucleus as a cellular mechanosensor.* Nat Cell Biol, 2018. **20**(4): p. 373-381.

91. Janota, C.S., F.J. Calero-Cuenca, and E.R. Gomes, *The role of the cell nucleus in mechanotransduction.* Curr Opin Cell Biol, 2020. **63**: p. 204-211.

92. Hamouda, M.S., C. Labouesse, and K.J. Chalut, *Nuclear mechanotransduction in stem cells.* Curr Opin Cell Biol, 2020. **64**: p. 97-104.

93. Donnaloja, F., et al., *Lamin A/C Mechanotransduction in Laminopathies.* Cells, 2020. **9**(5).

94. Enyedi, B. and P. Niethammer, *Nuclear membrane stretch and its role in mechanotransduction.* Nucleus, 2017. **8**(2): p. 156-161.

95. Cho, S., J. Irianto, and D.E. Discher, *Mechanosensing by the nucleus: From pathways to scaling relationships.* J Cell Biol, 2017. **216**(2): p. 305-315.

96. Donnaloja, F., et al., *Mechanosensing at the Nuclear Envelope by Nuclear Pore Complex Stretch Activation and Its Effect in Physiology and Pathology.* Front Physiol, 2019. **10**: p. 896.

97. Nava, M.M., et al., *Heterochromatin-Driven Nuclear Softening Protects the Genome against Mechanical Stress-Induced Damage.* Cell, 2020. **181**(4): p. 800-817 e22.

98. Gilbert, H.T.J., et al., *Nuclear decoupling is part of a rapid protein-level cellular response to high-intensity mechanical loading.* Nat Commun, 2019. **10**(1): p. 4149.

99. Elosegui-Artola, A., et al., *Force Triggers YAP Nuclear Entry by Regulating Transport across Nuclear Pores.* Cell, 2017. **171**(6): p. 1397-1410 e14.

100. Pocaterra, A., P. Romani, and S. Dupont, *YAP/TAZ functions and their regulation at a glance.* J Cell Sci, 2020. **133**(2).

101. Dupont, S., et al., *Role of YAP/TAZ in mechanotransduction.* Nature, 2011. **474**(7350): p. 179-83.

102. Heo, S.J., et al., *Biophysical Regulation of Chromatin Architecture Instills a Mechanical Memory in Mesenchymal Stem Cells.* Sci Rep, 2015. **5**: p. 16895.

103. Hoffman, L.M., et al., *Mechanical stress triggers nuclear remodeling and the formation of transmembrane actin nuclear lines with associated nuclear pore complexes.* Mol Biol Cell, 2020. **31**(16): p. 1774-1787.

104. Malviya, A.N. and P.J. Rogue, *"Tell me where is calcium bred": clarifying the roles of nuclear calcium.* Cell, 1998. **92**(1): p. 17-23.

105. Resende, R.R., et al., *Nucleoplasmic calcium signaling and cell proliferation: calcium signaling in the nucleus.* Cell Commun Signal, 2013. **11**(1): p. 14.

106. Kim, T.J., et al., *Distinct mechanisms regulating mechanical force-induced Ca(2)(+) signals at the plasma membrane and the ER in human MSCs.* Elife, 2015. **4**: p. e04876.

107. Kim, T.J., et al., *Prolonged mechanical stretch initiates intracellular calcium oscillations in human mesenchymal stem cells.* PLoS One, 2014. **9**(10): p. e109378.

108. Stephens, A.D., et al., *Physicochemical mechanotransduction alters nuclear shape and mechanics via heterochromatin formation.* Mol Biol Cell, 2019. **30**(17): p. 2320-2330.

109. Iyer, K.V., et al., *Mechanical activation of cells induces chromatin remodeling preceding MKL nuclear transport.* Biophys J, 2012. **103**(7): p. 1416-28.

110. Inoh, H., et al., *Uni-axial cyclic stretch induces the activation of transcription factor nuclear factor kappaB in human fibroblast cells.* FASEB J, 2002. **16**(3): p. 405-7.

111. Jain, N., et al., *Cell geometric constraints induce modular gene-expression patterns via redistribution of HDAC3 regulated by actomyosin contractility.* Proc Natl Acad Sci U S A, 2013. **110**(28): p. 11349-54.

112. Damodaran, K., et al., *Compressive force induces reversible chromatin condensation and cell geometry-dependent transcriptional response.* Mol Biol Cell, 2018. **29**(25): p. 3039-3051.

113. Li, Y., et al., *Biophysical regulation of histone acetylation in mesenchymal stem cells.* Biophys J, 2011. **100**(8): p. 1902-9.

114. Wade, P.A., D. Pruss, and A.P. Wolffe, *Histone acetylation: chromatin in action.* Trends Biochem Sci, 1997. **22**(4): p. 128-32.

115. Cheung, P. and P. Lau, *Epigenetic regulation by histone methylation and histone variants.* Mol Endocrinol, 2005. **19**(3): p. 563-73.

116. Toth, K.F., et al., *Trichostatin A-induced histone acetylation causes decondensation of interphase chromatin.* Journal of Cell Science, 2004. **117**(18): p. 4277-4287.

117. Miranda, T.B., et al., *DZNep is a global histone methylation inhibitor that reactivates developmental genes not silenced by DNA methylation.* Mol Cancer Ther, 2009. **8**(6): p. 1579-88.

118. Anlas, A.A. and C.M. Nelson, *Tissue mechanics regulates form, function, and dysfunction.* Curr Opin Cell Biol, 2018. **54**: p. 98-105.

119. Heo, S.J., et al., *Differentiation alters stem cell nuclear architecture, mechanics, and mechano-sensitivity.* Elife, 2016. **5**.

120. Le, H.Q., et al., *Mechanical regulation of transcription controls Polycomb-mediated gene silencing during lineage commitment.* Nat Cell Biol, 2016. **18**(8): p. 864-75.

121. Henderson, J.T., et al., *Direct measurement of intranuclear strain distributions and RNA synthesis in single cells embedded within native tissue.* Biophys J, 2013. **105**(10): p. 2252-61.

122. Jacobson, E.C., et al., *Migration through a small pore disrupts inactive chromatin organization in neutrophil-like cells.* BMC Biol, 2018. **16**(1): p. 142.

123. Sun, J., et al., *Force-induced gene up-regulation does not follow the weak power law but depends on H3K9 demethylation.* Sci Adv, 2020. **6**(14): p. eaay9095.

124. Stephens, A.D., E.J. Banigan, and J.F. Marko, *Separate roles for chromatin and lamins in nuclear mechanics.* Nucleus, 2018. **9**(1): p. 119-124.

125. Finan, J.D., H.A. Leddy, and F. Guilak, *Osmotic stress alters chromatin condensation and nucleocytoplasmic transport.* Biochemical and Biophysical Research Communications, 2011. **408**(2): p. 230-235.

126. Gerlitz, G. and M. Bustin, *Efficient cell migration requires global chromatin condensation.* J Cell Sci, 2010. **123**(Pt 13): p. 2207-17.

127. Gerlitz, G., *The Emerging Roles of Heterochromatin in Cell Migration.* Front Cell Dev Biol, 2020. **8**: p. 394.

128. Wei, F., et al., *Stress fiber anisotropy contributes to force-mode dependent chromatin stretching and gene upregulation in living cells.* Nat Commun, 2020. **11**(1): p. 4902.

129. Alisafaei, F., et al., *Regulation of nuclear architecture, mechanics, and nucleocytoplasmic shuttling of epigenetic factors by cell geometric constraints.* Proc Natl Acad Sci U S A, 2019. **116**(27): p. 13200-13209.

130. Wang, Y., et al., *Orientation and repositioning of chromosomes correlate with cell geometry-dependent gene expression.* Mol Biol Cell, 2017. **28**(14): p. 1997-2009.

131. Bonne, G., et al., *Mutations in the gene encoding lamin A/C cause autosomal dominant Emery-Dreifuss muscular dystrophy.* Nat Genet, 1999. **21**(3): p. 285-8.

132. Bione, S., et al., *Identification of a novel X-linked gene responsible for Emery-Dreifuss muscular dystrophy.* Nat Genet, 1994. **8**(4): p. 323-7.

133. Cao, H. and R.A. Hegele, *Nuclear lamin A/C R482Q mutation in canadian kindreds with Dunnigan-type familial partial lipodystrophy.* Hum Mol Genet, 2000. **9**(1): p. 109-12.

134. Zwerger, M., et al., *Myopathic lamin mutations impair nuclear stability in cells and tissue and disrupt nucleo-cytoskeletal coupling.* Hum Mol Genet, 2013. **22**(12): p. 2335-49.

135. De Sandre-Giovannoli, A., et al., *Homozygous defects in LMNA, encoding lamin A/C nuclear-envelope proteins, cause autosomal recessive axonal neuropathy in human (Charcot-Marie-Tooth disorder type 2) and mouse.* Am J Hum Genet, 2002. **70**(3): p. 726-36.

136. De Sandre-Giovannoli, A., et al., *Lamin a truncation in Hutchinson-Gilford progeria.* Science, 2003. **300**(5628): p. 2055.

137. Moindrot, B., P. Bouvet, and F. Mongelard, *Chromatin Structure and Organization: The Relation with Gene Expression During Development and Disease*, in *Epigenetics: Development and Disease*, T.K. Kundu, Editor. 2013, Springer, Dordrecht. p. 373-396.

138. Herman, J.G., et al., *Inactivation of the CDKN2/p16/MTS1 Gene Is Frequently Associated with Aberrant DNA Methylation in All Common Human Cancers.* Cancer Research, 1995. **55**: p. 4525-4530.

139. Fraga, M.F., et al., *Loss of acetylation at Lys16 and trimethylation at Lys20 of histone H4 is a common hallmark of human cancer.* Nat Genet, 2005. **37**(4): p. 391-400.

140. Wolberg, W.H., W.N. Street, and O.L. Mangasarian, *Importance of nuclear morphology in breast cancer prognosis.* Clin Cancer Res, 1999. **5**(11): p. 3542-8.

141. Debes, J.D., et al., *p300 modulates nuclear morphology in prostate cancer.* Cancer Res, 2005. **65**(3): p. 708-12.

142. Shah, P., et al., *Nuclear Deformation Causes DNA Damage by Increasing Replication Stress.* Curr Biol, 2020.

143. Gerlitz, G. and M. Bustin, *The role of chromatin structure in cell migration.* Trends Cell Biol, 2011. **21**(1): p. 6-11.

144. Beicker, K., et al., *Vertical Light Sheet Enhanced Side-View Imaging for AFM Cell Mechanics Studies.* Sci Rep, 2018. **8**(1): p. 1504.

145. Nelsen, E., et al., *Combined Atomic Force Microscope and Volumetric Light Sheet System for Correlative Force and Fluorescence Mechanobiology Studies.* Sci Rep, 2020. **10**(1): p. 8133.

146. Georgiades, P., et al., *Reduction of coherent artefacts in super-resolution fluorescence localisation microscopy.* J Microsc, 2016. **264**(3): p. 375-383.

147. Hard, R., R. Zeh, and R.D. Allen, *Phase-randomized laser illumination for microscopy.* J Cell Sci, 1977. **23**: p. 335-43.

148. Kuhn, J.R. and T.D. Pollard, *Real-time measurements of actin filament polymerization by total internal reflection fluorescence microscopy.* Biophys J, 2005. **88**(2): p. 1387-402.

149. Mattheyses, A.L., K. Shaw, and D. Axelrod, *Effective elimination of laser interference fringing in fluorescence microscopy by spinning azimuthal incidence angle.* Microsc Res Tech, 2006. **69**(8): p. 642-7.

150. Boulanger, J., et al., *Fast high-resolution 3D total internal reflection fluorescence microscopy by incidence angle scanning and azimuthal averaging.* Proc Natl Acad Sci U S A, 2014. **111**(48): p. 17164-9.

151. Ellefsen, K.L., J.L. Dynes, and I. Parker, *Spinning-Spot Shadowless TIRF Microscopy.* PLoS One, 2015. **10**(8): p. e0136055.

152. Fiolka, R., et al., *Even illumination in total internal reflection fluorescence microscopy using laser light.* Microsc Res Tech, 2008. **71**(1): p. 45-50.

153. van 't Hoff, M., V. de Sars, and M. Oheim, *A programmable light engine for quantitative single molecule TIRF and HILO imaging.* Opt Express, 2008. **16**(22): p. 18495-504.

154. Zong, W., et al., *Shadowless-illuminated variable-angle TIRF (siva-TIRF) microscopy for the observation of spatial-temporal dynamics in live cells.* Biomed Opt Express, 2014. **5**(5): p. 1530-40.

155. Schreiber, B., K. Elsayad, and K.G. Heinze, *Axicon-based Bessel beams for flat-field illumination in total internal reflection fluorescence microscopy.* Opt Lett, 2017. **42**(19): p. 3880-3883.

156. Wu, Y.I., et al., *A genetically encoded photoactivatable Rac controls the motility of living cells.* Nature, 2009. **461**(7260): p. 104-8.

157. Yoo, S.K., et al., *Differential regulation of protrusion and polarity by PI3K during neutrophil motility in live zebrafish.* Dev Cell, 2010. **18**(2): p. 226-36.

158. Olarte, O.E., et al., *Light-sheet microscopy: a tutorial.* Advances in Optics and Photonics, 2018. **10**(1): p. 111-179.

159. Chen, B.C., et al., *Lattice light-sheet microscopy: imaging molecules to embryos at high spatiotemporal resolution.* Science, 2014. **346**(6208): p. 1257998.

160. Dean, K.M., et al., *Deconvolution-free Subcellular Imaging with Axially Swept Light Sheet Microscopy.* Biophys J, 2015. **108**(12): p. 2807-15.

161. Fadero, T.C., et al., *LITE microscopy: Tilted light-sheet excitation of model organisms offers high resolution and low photobleaching.* J Cell Biol, 2018. **217**(5): p. 1869-1882.

162. Gebhardt, J.C., et al., *Single-molecule imaging of transcription factor binding to DNA in live mammalian cells.* Nat Methods, 2013. **10**(5): p. 421-6.

163. Haslehurst, P., et al., *Fast volume-scanning light sheet microscopy reveals transient neuronal events.* Biomedical Optics Express, 2018. **9**(5): p. 2154-2167.

164. Liu, T.L., et al., *Observing the cell in its native state: Imaging subcellular dynamics in multicellular organisms.* Science, 2018. **360**(6386).

165. Royer, L.A., et al., *Adaptive light-sheet microscopy for long-term, high-resolution imaging in living organisms.* Nat Biotechnol, 2016. **34**(12): p. 1267-1278.

166. Zhao, T., et al., *Multicolor 4D Fluorescence Microscopy using Ultrathin Bessel Light Sheets.* Sci Rep, 2016. **6**: p. 26159.

167. Galland, R., et al., *3D high- and super-resolution imaging using single-objective SPIM.* Nat Methods, 2015. **12**(7): p. 641-4.

168. Kashekodi, A.B., et al., *Miniature scanning light-sheet illumination implemented in a conventional microscope.* Biomedical Optics Express, 2018. **9**(9): p. 4263-4274.

169. Zagato, E., et al., *Microfabricated devices for single objective single plane illumination microscopy (SoSPIM).* Opt Express, 2017. **25**(3): p. 1732-1745.

170. Sapoznik, E., et al., *A Single-Objective Light-Sheet Microscope with 200 nm-Scale Resolution.* bioRxiv, 2020.

171. Yang, B., et al., *Epi-illumination SPIM for volumetric imaging with high spatial-temporal resolution.* Nat Methods, 2019. **16**(6): p. 501-504.

172. Nelsen, E., et al., *Combined Atomic Force Microscope and Volumetric Light Sheet System for Mechanobiology.* bioRxiv, 2019.

173. Liu, B., et al., *VIEW-MOD: a versatile illumination engine with a modular optical design for fluorescence microscopy.* Opt Express, 2019. **27**(14): p. 19950-19972.

174. Ponjavic, A., et al., *Sensitive light-sheet microscopy in multiwell plates using an AFM cantilever.* Biomed Opt Express, 2018. **9**(12): p. 5863-5880.

175. Voleti, V., et al., *Real-time volumetric microscopy of in vivo dynamics and large-scale samples with SCAPE 2.0.* Nat Methods, 2019. **16**(10): p. 1054-1062.

176. Bouchard, M.B., et al., *Swept confocally-aligned planar excitation (SCAPE) microscopy for high speed volumetric imaging of behaving organisms.* Nat Photonics, 2015. **9**(2): p. 113-119.

177. Kumar, S., et al., *High-speed 2D and 3D fluorescence microscopy of cardiac myocytes.* Opt Express, 2011. **19**(15): p. 13839-47.

178. Dunsby, C., *Optically sectioned imaging by oblique plane microscopy.* Opt Express, 2008. **16**(25): p. 20306-16.

179. Meddens, M.B., et al., *Single objective light-sheet microscopy for high-speed whole-cell 3D super-resolution.* Biomed Opt Express, 2016. **7**(6): p. 2219-36.

180. Ando, T., et al., *The 2018 correlative microscopy techniques roadmap.* J Phys D Appl Phys, 2018. **51**(44): p. 443001.

181. Bhat, S.V., et al., *Correlative atomic force microscopy quantitative imaging-laser scanning confocal microscopy quantifies the impact of stressors on live cells in real-time.* Sci Rep, 2018. **8**(1): p. 8305.

182. Zhou, L., et al., *Progress in the Correlative Atomic Force Microscopy and Optical Microscopy.* Sensors (Basel), 2017. **17**(4).

183. Bennet, M., et al., *Simultaneous Raman microspectroscopy and fluorescence imaging of bone mineralization in living zebrafish larvae.* Biophys J, 2014. **106**(4): p. L17-9.

184. Pully, V.V., A. Lenferink, and C. Otto, *Hybrid Rayleigh, Raman and two-photon excited fluorescence spectral confocal microscopy of living cells.* Journal of Raman Spectroscopy, 2010. **41**(6): p. 599-608.

185. de Boer, P., J.P. Hoogenboom, and B.N. Giepmans, *Correlated light and electron microscopy: ultrastructure lights up!* Nat Methods, 2015. **12**(6): p. 503-13.

186. van Rijnsoever, C., V. Oorschot, and J. Klumperman, *Correlative light-electron microscopy (CLEM) combining live-cell imaging and immunolabeling of ultrathin cryosections.* Nat Methods, 2008. **5**(11): p. 973-80.

187. Lee, S.H., *Optimal integration of wide field illumination and holographic optical tweezers for multimodal microscopy with ultimate flexibility and versatility.* Opt Express, 2018. **26**(7): p. 8049-8058.

188. Monkemoller, V., et al., *Multimodal super-resolution optical microscopy visualizes the close connection between membrane and the cytoskeleton in liver sinusoidal endothelial cell fenestrations.* Sci Rep, 2015. **5**: p. 16279.

189. Garbellotto, C. and J.M. Taylor, *Multi-purpose SLM-light-sheet microscope.* Biomed Opt Express, 2018. **9**(11): p. 5419-5436.

190. Gullapalli, R.R., et al., *Integrated multimodal microscopy, time-resolved fluorescence, and optical-trap rheometry: toward single molecule mechanobiology.* J Biomed Opt, 2007. **12**(1): p. 014012.

191. Khaw, I., et al., *Flat-field illumination for quantitative fluorescence imaging.* Opt Express, 2018. **26**(12): p. 15276-15288.

192. Tatsumi, H., Y. Katayama, and M. Sokabe, *Attachment of growth cones on substrate observed by multi-mode light microscopy.* Neurosci Res, 1999. **35**(3): p. 197-206.

193. Li, H. and H. Yang, *A versatile optical microscope for time-dependent single-molecule and single-particle spectroscopy.* J Chem Phys, 2018. **148**(12): p. 123316.

194. Annibale, P., A. Dvornikov, and E. Gratton, *Electrically tunable lens speeds up 3D orbital tracking.* Biomed Opt Express, 2015. **6**(6): p. 2181-90.

195. Ma, P., et al., *Volumetric optical mapping in early embryonic hearts using light-sheet microscopy.* Biomed Opt Express, 2016. **7**(12): p. 5120-5128.

196. Fahrbach, F.O., et al., *Rapid 3D light-sheet microscopy with a tunable lens.* Opt Express, 2013. **21**(18): p. 21010-26.

197. Grewe, B.F., et al., *Fast two-layer two-photon imaging of neuronal cell populations using an electrically tunable lens.* Biomed Opt Express, 2011. **2**(7): p. 2035-46.

198. Bathe-Peters, M., P. Annibale, and M.J. Lohse, *All-optical microscope autofocus based on an electrically tunable lens and a totally internally reflected IR laser.* Optics Express, 2018. **26**(3): p. 2359-2368.

199. Annibale, P., A. Dvornikov, and E. Gratton, *Optical measurement of focal offset in tunable lenses.* Opt Express, 2016. **24**(2): p. 1031-6.

200. Jabbour, J.M., et al., *Optical axial scanning in confocal microscopy using an electrically tunable lens.* Biomed Opt Express, 2014. **5**(2): p. 645-52.

201. Gao, L., et al., *3D live fluorescence imaging of cellular dynamics using Bessel beam plane illumination microscopy.* Nat Protoc, 2014. **9**(5): p. 1083-101.

202. Hecht, E., *Optics*. 4th ed. 2002, Reading, Mass.: Addison-Wesley. vi, 698 p.

203. Wolf, E., *Electromagnetic Diffraction in Optical Systems .1. An Integral Representation of the Image Field.* Proceedings of the Royal Society of London Series a-Mathematical and Physical Sciences, 1959. **253**(1274): p. 349-357.

204. Richards, B. and E. Wolf, *Electromagnetic Diffraction in Optical Systems .2. Structure of the Image Field in an Aplanatic System.* Proceedings of the Royal Society of London Series a-Mathematical and Physical Sciences, 1959. **253**(1274): p. 358-379.

205. Chon, H.S., et al., *Dependence of transverse and longitudinal resolutions on incident Gaussian beam widths in the illumination part of optical scanning microscopy.* J Opt Soc Am A Opt Image Sci Vis, 2007. **24**(1): p. 60-7.

206. Durnin, J., J. Miceli, Jr., and J.H. Eberly, *Diffraction-free beams.* Phys Rev Lett, 1987. **58**(15): p. 1499-1501.

207. Chang, B.J., K.M. Dean, and R. Fiolka, *Systematic and quantitative comparison of lattice and Gaussian light-sheets.* Opt Express, 2020. **28**: p. 27052-27077.

208. Fahrbach, F.O., et al., *Self-reconstructing sectioned Bessel beams offer submicron optical sectioning for large fields of view in light-sheet microscopy.* Opt Express, 2013. **21**(9): p. 11425-40.

209. Wang, X., et al., *Mechanical stability of the cell nucleus - roles played by the cytoskeleton in nuclear deformation and strain recovery.* J Cell Sci, 2018. **131**(13).

210. Krause, M., J. Te Riet, and K. Wolf, *Probing the compressibility of tumor cell nuclei by combined atomic force-confocal microscopy.* Phys Biol, 2013. **10**(6): p. 065002.

211. Yeo, T.T.E., et al., *Autofocusing for Tissue Microscopy.* Image and Vision Computing, 1993. **11**(10): p. 629-639.

212. Waters, J. and T. Wittmann, *Quantitative Imaging in Cell Biology*. 2014: Elsevier Science.

213. Kumar, A., et al., *Dual-view plane illumination microscopy for rapid and spatially isotropic imaging.* Nat Protoc, 2014. **9**(11): p. 2555-73.

214. Kress, H., et al., *Filopodia act as phagocytic tentacles and pull with discrete steps and a load-dependent velocity.* Proc Natl Acad Sci U S A, 2007. **104**(28): p. 11633-8.

215. Mattila, P.K. and P. Lappalainen, *Filopodia: molecular architecture and cellular functions.* Nat Rev Mol Cell Biol, 2008. **9**(6): p. 446-54.

216. Verdeny-Vilanova, I., et al., *3D motion of vesicles along microtubules helps them to circumvent obstacles in cells.* J Cell Sci, 2017. **130**(11): p. 1904-1916.

217. Biskou, O., et al., *The type III intermediate filament vimentin regulates organelle distribution and modulates autophagy.* Plos One, 2019. **14**(1).

218. Eckes, B., et al., *Impaired mechanical stability, migration and contractile capacity in vimentin-deficient fibroblasts.* J Cell Sci, 1998. **111 (Pt 13)**: p. 1897-907.

219. Nekrasova, O.E., et al., *Vimentin intermediate filaments modulate the motility of mitochondria.* Mol Biol Cell, 2011. **22**(13): p. 2282-9.

220. Helfand, B.T., et al., *Vimentin organization modulates the formation of lamellipodia.* Mol Biol Cell, 2011. **22**(8): p. 1274-89.

221. Fu, Y., et al., *Axial superresolution via multiangle TIRF microscopy with sequential imaging and photobleaching.* Proc Natl Acad Sci U S A, 2016. **113**(16): p. 4368-73.

222. Tokunaga, M., N. Imamoto, and K. Sakata-Sogawa, *Highly inclined thin illumination enables clear single-molecule imaging in cells.* Nat Methods, 2008. **5**(2): p. 159-61.

223. Boustany, N.N. and N.V. Thakor, *Light scatter spectroscopy and imaging of celular and subcellular events*, in *Biomedical Photonics*. 2003, CRC Press.

224. Baumgart, E. and U. Kubitscheck, *Scanned light sheet microscopy with confocal slit detection.* Opt Express, 2012. **20**(19): p. 21805-14.

225. Chang, B.J., et al., *Universal light-sheet generation with field synthesis.* Nat Methods, 2019. **16**(3): p. 235-238.

226. Vangindertael, J., et al., *An introduction to optical super-resolution microscopy for the adventurous biologist.* Methods Appl Fluoresc, 2018. **6**(2): p. 022003.

227. Meyvis, T.K., et al., *Fluorescence recovery after photobleaching: a versatile tool for mobility and interaction measurements in pharmaceutical research.* Pharm Res, 1999. **16**(8): p. 1153-62.

228. Tarbet, H.J., et al., *Site-specific glycosylation regulates the form and function of the intermediate filament cytoskeleton.* Elife, 2018. **7**.

229. Vorselen, D., et al., *Superresolved microparticle traction force microscopy reveals subcellular force patterns in immune cell-target interactions.* bioRxiv, 2019: p. 431221.

230. Fernandes, T., et al., *Synchronous, Crosstalk-free Correlative AFM and Confocal Microscopies/Spectroscopies.* arXiv, 2020.

231. Zhang, Q., et al., *Quantitative refractive index distribution of single cell by combining phase-shifting interferometry and AFM imaging.* Sci Rep, 2017. **7**(1): p. 2532.

232. Sun, M., et al., *Multiple membrane tethers probed by atomic force microscopy.* Biophys J, 2005. **89**(6): p. 4320-9.

233. Schmitz, J., M. Benoit, and K.E. Gottschalk, *The viscoelasticity of membrane tethers and its importance for cell adhesion.* Biophys J, 2008. **95**(3): p. 1448-59.

234. Hosu, B.G., et al., *Eukaryotic membrane tethers revisited using magnetic tweezers.* Phys Biol, 2007. **4**(2): p. 67-78.

235. Iarovaia, O.V., et al., *Nucleolus: A Central Hub for Nuclear Functions.* Trends Cell Biol, 2019. **29**(8): p. 647-659.

236. Nunez Villacis, L., et al., *New Roles for the Nucleolus in Health and Disease.* Bioessays, 2018. **40**(5): p. e1700233.

237. Li, L., et al., *Real-time imaging of Huntingtin aggregates diverting target search and gene transcription.* Elife, 2016. **5**.

238. Yeung, T., et al., *Receptor activation alters inner surface potential during phagocytosis.* Science, 2006. **313**(5785): p. 347-351.

239. Liu, B., et al., *VIEW-MOD: a versatile illumination engine with a modular optical design for fluorescence microscopy.* Optics Express, 2019. **27**(14): p. 19950-19972.

240. Blumenthal, D., et al., *Universal Approach to FRAP Analysis of Arbitrary Bleaching Patterns.* Scientific Reports, 2015. **5**.

241. Elson, E.L., *Fluorescence correlation spectroscopy: past, present, future.* Biophys J, 2011. **101**(12): p. 2855-70.

242. Machan, R., Y.H. Foo, and T. Wohland, *On the Equivalence of FCS and FRAP: Simultaneous Lipid Membrane Measurements.* Biophys J, 2016. **111**(1): p. 152-61.

243. Scipioni, L., et al., *Local raster image correlation spectroscopy generates high-resolution intracellular diffusion maps.* Commun Biol, 2018. **1**: p. 10.

244. Krieger, J.W., et al., *Dual-color fluorescence cross-correlation spectroscopy on a single plane illumination microscope (SPIM-FCCS).* Opt Express, 2014. **22**(3): p. 2358-75.

245. Wohland, T., et al., *Single plane illumination fluorescence correlation spectroscopy (SPIM-FCS) probes inhomogeneous three-dimensional environments.* Opt Express, 2010. **18**(10): p. 10627-41.

246. Singh, A.P., et al., *3D Protein Dynamics in the Cell Nucleus.* Biophys J, 2017. **112**(1): p. 133-142.

247. Buchholz, J., et al., *Widefield High Frame Rate Single-Photon SPAD Imagers for SPIM-FCS.* Biophys J, 2018. **114**(10): p. 2455-2464.

248. Rieckher, M., et al., *A customized light sheet microscope to measure spatio-temporal protein dynamics in small model organisms.* PLoS One, 2015. **10**(5): p. e0127869.

249. Sankaran, J., et al., *Accuracy and precision in camera-based fluorescence correlation spectroscopy measurements.* Anal Chem, 2013. **85**(8): p. 3948-54.

250. Schindelin, J., et al., *Fiji: an open-source platform for biological-image analysis.* Nat Methods, 2012. **9**(7): p. 676-82.

251. A, P. and S.C. Weber, *Evidence for and against Liquid-Liquid Phase Separation in the Nucleus.* Noncoding RNA, 2019. **5**(4).

252. Kitamura, A., Y. Nakayama, and M. Kinjo, *Efficient and dynamic nuclear localization of green fluorescent protein via RNA binding.* Biochem Biophys Res Commun, 2015. **463**(3): p. 401-6.

253. Miermont, A., et al., *Severe osmotic compression triggers a slowdown of intracellular signaling, which can be explained by molecular crowding.* Proc Natl Acad Sci U S A, 2013. **110**(14): p. 5725-30.

254. Royer, L.A., et al., *ClearVolume: open-source live 3D visualization for light-sheet microscopy.* Nat Methods, 2015. **12**(6): p. 480-1.

255. Wachsmuth, M., W. Waldeck, and J. Langowski, *Anomalous diffusion of fluorescent probes inside living cell nuclei investigated by spatially-resolved fluorescence correlation spectroscopy.* J Mol Biol, 2000. **298**(4): p. 677-89.

256. Braeckmans, K., et al., *Line FRAP with the confocal laser scanning microscope for diffusion measurements in small regions of 3-D samples.* Biophys J, 2007. **92**(6): p. 2172-83.

257. Maertens, G., et al., *Measuring protein-protein interactions inside living cells using single color fluorescence correlation spectroscopy. Application to human immunodeficiency virus type 1 integrase and LEDGF/p75.* FASEB J, 2005. **19**(8): p. 1039-41.

258. Seksek, O., J. Biwersi, and A.S. Verkman, *Translational diffusion of macromolecule-sized solutes in cytoplasm and nucleus.* J Cell Biol, 1997. **138**(1): p. 131-42.

259. Potma, E.O., et al., *Reduced protein diffusion rate by cytoskeleton in vegetative and polarized dictyostelium cells.* Biophys J, 2001. **81**(4): p. 2010-9.

260. Kilic, S., et al., *Phase separation of 53BP1 determines liquid-like behavior of DNA repair compartments.* EMBO J, 2019. **38**(16): p. e101379.

261. Pryde, F., et al., *53BP1 exchanges slowly at the sites of DNA damage and appears to require RNA for its association with chromatin.* J Cell Sci, 2005. **118**(Pt 9): p. 2043-55.

262. Kimura, H. and P.R. Cook, *Kinetics of core histones in living human cells: little exchange of H3 and H4 and some rapid exchange of H2B.* J Cell Biol, 2001. **153**(7): p. 1341-53.

263. Butin-Israeli, V., et al., *Nuclear lamin functions and disease.* Trends in Genetics, 2012. **28**(9): p. 464-471.

264. Lammerding, J., et al., *Abnormal nuclear shape and impaired mechanotransduction in emerin-deficient cells.* J Cell Biol, 2005. **170**(5): p. 781-91.

265. Tocco, V.J., et al., *The nucleus is irreversibly shaped by motion of cell boundaries in cancer and non-cancer cells.* J Cell Physiol, 2018. **233**(2): p. 1446-1454.

266. Hatch, E.M. and M.W. Hetzer, *Nuclear envelope rupture is induced by actin-based nucleus confinement.* Journal of Cell Biology, 2016. **215**(1): p. 27-36.

267. Patteson, A.E., et al., *Vimentin protects cells against nuclear rupture and DNA damage during migration.* J Cell Biol, 2019.

268. Lee, J.S.H., et al., *Nuclear lamin A/C deficiency induces defects in cell mechanics, polarization, and migration.* Biophysical Journal, 2007. **93**(7): p. 2542-2552.

269. Shimamoto, Y., et al., *Nucleosome-nucleosome interactions via histone tails and linker DNA regulate nuclear rigidity.* Mol Biol Cell, 2017. **28**(11): p. 1580-1589.

270. Stephens, A.D., et al., *Chromatin histone modifications and rigidity affect nuclear morphology independent of lamins.* Mol Biol Cell, 2018. **29**(2): p. 220-233.

271. Schreiner, S.M., et al., *The tethering of chromatin to the nuclear envelope supports nuclear mechanics.* Nat Commun, 2015. **6**: p. 7159.

272. Zhang, Q., et al., *Local, transient tensile stress on the nuclear membrane causes membrane rupture.* Mol Biol Cell, 2019. **30**(7): p. 899-906.

273. Katiyar, A., et al., *Nuclear size changes caused by local motion of cell boundaries unfold the nuclear lamina and dilate chromatin and intranuclear bodies.* Soft Matter, 2019. **15**(45): p. 9310-9317.

274. Donnaloja, F., et al., *Mechanosensing at the Nuclear Envelope by Nuclear Pore Complex Stretch Activation and Its Effect in Physiology and Pathology.* Frontiers in Physiology, 2019. **10**.

275. Cho, S., et al., *Mechanosensing by the Lamina Protects against Nuclear Rupture, DNA Damage, and Cell-Cycle Arrest.* Dev Cell, 2019. **49**(6): p. 920-935 e5.

276. Kim, D.H., et al., *Volume regulation and shape bifurcation in the cell nucleus.* Journal of Cell Science, 2015. **128**(18): p. 3375-3385.

277. Finan, J.D., et al., *Nonlinear Osmotic Properties of the Cell Nucleus.* Annals of Biomedical Engineering, 2009. **37**(3): p. 477-491.

278. Johnson, K.L., *Contact mechanics*. 1985, Cambridge Cambridgeshire ; New York: Cambridge University Press. xi, 452 p.

279. Vaziri, A. and M.R.K. Mofrad, *Mechanics and deformation of the nucleus in micropipette aspiration experiment.* Journal of Biomechanics, 2007. **40**(9): p. 2053-2062.

280. Caille, N., et al., *Contribution of the nucleus to the mechanical properties of endothelial cells.* J Biomech, 2002. **35**(2): p. 177-87.

281. Banigan, E.J., A.D. Stephens, and J.F. Marko, *Mechanics and Buckling of Biopolymeric Shells and Cell Nuclei.* Biophys J, 2017. **113**(8): p. 1654-1663.

282. Bennett, R.R., et al., *Elastic-Fluid Model for DNA Damage and Mutation from Nuclear Fluid Segregation Due to Cell Migration.* Biophys J, 2017. **112**(11): p. 2271-2279.

283. Mattaj, I.W., *Sorting out the nuclear envelope from the endoplasmic reticulum.* Nat Rev Mol Cell Biol, 2004. **5**(1): p. 65-9.

284. Buxboim, A., et al., *Coordinated increase of nuclear tension and lamin-A with matrix stiffness outcompetes lamin-B receptor that favors soft tissue phenotypes.* Mol Biol Cell, 2017. **28**(23): p. 3333-3348.

285. Chu, F.Y., S.C. Haley, and A. Zidovska, *On the origin of shape fluctuations of the cell nucleus.* Proc Natl Acad Sci U S A, 2017. **114**(39): p. 10338-10343.

286. Jacobson, E.C., et al., *Migration through a small pore disrupts inactive chromatin organization in neutrophil-like cells.* Bmc Biology, 2018. **16**.

287. Dimitriadis, E.K., et al., *Determination of elastic moduli of thin layers of soft material using the atomic force microscope.* Biophysical Journal, 2002. **82**(5): p. 2798-2810.

288. Sen, S., S. Subramanian, and D.E. Discher, *Indentation and adhesive probing of a cell membrane with AFM: theoretical model and experiments.* Biophys J, 2005. **89**(5): p. 3203-13.

289. Nobel, P.S., *Boyle-Vant Hoff Relation.* Journal of Theoretical Biology, 1969. **23**(3): p. 375-&.

290. Vella, D., et al., *The indentation of pressurized elastic shells: from polymeric capsules to yeast cells.* Journal of the Royal Society Interface, 2012. **9**(68): p. 448-455.

291. Rauschert, I., et al., *Promoter hypermethylation as a mechanism for Lamin A/C silencing in a subset of neuroblastoma cells.* Plos One, 2017. **12**(4).

292. Davidson, P.M. and J. Lammerding, *Broken nuclei - lamins, nuclear mechanics, and disease.* Trends in Cell Biology, 2014. **24**(4): p. 247-256.

293. Sakaue-Sawano, A., et al., *Visualizing spatiotemporal dynamics of multicellular cell-cycle progression.* Cell, 2008. **132**(3): p. 487-98.

294. Holaska, J.M., *Emerin and the nuclear lamina in muscle and cardiac disease.* Circ Res, 2008. **103**(1): p. 16-23.

295. Butin-Israeli, V., et al., *Nuclear lamin functions and disease.* Trends Genet, 2012. **28**(9): p. 464-71.

296. Helfand, B.T., et al., *Chromosomal regions associated with prostate cancer risk localize to lamin B-deficient microdomains and exhibit reduced gene transcription.* J Pathol, 2012. **226**(5): p. 735-45.

297. Papanicolaou, G.N. and H.F. Traut, *The diagnostic value of vaginal smears in carcinoma of the uterus. 1941.* Arch Pathol Lab Med, 1997. **121**(3): p. 211-24.

298. Lu, C., et al., *Nuclear shape and orientation features from H&E images predict survival in early-stage estrogen receptor-positive breast cancers.* Lab Invest, 2018. **98**(11): p. 1438-1448.

299. Radhakrishnan, A., et al., *Machine Learning for Nuclear Mechano-Morphometric Biomarkers in Cancer Diagnosis.* Sci Rep, 2017. **7**(1): p. 17946.

300. Davidson, P.M., et al., *High-throughput microfluidic micropipette aspiration device to probe time-scale dependent nuclear mechanics in intact cells.* Lab Chip, 2019. **19**(21): p. 3652-3663.

301. Ou, H.D., et al., *ChromEMT: Visualizing 3D chromatin structure and compaction in interphase and mitotic cells.* Science, 2017. **357**(6349).

302. Rauschert, I., et al., *Promoter hypermethylation as a mechanism for Lamin A/C silencing in a subset of neuroblastoma cells.* PLoS One, 2017. **12**(4): p. e0175953.

303. Vaziri, A., H. Lee, and M.R.K. Mofrad, *Deformation of the cell nucleus under indentation: Mechanics and mechanisms.* Journal of Materials Research, 2006. **21**(8): p. 2126-2135.

304. Wei, F., et al., *Poroelasticity of cell nuclei revealed through atomic force microscopy characterization.* Applied Physics Letters, 2016. **109**: p. 213701-213705.

305. Shimi, T., et al., *Structural organization of nuclear lamins A, C, B1, and B2 revealed by superresolution microscopy.* Mol Biol Cell, 2015. **26**(22): p. 4075-86.

306. Kittisopikul, M., et al., *Quantitative Analysis of Nuclear Lamins Imaged by Super-Resolution Light Microscopy.* Cells, 2019. **8**(4).

307. Turgay, Y., et al., *The molecular architecture of lamins in somatic cells.* Nature, 2017. **543**(7644): p. 261-264.

308. Woodcock, C.L. and R.P. Ghosh, *Chromatin Higher-order Structure and Dynamics.* Cold Spring Harbor Perspectives in Biology, 2010. **2**(5).

309. Aebi, U., et al., *The nuclear lamina is a meshwork of intermediate-type filaments.* Nature, 1986. **323**(6088): p. 560-4.

310. Lionetti, M.C., et al., *Chromatin and Cytoskeletal Tethering Determine Nuclear Morphology in Progerin-Expressing Cells.* Biophys J, 2020. **118**(9): p. 2319-2332.

311. Fletcher, D.A. and R.D. Mullins, *Cell mechanics and the cytoskeleton.* Nature, 2010. **463**(7280): p. 485-92.

312. Kornberg, R.D., *Chromatin structure: a repeating unit of histones and DNA.* Science, 1974. **184**(4139): p. 868-71.

313. Deveraux, S., R. Allena, and D. Aubry, *A numerical model suggests the interplay between nuclear plasticity and stiffness during a perfusion assay.* J Theor Biol, 2017. **435**: p. 62-77.

314. Giverso, C., A. Grillo, and L. Preziosi, *Influence of nucleus deformability on cell entry into cylindrical structures.* Biomech Model Mechanobiol, 2014. **13**(3): p. 481-502.

315. Heo, S.-J., et al., *Nuclear softening expedites interstitial cell migration in fibrous networks and dense connective tissues.* Science Advances, 2020. **6**.

316. Mukherjee, A., et al., *Nuclear Plasticity Increases Susceptibility to Damage During Confined Migration.* bioRxiv, 2020.

317. Wren, N.S., et al., *Modeling nuclear blebs in a nucleoskeleton of independent filament networks.* Cell Mol Bioeng, 2012. **5**(1): p. 73-81.

318. Funkhouser, C.M., et al., *Mechanical model of blebbing in nuclear lamin meshworks.* Proc Natl Acad Sci U S A, 2013. **110**(9): p. 3248-53.

319. Deviri, D., D.E. Discher, and S.A. Safran, *Rupture Dynamics and Chromatin Herniation in Deformed Nuclei.* Biophys J, 2017. **113**(5): p. 1060-1071.

320. Deviri, D., et al., *Scaling laws indicate distinct nucleation mechanisms of holes in the nuclear lamina.* Nature Physics, 2019. **15**(8): p. 823-829.

321. Li, Y., et al., *Moving Cell Boundaries Drive Nuclear Shaping during Cell Spreading.* Biophys J, 2015. **109**(4): p. 670-86.

322. Kim, D.H., A.B. Chambliss, and D. Wirtz, *The multi-faceted role of the actin cap in cellular mechanosensation and mechanotransduction.* Soft Matter, 2013. **9**(23): p. 5516-5523.

323. Thiam, H.R., et al., *Perinuclear Arp2/3-driven actin polymerization enables nuclear deformation to facilitate cell migration through complex environments.* Nat Commun, 2016. **7**: p. 10997.

324. Paonessa, F., et al., *Microtubules Deform the Nuclear Membrane and Disrupt Nucleocytoplasmic Transport in Tau-Mediated Frontotemporal Dementia.* Cell Rep, 2019. **26**(3): p. 582-593 e5.

325. Biedzinski, S., et al., *Microtubules deform the nucleus and force chromatin reorganization during early differentiation of human hematopoietic stem cells.* bioRxiv, 2019.

326. Janmey, P.A., et al., *Viscoelastic properties of vimentin compared with other filamentous biopolymer networks.* J Cell Biol, 1991. **113**(1): p. 155-60.

327. Kreplak, L., et al., *Exploring the mechanical behavior of single intermediate filaments.* J Mol Biol, 2005. **354**(3): p. 569-77.

328. Lowery, J., et al., *Intermediate Filaments Play a Pivotal Role in Regulating Cell Architecture and Function.* J Biol Chem, 2015. **290**(28): p. 17145-53.

329. Patteson, A.E., et al., *Vimentin protects cells against nuclear rupture and DNA damage during migration.* J Cell Biol, 2019. **218**(12): p. 4079-4092.

330. Shimi, T., et al., *The A- and B-type nuclear lamin networks: microdomains involved in chromatin organization and transcription.* Genes Dev, 2008. **22**(24): p. 3409-21.

331. Earle, A.J., et al., *Mutant lamins cause nuclear envelope rupture and DNA damage in skeletal muscle cells.* Nat Mater, 2020. **19**(4): p. 464-473.

332. Panorchan, P., et al., *Nuclear envelope breakdown requires overcoming the mechanical integrity of the nuclear lamina.* J Biol Chem, 2004. **279**(42): p. 43462-7.

333. Banerjee, A., et al., *Viscoelastic behavior of human lamin A proteins in the context of dilated cardiomyopathy.* PLoS One, 2013. **8**(12): p. e83410.

334. Ji, J.Y., et al., *Cell nuclei spin in the absence of lamin b1.* J Biol Chem, 2007. **282**(27): p. 20015-26.

335. Vortmeyer-Krause, M., et al., *Lamin B2 follows lamin A/C- mediated nuclear mechanics and cancer cell invasion efficacy.* bioRxiv, 2020.

336. Dechat, T., et al., *Nuclear lamins.* Cold Spring Harb Perspect Biol, 2010. **2**(11): p. a000547.

337. Furusawa, T., et al., *Chromatin decompaction by the nucleosomal binding protein HMGN5 impairs nuclear sturdiness.* Nat Commun, 2015. **6**: p. 6138.

338. Herraez-Aguilar, D., et al., *Multiple particle tracking analysis in isolated nuclei reveals the mechanical phenotype of leukemia cells.* Sci Rep, 2020. **10**(1): p. 6707.

339. Luxton, G.W., et al., *Linear arrays of nuclear envelope proteins harness retrograde actin flow for nuclear movement.* Science, 2010. **329**(5994): p. 956-9.

340. Banigan, E.J., et al., *Heterogeneous CD8+ T cell migration in the lymph node in the absence of inflammation revealed by quantitative migration analysis.* PLoS Comput Biol, 2015. **11**(2): p. e1004058.

341. Liu, Y., K. Mollaeian, and J. Ren, *Finite element modeling of living cells for AFM indentation-based biomechanical characterization.* Micron, 2019. **116**: p. 108-115.

342. Chen, J. and G. Lu, *Finite element modelling of nanoindentation based methods for mechanical properties of cells.* J Biomech, 2012. **45**(16): p. 2810-6.

343. Krause, M., et al., *Cell migration through three-dimensional confining pores: speed accelerations by deformation and recoil of the nucleus.* Philos Trans R Soc Lond B Biol Sci, 2019. **374**(1779): p. 20180225.

344. Liu, L., et al., *Nucleus and nucleus-cytoskeleton connections in 3D cell migration.* Exp Cell Res, 2016. **348**(1): p. 56-65.

345. Ahearn, M.J., et al., *The association of nuclear blebs with aneuploidy in human acute leukemia.* Cancer Res, 1974. **34**(11): p. 2887-96.

346. Coffinier, C., et al., *Deficiencies in lamin B1 and lamin B2 cause neurodevelopmental defects and distinct nuclear shape abnormalities in neurons.* Mol Biol Cell, 2011. **22**(23): p. 4683-93.

347. Tamashunas, A.C., et al., *High-throughput gene screen reveals modulators of nuclear shape.* Mol Biol Cell, 2020: p. mbcE19090520.

348. Zhong, Z., K.L. Wilson, and K.N. Dahl, *Beyond lamins other structural components of the nucleoskeleton.* Methods Cell Biol, 2010. **98**: p. 97-119.

349. Vargas, J.D., et al., *Transient nuclear envelope rupturing during interphase in human cancer cells.* Nucleus, 2012. **3**(1): p. 88-100.

350. Peters, R., *Translocation through the nuclear pore complex: selectivity and speed by reduction-of-dimensionality.* Traffic, 2005. **6**(5): p. 421-7.

351. Stephens, A.D., *Chromatin rigidity provides mechanical and genome protection.* Mutation Research/Fundamental and Molecular Mechanisms of Mutagenesis, 2020. **821**: p. 111712.

352. Parada, L. and T. Misteli, *Chromosome positioning in the interphase nucleus.* Trends Cell Biol, 2002. **12**(9): p. 425-32.

353. Briand, N. and P. Collas, *Laminopathy-causing lamin A mutations reconfigure lamina-associated domains and local spatial chromatin conformation.* Nucleus, 2018. **9**(1): p. 216-226.

354. McCord, R.P., et al., *Correlated alterations in genome organization, histone methylation, and DNA-lamin A/C interactions in Hutchinson-Gilford progeria syndrome.* Genome Res, 2013. **23**(2): p. 260-9.

355. Crisp, M., et al., *Coupling of the nucleus and cytoplasm: role of the LINC complex.* J Cell Biol, 2006. **172**(1): p. 41-53.

356. Lombardi, M.L., et al., *The interaction between nesprins and sun proteins at the nuclear envelope is critical for force transmission between the nucleus and cytoskeleton.* J Biol Chem, 2011. **286**(30): p. 26743-53.

357. Hale, C.M., et al., *Dysfunctional connections between the nucleus and the actin and microtubule networks in laminopathic models.* Biophys J, 2008. **95**(11): p. 5462-75.

358. Meinke, P., et al., *Muscular dystrophy-associated SUN1 and SUN2 variants disrupt nuclear-cytoskeletal connections and myonuclear organization.* PLoS Genet, 2014. **10**(9): p. e1004605.

359. Boquet-Pujadas, A., et al., *BioFlow: a non-invasive, image-based method to measure speed, pressure and forces inside living cells.* Sci Rep, 2017. **7**(1): p. 9178.

360. Lele, T.P., R.B. Dickinson, and G.G. Gundersen, *Mechanical principles of nuclear shaping and positioning.* Journal of Cell Biology, 2018. **217**(10): p. 3330-3342.

361. Hobson, C.M., et al., *Combined Selective Plane Illumination Microscopy and FRAP Maps Intranuclear Diffusion of NLS-GFP.* Biophys J, 2020.

362. Lomakin, A.J., et al., *The nucleus acts as a ruler tailoring cell responses to spatial constraints.* Science, 2020. **370**(6514).

363. Venturini, V., et al., *The nucleus measures shape changes for cellular proprioception to control dynamic cell behavior.* Science, 2020. **370**(6514).

364. Cosgrove, B.D., et al., *Nuclear envelope wrinkling predicts mesenchymal progenitor cell mechano-response in 2D and 3D microenvironments.* Biomaterials, 2021: p. 120662.

365. Skamrahl, M., et al., *Simultaneous Quantification of the Interplay Between Molecular Turnover and Cell Mechanics by AFM-FRAP.* Small, 2019. **15**(40): p. e1902202.